IDENTIFICATION AND DEVELOPMENT OF A RELIABLE FRAMEWORK TO PREDICT PASSIVE SCALAR TRANSPORT FOR TURBULENT BOUNDED SHEAR FLOWS

A DISSERTATION IN

Mechanical Engineering

and

Mathematics

Presented to the Faculty of the University of
Missouri-Kansas City in partial fulfillment
of the requirements for the degree

DOCTOR OF PHILOSOPHY

by

MATTHIAS ZIEFUSS

B.S., RWTH Aachen, Germany, 2015

M.S., RWTH Aachen, Germany, 2017

IDENTIFICATION AND DEVELOPMENT OF A RELIABLE FRAMEWORK

TO PREDICT PASSIVE SCALAR TRANSPORT

FOR TURBULENT BOUNDED SHEAR FLOWS

MATTHIAS ZIEFUSS, Candidate for the Doctor of Philosophy Degree

University of Missouri-Kansas City, 2020

ABSTRACT

Heat transfer modeling plays an integral role in optimization and development of highly efficient modern thermal-fluid systems. However, currently available heat flux models suffer from fundamental shortcomings. For example, their development is based on the general notion that an accurate prediction of the flow field will guarantee an appropriate prediction of the thermal field, as the Reynolds Analogy does. Furthermore, literature about advanced models that aim to overcome this notion, does not provide reliable information about prediction capabilities. These advanced models can be separated into two distinct heat flux model categories, namely the implicit and explicit models. Both model categories differ fundamentally in their mathematical and physical formulation.

Hence, this dissertation presents a comprehensive assessment of the Reynolds Analogy regarding steady and unsteady calculations. It further analyses the entropy generation capability in detail and evaluates the prediction accuracy of implicit and explicit models when applied to turbulent shear flows of fluids with different Prandtl numbers. Moreover, the implicit and explicit models are modified such that important thermal second order statistics are included. This enables deeper insight into the mechanics of thermal dissipation and delivers a better understanding towards the sensitivity and reliability of predictions using heat flux models. Finally, to overcome the shortcomings of the Reynolds Analogy in unsteady calculations, an anisotropic extension is proposed.

This dissertation shows that even for first order statistics within steady state calculations, the Reynolds Analogy is only appropriate for fluids with Prandtl numbers around unity. For second order statistics within unsteady simulations, the Reynolds Analogy could provide acceptable results only if an appropriate grid design/resolution is provided that allows resolving essential dynamics of the thermal field. Concerning entropy generation, the Reynolds Analogy provides acceptable results only for mean entropy generation, while it fails to predict entropy generation at small/sub-grid scales. The anisotropic extension of the Reynolds Analogy is a promising approach to overcome these shortcomings.

Furthermore and concerning the implicit and explicit heat flux models, this work shows that only the explicit framework is potentially capable of dealing with complex turbulent thermal fields and to address longstanding shortcomings of currently available models, if the flow field is predicted accurately. Moreover, it has been shown that thermal time scale plays an integral role to predict thermal phenomena, particularly those of fluids with low/high Pr numbers.

APPROVAL PAGE

The faculty listed below, appointed by the Dean of the School of Graduate Studies, have examined a theses titled ”Identification and Development of a Reliable Framework to Predict Passive Scalar Transport for Turbulent Bounded Shear Flows”, presented by Matthias Ziefuss, candidate for the Interdisciplinary Ph.D. in Mechanical Engineering and Mathematics, and certify that in their opinion is worthy of acceptance.

Supervisory Committee

Amirfarhang Mehdizadeh, Dr. Ing., Committee Chair
Department of Civil and Mechanical Engineering, UMKC

Majid Bani-Yaghoub, Ph.D., Co-Committee Chair
Department of Mathematics and Statistics, UMKC

James Mahoney, P.E.
Department of Civil and Mechanical Engineering, UMKC

Sarvenaz Sobhansarbandi, Ph.D.
Department of Civil and Mechanical Engineering, UMKC

Fengpeng Sun, Ph.D.
Department of Earth and Environmental Sciences, UMKC

Nader Karimi, Ph.D.
School of Engineering and Materials Science, Queen Mary University of London

TABLE OF CONTENTS

Page

LIST OF ILLUSTRATIONS

Figure Page

LIST OF TABLES

Table Page

ABBREVIATIONS

res resolved

rms root mean square

sgs subgrid-scale

AFM algebraic heat flux model

CFD Computational Fluid Dynamics

DNS Direct Numerical Simulation

EDM Eddy Diffusivity model

GGDH generalized gradient diffusion hypothesis

IDDES improved delayed ettached Eddy simulation

SGDH Simple Gradient Diffusion Hypothesis

LES Large Eddy Simulation

nMAE normalized mean absolute error

RANS Reynolds Averaged Navier Stokes equation

THF turbulent heat flux

URANS Unsteady Reynolds Averaged Navier Stokes equation

ACKNOWLEDGEMENTS

First and foremost I would like to thank my adviser, Dr. Amirfarhang Mehdizadeh, for being a reliable mentor, support, and guide. Special thanks to my lab mates, Rohit Saini and Mohan Kumar, who warmly welcomed me. A grateful thank you to all my committee members, Dr. Bani-Yaghoub, P.E. Mahoney, Dr. Sobhansarbandi, Dr. Sun and Dr. Karimi, for taking time to be a part of my journey. I would also like to thank Wolf for his technical support in the wide field of coding languages. Dennis and Alex shall not be forgotten, as they supplied me with many memorable memes. Moreover, I have to thank my loving family who always encourages me to follow my dreams. Last but not least I have to thank my wonderful girlfriend who had to miss me too long.

CHAPTER 1

INTRODUCTION

The majority of flows that occur in engineering and nature are turbulent and confined by solid walls. Hence, turbulent shear flows play an integral role in development and design of various advanced and emerging systems. In this context, not only the fluid flow is of importance, but also the passive transport of heat in this turbulent environment plays a major role in many applications. These include cooling systems for nuclear power plants, where liquid metal is used as coolant [71, 12], boiler systems for biomass combustion [50], and heat exchange devices in the petroleum/petrochemical industry [78], to name only a few. All previously mentioned applications share an important commonality: experimental investigations are either prohibitively expensive or not possible [106]. Nevertheless, optimization of these systems requires detailed insight into the complex dynamics of heat transfer inside, which necessitates reliable models. In addition, various systems use fluids with significantly different Prandtl (denoted as Pr) numbers (ranging from Pr $<<$ 1 for liquid metal to a few hundred for crude oils). This variety in Pr numbers not only stresses the required prediction capabilities of turbulent heat flux models at an acceptable level of accuracy, it also challenges numerical simulations in terms of stability and mesh design.

The complexity of this phenomenon has introduced a major challenge in understanding and modeling of the turbulent heat transfer in the past decade [24]. The underlying and inevitable challenge is that the flow field (turbulent momentum) and heat transfer are based on the same physical mechanism of cross-streamwise mixing of fluid elements [107]. Hence, a reliable model for the turbulent momentum is a mandatory condition for a model of turbulent heat transfer. As a consequence, the main focus in research and modeling was focused on the momentum field in the past decades [107]. Moreover, this focus led to the fundamental assumption that a correct prediction of the momentum transport leads to an appropriate prediction of heat transfer. This analogy is based on the eddy diffusivity approach and is known as the Reynolds Analogy [125].

While this concept is a drastic simplification, it is still widely applied to a majority of industrial applications of Computational Fluid Dynamics (CFD) when first-order statistical quantities such as mean temperature and Nußelt number are of interest. It is worth noting that these applications mostly deal with working fluids with Pr number around unity [7]. As a consequence, the applicability of the Reynolds Analogy for predicting second order statistics, such as temperature variance, has not been thoroughly assessed—even in investigations where shortcomings of this analogy are discussed [54]. More importantly, this led to a lack of comprehensive investigations, which include first and second order statistics when applied to turbulent flows of working fluids with Pr number divergent from unity, especially for high Pr numbers. Thus, Chapter 2 of this dissertation includes a comprehensive study of the Reynolds Analogy for first and second order statistics when applied to 3D wall-bounded shear flows with various fluid properties. The assessment includes sensitivity analyses with respect to the turbulence model, grid resolution and performance of the Reynolds Analogy. These assessments are carried out for steady state (Reynolds Averaged Navier Stokes equation (RANS) simulations) and unsteady simulations (Unsteady Reynolds Averaged Navier Stokes equation (URANS)/Large Eddy Simulation (LES)) where the analogy is a subgrid scale model.

Furthermore, turbulent flows are thermodynamic processes and the directions of all such processes are restricted by the second law of thermodynamics. Thus, this law can be used for critical evaluation of turbulence and heat transfer models as discussed in [91]. For fluids hat include a temperature field, the second law of thermodynamics states that irreversibilities decrease the available energy of the working fluid [4], which leads to an increase of system entropy [41, 120, 119]. Regarding the use of this entropy concept, several publications can be found in literature investigating the processes both numerically and analytically for a better understanding [91, 88, 46, 59]. These studies include steady and unsteady state investigations. Concerning heat transfer modeling, it is worth noting that both steady and unsteady approaches mainly employ the Reynolds Analogy to predict thermal quantities. But the currently available literature does not

provide sufficient information about the prediction capability of the Reynolds Analogy for entropy generation. Thus, Chapter 3 provides a comprehensive assessment of the capability of the Reynolds Analogy to predict the entropy generation dynamics particularly through heat transfer in different turbulent environments, i.e. working fluids with different Prandtl and Reynolds numbers.

Unsteady simulations in the framework of LES technique have proven to be a promising approach to predict complex heat and fluid flow phenomena in many thermo-fluid systems, for instance automotive applications [29, 69, 97]. In LES, the large three-dimensional unsteady turbulent motions are explicitly computed, whilst a turbulence closure model accounts for the influence of the unresolved more universal scales [48, 100]. The computational expense of LES is significantly lower than in fully resolved DNS. Only small scale turbulent structures with a small amount of turbulent energy have to be modeled, which are—in this context—believed to be universal, homogeneous and isotropic. This simplifies the turbulence modeling, improves the predictive capability compared to approaches based on the solution of the RANS, and makes LES valid for a broad range of flow situations with complex physics. However, despite the anisotropic behavior of small turbulent thermal structures, isotropic models are most often employed in LES of turbulent heat transport. Thereby, the subgrid-scale thermal diffusivity is traditionally represented based on the Reynolds analogy and the concept of turbulent Prandtl number. To overcome that issue, a new wall-adapted anisotropic explicit heat flux model concept for LES is proposed in Chapter 5. This concept extends the Reynolds Analogy with a generalized gradient diffusion hypothesis (GGDH) term to support anisotropic features.

While the previously introduced LES-approach is an extension of the Reynolds Analogy extended with a GGDH-term, several more different concepts have been proposed to enhance heat transfer prediction capabilities. These concepts are e.g. the GGDH—which in contrast to the Reynolds Analogy—can employ separate time scales for the velocity and temperature field [14, 33], or algebraic heat flux models (AFM), which introduce additional correlations to predict the heat flux [62, 55, 44]. However,

these approaches have never been extensively assessed and their applications are often limited to specific configurations (e.g. 2D, steady state, working fluid with Pr number around unity), for which they have been tuned. Comprehensive reviews of these methods for various Pr numbers can be found in [76, 23]. Nevertheless, it should be noted that AFM may offer promising potential to overcome the short comings of the Reynolds Analogy, based on limited information in the literature, e.g. [25, 124, 42]. There are two major variants of the AFM which are distinguished by two fundamentally different approaches: implicit and explicit models. The former is a result of truncating the unmodeled flux equation, e.g. [39, 27], while the latter is derived based on the representation theorem, e.g. [124, 64]. There are few recent efforts on applications of the implicit methods to predict thermal behavior of low Pr number fluids in turbulent wall bounded channel flow [107, 96], using modified and simplified versions of the implicit model. Although, some improvement was achieved compared to the Reynolds Analogy, these studies do not provide some relevant statistical quantities, such as the heat flux or dissipation of temperature variance. Therefore, Chapter 6 focuses on these models and aims to provide a comprehensive assessment of them when applied to a fully attached turbulent boundary layer using different working fluids, including a sensitivity analysis with respect to the turbulence model used to describe the flow field. More importantly, both implicit and explicit models considered here, and in recent literature, use only mechanical time scale in their formulations. As a result of this, relevance and effect of thermal time scale in prediction capability of heat flux models remains unclear. This part of the dissertation aims to study the effects of the thermal time scale on the predictive capabilities of both model categories. Therefore, the existing mechanical time scale is modified by including the thermal time scale in both models.

CHAPTER 2

A COMPREHENSIVE ASSESSMENT OF THE REYNOLDS ANALOGY IN PREDICTING HEAT TRANSFER IN TURBULENT WALL-BOUNDED SHEAR FLOWS

The paper is published in *International Journal of Heat and Fluid Flow* and written by Matthias Ziefuss[1] and Amirfarhang Mehdizadeh[1]*.

[1] Civil and Mechanical Engineering Department, School of Computing and Engineering, University of Missouri-Kansas City, Kansas City, MO 64110, USA
* Corresponding author: mehdizadeha@umkc.edu

International Journal of Heat and Fluid Flow, Volume 81, February 2020, 108527; https://doi.org/10.1016/j.ijheatfluidflow.2019.108527

2.1 **Abstract**

Heat transfer modeling plays a major role in design and optimization of modern and efficient thermal-fluid systems. However, currently the available models suffer from a fundamental shortcoming: their development is based on the general notion that accurate prediction of the flow field will guarantee an appropriate prediction of the thermal field, known as the Reynolds Analogy. This investigation presents a comprehensive assessment of the capability of the Reynolds Analogy in predicting turbulent heat transfer when applied to turbulent shear flows of fluids with different Prandtl numbers. It turns out that the Reynolds Analogy is able to provide acceptable results for first order statistics only when fluids with Prandtl number close to unity are considered. Further, it is shown that unsteady simulations could provide acceptable results on the second order statistics concerning fluids with different Prandtl numbers, if appropriate grid design/resolution is provided that allows to resolve essential dynamics of the thermal field. However, accurate prediction of higher order statistics close to solid surface requires more advanced heat transfer models that can provide accurate information on thermal time scales, in case the grid is too coarse to support accurate resolving of the essential thermal dynamics in these regions.

2.2 Introduction

There are many reasons why turbulent heat transfer plays an integral role in the development and optimization of various advanced systems. These include cooling systems for nuclear power plants, where liquid metal is used as coolant [71, 12], boiler systems for biomass combustion [50], and heat exchange devices in the petroleum/petrochemical industry [78], to name only a few. All former mentioned applications share an important commonality: experimental investigations are either not possible or prohibitively expensive [106]. However, optimization of these systems requires information on the complex dynamics of heat/mass transfer inside the systems, which in turn necessitate the application of reliable models. Further, the application of different fluids in various systems with significantly different Prandtl (denoted as Pr) numbers (ranging from $Pr \ll 1$ for liquid metal to a few thousands for crude oils) imposes an additional challenge for models in predicting turbulent heat transfer phenomena at an acceptable level of accuracy.

Understanding and correctly modeling turbulent heat transfer have introduced a major challenge in the past decades due to the complexity of this phenomenon [24]. The first and underlying challenge when modeling turbulent heat transfer is its strong and complex coupling to the turbulent flow field. As a result, an appropriate model for momentum transport (flow field) is a necessary condition to predict the turbulent heat transfer accurately. Therefore, the main focus has been put on the turbulent flow field modeling in the past few decades [107].

The physical mechanism of cross-streamwise mixing is known to be the major underlying mechanism for both momentum and heat transfer [107]. Thus, it is often assumed that the turbulent heat transfer can be solely predicted by knowledge of the momentum transport, leading to the development of the Reynolds Analogy, a well-known concept based on the eddy diffusivity approach [107]. While this analogy is a drastic simplification of the physical mechanism, it has been applied successfully to a large majority of industrial applications of CFD to predict first order statistical quantities such as the mean temperature and Nusselt number, throughout the past decades.

Additionally, it should be noted that these applications mostly deal with working fluids with Pr number around unity [7].

Müller et al. [70] showed that the Reynolds Analogy faces severe challenges when used to capture essential dynamics of turbulent heat transfer in fluids with Pr number different than unity as well as for flows with natural or mixed convection. However, their investigation was limited to first order statistics of the temperature field, i.e. temperature variance was not studied.

To address the shortcomings of the Reynolds Analogy, several approaches have been proposed to enhance heat transfer prediction capabilities. These approaches are e.g. the GGDH, which in contrast to the Reynolds Analogy, employ separate time scales for the velocity and temperature field [14, 33], or AFM, which introduce additional correlations to predict the heat flux [62, 55, 44]. However, these approaches have never been extensively assessed and their applications are often limited to specific configurations (e.g. 2D, steady state, working fluid with Pr number around unity), for which they have been tuned. Comprehensive reviews of these methods for various Pr numbers can be found in [76, 25].

As mentioned before, applications of the Reynolds Analogy have been mostly limited to first order statistics of working fluids with Pr number around unity, e.g. [15, 25, 107]. As a result, the capability of the Reynolds Analogy for predicting second order statistics, such as temperature variance, has not been thoroughly assessed—even in investigations where shortcomings of this analogy are discussed [54]. Moreover, there is a lack of comprehensive assessment including first and second order statistics of this analogy when applied to turbulent flows of fluids with Pr number significantly different than unity, especially for high Pr numbers. The current study presents a comprehensive assessment of the predictive capabilities of the Reynolds Analogy for first and second order statistics when applied to 3D wall-bounded shear flow with various fluid properties. The assessment includes sensitivity analyses with respect to the turbulence model, grid resolution and performance of the Reynolds Analogy as a sub-grid scale model in unsteady simulations.

The present investigation provides useful directions towards the development of more advanced turbulent heat flux models by identifying major shortcomings of the Reynolds Analogy. Furthermore, it provides some guidance on grid requirement to appropriately resolve the temperature spectrum when dealing with low Pr number fluids.

The chapter is organized as follows: in section 2.3, the employed turbulence models along with relevant transport equations will be presented and discussed. In section 2.4, an overview of test cases and the numerical approach is provided. Results obtained from the simulations are presented and discussed in section 2.5. The chapter concludes with a summary and conclusion in section 2.6.

2.3 Governing Equations

The current study aims to provide a comprehensive assessment of the prediction capabilities of the Reynolds Analogy when applied to turbulent attached wall-bounded shear flows of fluids with different Pr numbers. Towards this end, various aspects of this analogy will be investigated. First, the sensitivity of the Reynolds Analogy with respect to the turbulence model employed to predict the flow field will be investigated. Therefore, two different turbulence models, i.e. $k-\omega-$ SST and $k-\epsilon-\zeta-f$, will be used for steady state (RANS) simulations. In order to preclude effects of numerical instabilities/uncertainties on the model performance, a 3-dimensional computational domain with different mesh resolutions have been used for the RANS simulations.

As the next step, performance of the Reynolds Analogy in unsteady simulations where the analogy provides a subgrid-scale (sgs) model is assessed. Sensitivity to grid resolution is investigated as it is an indicator of basic properties of sgs-models. The $k-\omega-$SST-IDDES model will be used for the unsteady simulations. This model is a hybrid URANS/LES model and is able to provide an accurate prediction of the flow field—comparable to wall-modeled LES—at affordable computational cost [11]. Furthermore, this model treats the near-wall region in URANS-model, while transitioning to LES-mode away from the wall. This will allow investigation on the dynamics of the transition of the Reynolds Analogy from URANS to LES-mode, where this analogy operates as

a sgs-model. The mathematical formulation of turbulence models used in the current study in conjunction with other transport equations (energy and temperature variance) will be presented and discussed in the following.

2.3.1 Turbulence models

2.3.1.1 The $k-\omega-$ SST model

The $k-\omega-$ SST model is one of the most commonly used models. It employs two transport equations, one for turbulent kinetic energy k and one for the inverse of dissipation rate ω to provide necessary turbulence scales [61]. The model equations read:

$$\frac{Dk}{Dt} = \frac{\partial}{\partial x_i}\Big[\Big(\nu + \frac{\nu_t}{\sigma_k}\Big)\frac{\partial k}{\partial x_i}\Big] + \tilde{P_k} - \beta^\star \rho\omega k, \tag{2.1}$$

$$\frac{D\omega}{Dt} = \frac{\partial}{\partial x_i}\Big[\Big(\nu + \frac{\nu_t}{\sigma_\omega}\Big)\frac{\partial \omega}{\partial x_i}\Big] + 2(1-F_1)\frac{\sigma_{\omega 2}}{\omega}\frac{\partial k}{\partial x_i}\frac{\partial \omega}{\partial x_i} + \frac{\gamma}{\nu_t}P_k - \beta\omega^2, \tag{2.2}$$

with $\tilde{P_k} = \min(P_k; c_l\epsilon)$ and $P_k = \tau_{ij}\frac{\partial \overline{u_i}}{\partial x_j}$ as mechanical turbulent production. Further details on model constants and functions, i.e. $c_l, \beta, \beta^\star, \gamma, \tau_{ij}, \sigma_{\omega 2}, F_1$, are provided in [61].

2.3.1.2 The $k-\epsilon-\zeta-f$ model

The $k-\epsilon-\zeta-f$ is well known to be able to predict near wall effects in shear flows [28]. In addition to the transport equation for kinetic energy k and its dissipation ε, two more equations must be solved. The first one is a transport equation for the velocity scale ratio $\zeta = \overline{v^2}/k$ and the second one is an elliptic relaxation concept to

sensitize ζ. For brevity, the model is referred as $\zeta - f$ model. The model equations are as follows:

$$\frac{Dk}{Dt} = \frac{\partial}{\partial x_i}\Big[\Big(\nu + \frac{\nu_t}{\sigma_k}\Big)\frac{\partial k}{\partial x_i}\Big] + P_k - \varepsilon, \tag{2.3}$$

$$\frac{D\varepsilon}{Dt} = \frac{\partial}{\partial x_i}\Big[\Big(\nu + \frac{\nu_t}{\sigma_\varepsilon}\Big)\frac{\partial \varepsilon}{\partial x_i}\Big] + \frac{C_{\varepsilon 1}P_k - C_{\varepsilon 2}\varepsilon}{\tau}, \tag{2.4}$$

$$\frac{D\zeta}{Dt} = \frac{\partial}{\partial x_i}\Big[\Big(\nu + \frac{\nu_t}{\sigma_\zeta}\Big)\frac{\partial \zeta}{\partial x_i}\Big] - \frac{\zeta}{k}P_k + f, \tag{2.5}$$

$$L^2\frac{\partial^2 f}{\partial x_i^2} - f = \frac{1}{\tau}\Big(c_1 + C_2'\frac{P_k}{\varepsilon}\Big)\Big(\zeta - \frac{2}{3}\Big), \tag{2.6}$$

with $P_k = \tau_{ij}\partial\overline{u_i}/\partial x_j$ and $\nu_t = C_\mu \zeta k \tau$. The corresponding set of coefficients is given in table 2.1. To complete the model, the Kolmogorov time and length scales are used in combination with the realizability constrains introduced as lower bounds [16]:

$$\tau = \max\left(\min\left(\frac{k}{\varepsilon}; \frac{a}{\sqrt{6}C_\mu|S|\zeta}\right); C_\tau\Big(\frac{\nu}{\varepsilon}\Big)^{1/2}\right), \tag{2.7}$$

$$L = C_L \max\left(\min\left(\frac{k^{3/2}}{\varepsilon}; \frac{k^{1/2}}{\sqrt{6}C_\mu|S|\zeta}\right); C_\eta\Big(\frac{\nu^3}{\varepsilon}\Big)^{1/4}\right). \tag{2.8}$$

Table 2.1: Model coefficients for the $k - \epsilon - \zeta - f$ model

a	$C\mu$	$C_{\varepsilon 1}$	$C_{\varepsilon 2}$	c_1	C_2'	σ_k	σ_ε	σ_ζ	C_τ	C_L	C_η
0.6	0.22	$1.4(1 + 0.012/\zeta)$	1.9	0.4	0.65	1	1.3	1.2	6.0	0.36	85

2.3.1.3 The $k-\omega-$ SST-IDDES model

$k-\omega-$ SST-IDDES employs a modified version of $k-\omega-$ SST model to improve near-wall prediction and enable unsteady calculations. It is defined with two transport equations for k and ω:

$$\frac{Dk}{Dt} = \frac{\partial}{\partial x_i}\Big[\Big(\nu + \frac{\nu_t}{\sigma_k}\Big)\frac{\partial k}{\partial x_i}\Big] + P_k - \sqrt{k^3}/l_{IDDES}, \tag{2.9}$$

$$\frac{D\omega}{Dt} = \frac{\partial}{\partial x_i}\Big[\Big(\nu + \frac{\nu_t}{\sigma_\omega}\Big)\frac{\partial \omega}{\partial x_i}\Big] + 2(1-F_1)\frac{\sigma_{\omega 2}}{\omega}\frac{\partial k}{\partial x_i}\frac{\partial \omega}{\partial x_i} + \frac{\gamma}{\nu_t}P_k - \beta\omega^2, \tag{2.10}$$

where blending function F_1, production term P_k, and model constants (γ, σ_k, σ_w, σ_{w2} and β) are imported from the original $k-\omega-$SST model [61]. It should be noted that within $k-\omega-$ SST-IDDES, only the destruction term in the k-equation is modified by introducing the l_{IDDES} term, whereas the ω-equation remains unchanged. l_{IDDES} is responsible for triggering a transition from URANS mode into a scale-resolving mode. A detailed description of this methodology can be found in [23, 101].

2.3.2 Internal energy equation

The Reynolds-averaged internal energy equation follows as [27]:

$$\rho c_p \frac{DT}{Dt} = S_T + \frac{\partial}{\partial x_i}\Big[\Big(\lambda\frac{\partial T}{\partial x_i}\Big) - \rho c_p \overline{\theta u_i}\Big], \tag{2.11}$$

Assuming incompressible flow, constant physical properties and neglecting addition source terms (such as radiation), the equation can be written as below:

$$\frac{DT}{Dt} = \frac{\partial}{\partial x_i}\Big[\Big(\frac{\nu}{Pr}\frac{\partial T}{\partial x_i}\Big) - \overline{\theta u_i}\Big]. \tag{2.12}$$

The quantity $\overline{\theta u_i}$ on the right hand side is called turbulent heat flux and is the Reynolds-averaged fluctuating velocity-temperature correlation. This quantity needs to be modeled in order to close the equation.

The simplest and mostly used approach to model the turbulent heat flux is the Reynolds Analogy. This approach is based on the assumption that the momentum and thermal layer overlay and thus, have the same thickness. Therefore, it is assumed that an accurate computation of the momentum transport leads to an accurate prediction of the temperature field. In addition, it is assumed that the turbulent heat flux is proportional to the mean temperature gradient [44], which leads to the following relation:

$$\overline{\theta u_i} = -\frac{\nu_t}{\sigma_t}\frac{\partial T}{\partial x_i}, \tag{2.13}$$

with σ_t as turbulent Prandtl number, usually taken constant equal to 0.9. Concerning low Pr number fluids, this value is significantly lower than the reference value obtained from DNS, see Fig. 2.1. In contrast, this value provides a reasonable estimation for high Pr number fluids except for regions very close to solid surfaces, i.e. $y^+ < 3$. Nevertheless, this constant value has been often applied irrespective of working fluids under investigation (e.g. [107, 25, 52]). In this present work, various effects of applying that constant for different working fluids will be thoroughly investigated and discussed.

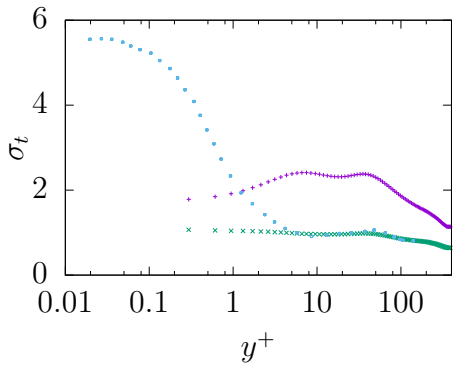

Figure 2.1: Variation of turbulent Prandtl number σ_t at different Re_τ and Pr numbers: $Re_\tau = 395$ with $Pr = 0.025$ [38] (+) and $Pr = 0.71$[38] (×), and $Re_\tau = 150$ with $Pr = 200$ [8] (○)

Moreover, it is immediately clear that the capability of the Reynolds Analogy is limited to only first order statistics in non-homogeneous directions, and fails to predict the heat flux in homogeneous direction when employed for steady state simulations, as will be shown in section 2.5.

It is worth to take a closer look at the internal energy equation, Eq. 2.12, considering a uniform heat flux along solid walls, see Fig. 2.2. The right-hand side composes out of the thermal diffusivity term $(\nu/Pr)(\partial T/\partial x_i)$, with $\nu/Pr = \alpha$, and the heat flux vector $\overline{\theta u_i}$. Considering small Pr numbers, the thermal diffusivity term is high and thus, the molecular diffusion—convection—has a major effect, even away from solid walls where effects of viscosity on the flow field are fairly small. In contrast, at high Pr numbers flows the thermal diffusivity is small and the molecular diffusion is limited to regions close to solid surfaces, usually limited to the viscous sublayer region. This makes high Pr number flows computationally more challenging due to the mesh requirement to capture high non-linear near-wall effects [8, 9].

In case of unsteady calculations, the internal energy equation (Eq. 2.12) as well as the Reynolds Analogy (Eq. 2.13) take the following form:

$$\frac{DT}{Dt} = \frac{\partial}{\partial x_i}\left[\left(\frac{\nu}{Pr}\frac{\partial T}{\partial x_i}\right) - \overline{\theta u_i}^{sgs}\right]$$
$$\overline{\theta u_i}^{sgs} = -\frac{{\nu_t}^{sgs}}{\sigma_{t,sgs}}\frac{\partial T}{\partial x_i}, \tag{2.14}$$

where $\overline{\theta u_i}^{sgs}$ and ${\nu_t}^{sgs}$ represent sub-grid heat flux and sub-grid eddy viscosity, respectively. Thus, the total heat flux is the sum out of sgs and resolved (res) components.

2.3.3 Temperature variance equation

As for a turbulent flow field, for which the characteristic time is provided by $\tau_m = k/\varepsilon$, it is also of interest to introduce a characteristic time scale for thermal mixing, which is defined as $\tau_\theta = \overline{\theta^2}/2\varepsilon_\theta$, where $\overline{\theta^2}$ is the temperature variance and ε_θ its dissipation. The associated transport equations can be solved to gain insight to the dynamics of the temperature fluctuations and also, to assess the Reynolds Analogy in

providing such information. The modeled transport equation for $\overline{\theta^2}$ reads as follows [107]:

$$\frac{D\overline{\theta^2}}{Dt} = 2P_{\overline{\theta^2}} - 2\varepsilon_\theta + \frac{\partial}{\partial x_i}\Big[\Big(\frac{\nu}{Pr} + \frac{\nu_t}{\sigma_t}\Big)\frac{\partial\overline{\theta^2}}{\partial x_i}\Big], \tag{2.15}$$

where $P_{\overline{\theta^2}} = -\overline{\theta u_i}\partial T/\partial x_i$ is the production of temperature variance and ε_θ is the dissipation of temperature variance. Introducing an additional transport equation for this quantity would be the most consistent approach. However, closing this equation is more complex compared to modeling the equation for the dissipation of turbulent kinetic energy ε. As stated in [107, 54], twice as many free parameters, including two turbulent time scales (mechanical and thermal), and two production terms need to be determined. These issues have been discussed in few investigations [110, 76, 25, 60].

However, often a simpler approach that assumes a constant thermal to mechanical time-scale ratio, denoted as $\mathcal{R} = \tau_\theta/\tau_m$, is used to provide information on thermal time scale [107, 43]. Several studies [45, 109, 44] have shown that the assumption of a constant ratio—with a typical value of $\mathcal{R} = 0.5$—works pretty well for fluids with Pr number around unity. Nevertheless, it is commonly used even when dealing with Pr numbers significantly different than unity [107], despite the lack of extensive assessment and validation. Using the typical value of 0.5 for $\mathcal{R}$ leads to the following relation for ε_θ and is used in this study along with the Reynolds Analogy to determine ε_θ in the temperature variance equation:

$$\varepsilon_\theta = \frac{\varepsilon\overline{\theta^2}}{k}. \tag{2.16}$$

In case of unsteady calculations, the transport equation for the temperature variance (Eq. 2.15) takes the following form:

$$\frac{D\overline{\theta^2}^{sgs}}{Dt} = 2P_{\overline{\theta^2}}^{sgs} - 2\varepsilon_\theta^{sgs} + \frac{\partial}{\partial x_i}\Big[\Big(\frac{\nu}{Pr} + \frac{\nu_t^{sgs}}{\sigma_{t,sgs}}\Big)\frac{\partial\overline{\theta^2}^{sgs}}{\partial x_i}\Big], \tag{2.17}$$

with

$$P_{\overline{\theta^2}}^{sgs} = -\overline{\theta u_i}^{sgs} \frac{\partial T}{\partial x_i} \quad \text{and} \quad \varepsilon_{\theta}^{sgs} = \frac{\varepsilon^{sgs} \overline{\theta^2}^{sgs}}{k^{sgs}}. \tag{2.18}$$

Thus, the total temperature variance is the sum of res and modeled/sgs components.

2.4 Numerical Setup

The Reynolds Analogy is assessed using previously mentioned turbulence models at different Reynolds and Prandtl numbers. The details of the numerical schemes and the flow configuration are described in the following section.

2.4.1 Flow configuration

The configuration is a fully developed turbulent channel flow, shown in Fig. 2.2. The size of the computational domain is $2\pi\delta, 2\delta, \pi\delta$. Different Reynolds and Prandtl numbers have been considered based on the availability of reference (DNS) data. The details of all simulations are summarized in table 2.2. Note that the Reynolds number is defined based on the friction velocity at wall (U_τ) and channel half height δ. A constant pressure gradient is applied via an additional source term in the momentum equation to drive the flow to the targeted Reynolds number, see 2.6.2.

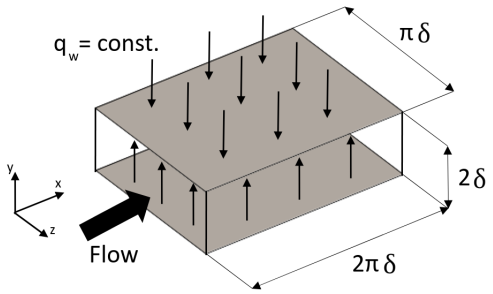

Figure 2.2: Sketch of horizontal channel flow configuration

Periodic boundary conditions are imposed in the streamwise and the spanwise directions, and no-slip condition is used at both walls. For the temperature field, a mean uniform heat flux at the walls, and periodic boundary conditions in the streamwise and

the spanwise directions have been applied. Further, it is important to mention that the temperature variance is set to zero at the wall. Detailed information on the influence of the boundary condition can be found in [110, 60, 83]. The results are normalized by the channel half width δ, the friction velocity U_τ, the kinematic viscosity ν, the density ρ and the friction temperature T_τ. Detailed information on the mesh resolutions used

Table 2.2: Overview of simulations

Re_τ	Pr	Reference Data	Type	Resolution	Grids
395	0.025	Kawamura et al. [38]	steady	$48 \times 72 \times 48$	A-100
			unsteady	$48 \times 72 \times 48$	A-100
				$128 \times 192 \times 48$	B-100
				$64 \times 192 \times 48$	I-100
				$96 \times 72 \times 48$	J-100
395	0.71	Kawamura et al. [38]	steady	$48 \times 72 \times 48$	A-100
			unsteady	$48 \times 72 \times 48$	A-100
				$128 \times 192 \times 48$	B-100
150	200	Bergant et al. [8]	steady	$48 \times 72 \times 48$	A-100/1000
				$48 \times 144 \times 48$	M-500
			unsteady	$48 \times 72 \times 48$	A-1000
				$128 \times 192 \times 96$	C-250

for the unsteady state simulations are given in the corresponding sections. A simple gradient spacing is used to achieve appropriate distribution in the wall-normal direction, however, different spacing ratios are investigated for certain cases. Further, it should be noted that the stretch factor **r** should be less than ≈ 1.2 [111, 99], which is fulfilled for all meshes.

2.4.2 Code description

All numerical simulations presented in this chapter are performed using OpenFOAM-v1706 with necessary modifications, provided in 2.6.2. The PISO algorithm has been used for steady and unsteady calculations. Second order schemes have been used for velocity, turbulence and thermal quantities for both steady and unsteady simulations. Further, a Courant number around 0.05 was chosen for a reliable prediction of the velocity and temperature field for unsteady calculations as suggested in [23].

2.5 Results and Discussion

In the framework of the present study, the prediction capabilities of the Reynolds Analogy for first and second order statistics at different Reynolds and Prandtl numbers are investigated, as provided in table 2.2. This covers a wide range of Pr numbers ($O(0.01)$, $O(1)$ and $O(100)$) to study capabilities of the Reynolds Analogy when dynamics of heat transfer are significantly different. The main goal here is to provide a comprehensive assessment by investigating various aspects of the Reynolds Analogy. The results obtained from different simulations will be presented and discussed in the following.

2.5.1 Steady state simulations

The steady state simulations are carried out using $k-\omega-$ SST and $\zeta-f$ RANS models. It should be noted that mesh convergence studies have been done for all simulations. While only mesh independent results are presented, a detailed analysis on mesh requirements is presented for the simulations for $Pr = 200$.

2.5.1.1 $Pr = 0.71$

Fig. 2.3 presents results obtained for $Pr = 0.71$ at $Re_\tau = 395$. Mean velocity, mean temperature and mean heat flux in wall-normal direction are in good agreements with the DNS data. Accurate prediction of the mean temperature is also reflected in the predicted mean Nusselt number provided in table 2.3. However, as expected the Reynolds Analogy is incapable to predict the heat flux in the streamwise (homogeneous) direction. This is due to the fundamental assumption underlying this methodology, which is presented in Eq. 2.13, and leads to a non-existing streamwise heat flux.

Table 2.3: Comparison of mean Nusselt number at $Re_\tau = 395$ for $Pr = 0.71$

	DNS [40]	$k-\omega-$ SST	$\zeta-f$
Nu	36.65	36.54	37.23

Further, rms value of temperature fluctuation (θ_{rms}) is mispredicted by both turbulence models. A detailed analysis of the transport equation for $\overline{\theta^2}$ (Eq. 2.15) will help to understand the reason behind the misprediction of this quantity. The production of $\overline{\theta^2}$, given as $P_{\overline{\theta^2}} = -\overline{\theta u_i}\partial T/\partial x_i$, is well predicted as shown in Fig. 2.4, indicating that the production is primary due to the temperature gradient in the wall-normal direction. However, the thermal dissipation rate ε_θ is mispredicted particularly in the near-wall region, which is thought to be the main reason of misprediction of $\overline{\theta^2}$ and thus, θ_{rms}. This is most likely due to the assumption of a constant thermal to mechanical time-scale ratio ($\mathcal{R}$). This assumption describes ε_θ based on ε, which could lead to a misprediction of ε_θ in near-wall region, see Eq. 2.16 for details.

The Reynolds Analogy introduces a coupling between the flow field and the thermal field via the eddy viscosity. However, a sensitivity with respect to flow field—different prediction of ν_t by both turbulence models—can only be observed in θ_{rms}; the second order statistical quantity. Further, a notable difference is only in the near-wall region, where eddy viscosities obtained from both turbulence models are nearly identical, in contrast to the core region where the predicted eddy viscosities are significantly different. This suggests that using the eddy viscosity to establish a coupling between flow and thermal fields may not be sufficient to establish a consistent and responsive coupling.

2.5.1.2 $Pr = 0.025$

The simulation for $Pr = 0.025$ is carried out at $Re_\tau = 395$ as provided in table 2.2. It should be noted that the flow field results are not shown as the temperature is considered to be a passive scalar. Fig. 2.5 presents mean temperature and temperature rms profiles along with heat flux in the streamwise and wall-normal directions. In contrast to the previous simulation concerning $Pr = 0.71$, there are discrepancies in mean temperature (underprediction of $\approx 25\%$ at the channel center, also reflected in the predicted mean Nusselt number provided in table 2.4) and heat flux in wall-normal direction (overprediction of $\approx 40\%$ in the core region) compared to DNS data. The dis-

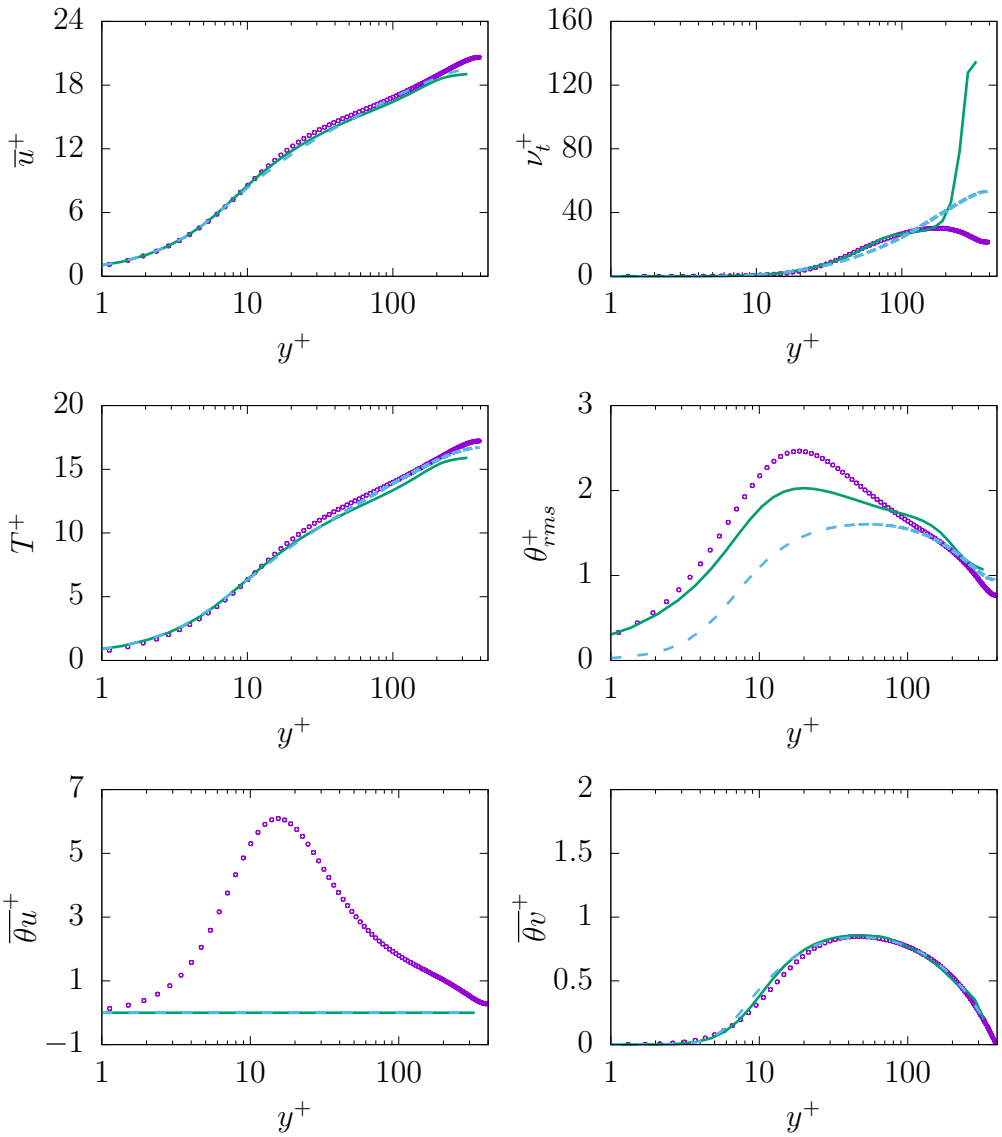

Figure 2.3: Evolution of mean streamwise velocity (top left), turbulent viscosity (top right), temperature (middle left), temperature rms (middle right), streamwise heat flux (bottom left) and wall-normal heat flux (bottom right) at $Re_\tau = 395$ for $Pr = 0.71$. $\zeta - f$: —, $k - \omega -$ SST: - - -, DNS: ○

crepancies are thought to be due to the inappropriate turbulent Prandtl number σ_t used in the Reynolds Analogy which is significantly lower than reference value throughout the channel, see Fig. 2.1.

Table 2.4: Comparison of mean Nusselt number at $Re_\tau = 395$ for $Pr = 0.025$

	DNS [40]	$k - \omega -$ SST	$\zeta - f$
Nu	6.60	9.12	9.33

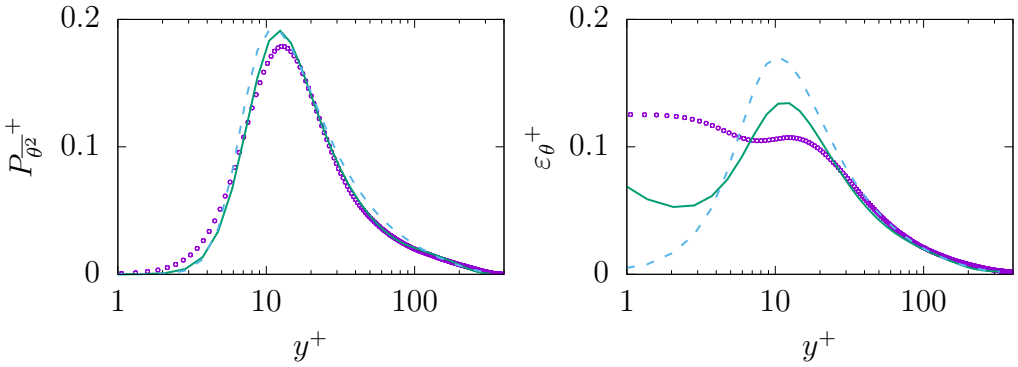

Figure 2.4: Evolution of production (left) and dissipation (right) of $\overline{\theta^2}$ at $Re_\tau = 395$ for $Pr = 0.71$. $\zeta - f$: —, $k - \omega -$ SST: - - -, DNS: ○

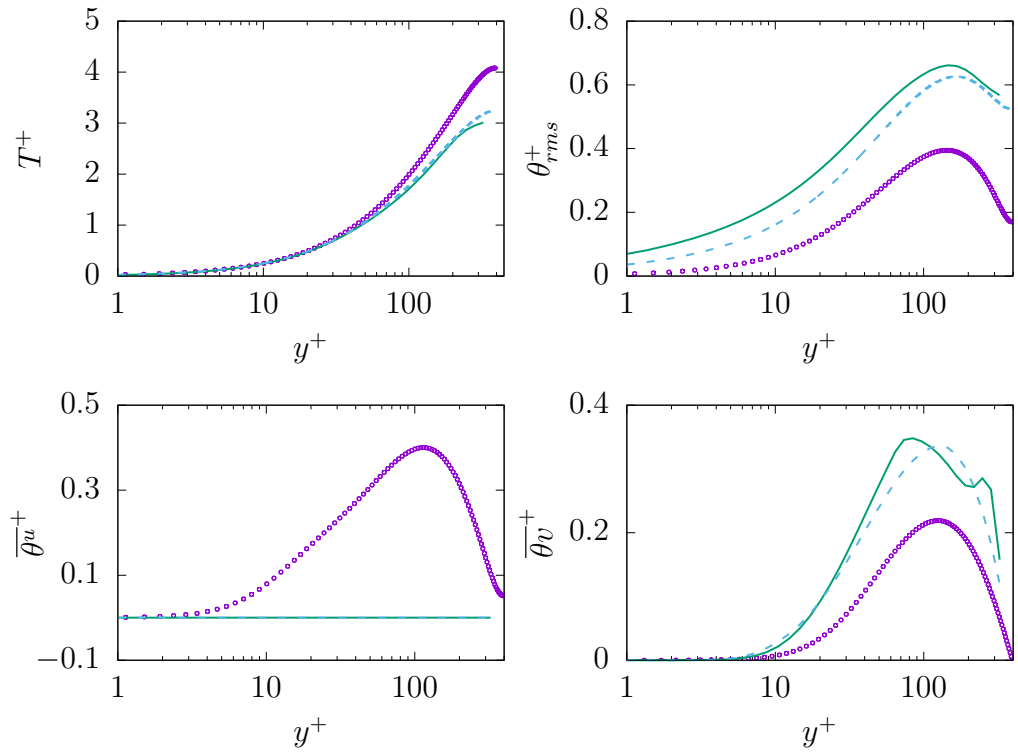

Figure 2.5: Evolution of temperature (top left), temperature rms (top right), streamwise heat flux (bottom left) and wall-normal heat flux (bottom right) at $Re_\tau = 395$ for $Pr = 0.025$. $\zeta - f$: —, $k - \omega -$ SST: - - -, DNS: ○

Unlike the simulations for $Pr = 0.71$, θ_{rms} is severely overpredicted over the whole channel domain. Fig. 2.6 demonstrates production and dissipation in the transport equation of $\overline{\theta^2}$. Contrary to the previous simulation, production is overestimated which results in the overprediction of θ_{rms}. The situation is worse for the dissipation: as shown, both turbulence models fail to predict the plateau behavior of ε_θ, i.e. it is mispredicted in the most part of the domain, in contrast to the previous case concerning

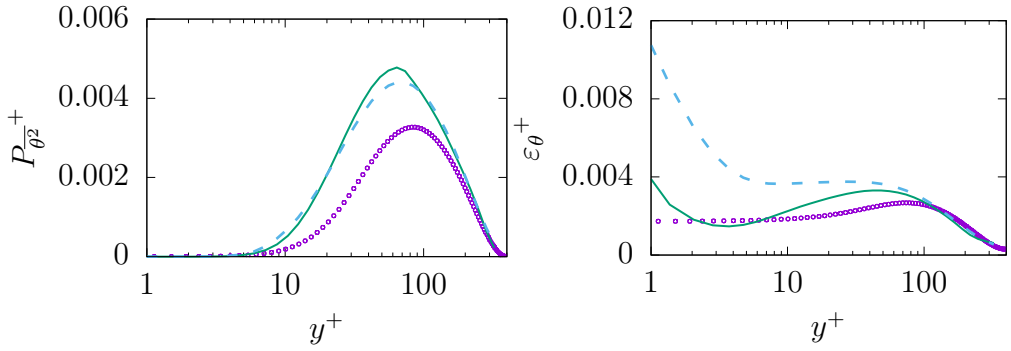

Figure 2.6: Evolution of production (left) and destruction (right) of $\overline{\theta^2}$ at $Re_\tau = 395$ for $Pr = 0.025$. $\zeta - f$: —, $k - \omega -$ SST: - - -, DNS: ○

$Pr = 0.71$. This confirms that the thermal time-scale cannot be predicted solely based on mechanical time-scale when dealing with significantly low Pr numbers, which is also important for the development of more advanced heat transfer models.

Further, it is worth mentioning that more advanced turbulence models, such as $\zeta - f$, might be a necessary requirement to accurately predict the thermal dissipation. In conclusion, the results for low Pr indicate that more advanced modeling approach is necessary even for the prediction of first order statistics.

2.5.1.3 $Pr = 200$

In contrast to previous numerical experiments, simulations for $Pr = 200$ are carried out at $Re_\tau = 150$, due the lack of sufficient reference data at higher Re_τ. However, it was shown in [25] that for $Pr = 0.71$ and larger, the temperature field development is less impacted by hydrodynamics, i.e. it is almost independent of Re_τ.

Table 2.5: Details of the grid resolution for fully developed turbulent channel flow for steady state at $Re_\tau = 150$ with $Pr = 200$

Grids	model	Δx^+	$\Delta y^+_w - \Delta y^+_c$	Δz^+	N_x	N_y	N_z	**r**
DNS [8]		4.9	0.04-3.3	3.7	192	145	128	-
A-100	$k - \omega -$ SST $\zeta - f$	19.8	0.19-18.8	9.9	48	72	48	1.14
A-1000	$k - \omega -$ SST $\zeta - f$	19.8	0.03-27.2	9.9	48	72	48	1.21
M-500	$k - \omega -$ SST $\zeta - f$	19.8	0.03-12.7	9.6	48	144	48	1.09

It is worth to mention that high Prandtl number fluids impose some computational challenges. As stated in [9, 8], appropriate modeling of turbulent heat transfer requires to distinguish between the dissipative scales of velocity and temperature. This is particularly important in high Pr number fluids, since unlike in fluids with $Pr \approx 1$ and smaller, the dissipative scales are significantly smaller at high Pr number fluids: the temperature scale is inversely proportional to the square root of the Pr number, $l_\theta \approx 1/\sqrt{Pr}$. Furthermore, it is shown in [40, 39, 113] that at $Pr \approx 5$ the smallest temperature scales are roughly twice as small as the smallest velocity scales. High Pr numbers fluids have very thin thermal boundary layers close to solid surfaces—significantly thinner than the hydrodynamic boundary layer— which leads to extremely high temperature gradients close to the solid surface. Thus, higher grid resolutions in wall-normal direction are required to predict the gradients accurately and to avoid numerical instabilities, which has been confirmed in [10, 65] concerning $Pr = 5.4$ and $Pr = 10$.

Therefore, a mesh convergence study has been performed for both turbulence models including not only refinement, but also different spacing of the points in wall-normal direction, see table 2.5. The meshes are chosen as follows: mesh A-100 is the same as used for previous simulations, mesh A-1000 has a higher stretching factor—while keeping same number of total cells—to decrease the size of the first cell adjacent to the wall (Δy_w^+) such that a value close to the one used in the DNS-calculation is reached. Mesh M-500 is only in wall-normal direction refined by factor 2 while keeping Δy_w^+ same as in A-1000. It should be noted, that the results for $k-\omega-$ SST on mesh M-500 are not shown since no further improvement of the results were obtained.

Fig. 2.7 presents mean velocity, mean temperature, rms of temperature fluctuations and mean heat flux in wall-normal direction obtained on different meshes. It should be noted that generally turbulence models have been developed based on high Reynolds number assumption. Therefore, prediction quality of such models when dealing with relatively low Reynolds number, such as the present case, might be de-

creased. This is best shown in Fig. 2.8 which demonstrates the log-law indicator $\phi = \delta\overline{u}/\delta y * y/\kappa$.

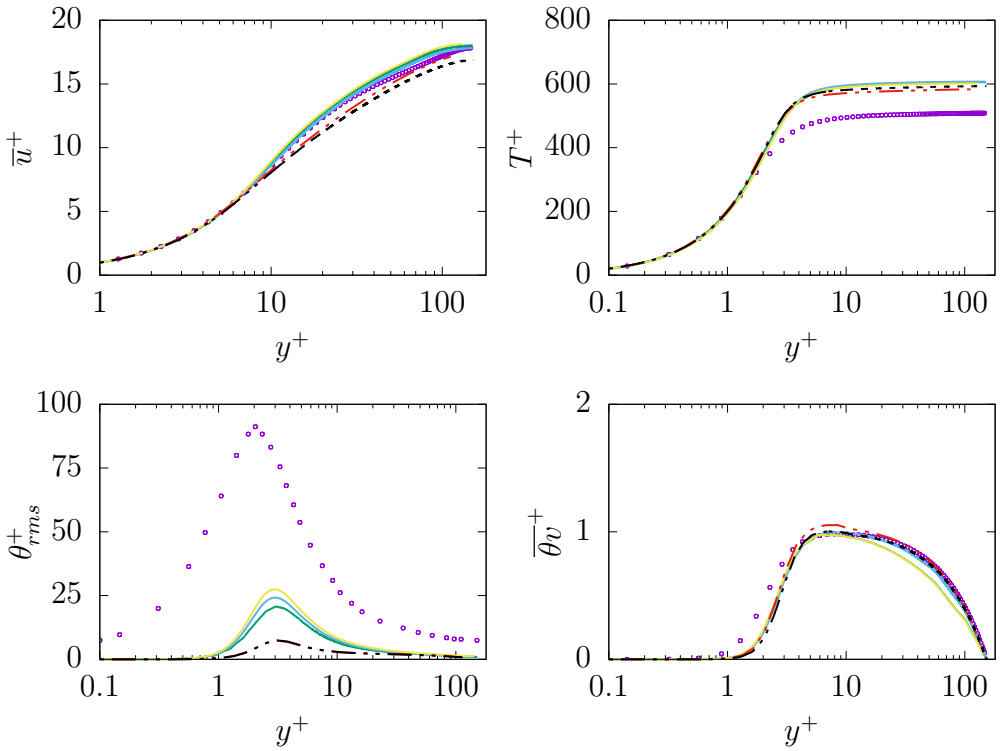

Figure 2.7: Evolution of mean streamwise velocity (top left), temperature (top right), temperature rms (bottom left), wall-normal heat flux (bottom right) at $Re_\tau = 150$ for $Pr = 200$. Mesh A-100 $\zeta - f$: —, $k - \omega -$ SST: - - -, Mesh A-1000 $\zeta - f$: —, $k - \omega -$ SST: - - -, Mesh M-500 $\zeta - f$: —

Mean temperature is overpredicted by roughly 15% in the core region by both turbulence models on all grids and, both models capture the general behavior correctly while there is no sensitivity regarding the turbulence models. As shown in Fig. 2.1, assuming a constant value of 0.9 for σ_t is reasonable to expect for the regions very close to the wall with $y^+ < 3$. Therefore, the discrepancy in mean temperature is likely due to the inaccurate prediction of the velocity field as shown in Fig. 2.7 and 2.8, which is somehow magnified in the mean temperature field. Concerning the heat flux in wall-normal direction $\overline{\theta v}$, a notable discrepancy/underprediction is observed in near wall-region ($y^+ < 3$) which can be a direct consequence of the constant σ_t within the Reynolds Analogy. Further, no sensitivity regarding the turbulence model is present in the wall-normal heat flux. In contrast to first order statistics, there is a significant

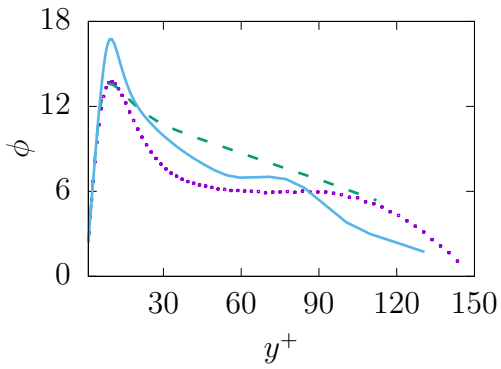

Figure 2.8: Log-law indicator ϕ at $Re_\tau = 150$. $\zeta - f$ on mesh M-500 and $k-\omega-$SST on A-1000. $\zeta - f$: —, $k-\omega-$SST: - - -, DNS: ○

discrepancy between model predictions and the reference DNS-data for θ_{rms}. The $k-\omega-$SST model underpredicts by a factor of ≈ 8, irrespective of grid resolution and design. In contrast, the $\zeta - f$ model shows sensitivity to the mesh design and in particular, grid spacing, i.e. different Δy_w^+. It is shown that model predictions are improved when Δy_w^+ approaches value close to the corresponding DNS value. Further, refinement in the streamwise and spanwise directions did not lead to notable improvements. However, despite improved results obtained from the $\zeta - f$ model, there is still a significant underprediction for θ_{rms}. The underprediction of θ_{rms} is reflected in production and dissipation of $\overline{\theta^2}$ as shown in Fig. 2.9. While the production is well predicted, the dissipation in near-wall region is severely mispredicted inside the thermal boundary layer. The overprediction at $y^+ \approx 2.5$ leads to a strong underprediction of θ_{rms}. These

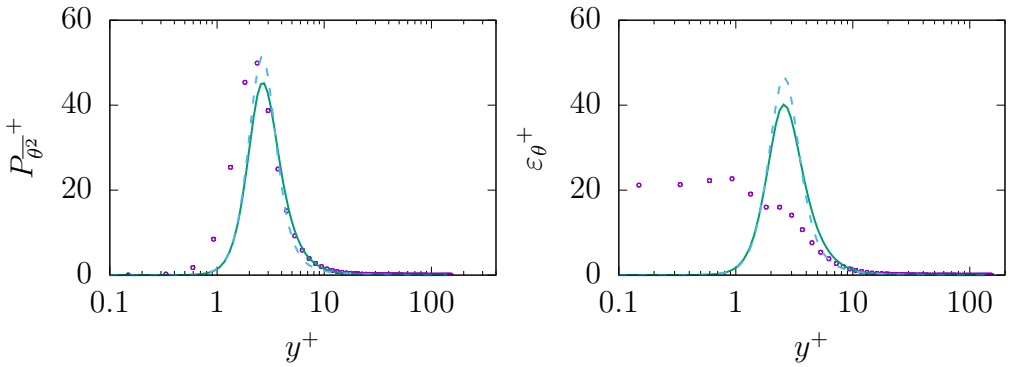

Figure 2.9: Evolution of production (left) and destruction (right) of $\overline{\theta^2}$ at $Re_\tau = 150$ for $Pr = 200$. $\zeta - f$ on mesh M-500 and $k-\omega-$SST on A-1000. $\zeta - f$: —, $k-\omega-$SST: - - -, DNS: ○

results suggest again that the underlying assumption of complete similarity between

thermal and mechanical time steps—or in other words ε and ε_θ—faces sever challenges when dealing with non-unity Pr number fluids.

2.5.2 Unsteady simulations

Unsteady simulations have been carried out using the $k-\omega-$ SST-IDDES model. Three different Pr numbers, i.e. 0.71, 0.025 and 200, have been considered; similar to the steady simulations. All three Pr numbers are investigated with at least two different resolutions to demonstrate the influence of mesh resolution, and more importantly, to study the behavior of the Reynolds Analogy when operating as a sgs-model. All presented results are spatial and time averaged.

2.5.2.1 Flow field considerations

It is well known that the dynamics of resolved and sub-grid flow quantities of unsteady/hybrid calculations rely on the mesh resolution. Fig. 2.10 depicts mean velocity as well as modeled and resolved turbulent kinetic energy obtained from simulations on different mesh resolutions, i.e. mesh A-100 and B-100, described in table 2.6. The mean velocity is marginally influenced by the mesh resolution. Further, the composition of the kinetic energy depends on the mesh: the higher the resolution, the smaller is the modeled kinetic energy while the total kinetic energy does not change significantly. This is an appropriate response to mesh resolution coming from the sgs-model for the flow field. However, a higher amount of modeled turbulent kinetic energy (compared to the resolved part) is expected in near-wall region as model operates in URANS-mode in those regions. This is a known problem of this methodology and has been discussed in detail in [101]. The main purpose of the current investigation is to determine if the sgs-model for heat transfer, based on the Reynolds Analogy, shows same dynamics as for the flow field or responds differently to mesh resolution. Therefore, in order to find out if that is the case the Reynolds Analogy along with the assumption of constant $\mathcal{R}$–0.5–in the transport equation of $\overline{\theta^2}$ is applied in unsteady calculations.

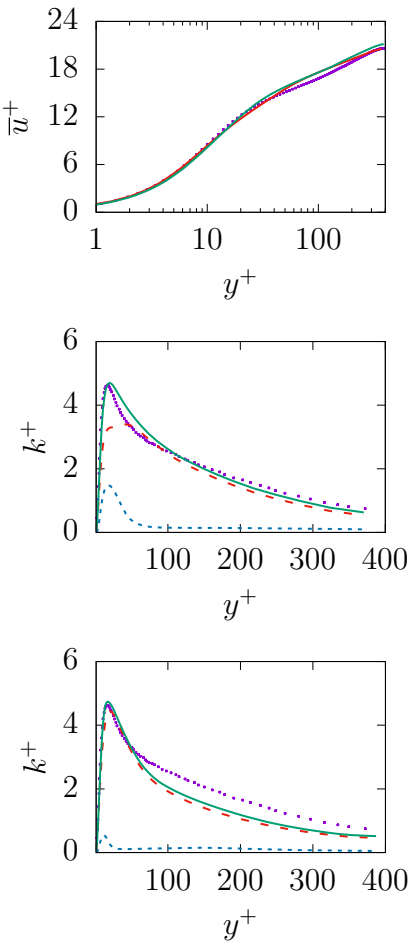

Figure 2.10: Evolution of mean streamwise velocity (top) for mesh A-100 (—) and B-100 (—), as well as kinetic energy for mesh A-100 (middle) and at mesh B-100 (bottom) for $Re_\tau = 395$. Total: —, resolved: - -, modeled: ---, DNS: ○

2.5.2.2 $Pr = 0.71$

The employed mesh resolutions are presented in table 2.6. Mesh A-100 is the same mesh as used for steady simulations, which delivers mesh independent results for steady state simulations for $Pr = 0.71$ and lower. Further, mesh B-100 is refined in the streamwise and wall-normal directions as a refinement in the spanwise direction did not show any remarkable effects. Fig. 2.11 presents the results obtained for $Pr = 0.71$

Table 2.6: Details of the grid resolution for fully developed turbulent channel flow at $Re_\tau = 395$ and $Pr = 0.71$

Grids	Δx^+	$\Delta y_w^+ - \Delta y_c^+$	Δz^+	N_x	N_y	N_z	**r**
DNS [38]	9.88	0.15-6.52	4.49	512	192	512	-
A-100	51.7	0.5-49.1	25.9	48	72	48	1.14
B-100	19.5	0.19-19.0		128	192	48	1.05

at $Re_\tau = 395$ on the coarse resolution, i.e. mesh A-100. This includes mean temperature, temperature rms (resolved and modeled), and heat fluxes (resolved and modeled) in both the streamwise and wall-normal directions (the mean velocity is shown in Fig. 2.10). It can be observed that the mean temperature profile is overpredicted by roughly

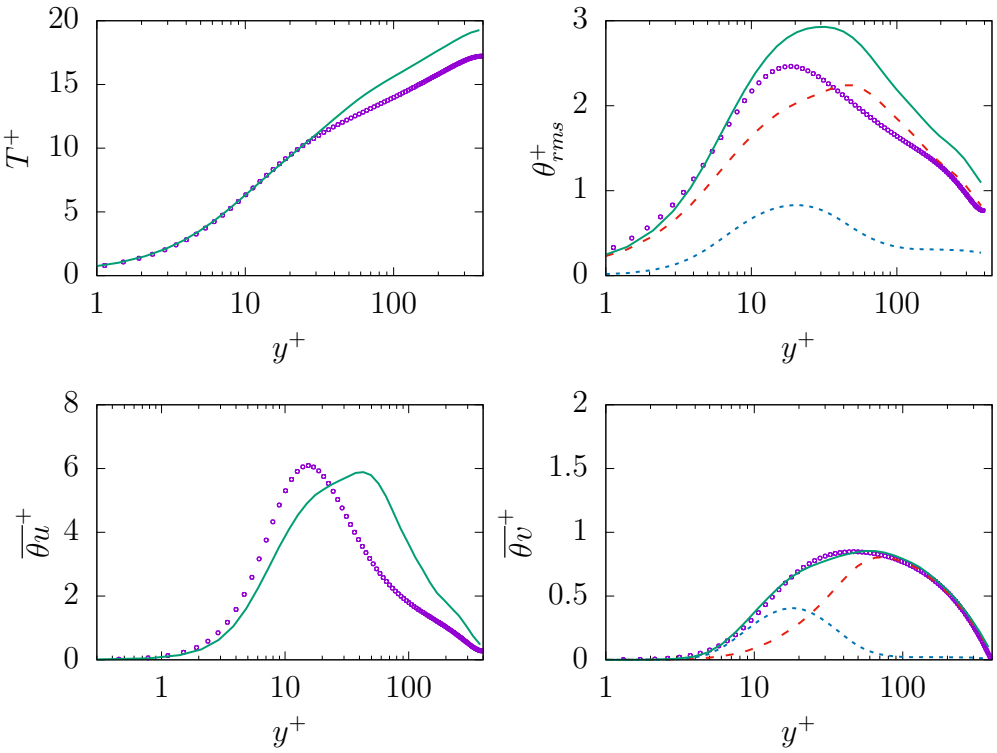

Figure 2.11: Evolution of temperature (top left), temperature rms (top right), streamwise heat flux (bottom left), wall-normal heat flux (bottom right) at $Re_\tau = 395$ for $Pr = 0.71$ on mesh A-100. Mean/total: —, resolved: - -, modeled: ---, DNS: ○

15% around the channel center line, in contrast to the steady state simulation on the same mesh. Regarding θ_{rms}, the near-wall behavior of the total quantity is in acceptable agreement with DNS data while the behavior further away is mispredicted. More importantly, a higher amount of the modeled part—compared to resolved part—is expected in near-wall region. This may lead to conclusion that the model tries to resolve most of thermal structures irrespective of mesh resolution, a similar behavior as the turbulent kinetic energy in the flow field.

Concerning heat fluxes, there is only the resolved part for the streamwise heat flux $\overline{\theta u_x}$, which shows the same mispredicted behavior as θ_{rms}. Concerning the wall-normal heat flux $\overline{\theta v}$, it can be seen that the total heat flux is in good agreement with the

reference data with a non-negligible amount of modeled part in the near-wall region. This behavior is consistent when performing simulation on a mesh, which does not support DNS/LES in near-wall region.

Table 2.7: Comparison of mean Nusselt number at $Re_\tau = 395$ for $Pr = 0.71$

	DNS [40]	A-100	B-100
Nu	36.65	33.70	34.23

The same quantities obtained on the finer resolution, mesh B-100, are presented in Fig. 2.12. As expected, all results (including mean Nusselt number, see table 2.7) have been improved, while modeled part of $\overline{\theta v}$ and θ_{rms} are vanished. The reduction of the modeled part is a consistent/appropriate response to mesh refinement. It should be noted again that even the finer resolution is still not appropriate to perform DNS calculation for thermal quantities and thus, (almost) complete vanishing of modeled parts of $\overline{\theta v}$ and θ_{rms} should not happen. This may lead to the conclusion that the sgs-model for thermal effects provided by the Reynolds Analogy does not indicate a consistent/appropriate sensitivity to mesh resolution, particularly concerning second order statistics. Therefore, application of such model to capture complex near-wall phenomena might lead to inaccuracies.

2.5.2.3 $Pr = 0.025$

Table 2.8: Details of the grid resolution for fully developed turbulent channel flow at $Re_\tau = 395$ for $Pr = 0.025$

Grids	Δx^+	$\Delta y_w^+ - \Delta y_c^+$	Δz^+	$\mathcal{AR}_c$	N_x	N_y	N_z	**r**
DNS [38]	9.88	0.15-6.52	4.49	-	512	192	512	-
A-100	51.69	0.5-49.1	25.9	1.05	48	72	48	1.14
B-100	19.47	0.19-19.0		1.02	128	192		1.05
I-100	38.84	0.19-18.90	26.0	2.05	64	192	48	1.05
J-100	26.17	0.50-49.73		0.53	96	72		1.14

Warhaft [122] performed theoretical investigation on dynamics of heat transfer and thermal boundary layer concerning fluids with different Pr numbers. It was suggested that the isotropy of mesh may play a role to capture/resolve the temperature spectrum of low Pr number fluids. Thus, these fluids may need certain requirements on the

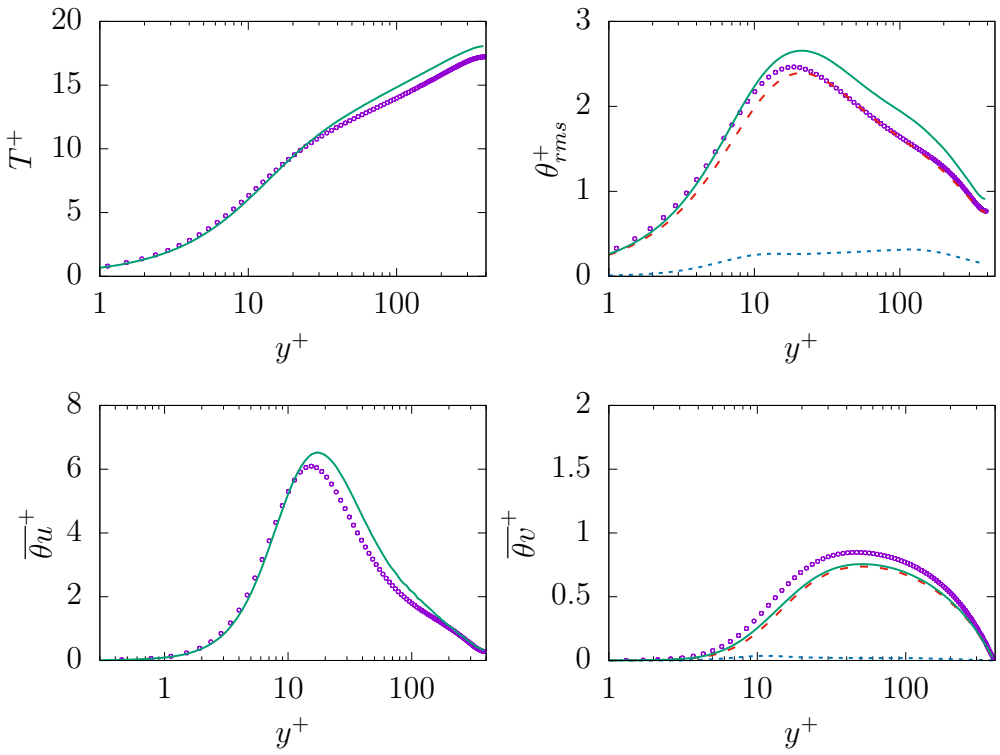

Figure 2.12: Evolution of temperature (top left), temperature rms (top right), streamwise heat flux (bottom left), wall-normal heat flux (bottom right) at $Re_\tau = 395$ for $Pr = 0.71$ on mesh B-100. Mean/total: ——, resolved: - - -, modeled: - - -, DNS: ○

mesh design. To investigate this assumption, four different grids with different designs and resolutions are considered, see table 2.8. This table provides additional information on mesh design such as grid aspect ratio at the channel center $\mathcal{AR}_c = \Delta x/\Delta y_c$. While grid A-100 and B-100 are isotrop ($\mathcal{AR}_c$ of $O(1)$), other grids—I-100 and J-100—are anisotrop around the channel center, see Fig. 2.13.

The grid sizes are chosen as follows: grid A-100 and B-100 are presented to show influence of the mesh resolution on model behavior (as previously done for $Pr = 0.71$). Grids I-100 and J-100 are in addition—with higher degrees of anisotropy away from the wall—to demonstrate the behavior of certain statistics on these meshes. Further, all used meshes are highly anisotrop in wall-region (see Fig. 2.13) since $k-\omega-$SST-IDDES operates in URANS-mode in near-wall region and thus, a RANS-type meshing is necessary. Results obtained on different resolutions in the spanwise direction (not shown) did not show remarkable differences, i.e. mesh/grid resolution in z-direction does not have a notable impact on the results—as long as mesh resolution in

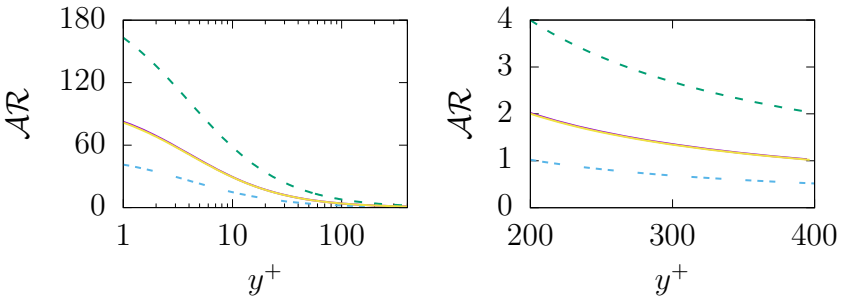

Figure 2.13: Variation of $\mathcal{AR}$ for different grids. It should be noted that the lines for both isotropic meshes, A-100 and B-100, overly. Mesh A-100: ——, Mesh B-100: ——, Mesh I-100: - - -, Mesh J-100: ---

spanwise direction is enough to allow the full development of the turbulent field in this direction.

Mean velocity, kinetic energy (sgs, resolved and total components), mean temperature and rms of temperature fluctuations (sgs, resolved and total components) obtained on four different mesh designs are shown in Fig. 2.14. As expected, flow field does not show a great sensitivity to mesh design and all associated quantities such as mean velocity and total turbulent kinetic energy are fairly well predicted. Further, for both isotropic meshes (A-100 and B-100), the mean temperature as well as θ_{rms} are in good agreement with the reference data, while for the anisotropic meshes (I-100 and J-100) both quantities are overestimated. Table 2.9 provides mean Nusselt number obtained on different grids, which shows consistancy with the mean temperature prediction accuracy. Thus, especially the second order statistic of the temperature shows a high sensitivity to the mesh design at low Pr numbers. Further, the sgs-component of θ_{rms} does not show any mesh sensitivity—regardless of the mesh design. This is also present in the behavior of the heat fluxes, see Fig. 2.15.

The obtained results suggest that anisotropy in the mesh for LES-part of the simulation (core region of the channel), where large scale thermal structures need to be resolved will lead to misprediction of the temperature spectrum and ultimately misprediction of mean temperature and temperature variance/θ_{rms}. This is also reflected

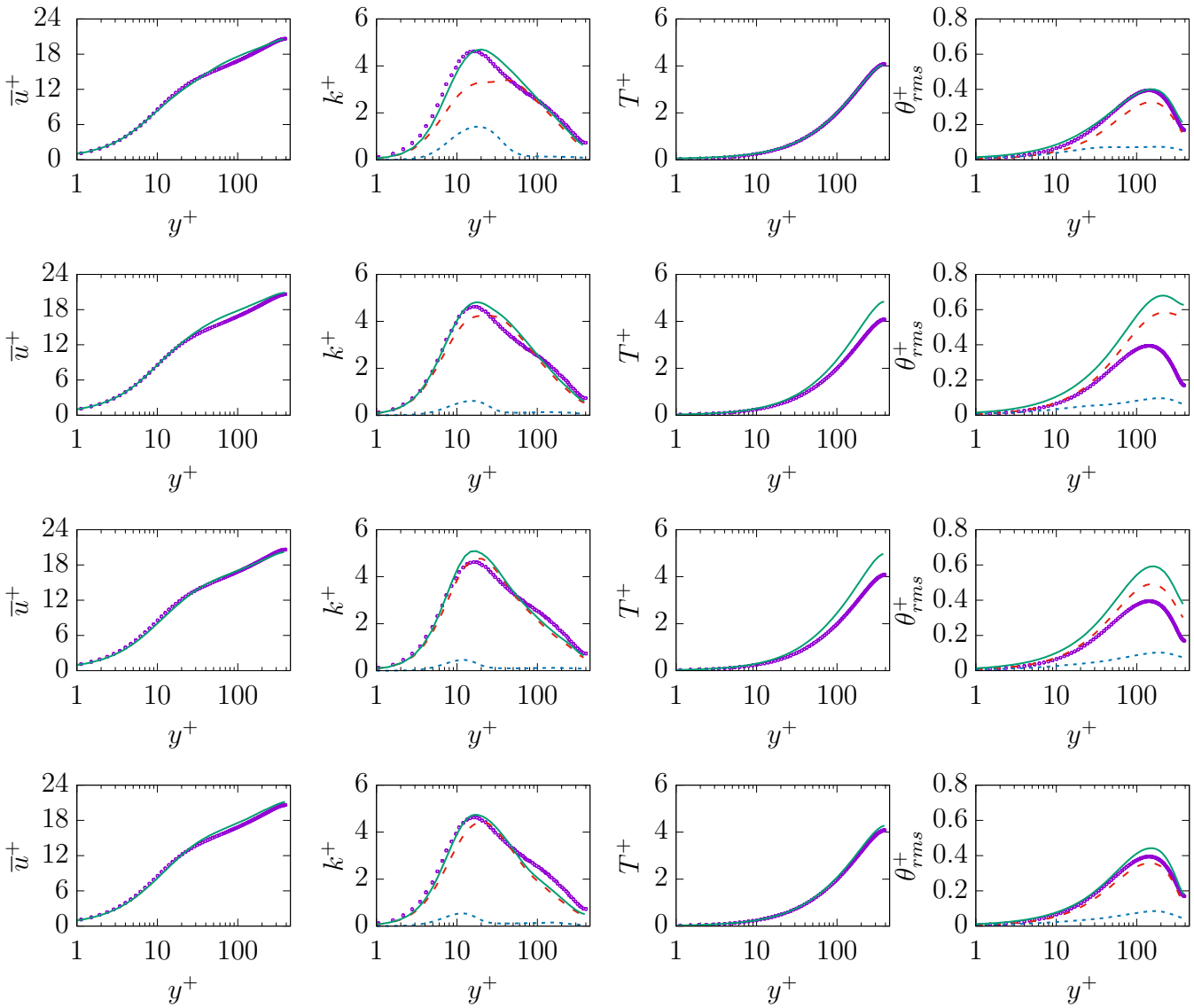

Figure 2.14: Mean velocity (first column), kinetic energy (second column), mean temperature (third column) and temperature rms (fourth column) for mesh A-100 (first row), I-100 (second row), J-100 (third row) and B-100 (fourth row) at $Re_\tau = 395$ for $Pr = 0.025$. Mean/total: ——, resolved: - - -, modeled: - - -, DNS: ○

in mesh design of the corresponding DNS-simulation, which have isotropic cells in the core region, see table. 2.8.

Table 2.9: Comparison of mean Nusselt number at $Re_\tau = 395$ for $Pr = 0.025$

	DNS [40]	A-100	B-100
Nu	6.60	6.57	6.30

Further, it seems that the grid shape ($\mathcal{AR}$) plays a more important role for resolving the thermal structure compared to the grid resolution. It seems that isotropic

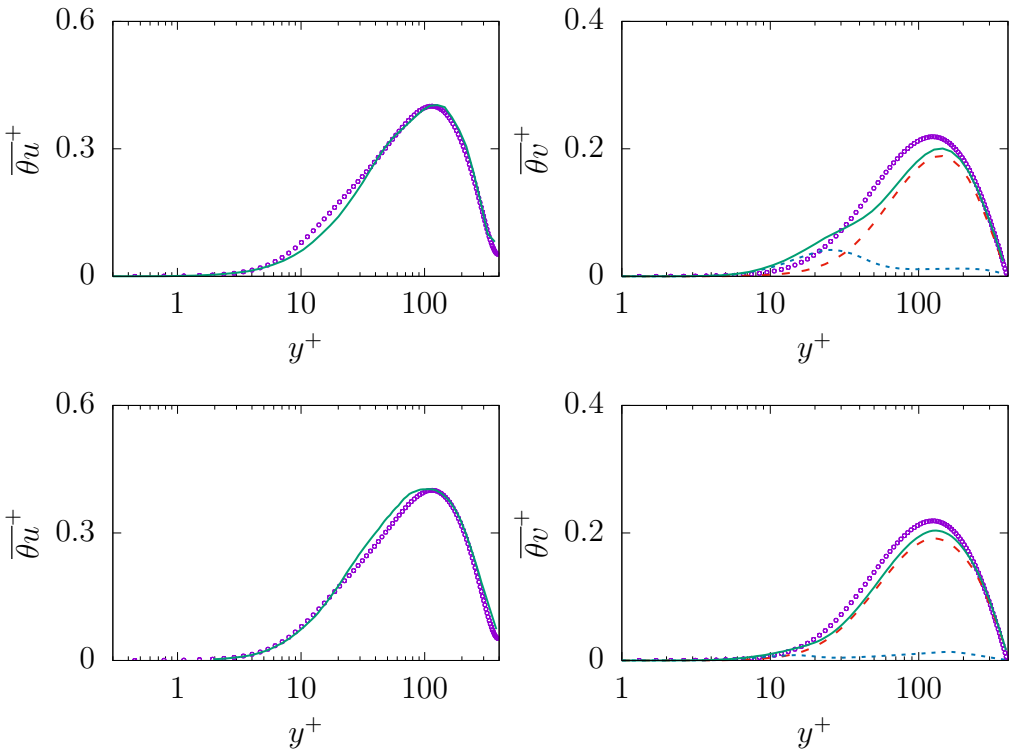

Figure 2.15: Comparison of streamwise heat flux (left) and normal heat flux (right) for mesh A-100 (top) and B-100 (bottom) at $Re_\tau = 395$ for $Pr = 0.025$. Mean/total: —, resolved: - -, modeled: ---, DNS: ○

mesh ($\mathcal{AR} \approx 1$) is necessary to accommodate (isotropic) thermal structures in isotropic (close to isotropic) cells in the core region to prevent destroying them by for example over-resolving. Therefore, it may be concluded that designing a mesh fine enough to capture—resolve unsteady—flow structures accurately (but close to isotropic in the core region) is just enough to capture large thermal structures residing away from solid surfaces.

2.5.2.4 $Pr = 200$

Table 2.10: Details of the grid resolution for fully developed turbulent channel flow at $Re_\tau = 150$ for $Pr = 200$

Grids	Δx^+	$\Delta y_w^+ - \Delta y_c^+$	Δz^+	N_x	N_y	N_z	**r**
DNS [8]	12.3	0.04-3.3	4.6	192	145	128	-
A-1000	19.5	0.03-27.7	9.7	48	72	48	1.21
C-250	7.5	0.03-8.7	5.1	128	192	96	1.06

As already discussed for steady state simulations of $Pr = 200$ at $Re_\tau = 150$, the grid spacing/resolution plays an integral role. Thus, a mesh convergence study was done using two different resolutions, described in table 2.10. The grids are chosen as follows: mesh A-1000 is the same as for the steady state case and mesh C-250 keeps the same Δy_w^+ value—close to DNS—with increased resolution in all directions. Further, in contrast to low Pr numbers, the aspect ratio of center cells around the channel center does not play a role for high Pr numbers (results are not shown).

As mentioned before, capturing the thermal effects at high Pr numbers fluids is very challenging as the thermal boundary layer is very thin—compared to the boundary of the flow, which leads to very dominant wall effects. As a results, investigating thermal boundary layers at high Pr numbers are limited to relatively low Re_τ due to the prohibitively expensive computational cost [9, 8]. This also indicates the necessity to develop more advanced turbulent heat transfer models, which are computationally affordable.

Results obtained for mean temperature, temperature fluctuations (θ_{rms}), as well as heat fluxes—the streamwise and wall-normal directions—on mesh A-1000 are shown in Fig. 2.16. In contrast to previous simulations, mean temperature is underpredicted by roughly 5% while the streamwise heat flux is overpredicted at the peak value. The situation for θ_{rms} is worse with negligible modeled part. The sgs-model is incapable to capture the near-wall dynamics and provide appropriate results, while the resolution is too coarse to capture dynamics of θ_{rms} accurately near the wall. The heat flux in wall-normal direction shows a mispredicted tendency compared to DNS data. Further, the modeled part of the heat flux—calculated by the Reynolds Analogy—is considerably high close to the wall. However, due to intrusion (a known problem discussed in [101]), the resolved part of the flux is not negligible in this region, which leads to inaccurate prediction of the total heat flux.

Fig. 2.17 presents the same results obtained on a finer resolution, mesh C-250. While general improvements can be observed for temperature and θ_{rms}, the mesh resolution is not fine enough to deliver acceptable results for the thermal second order

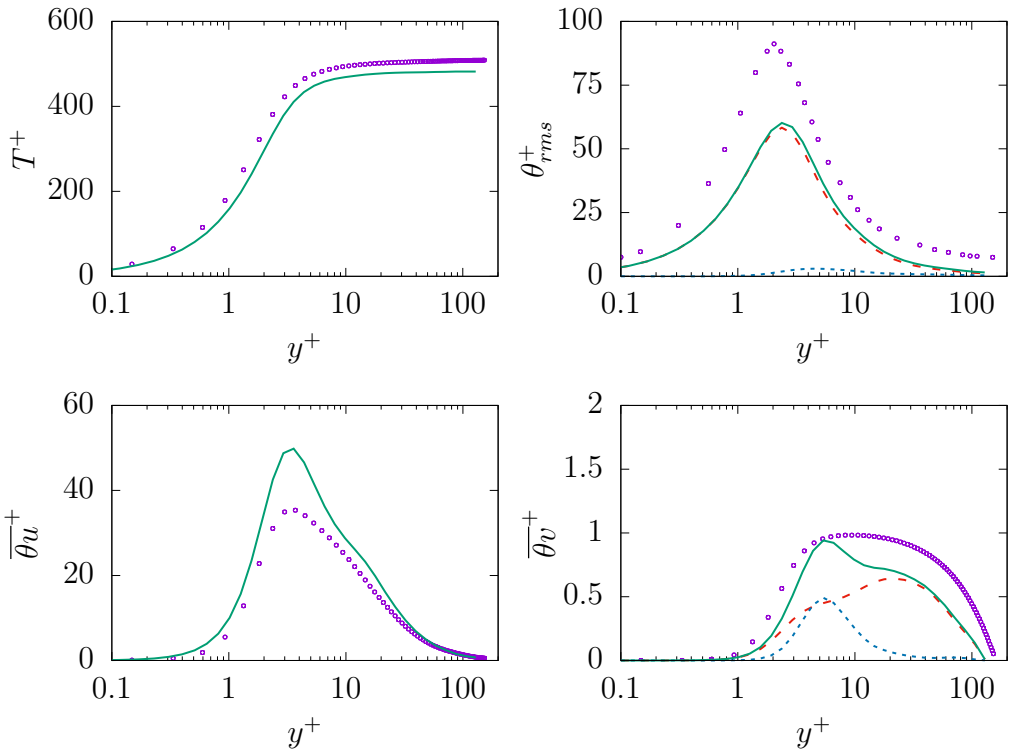

Figure 2.16: Evolution of temperature (top left), temperature rms (top right), streamwise heat flux (bottom left) and wall-normal heat flux (bottom right) at $Re_\tau = 150$ for $Pr = 200$ on mesh A-1000. Mean/total: —, resolved: - -, modeled: ---, DNS: ○

statistics. Concerning heat fluxes, there are no remarkable improvements as the resolution is increased. This might be due to the fact that (almost) all turbulence models are developed to predict high Reynolds number flows and therefore, appropriate response to grid resolution at this low Re_τ may not be expected.

The results obtained for various Pr numbers suggest that the Reynolds Analogy cannot play an integral role in modeling sub-grid thermal effects and fails to feature basic properties of an appropriate sgs-model particularly for high Pr number fluids.

2.6 Conclusion and Outlook

In this study, capability of the Reynolds Analogy to predict turbulent heat transfer has been thoroughly assessed. This includes the application of this analogy to turbulent wall-bounded shear flows at different Reynolds and Prandtl numbers within steady and unsteady state calculations. In case of steady state calculations, the Reynolds Analogy is able to provide acceptable results for first order statistics, i.e. mean temperature in

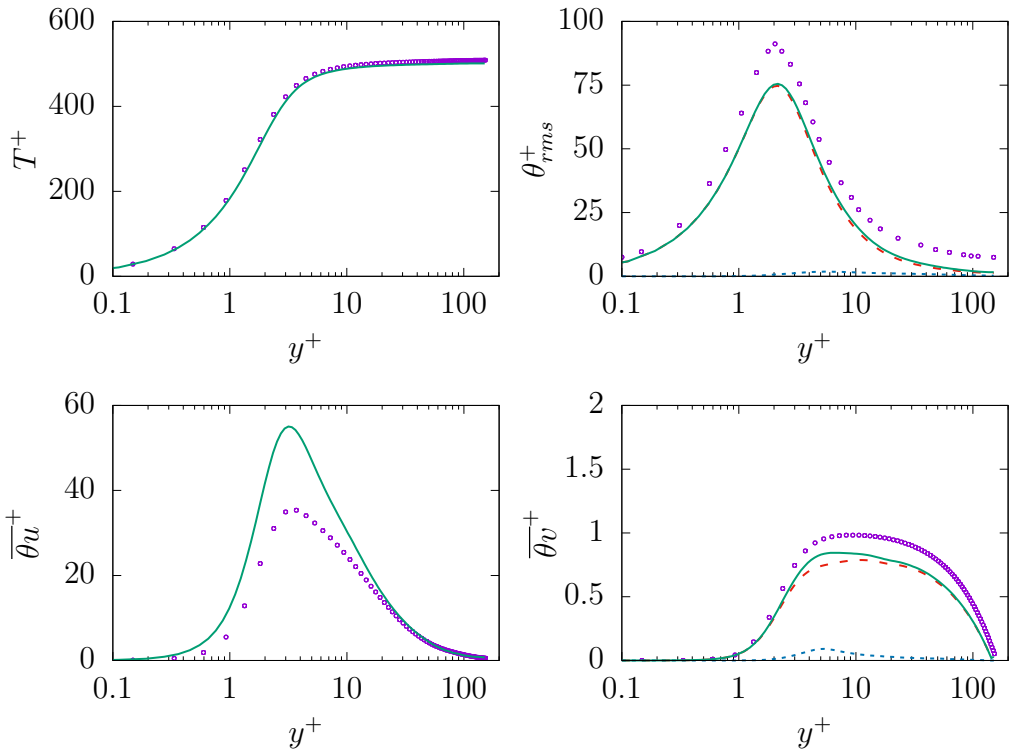

Figure 2.17: Evolution of temperature (top left), temperature rms (top right), streamwise heat flux (bottom left) and wall-normal heat flux (bottom right) at $Re_\tau = 150$ for $Pr = 200$ on mesh C. Mean/total: ——, resolved: - - -, modeled: - - -, DNS: ○

non-homogeneous direction limited only to fluids with Prandtl numbers close to unity. Concerning unsteady simulations, this methodology fails to feature basic properties of an appropriate sub-grid scale model, mainly due to insensitivity to mesh resolution, i.e. pushing simulation towards direct numerical simulation on any grid resolution. This could lead to enormous prediction error when near-wall phenomena are of importance and thus, the Reynolds Analogy may not be considered as a reliable sub-grid scale modeling strategy.

Further, it was shown that capturing/resolving the temperature spectrum of low Pr number fluids needs a certain mesh design, i.e. isotropic away from the solid surface to avoid misprediction. In contrast, an extremely high resolution mesh along with specific spacing in near-wall regions is necessary to achieve acceptable prediction accuracies of thermal field of high Pr number fluids. However, it was shown that there is a need for advanced models that can provide accurate prediction of the thermal time scale (or ε_θ), in addition to appropriate grid design in near-wall regions.

The obtained results suggest that using zero-equation approach (the Reynolds Analogy) cannot be deemed as an appropriate predictive tool for design and optimization purposes. This strongly suggests moving towards more advanced turbulent heat transfer models consistent with thermodynamic laws. This requires the application of one-equation or algebraic models to model heat transfer phenomena [109], in conjunction with advanced turbulence models capable of capturing complex, nonlinear, and anisotropic near-wall effects.

Addendum

Conflict of interest None declared.

Acknowledgment This work was supported using start-up funds from the University of Missouri-Kansas City.

2.6.1 Nomenclature

	Name
c_p	specific heat capacity at constant pressure
f	elliptic relaxation
h	convective heat transfer coefficient
k	kinetic energy
r	grid stretching factor in y-direction
u_i	velocity fluctuations
$\overline{u}_i$	mean velocity
q_i	heat flux density vector
q_w	wall heat flux
y^+	yPlus
L	characteristic length
$\mathcal{AR} = \Delta x/\Delta y_c$	cell size ratio
Pr	Prandtl
$\mathcal{R} = \tau_\theta/\tau_m$	mechanical to thermal time scale ratio
$Nu = hL/\lambda$	mean Nusselt number
$Re_\tau = U_\tau \delta/\nu$	turbulent Reynolds number
S_T	source terms in temperature equation
T	mean temperature
$T_\tau = \rho/c_p q_w U_\tau$	friction temperature
T_w	wall temperature
$U_\tau = Re_\tau \nu/\delta = \sqrt{\tau_w/\delta}$	friction velocity
$U_i = \overline{u}_i + u_i$	total velocity

U_b	bulk velocity
$\alpha = \lambda/\rho c_p$	thermal diffusivity
δ	channel half height
ϵ	dissipation of kinetic energy
ε_θ	dissipation of the temperature variance
$\zeta = \overline{v^2}/k$	velocity scale ratio
θ	Temperature fluctuations
$\overline{\theta u_i}$	turbulent heat flux
$\overline{\theta^2}$	temperature variance
$\kappa = 0.41$	von Karman constant
λ	thermal conductivity
μ	dynamic viscosity
ν	kinematic viscosity
ν_t	turbulent kinematic viscosity
ρ	density
σ_{sgs}	turbulent Prandtl number for sgs
σ_t	turbulent Prandtl number
$\tau_m = k/\varepsilon$	mechanical time scale
$\tau_\theta = \overline{\theta^2}/2\varepsilon_\theta$	thermal time scale
τ_w	wall shear stress
$\phi = \delta\overline{u}/\delta y * y/\kappa$	log-law indicator
ω	dissipation rate of kinetic energy
$\Delta x^+, \Delta y^+, \Delta z^+$	normalized cell size in x,y,z-direction
$\Delta y_w^+, \Delta y_c^+$	normalized cell size in y-direction for first cell adjacent to the wall and channel center, respectively
$(\,)^{sgs}$	sub-grid component
$(\,)^{res}$	resolved component
$(\,)^{tot}$	total
$\overline{(\,)}$	mean value
$\langle(\,)\rangle$	spatial and time averaged
$(\,)'$	fluctuating component
$(\,)^+$	normalized by wall variables/fluid properties

Appendix

2.6.2 Modification of momentum and energy equations

To drive the flow, a momentum source term S_u is added to the momentum equation, for details see e.g. [38]. The momentum equation as implemented in OpenFOAM with $p^\star = p/\rho$ as follows:

$$\frac{Du_i}{Dt} = -\frac{\partial p^\star}{\partial x_i} + \tau_{ij}\frac{\partial u_i}{\partial x_i} + S_u \tag{2.19}$$

where $S_u = U_\tau^2/\delta$.

Since cyclic boundary conditions are used in combination with a uniform heat flux at the walls, the energy equation must be rewritten with an additional source term S_T to obtain a physical correct solution. While the original reformulation given by [80] includes dimensions, the dimensionless temperature equation as given by [38] is used by most authors. However, the variation formulated by [15] is used; given as following:

$$\frac{DT}{Dt} = \frac{\partial}{\partial x_i}\left(\frac{\nu}{\mathrm{Pr}}\frac{\partial T}{\partial x_i} - \overline{\theta u_i}\right) + S_T \tag{2.20}$$

where $S_T = \overline{u}_x \overline{q}_w/(\rho c_p \overline{u}_b \delta)$.

CHAPTER 3

ENTROPY GENERATION ASSESSMENT FOR WALL-BOUNDED TURBULENT SHEAR FLOWS BASED ON REYNOLDS ANALOGY ASSUMPTIONS

The paper is published in *Entropy* and written by Matthias Ziefuss[1], Nader Karimi[2], Florian Ries[3]*, Amsini Sadiki[3] and Amirfarhang Mehdizadeh[1].

[1] Civil and Mechanical Engineering Department, School of Computing and Engineering, University of Missouri-Kansas City, Kansas City, MO 64110, USA
[2] School of Engineering, University of Glasgow, Glasgow G12 8QQ, UK
[3] Department of Mechanical Engineering, Institute of Energy and Power Plant Technology, Technische Universität Darmstadt, 64289 Darmstadt, Germany
* Corresponding author: ries@ekt.tu-darmstadt.de

Entropy 2019, 21(12), 1157; https://doi.org/10.3390/e21121157

3.1 **Abstract**

Heat transfer modeling plays a major role in design and optimization of modern and efficient thermal-fluid systems. Further, turbulent flows are thermodynamic processes, and thus, the second law of thermodynamics can be used for critical evaluations of such heat transfer models. However, currently available heat transfer models suffer from a fundamental shortcoming: their development is based on the general notion that accurate prediction of the flow field will guarantee an appropriate prediction of the thermal field, known as the Reynolds Analogy. In this work, an assessment of the capability of the in predicting turbulent heat transfer when applied to shear flows of fluids of different Prandtl numbers will be given. Towards this, a detailed analysis of the predictive capabilities of the concerning entropy generation is presented for steady and unsteady state simulations. It turns out that the Reynolds Analogy provides acceptable results only for mean entropy generation, while fails to predict entropy generation at small/sub-grid scales.

3.2 Introduction

There are various systems where turbulent heat transfer plays an important role in the development and optimization. These include cooling systems for nuclear power plants, where liquid metal is used as coolant [71, 12], boiler systems for biomass combustion [50], and heat exchange devices in petroleum industry [78], to name just a few. Further, all of these systems share important commonalities: first, experimental investigations are either not possible or prohibitively expensive [106] and second, the underlying thermodynamics process must be as efficient as possible to avoid loss of energy. Optimizing these systems require a detailed insight into the complex dynamics of heat and mass transfer, demanding advanced and reliable models. In addition, various systems employ working fluids with significantly different Prandtl (denoted as Pr) numbers (ranging from $Pr \ll 1$ for liquid metal to a few hundreds for crude oils). The variety in Pr numbers stresses the prediction capabilities of turbulent heat transfer models. Further, the challenge of modeling turbulent heat transfer arises from its strong and complex coupling to the turbulent field. Thus, a reliable model for the flow field (momentum transport) is a mandatory condition for a model of turbulent heat transfer. As a consequence, the main focus in research/modeling was on the modeling of momentum field in the past decades [107].

Turbulent momentum and heat transfer are based on the same underlying physical mechanism of cross-streamwise mixing of fluid elements [107]. Thus, the fundamental assumption that a correct prediction of the momentum transport leads to appropriate prediction of the heat transfer is often made. This analogy is based on the eddy diffusivity approach and well-known as Reynolds Analogy [107]. While this concept is a drastic simplification, it is still widely applied to a large majority of industrial applications of CFD when first order statistical quantities such as mean temperature and Nußelt number are of interest.

Furthermore, turbulent flows are thermodynamic processes and the directions of all such processes are restricted by the second law of thermodynamics. Thus, this law can be used for critical evaluation of turbulence and heat transfer models as

discussed in [91]. In applications, irreversibilities—described by the second law of thermodynamics—decrease the available energy of the working fluid [4]. This leads to an increase of system entropy and entropy generation [41, 120, 119]. In conjunction with heat transfer and fluid mechanic principles, it is possible to evaluate the impact of irreversibilities related to heat transport and thermo-fluid systems. Various investigations using the entropy concept including different configurations and physical processes with a variety of numerical and analytical approaches to better understanding of the process can be found in [3, 88, 46, 59, 91].

Based on this concept, only a few DNS can be found in literature [93, 89, 73, 19, 37, 47], which are restricted to simple geometries and low-to-medium Reynolds numbers due to the high computational cost. To overcome this problem, RANS approaches have been often used to study entropy generation dynamics at high Reynolds numbers. These investigations are reported in few studies [121, 36, 103, 104, 114]. However, it is well known, that prediction capabilities of RANS models are limited when dealing turbulent flows with large scale and unsteady characteristics. Unsteady approaches could offer a potential alternative strategy that allow prediction of unsteady dynamics of the flow field, such as hybrid URANS/LES. These overcome restrictions by DNS and RANS simulations to predict flow and thermal statistics accurately, yet computationally affordable. Despite the potential of LES and hybrid approaches, only a few publications using these concepts for entropy analyses are available [91, 30].

Concerning heat transfer modeling, it is to note that both RANS (steady) and unsteady approaches employ mainly the Reynolds Analogy to predict the thermal quantities (total/sub-grid part). This investigation aims to provide a comprehensive assessment of capabilities of the Reynolds Analogy to predict the entropy generation dynamics particularly through heat transfer in different turbulent environments (working fluids with different Prandtl numbers).

The rest of this chapter is organized as follows: in section 3.3, the employed turbulence models along with relevant transport equations will be presented and discussed. In section 3.4, an overview of test cases and numerical approach is provided. Results

obtained from the simulations are presented and discussed in section 3.5. The chapter ends up with a summary and conclusion in section 3.6.

3.3 Governing Equations

The current study aims to provide a comprehensive assessment of the prediction capabilities of the Reynolds Analogy for entropy production when applied to turbulent attached wall-bounded shear flows of fluids with different Pr numbers. Towards this end, various aspects of this analogy regarding entropy production will be investigated. First, the sensitivity of the Reynolds Analogy with respect to the turbulence model employed to predict the flow field will be investigated. Therefore, two different turbulence models, i.e. $k-\omega-$ SST and $k-\epsilon-\zeta-f$, will be used for steady state (RANS) simulations. In order to prelude effects of numerical instabilities/uncertainties on the model performance, 3-dimensional domains with appropriate mesh resolutions have been used for the RANS simulations.

As the next step, performance of the Reynolds Analogy in unsteady simulations where the analogy operates as a sgs model is assessed. Sensitivity to grid resolution is investigated as it is an indicator of basic properties of sgs-models. The $k-\omega-$ SST-IDDES model will be used for the unsteady simulations. This model is a hybrid URANS/LES model and is able to provide an accurate prediction of the flow field—comparable to wall-modeled LES—at affordable computational cost [11]. The mathematical formulation of turbulence models used in the current study in conjunction with other transport equations (energy, temperature variance and entropy) will be presented and discussed in the following.

3.3.1 Turbulence Models

3.3.1.1 The $k-\omega-$ SST model

The $k-\omega-$ SST model is one of the most commonly used models. It employs two transport equations, one for turbulent kinetic energy k and one for the inverse of

dissipation rate ω to provide necessary turbulence scales [61]. The model equations read:

$$\frac{Dk}{Dt} = \frac{\partial}{\partial x_i}\Big[\Big(\nu + \frac{\nu_t}{\sigma_k}\Big)\frac{\partial k}{\partial x_i}\Big] + \tilde{P}_k - \beta^\star \rho\omega k, \tag{3.1}$$

$$\frac{D\omega}{Dt} = \frac{\partial}{\partial x_i}\Big[\Big(\nu + \frac{\nu_t}{\sigma_\omega}\Big)\frac{\partial \omega}{\partial x_i}\Big] + 2(1-F_1)\frac{\sigma_{\omega 2}}{\omega}\frac{\partial k}{\partial x_i}\frac{\partial \omega}{\partial x_i} + \frac{\gamma}{\nu_t}P_k - \beta\omega^2, \tag{3.2}$$

with $\tilde{P}_k = \min(P_k; c_l\epsilon)$ and $P_k = \tau_{ij}\frac{\partial \overline{u_i}}{\partial x_j}$ as mechanical turbulent production. Further details on model constants and functions, i.e. $c_l, \beta, \beta^\star, \gamma, \tau_{ij}, \sigma_{\omega 2}, F_1$, are provided in [61].

3.3.1.2 The $k-\epsilon-\zeta-f$ model

The $k-\epsilon-\zeta-f$ is well known to be able to predict near wall effects in shear flows [28]. In addition to the transport equation for kinetic energy k and its dissipation ε, two more equations are solved. The first one is a transport equation for the velocity scale ratio $\zeta = \overline{v^2}/k$ and the second one is an elliptic relaxation concept, f, to sensitize ζ. For brevity, the model is referred as $\zeta - f$ model. The model equations are as follows:

$$\frac{Dk}{Dt} = \frac{\partial}{\partial x_i}\Big[\Big(\nu + \frac{\nu_t}{\sigma_k}\Big)\frac{\partial k}{\partial x_i}\Big] + P_k - \varepsilon, \tag{3.3}$$

$$\frac{D\varepsilon}{Dt} = \frac{\partial}{\partial x_i}\Big[\Big(\nu + \frac{\nu_t}{\sigma_\varepsilon}\Big)\frac{\partial \varepsilon}{\partial x_i}\Big] + \frac{C_{\varepsilon 1}P_k - C_{\varepsilon 2}\varepsilon}{\tau}, \tag{3.4}$$

$$\frac{D\zeta}{Dt} = \frac{\partial}{\partial x_i}\Big[\Big(\nu + \frac{\nu_t}{\sigma_\zeta}\Big)\frac{\partial \zeta}{\partial x_i}\Big] - \frac{\zeta}{k}P_k + f, \tag{3.5}$$

$$L^2\frac{\partial^2 f}{\partial x_i^2} - f = \frac{1}{\tau}\Big(C_1 + C_2'\frac{P_k}{\varepsilon}\Big)\Big(\zeta - \frac{2}{3}\Big), \tag{3.6}$$

with $P_k = \tau_{ij}\frac{\partial \overline{u_i}}{\partial x_j}$ and $\nu_t = C_\mu \zeta k \tau$. Further details on model constants and functions, i.e. $\tau_{ij}, \tau, C_1, C_2^{'}, C_{\epsilon 1}, C_{\epsilon 2}$, are provided in [28].

3.3.1.3 The $k-\omega-$ SST-IDDES model

$k-\omega-$ SST-IDDES employs a modified version of $k-\omega-$ SST model to improve near-wall prediction and enable unsteady calculations. It is defined with two transport equations for k and ω:

$$\frac{Dk}{Dt} = \frac{\partial}{\partial x_i}\Big[\Big(\nu + \frac{\nu_t}{\sigma_k}\Big)\frac{\partial k}{\partial x_i}\Big] + P_k - \sqrt{k^3}/l_{IDDES}, \tag{3.7}$$

$$\frac{D\omega}{Dt} = \frac{\partial}{\partial x_i}\Big[\Big(\nu + \frac{\nu_t}{\sigma_\omega}\Big)\frac{\partial \omega}{\partial x_i}\Big] + 2(1-F_1)\frac{\sigma_{\omega 2}}{\omega}\frac{\partial k}{\partial x_i}\frac{\partial \omega}{\partial x_i} + \frac{\gamma}{\nu_t}P_k - \beta\omega^2, \tag{3.8}$$

where blending function F_1, production term P_k, and model constants (γ, σ_k, σ_w, σ_{w2} and β) are imported from the original $k-\omega-$SST model [61]. It should be noted that within $k-\omega-$ SST-IDDES, only the destruction term in the k-equation is modified by introducing the l_{IDDES} term, whereas the ω-equation remains unchanged. l_{IDDES} is responsible for triggering a transition from URANS mode into a scale-resolving mode. A detailed description of this methodology can be found in [23, 101].

3.3.2 Energy equation and heat transfer model

The Reynolds-averaged energy equation follows as [27]:

$$\rho c_p \frac{DT}{Dt} = S_T + \frac{\partial}{\partial x_i}\Big[\Big(\lambda\frac{\partial T}{\partial x_i}\Big) - \rho c_p \overline{\theta u_i}\Big], \tag{3.9}$$

Assuming incompressible flow, constant physical properties and neglecting addition source, S_T, terms such as radiation, the equation for the mean temperature T can be written as below:

$$\frac{DT}{Dt} = \frac{\partial}{\partial x_i}\Big[\Big(\frac{\nu}{Pr}\frac{\partial T}{\partial x_i}\Big) - \overline{\theta u_i}\Big]. \tag{3.10}$$

The quantity $\overline{\theta u_i}$ on the right hand side is called turbulent heat flux and is the Reynolds-averaged fluctuating velocity-temperature correlation. This quantity needs to be modeled in order to close the equation.

The simplest and mostly used approach to model the turbulent heat flux is the Reynolds Analogy. This approach is based on the assumption that the momentum and thermal layer overlay and thus, have the same thickness. Therefore, it is assumed that an accurate computation of the momentum transport leads to an accurate prediction of the temperature field. In addition, it is assumed that the turbulent heat flux is proportional to the mean temperature gradient [44], which leads to the following relation:

$$\overline{\theta u_i} = -\frac{\nu_t}{\sigma_t}\frac{\partial T}{\partial x_i}, \tag{3.11}$$

with σ_t as turbulent Prandtl number, usually taken constant equal to 0.9 [107]. This value is suitable/appropriate only for fluids with Pr number around unity. Concerning low Pr number fluids, this value is significantly lower than the averaged reference value obtained from DNS, see Figure 3.1. However, this value provides a reasonable estimation for high Pr number fluids except for regions very close to solid surfaces, i.e. $y^+ < 3$, see Fig. 3.1.

Moreover, it is immediately clear that the capability of the Reynolds Analogy is limited to only first order statistics in non-homogeneous directions, and thus, fails to predict the heat flux in homogeneous direction when employed for steady state simulations.

In case of unsteady calculations, the internal energy equation (Eq. 3.10) as well as the Reynolds Analogy (Eq. 3.11) take the following form:

$$\frac{DT}{Dt} = \frac{\partial}{\partial x_i}\left[\left(\frac{\nu}{Pr}\frac{\partial T}{\partial x_i}\right) - \overline{\theta u_i}^{sgs}\right] \quad \text{and} \quad \overline{\theta u_i}^{sgs} = -\frac{{\nu_t}^{sgs}}{\sigma_t^{sgs}}\frac{\partial T}{\partial x_i}, \tag{3.12}$$

where $\overline{\theta u_i}^{sgs}$ and ${\nu_t}^{sgs}$ represent sub-grid heat flux and sub-grid eddy viscosity, respectively. Thus, the total heat flux is the sum out of subgrid-scale (sgs) and res components.

3.3.3 Temperature variance equation

As for a turbulent flow field, for which the characteristic time is provided by $\tau_m = k/\varepsilon$, it is also of interest to introduce a characteristic time scale for thermal mixing which can be given as $\tau_\theta = \overline{\theta^2}/2\varepsilon_\theta$, where $\overline{\theta^2}$ is the temperature variance and ε_θ its dissipation. This quantities are important for an entropy analyses as will be shown later. The modeled transport equation for $\overline{\theta^2}$ reads as follows [107]:

$$\frac{D\overline{\theta^2}}{Dt} = 2P_{\overline{\theta^2}} - 2\varepsilon_\theta + \frac{\partial}{\partial x_i}\left[\left(\frac{\nu}{Pr} + \frac{\nu_t}{\sigma_t}\right)\frac{\partial \overline{\theta^2}}{\partial x_i}\right], \tag{3.13}$$

where $P_{\overline{\theta^2}} = -\overline{\theta u_i}\partial T/\partial x_i$ is the production of temperature variance and ε_θ is the dissipation of temperature variance. Introducing an additional transport equation for this quantity would be the most consistent approach to close equation 3.13. However, closing this equation is more complex compared to modeling the equation for the

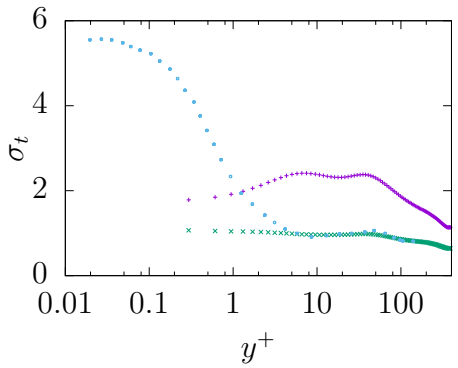

Figure 3.1: Variation of turbulent Prandtl number σ_t at different Re_τ and Pr numbers: $Re_\tau = 395$ with $Pr = 0.025$ [38] (+) and $Pr = 0.71$[38] (×), and $Re_\tau = 150$ with $Pr = 200$ [8] (○)

dissipation of turbulent kinetic energy ε. As stated in [107], twice as many free parameters, including two turbulent time scales (mechanical and thermal), and two production terms need to be determined. These issues have been discussed in few investigations [110, 76, 25, 60].

However, often a simpler approach that assumes a constant thermal to mechanical time-scale ratio, denoted as $\mathcal{R} = \tau_\theta/\tau_m$, is used to provide information on thermal time scale [107, 43]. Several studies [45, 109, 44] have shown that the assumption of a constant ratio—with a typical value of $\mathcal{R} = 0.5$—works pretty well for fluids with Pr number around unity. Nevertheless, it is commonly used even when dealing with Pr numbers significantly different than unity [107], despite the lack of extensive assessment and validation. Using the typical value of 0.5 for $\mathcal{R}$ leads to the following relation for ε_θ and is used in this study along with the Reynolds Analogy to determine ε_θ in the temperature variance equation:

$$\varepsilon_\theta = \frac{\varepsilon\overline{\theta^2}}{k}. \tag{3.14}$$

In case of unsteady calculations, the transport equation for the temperature variance (equation 3.13) takes the following form:

$$\frac{D\overline{\theta^2}^{sgs}}{Dt} = 2P_{\overline{\theta^2}}^{sgs} - 2\varepsilon_\theta^{sgs} + \frac{\partial}{\partial x_i}\Big[\Big(\frac{\nu}{Pr} + \frac{\nu_t^{sgs}}{\sigma_k^{sgs}}\Big)\frac{\partial\overline{\theta^2}^{sgs}}{\partial x_i}\Big], \tag{3.15}$$

with

$$P_{\overline{\theta^2}}^{sgs} = -\overline{\theta u_i}^{sgs}\frac{\partial T}{\partial x_i} \quad \text{and} \quad \varepsilon_\theta^{sgs} = \frac{\varepsilon^{sgs}\overline{\theta^2}^{sgs}}{k^{sgs}}. \tag{3.16}$$

Thus, the total temperature variance is the sum of res and sgs components.

3.3.4 Entropy equation

Entropy generation due to different mechanisms will be presented and discussed in the following. Under the assumptions of Cartesian coordinates, incompressible fluid,

single-phase flow, non-reacting and Fourier heat conduction the second law of thermodynamics can be expressed as a local imbalance as below [112]:

$$\rho\frac{Ds}{Dt} + \frac{\partial}{\partial x_i}\Big[\frac{q_i}{\Theta}\Big] = \Pi_v + \Pi_q \geq 0. \tag{3.17}$$

The two production terms, Π_v and Π_q, represent important mechanisms for entropy production. If production due to radiation is neglected, these two are as below:

$$\Pi_v = \frac{\mu}{\Theta}\Big(\frac{\partial U_i}{\partial x_j} + \frac{\partial U_j}{\partial x_i}\Big)\frac{\partial U_i}{\partial x_j}, \tag{3.18}$$

$$\Pi_q = \frac{1}{\Theta^2} q_i \frac{\partial \Theta}{\partial x_i} = \frac{\lambda}{\Theta^2}\frac{\partial \Theta}{\partial x_i}\frac{\partial \Theta}{\partial x_i}, \tag{3.19}$$

where Π_v is the production due to the viscous dissipation and Π_q is the production by heat transfer due to finite temperature gradients. These terms are always positive and thus, act as source terms. Both terms need to be calculated for entropy generation analysis, since they are responsible for irreversibilities evolving in heat transferring viscous fluid flows.

3.3.4.1 Entropy production - steady state calculations

In the concept of Reynolds Averaged Navier Stokes equation (RANS), equation 3.17 holds the instantaneous values, and following the Reynolds decomposition [51, 52], this equation can be decomposed into mean and fluctuating parts. Accordingly, entropy production due to viscous dissipation can be decomposed into mean and fluctuating parts, i.e. $\Pi_v = \overline{\Pi}_v + \Pi_v^{'}$, with

$$\overline{\Pi}_v = \frac{\mu}{T}\Big(\frac{\partial \overline{u}_i}{\partial x_j} + \frac{\partial \overline{u}_j}{\partial x_i}\Big)\frac{\partial \overline{u}_i}{\partial x_j}, \tag{3.20}$$

$$\Pi_v^{'} = \frac{\mu}{T}\overline{\Big(\frac{\partial u_i}{\partial x_j} + \frac{\partial u_j}{\partial x_i}\Big)\frac{\partial u_i}{\partial x_j}} = \frac{\mu}{T}\underbrace{\overline{\Big(\frac{\partial u_i}{\partial x_j}\Big)^2}}_{A}. \tag{3.21}$$

Calculation of $\overline{\Pi}_v$ is possible using knowledge on mean values of velocity and temperature, which are always known in calculations. In contrast, $\Pi_v^{'}$ is not closed and has to be modeled. Considering the exact equation for turbulent dissipation, $\varepsilon = \nu\overline{(\partial u_i/\partial x_j)^2}$, and thus, by assuming an equivalence between ε and the term A, discussed in [51], equation 3.21 can be approximated via known mean-values as below:

$$\Pi_v^{'} = \frac{\rho}{T}\varepsilon. \tag{3.22}$$

Similarly, entropy production due to heat transfer can be decomposed into mean and fluctuation parts, i.e. $\Pi_q = \overline{\Pi}_q + \Pi_q^{'}$, with

$$\overline{\Pi}_q = \frac{\lambda}{T^2}\frac{\partial T}{\partial x_i}\frac{\partial T}{\partial x_i}, \tag{3.23}$$

$$\Pi_q^{'} = \frac{\lambda}{T^2}\overline{\frac{\partial \theta}{\partial x_i}\frac{\partial \theta}{\partial x_i}} = \frac{\lambda}{T^2}\underbrace{\overline{\left(\frac{\partial \theta}{\partial x_i}\right)^2}}_{B}. \tag{3.24}$$

Again, $\overline{\Pi}_q$ can be calculated via known mean-quantities while $\Pi_q^{'}$ needs to be modeled. Considering the exact equation for thermal dissipation, $\varepsilon_\theta = 2\alpha\overline{(\partial\theta/\partial x_i)^2}$, and thus, by assuming a local equilibrium between ε_θ and term B entropy production due to heat transfer as well as using the Boussinesq approximation for the production term, discussed in [51], equation 3.24 can be approximated as:

$$\Pi_q^{'} = \frac{\rho c_p}{T^2}\varepsilon_\theta. \tag{3.25}$$

Since ε_θ is not directly known without a transport equation, it can be calculated using the model given by equation 3.14.

3.3.4.2 *Entropy production - unsteady calculations*

In contrast to the steady state approach, the entropy production terms in equation 3.17 must be split in res- and sgs-components as below:

$$\Pi_v \approx \underbrace{\left\langle \frac{\mu}{T}\left(\frac{\partial \overline{u}_i}{\partial x_j} + \frac{\partial \overline{u}_j}{\partial x_i}\right)\frac{\partial \overline{u}_i}{\partial x_j} \right\rangle}_{\langle \Pi_v^{res} \rangle} + \underbrace{\left(\langle \Pi_v \rangle - \left\langle \frac{\mu}{T}\left(\frac{\partial \overline{u}_i}{\partial x_j} + \frac{\partial \overline{u}_j}{\partial x_i}\right)\frac{\partial \overline{u}_i}{\partial x_j} \right\rangle \right)}_{\langle \Pi_v^{sgs} \rangle}, \tag{3.26}$$

$$\Pi_q \approx \underbrace{\left\langle \frac{\lambda}{T^2}\frac{\partial T}{\partial x_i}\frac{\partial T}{\partial x_i} \right\rangle}_{\langle \Pi_q^{res} \rangle} + \underbrace{\left(\langle \Pi_q \rangle - \left\langle \frac{\lambda}{T^2}\frac{\partial T}{\partial x_i}\frac{\partial T}{\partial x_i} \right\rangle \right)}_{\langle \Pi_q^{sgs} \rangle}, \tag{3.27}$$

where $\langle(\ )\rangle$ donates spatial and time averaging (ensemble averaging). The res-components can be calculated via known mean quantities while sgs-components will be approximated following [91] as below:

$$\langle \Pi_v^{sgs} \rangle \approx \frac{\rho}{T}\langle \varepsilon_{sgs} \rangle, \tag{3.28}$$

$$\langle \Pi_q^{sgs} \rangle \approx \frac{c_p \rho}{T^2}\langle \varepsilon_{\theta sgs} \rangle. \tag{3.29}$$

3.4 **Numerical Setup**

The Reynolds Analogy is assessed using previously mentioned turbulence models at different Reynolds and Prandtl numbers. The details of the numerical schemes and the respective flow configuration are described in the following section.

3.4.1 Flow configuration

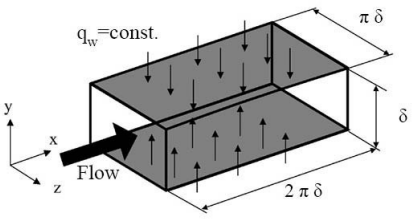

Figure 3.2: Sketch of horizontal channel flow configuration [39]

The configuration is a fully developed turbulent channel flow, shown in Figure 3.2. The size of the computational domain is $2\pi\delta, 2\delta, \pi\delta$. Different Reynolds and Prandtl numbers have been considered based on the availability of reference (DNS) data. The details of all simulations are summarized in Table 3.1. Note that the Reynolds number is defined based on the friction velocity at wall (U_τ) and channel half height δ. A constant pressure gradient is applied via an additional source term in the momentum equation to drive the flow to the targeted Reynolds number. Periodic boundary conditions are imposed in the streamwise and the spanwise directions, and no-slip condition is used at both walls. For the temperature field, a mean uniform heat flux at the walls, and periodic boundary conditions in the streamwise and the spanwise directions have been applied. Further, it is important to mention that the temperature variance is set to zero at the wall. Detailed information on the influence of the boundary condition can be found in [110, 60, 83]. The results are normalized by the channel half width δ, the friction velocity U_τ, the kinematic viscosity ν, the density ρ, the friction temperature T_τ, and the friction entropy production rate S_τ.

Detailed information on the mesh resolutions used for the unsteady state simulations are given in Table 3.2. A simple gradient spacing is used to achieve appropriate distribution in the wall-normal direction. Further, it should be noted that the stretch factor **r** should be less than ≈ 1.2 [111, 99], which is fulfilled for all meshes.

It is worth mentioning that, to the best of authors' knowledge, no explicit DNS data are available on the entropy generation in a fully developed turbulent channel flow,

Table 3.1: Overview of simulations

Re_τ	Pr	Reference	Type	Resolution	Grids
395	0.025	Kawamura et al. [38]	steady unsteady	$48 \times 72 \times 48$	A-100
			unsteady	$128 \times 192 \times 48$	B-100
395	0.71	Kawamura et al. [38]	steady unsteady	$48 \times 72 \times 48$	A-100
			unsteady	$128 \times 192 \times 48$	B-100
150	200	Bergant et al. [8]	steady unsteady	$48 \times 72 \times 48$	A-1000
			unsteady	$128 \times 192 \times 96$	C-250

i.e. entropy production has been calculated using available DNS data for quantities such as velocity and temperature as input data for relations discussed in Section 3.3.4. For this study the required DNS data have been taken from [38, 8].

Table 3.2: Details of the grid resolution for fully developed turbulent channel flow for unsteady state simulations

Re_τ	Grids	Δx^+	$\Delta y_w^+ - \Delta y_c^+$	Δz^+	N_x	N_y	N_z	r
395	DNS [38]	9.88	0.15-6.52	4.59	512	192	512	-
	Mesh A-100	51.7	0.49-19.1	25.9	48	72	48	1.14
	Mesh B-100	19.5	0.19-19.0		128	192		1.05
150	DNS [8]	12.3	0.04-3.3	4.6	192	145	128	-
	Mesh A-1000	19.5	0.03-27.7	9.7	48	72	48	1.21
	Mesh C-250	7.5	0.03-8.7	5.1	128	192	96	1.06

3.4.2 Code description

All numerical simulations presented in this chapter are performed using OpenFOAM-v1706 with necessary modifications. PISO algorithm has been used for steady and unsteady calculations. Second order schemes have been used for velocity, turbulence and thermal quantities for both steady and unsteady simulations. Further, a Courant number around 0.05 was chosen for a reliable prediction of the velocity and temperature field for unsteady calculations as suggested in [23].

3.5 Results and Discussion

In the framework of the present study, prediction capabilities of the Reynolds Analogy in accordance with the second law of thermodynamics for turbulent thermal effects at different Reynolds and Prandtl numbers are investigated, as provided in Table 3.1. This covers a wide range of Pr numbers, i.e. $Pr = 0.025, 0.71, 200$, to study capabilities of the Reynolds Analogy when dynamics of heat transfer are significantly different. The main goal here is to provide an assessment by investigating the entropy prediction capabilities of the Reynolds Analogy. The results obtained from different simulations will be explained and discussed in the following.

3.5.1 Steady state simulations

The steady state simulations are carried out using the $k-\omega-$ SST and $\zeta-f$ RANS-based models. It should be noted that mesh convergence studies have been done for all simulations. While only mesh independent results are presented, the detailed analyses can be found in [126].

3.5.1.1 $Pr = 0.71$

Figure 3.3 presents mean velocity, dissipation of turbulent kinetic energy k, mean temperature, rms value of temperature fluctuations, as well as production and dissipation of $\overline{\theta^2}$ at $Re_\tau = 395$ for $Pr = 0.71$. As expected, mean velocity and mean temperature profiles are in good agreements with the DNS data. In contrast, ε is mispredicted in the near-wall region and shows only good agreement with DNS data after the buffer layer, i.e. $y^+ > 30$. Further, the rms value of temperature fluctuation (θ_{rms}) is mispredicted by both turbulence models. A detailed analysis of the transport equation for $\overline{\theta^2}$ (Eq. 3.13) will help to understand the reason behind the misprediction. The production of $\overline{\theta^2}$ is well predicted, indicating the production is primary due to the temperature gradient in the wall-normal direction. However, the thermal dissipation ε_θ is mispredicted particularly in the near-wall region, which is thought to be the main reason of misprediction of $\overline{\theta^2}$ and thus, θ_{rms}. For this study, the assumption of a constant ther-

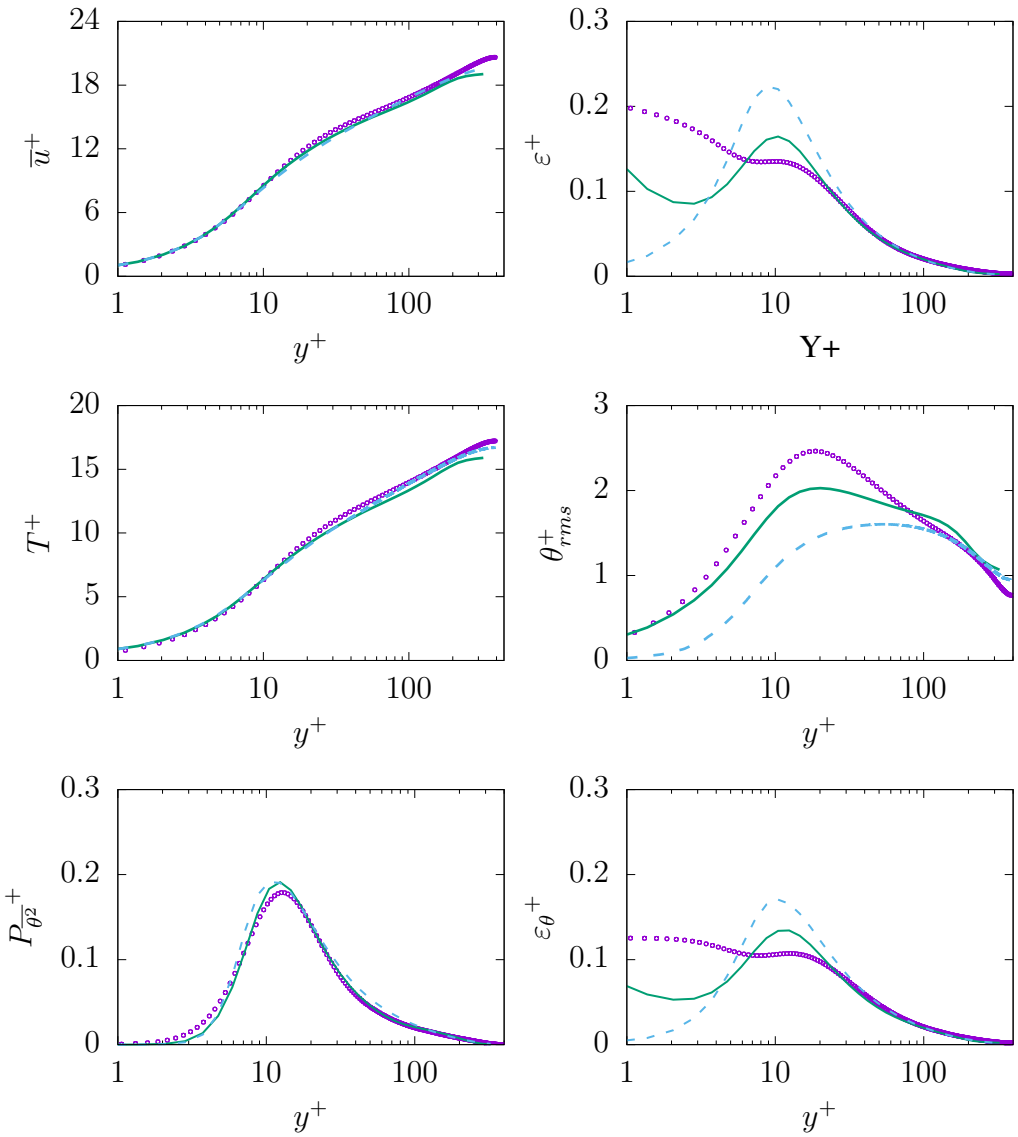

Figure 3.3: Evolution of streamwise velocity (top left), dissipation of k (top right), temperature (middle left), temperature rms (middle right), production of $\overline{\theta^2}$ (bottom left) and dissipation of $\overline{\theta^2}$ (bottom right) at $Re_\tau = 395$ for $Pr = 0.71$. $\zeta - f$: —, $k - \omega -$ SST: - - -, DNS: ○

mal to mechanical time-scale ratio ($\mathcal{R}$) is used to derive ε_θ. This assumption describes ε_θ based on ε, which could lead to misprediction of ε_θ in near-wall region, since ε is mispredicted in the near-wall region.

Figure 3.4 presents entropy production due to viscous dissipation (mean and fluctuation) and production due to heat transfer (mean and fluctuation). It can be observed that both mean entropy generations are well predicted as they are directly related to the mean velocity and temperature, which are well predicted by both turbulence mod-

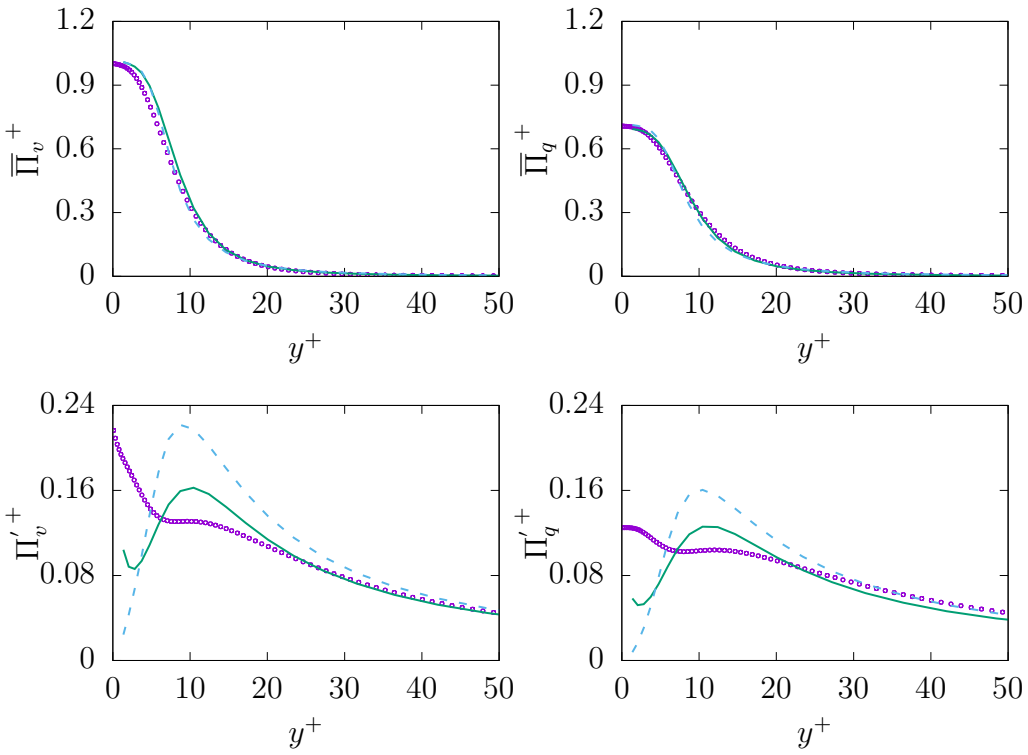

Figure 3.4: Evolution of mean entropy production $\overline{\Pi}_i$ (top) and fluctuation entropy production Π_i' (bottom) due to viscous dissipation (v, left) and heat transfer (q, right) at $Re_\tau = 395$ for $Pr = 0.71$. $\zeta - f$: —, $k - \omega$ − SST: - - -, DNS: ○

els. However, the entropy productions due to fluctuations are mispredicted in near-wall region for both generation mechanisms. Further away from the wall, both fluctuation quantities follow a very similar tendency compared to DNS data. Moreover, the assumption of a constant thermal to mechanical ratio (constant $\mathcal{R}$) seems to be reasonable for fluids with Pr number around unity, as ε and ε_θ show pretty much similar dynamics as shown in Figure 3.3. However, more advanced models for ε are required to accurately predict ε and consequently, ε_θ as well as entropy generation by fluctuations in near-wall region. Furthermore, it can be seen that both entropy generation mechanisms almost equally contribute to the total amount of entropy generated in the process.

3.5.1.2 $Pr = 0.025$

The simulation for $Pr = 0.025$ is carried out at $Re_\tau = 395$ as provided in Table 3.1. It should be noted that the flow field results are not shown as the temperature is considered to be a passive scalar. Figure 3.5 presents mean temperature and tempera-

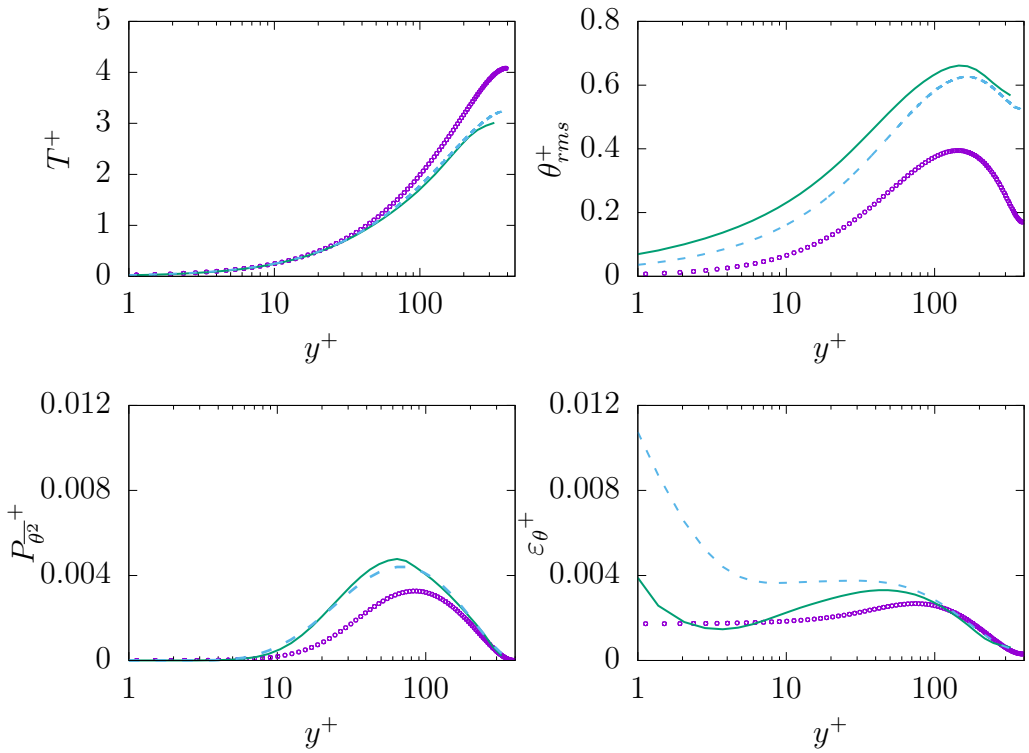

Figure 3.5: Evolution of temperature (top left), temperature rms (top right), production of $\overline{\theta^2}$ (bottom left) and dissipation of $\overline{\theta^2}$ (bottom right) at $Re_\tau = 395$ for $Pr = 0.025$. $\zeta - f$: —, $k - \omega -$ SST: - - -, DNS: ○

ture rms profiles along with production and dissipation of $\overline{\theta^2}$. In contrast to the previous simulation concerning $Pr = 0.71$, there are discrepancies in mean temperature (underprediction of $\approx 25\%$) and temperature variance (equivalently θ_{rms}) is severely overpredicted over the whole channel domain. As discussed in [126] and shown in Figure 3.1, the misprediction of the temperature is likely to be a result of the assumption of a constant turbulent Prandtl number in the Reynolds Analogy. Further, the overprediction of the production of $\overline{\theta^2}$ leads to the discrepancy in θ_{rms}. However, the situation is worse for the dissipation: as shown, both turbulence models fail to predict the plateau behavior of ε_θ. Furthermore, it clearly can be seen that the assumption of constant thermal to mechanical time scale ($\mathcal{R}$) is not reasonable for fluids with Pr numbers significantly less than unity, as ε (shown in Figure 3.3) indicates completely different tendency compared to ε_θ—in contrast to fluids with Pr number around unity.

Figure 3.6 presents entropy production due to viscous dissipation (mean and fluctuation) and production due to heat transfer (mean and fluctuation). As expected,

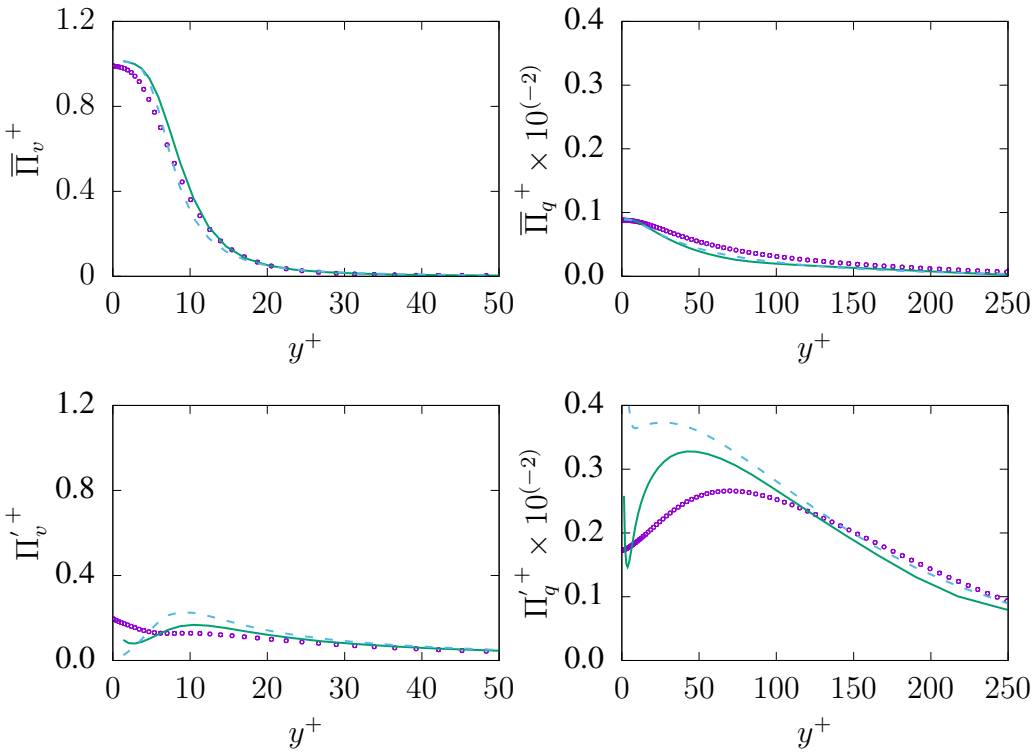

Figure 3.6: Evolution of mean entropy production $\overline{\Pi}_i$ (top) and fluctuation entropy production Π_i' (bottom) due to viscous dissipation (v, left) and heat transfer (q, right) at $Re_\tau = 395$ for $Pr = 0.025$. $\zeta - f$: —, $k - \omega -$ SST: - - -, DNS: ○

mean entropy generation due to viscous dissipation is in reasonable agreement with the DNS data. Further, mean entropy generation due to heat transfer follows closely DNS data, with a slight deviation. Similar to the previous simulation, entropy generation due to the fluctuations is in the near-wall region not accurately predicted, mainly due to misprediction of ε and accordingly misprediction of ε_θ in near-wall region. However, the prediction is in good agreement with the reference data further away form the wall. It is worth to mention, that in contrast to $Pr = 0.71$, the total entropy generation and therefore, the irreversibilities of the process mainly stems from the viscous dissipation as it dominates over the entropy production due to heat transfer. This is probably to high thermal conductivity of fluids with low Pr numbers that allows an efficient heat transfer.

3.5.1.3 $Pr = 200$

In contrast to previous simulations, simulations for $Pr = 200$ are carried out at $Re_\tau = 150$ due lack of sufficient reference data at higher Re_τ. It was shown in [25] that for $Pr = 0.71$ and larger, temperature field data is roughly independent of Re_τ and the temperature field mainly depends on Pr number. It is worth to mention that high Prandtl number fluids impose some computational challenges and thus, certain mesh requirements need to be considered [9, 8, 126]. However, only mesh independent results are presented in this study.

Figure 3.7 presents mean velocity, dissipation of k, mean temperature, rms of temperature fluctuations, as well as production and dissipation of $\overline{\theta^2}$. It should be noted that generally turbulence models have been developed based on high Reynolds number assumption. Therefore, prediction quality of these models when dealing with relatively low Reynolds number, as in the present case, might be decreased [126], such as for the mean velocity profile, which is thought to be the main reason of the overprediction of mean temperature. In contrast to the mean temperature, θ_{rms} is strongly underpredicted by both turbulence models, mainly due to the misprediction of dissipation of $\overline{\theta^2}$, i.e. ε_θ. While the production is in good agreement with DNS data, the dissipation in near-wall region is severely mispredicted inside the thermal boundary layer, i.e. $y^+ \approx 4$.

Figure 3.8 presents entropy production due to viscous dissipation (mean and fluctuation) and production due to heat transfer (mean and fluctuation). It is worth to mention that the very thin thermal boundary layer with its high temperature gradient is clearly visible, especially in the evaluation of Π_q which vanishes for $y^+ > 3$. Again, it can be observed that both mean entropy generations, i.e. $\overline{\Pi}_v$ and $\overline{\Pi}_q$, are overall fairly well predicted as they are directly related to the mean velocity and temperature values, which are in good agreement with the DNS data for both turbulence models. Similarly, entropy production due to fluctuating quantities indicate acceptable predictions except for regions very close to the wall. More importantly, entropy generation due to heat transfer is the dominant mechanism, in contrast to previous simulation concerning low Pr fluids. This is most likely due to very low thermal conductivity of the fluids, which

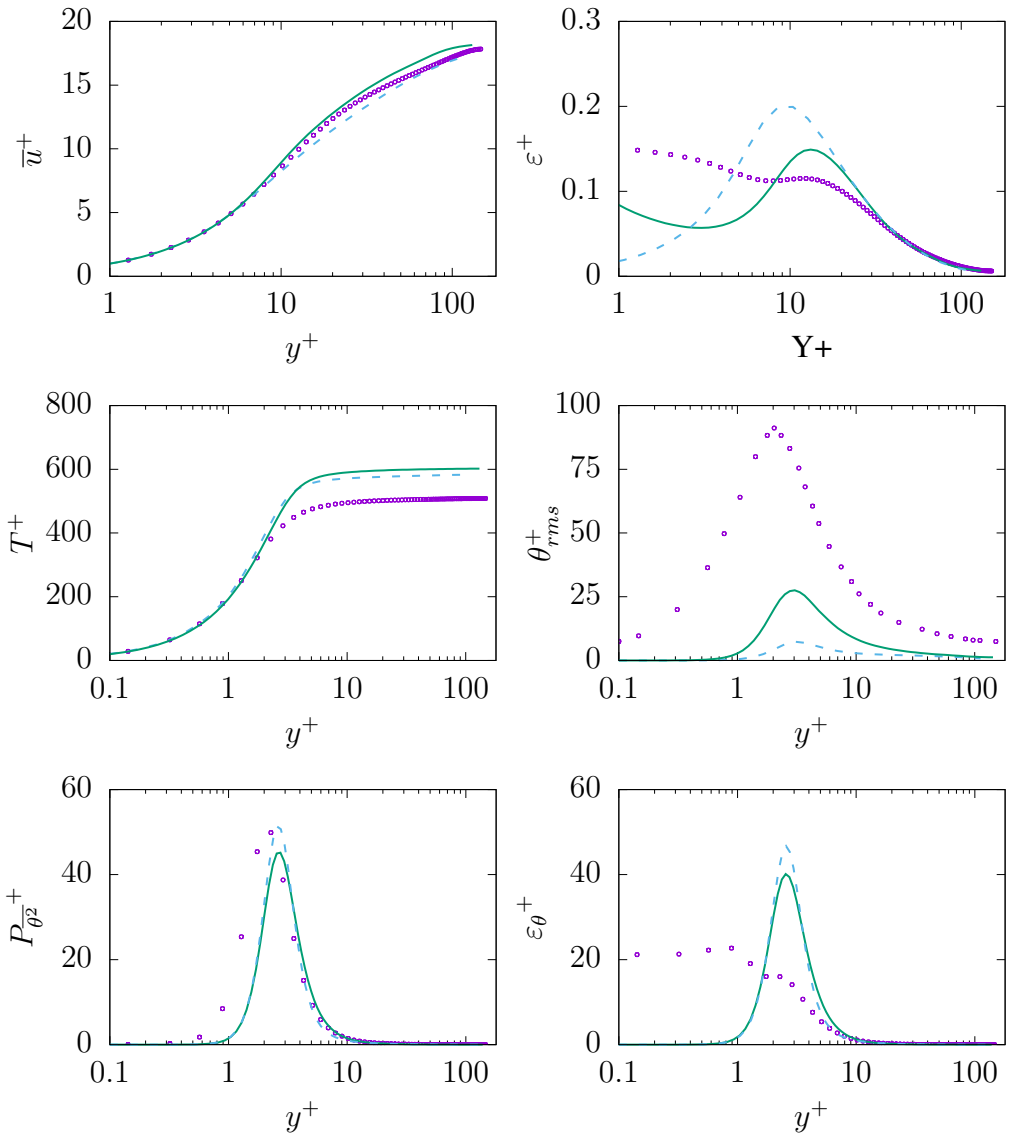

Figure 3.7: Evolution of streamwise velocity (top left), dissipation of k (top right), temperature (middle left), temperature rms (middle right), production of $\overline{\theta^2}$ (bottom left) and dissipation of $\overline{\theta^2}$ (bottom right) at $Re_\tau = 150$ for $Pr = 200$. $\zeta - f$: —, $k - \omega -$ SST: - - -, DNS: ○

leads to a very high temperature gradient at the surface to reach the targeted energy that needs to be transferred to the fluid at the wall via conduction.

3.5.2 Unsteady Simulations

Unsteady simulations have been carried out using the $k - \omega -$ SST-IDDES model. Three different Pr numbers, i.e. 0.71, 0.025 and 200, have been considered. All three Pr numbers are investigated with two different resolutions to demonstrate

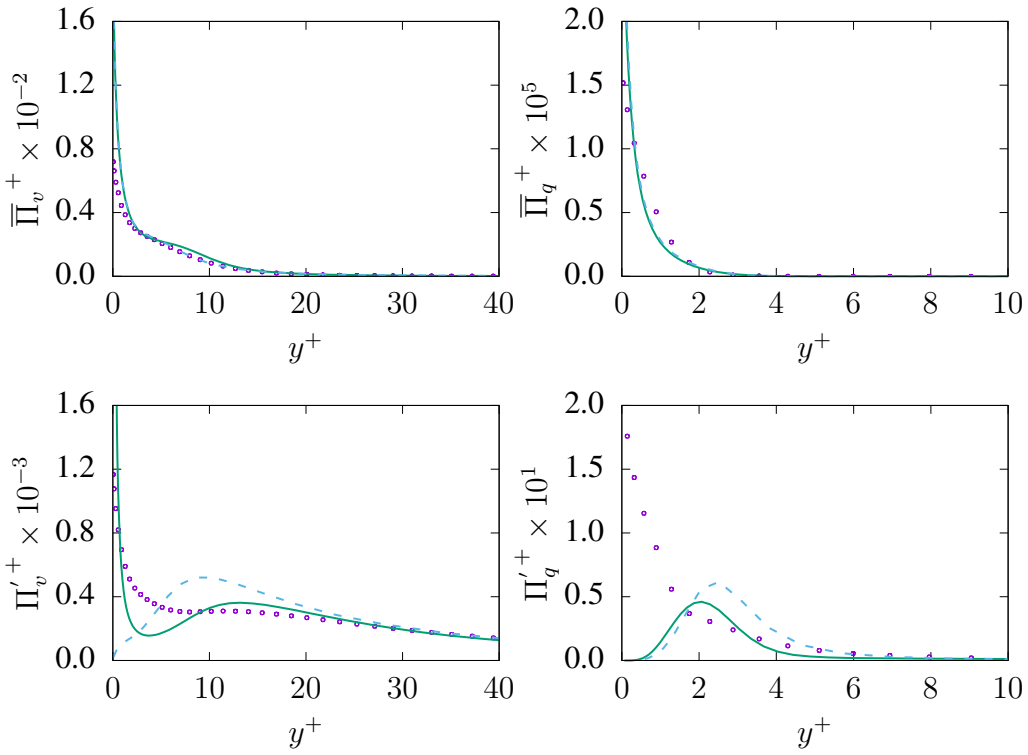

Figure 3.8: Evolution of mean entropy production $\overline{\Pi}_i$ (top) and fluctuation entropy production Π_i' (bottom) due to viscous dissipation (v, left) and heat transfer (q, right) at $Re_\tau = 150$ for $Pr = 200$. $\zeta - f$: —, $k - \omega -$ SST: - - -, DNS: ○

the influence of mesh resolution, and more importantly, to study the behavior of the Reynolds Analogy when operating as a sgs-model. Further, only results on adequate grids will be presented, for details see [126], and all presented results are spatial and time averaged, which corresponds to $\langle(\,)\rangle$; as described in the nomenclature.

The $k - \omega -$ SST-IDDES model is a hybrid URANS/LES approach and is able to provide an accurate prediction of the flow field comparable to wall-modeled LES at affordable computational cost [11]. Furthermore, this model treats the near-wall region in URANS-model, while transitioning to LES-mode away from the wall. This will allow investigation on the dynamics of the transition of the Reynolds Analogy from URANS to LES-mode, where this analogy operates as a sgs-model.

3.5.2.1 $Pr = 0.71$

Figure 3.9 presents the results obtained at $Re_\tau = 395$ for $Pr = 0.71$ on mesh A-100 and B-100. This includes mean velocity, mean temperature, modeled viscous

and thermal dissipations (ε and ε_θ). It is important to mention, that the resolved—and thus, total—components of ε and ε_θ are not presented because they are not contributing in the calculation of entropy generation.

It can be observed that the mean velocity is marginally influenced by mesh resolution. In contrast, the mean temperature improves with increasing the resolution. Further, the model is not capable of predicting the near-wall behavior of modeled ε and consequently, ε_θ. More importantly, both quantities vanish with increasing mesh resolution. This is particularly important for calculation of entropy production, as the modeled part of ε and ε_θ contribute to determine irreversibilities of the process. However, the Reynolds Analogy operating as a sgs-model for thermal effects within IDDES-methodology indicates similar response to mesh resolution as the flow quantities, i.e. k and ε. This has been discussed in detail in [126]. Vanishing of modeled ε and ε_θ in response to mesh refinement cannot be considered appropriate, as the fine resolution is still too coarse to support DNS. Therefore, the Reynolds Analogy needs to be cautiously applied in unsteady simulations as it may fail to capture phenomena that mostly occur at small scale/sgs-level.

Similar behavior is present in the prediction of θ_{rms}, see figure 3.10. The near-wall behavior of the total quantity is in acceptable agreement with DNS data while the behavior further away is mispredicted on the coarse mesh (A-100). More importantly, the results are improved on the finer resolution (B-100) and the resolved part of θ_{rms} is well predicted while sgs-part shows rather a nonphysical plateau profile. Thus, it may be concluded that the model tries to resolve most of thermal structures irrespective of mesh resolution.

The entropy production obtained on both mesh resolutions is given in Figure 3.11. As expected, both resolved quantities, i.e. $\langle \Pi_v^{res} \rangle$ and $\langle \Pi_q^{res} \rangle$, are well predicted with a negligible discrepancy at the wall. However, the modeled-/sgs-parts are not predicted accurately, due to inaccurate prediction of ε and consequently ε_θ. It is worth mentioning that the reduction of the modeled part is a consistent response to mesh refinement. However, the extend of the reduction (vanishing) on a mesh that cannot sup-

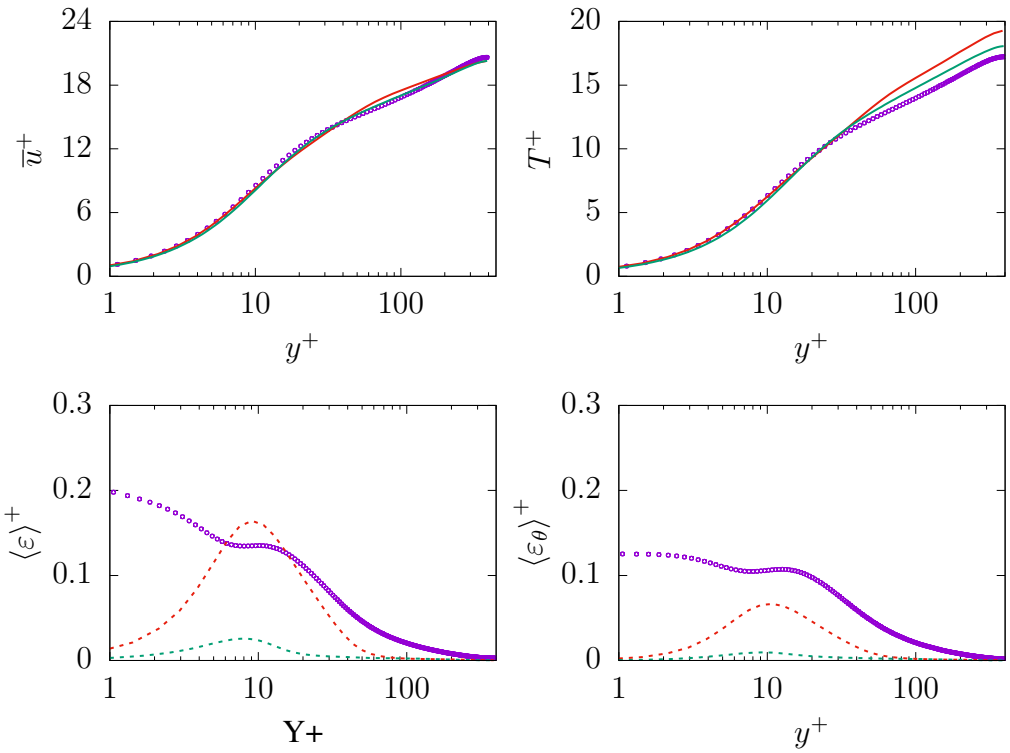

Figure 3.9: Evolution of the streamwise mean velocity (top left), mean temperature (top right), modeled dissipation of k (bottom left) and dissipation of $\overline{\theta^2}$ (bottom right) at $Re_\tau = 395$ for $Pr = 0.71$ obtained on different meshes. A-100: —, B-100: —, A-100: - - -, B-100: - - -, DNS: ○

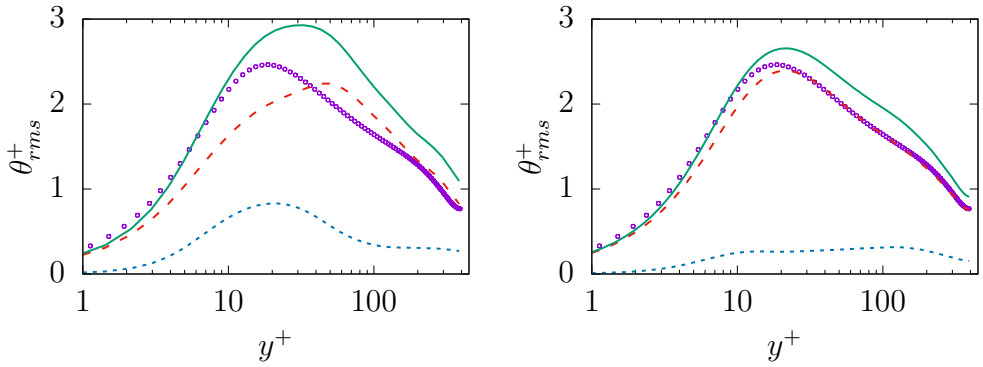

Figure 3.10: Evolution of θ_{rms} at $Re_\tau = 395$ for $Pr = 0.71$ obtained on different meshes; A-100 (left) and B-100 (right). total: —, resolved: - -, modeled: - - -, DNS: ○

port DNS is concerning. Regarding total entropy production due to both mechanisms, it can be observed that results obtained on the coarse mesh are in better agreement with the DNS data compared to results obtained on the fine mesh. This will lead to the conclusion, that the $k-\omega-$ SST-IDDES model tries to resolve most structures especially on the fine mesh, but fails to improve the resolved quantities accordingly.

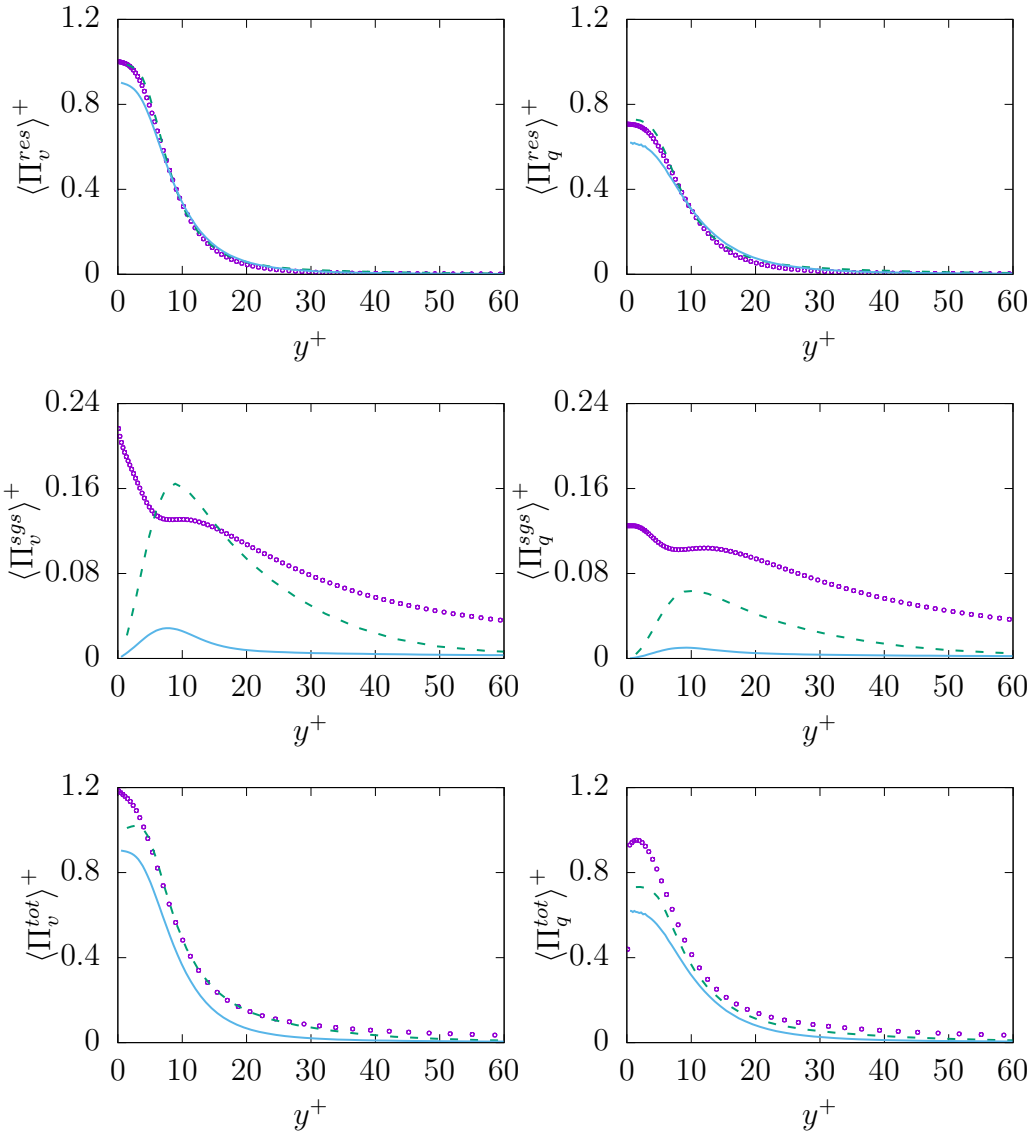

Figure 3.11: Evolution of entropy production due to resolved $\langle \Pi_i^{res} \rangle$ (top), sub-grid $\langle \Pi_i^{sgs} \rangle$ (middle) and total $\langle \Pi_i^{tot} \rangle$ (bottom) parts due to viscous dissipation (v, left) and heat transfer (q, right) at $Re_\tau = 395$ for $Pr = 0.7$ obtained on different meshes. DNS: ○, A: —, B: - -

3.5.2.2 $Pr = 0.025$

It is shown in [126] that mesh design plays an integral role to capture thermal statistics at low Pr numbers in unsteady state simulations and thus, only appropriate grids are employed for this study, see Table 3.2 for details. It was shown that mesh needs to be close to isotropic in the core region of channel in order to accurately resolve thermal structures. Furthermore, it should be noted that the temperature is a passive scalar and thus, the flow quantities are not presented again.

Results obtained for mean temperature and modeled ε_θ on mesh A-100 and B-100 are presented in Figure 3.12. The temperature profile is well predicted on both grids and shows no remarkable sensitivity regarding the mesh resolution. As expected, modeled ε_θ is mispredicted on both grids over the whole domain and vanishes with increasing resolution. In contrast, the prediction of θ_{rms} shows a slight mesh sensitivity, see Figure 3.13. The IDDES-model tries to resolve θ_{rms} completely and pushes the simulation towards DNS. However, the modeled part does not vanish completely and finally, leads to a slight overprediction on the fine mesh.

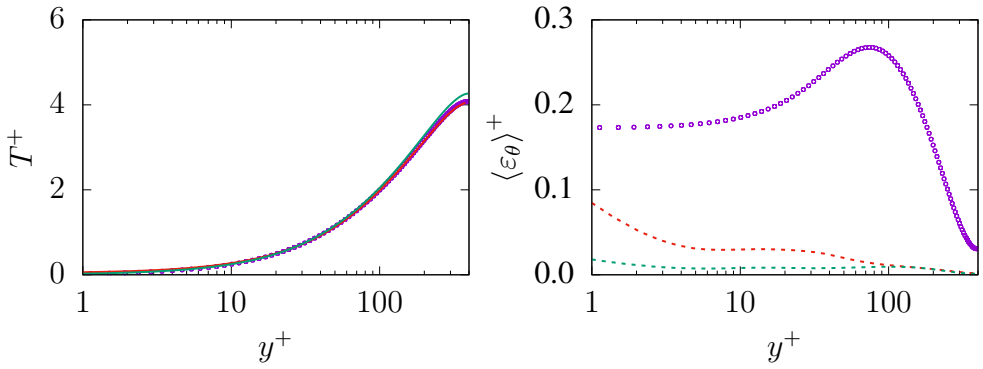

Figure 3.12: Evolution of the mean temperature (left) and modeled dissipation of ε_θ (right) at $Re_\tau = 395$ for $Pr = 0.025$ obtained on different meshes. A-100: —, B-100: —, A-100: - - -, B-100: - - -, DNS: ○

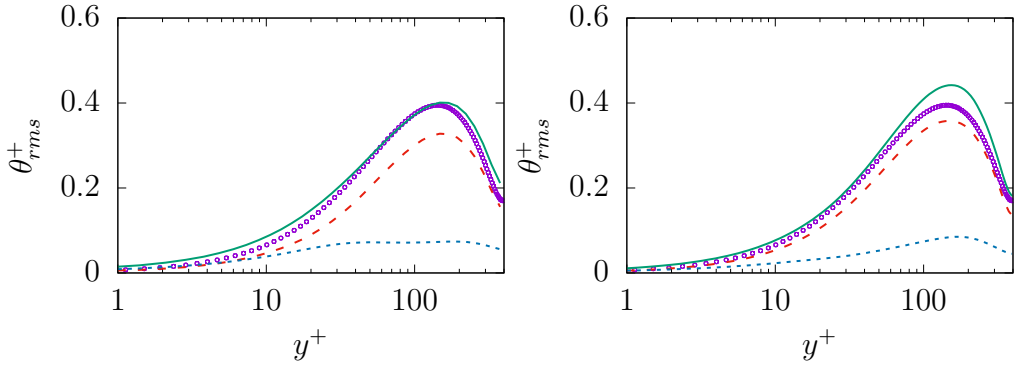

Figure 3.13: Evolution of θ_{rms} at $Re_\tau = 395$ for $Pr = 0.025$ obtained on different meshes. A-100 (left) and B-100 (right). total: —, resolved: - -, modeled: - - -, DNS: ○

The entropy production obtained on both mesh resolutions is given in Figure 3.14. As expected, both resolved quantities, i.e. $\langle\Pi_v^{res}\rangle$ and $\langle\Pi_q^{res}\rangle$ show reasonable agreement with the DNS data. However, the sgs-entropy generation, i.e. $\langle\Pi_v^{sgs}\rangle$ and

$\langle \Pi_q^{sgs} \rangle$, are severely mispredicted. This is mainly due to the fact that the viscous dissipation rate ε is not accurately predicted and consequently, the thermal dissipation rate ε_θ suffers from the same misprediction. Total entropy production due to viscous dissipation $\langle \Pi_v^{tot} \rangle$ is in good agreement with DNS data. Similar to previous simulation for $Pr = 0.71$, the prediction capabilities decrease slightly with increasing resolution. However, $\langle \Pi_q^{tot} \rangle$ is mispredicted over the whole domain. Taking into account that in contrast to $Pr = 0.71$, the sgs-part of entropy production due to heat transfer is roughly twice as big than the res-part, the incapability of the methodology to predict the sgs-part accurately is believed to be the reason for the misprediction of $\langle \Pi_q^{tot} \rangle$.

The results suggest, that the main assumption of the Reynolds Analogy—strong similarity between mechanical and thermal fields in combination with a constant thermal-mechanical time scale $\mathcal{R}$—is facing severe challenges in case of fluids with Pr numbers significantly less than unity, calling for more advanced models for the heat flux as well as for ε_θ.

Similar to the previous RANS simulations concerning $Pr = 0.025$, comparing total entropy production due to the viscous dissipation and heat transfer leads to conclusion that viscous dissipation is the dominant mechanism, causing most irreversibilities of processes dealing with low Pr fluids.

3.5.2.3 $Pr = 200$

Simulations for $Pr = 200$ have been performed at $Re_\tau = 150$ on two different resolutions, see Table 3.1. As mentioned before, capturing the thermal effects at high Pr numbers fluids is very challenging as the thermal boundary layer is very thin—compared to the boundary of the flow, which leads to very dominant wall effects. As a result, investigating thermal boundary layers at high Pr numbers are limited to relatively low Re_τ due to the prohibitively expensive computational cost [9, 8].

Results obtained for mean temperature, modeled dissipation of k and $\overline{\theta^2}$ on both meshes are shown in Figure 3.15. Concerning temperature profile, the result is underpredicted on the coarse grid (A-1000) by roughly 10%. However, the prediction

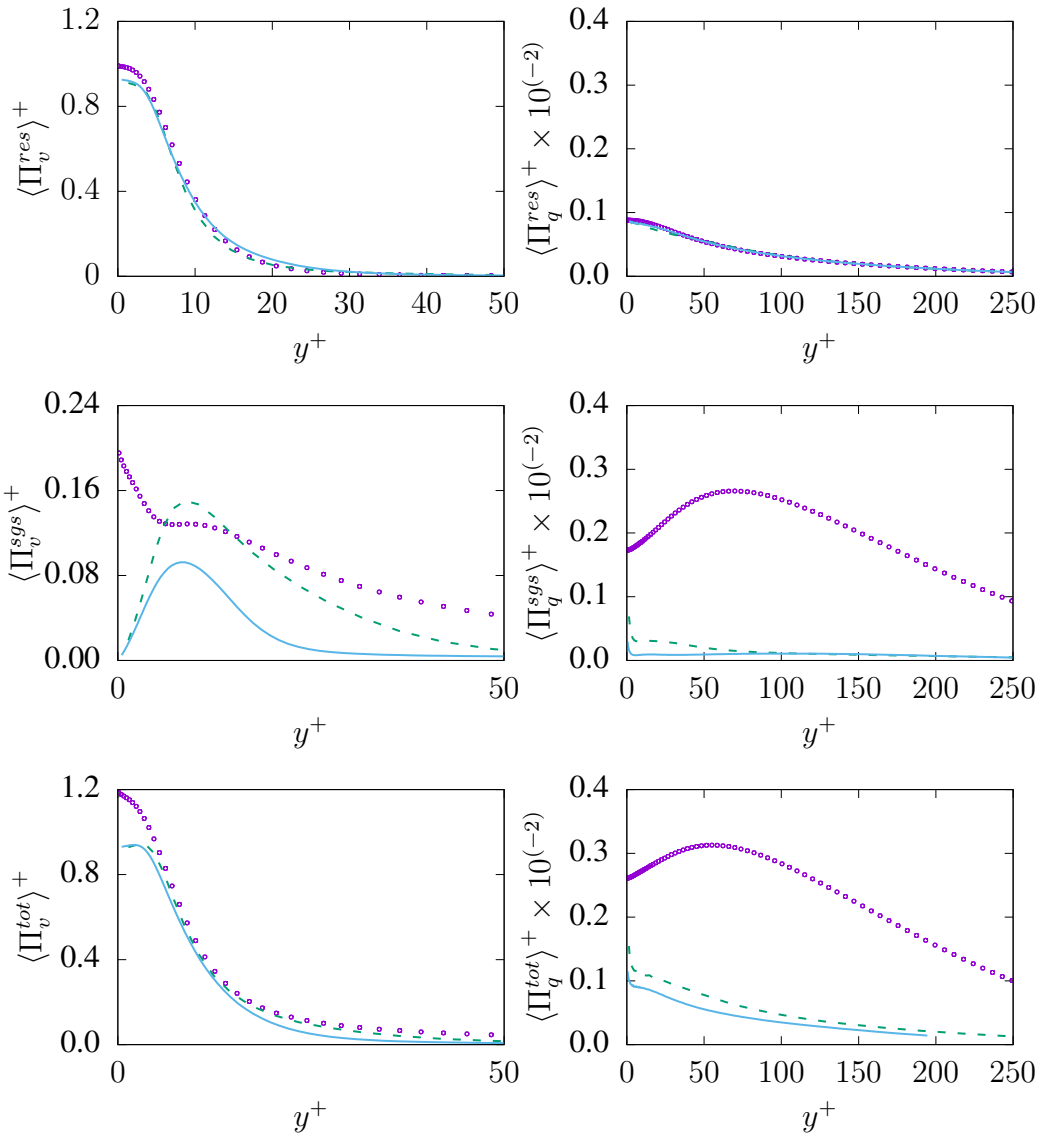

Figure 3.14: Evolution of entropy production due to resolved $\langle \Pi_i^{res} \rangle$ (top), sub-grid $\langle \Pi_i^{sgs} \rangle$ (middle) and total $\langle \Pi_i^{tot} \rangle$ (bottom) parts due to viscous dissipation (v, left) and heat transfer (q, right) at $Re_\tau = 395$ for $Pr = 0.025$ obtained on different meshes. DNS: ○, A: —, B: - -

improves on the fine mesh (B-250) and the profile is in good agreement with DNS data. Regarding modeled dissipation of k, the quantity is mispredicted especially close to the wall. Furthermore, the situation is worse for modeled ε_θ where the near-wall region is completely mispredicted.

θ_{rms} obtained on the same grids is presented in figure 3.16. The profile is underpredicted over the whole domain with negligible modeled part on the coarse mesh. The sgs-model is incapable to capture the near-wall dynamics and provide appropriate

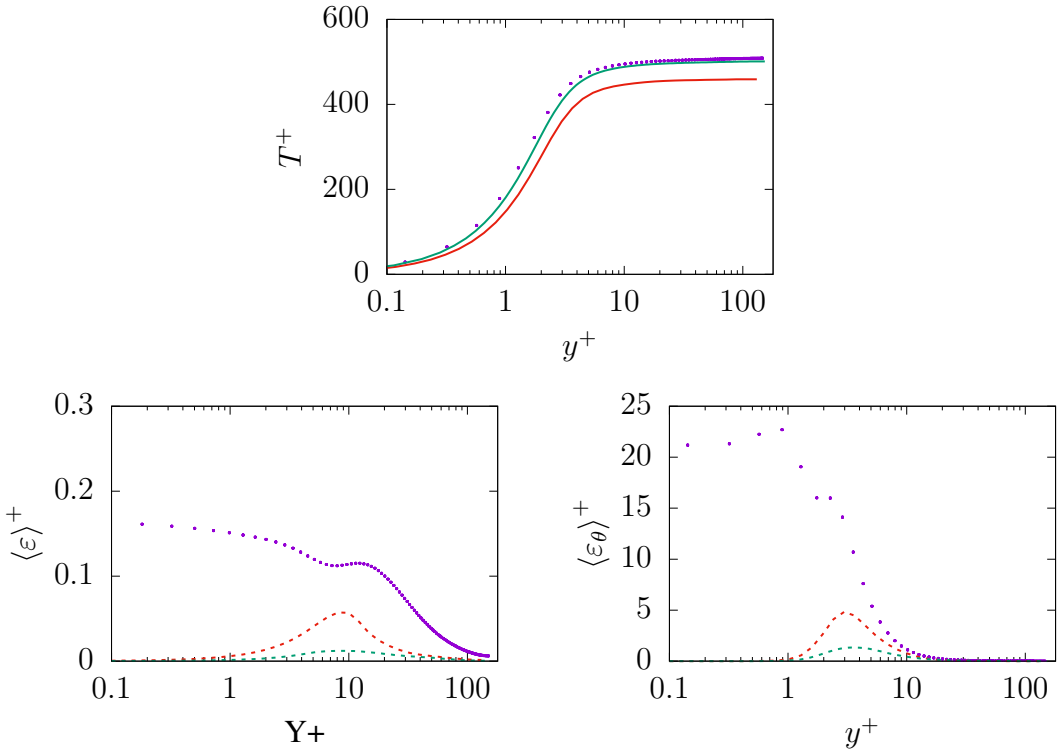

Figure 3.15: Evolution of mean temperature (top), modeled dissipation of k (bottom left) and dissipation of $\overline{\theta^2}$ (bottom right) at $Re_\tau = 150$ for $Pr = 200$ obtained on different meshes. A-1000: —, C-250: —, A-1000: - - -, C-250: - - -, DNS: ○

results, while the resolution is too coarse to capture dynamics of θ_{rms}. While general improvement can be observed for θ_{rms} on the finer mesh, the mesh resolution is not fine enough to deliver acceptable results for the thermal second order statistics.

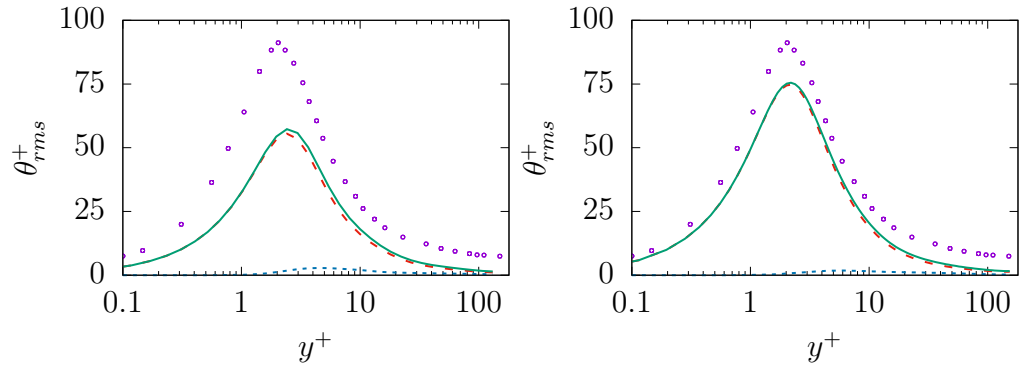

Figure 3.16: Evolution of θ_{rms} at $Re_\tau = 150$ for $Pr = 200$ obtained on different meshes. A-1000 (left) and C-250 (right). total: —, resolved: - -, modeled: - - -, DNS: ○

Figure 3.17 demonstrates the entropy generation due to different mechanism for $Pr = 200$. As expected, the entropy generation due to resolved quantities, i.e.

$\langle \Pi_v^{res} \rangle$ and $\langle \Pi_q^{res} \rangle$, are well predicted with no significant sensitivity to grid resolution. In contrast, the entropy generation due to the sgs-model, e.g. $\langle \Pi_v^{sgs} \rangle$ and $\langle \Pi_q^{sgs} \rangle$, are mispredicted mainly due to the misprediction of the modeled dissipation rate ε and consequently, the modeled thermal dissipation rate ε_θ. However, in contrast to previous cases, sgs-parts of entropy generation plays a minor role compared to the res-part. Thus, the misprediction of sgs-parts is not notably present in the total value.

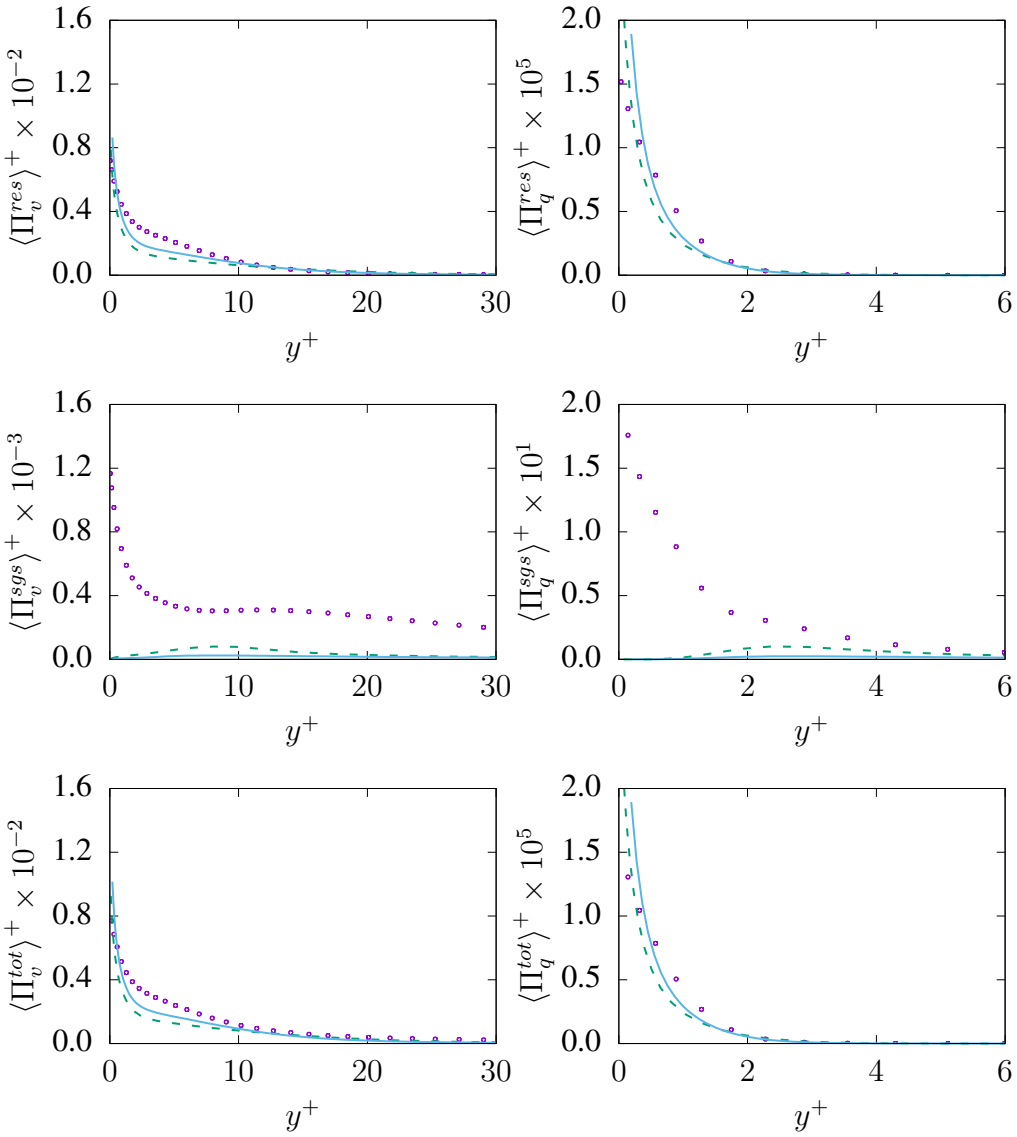

Figure 3.17: Evolution of entropy production due to resolved $\langle \Pi_i^{res} \rangle$ (top), sub-grid $\langle \Pi_i^{sgs} \rangle$ (middle) and total $\langle \Pi_i^{tot} \rangle$ (bottom) parts due to viscous dissipation (v, left) and heat transfer (q, right) at $Re_\tau = 150$ for $Pr = 200$ obtained on different meshes. A-1000: - -, C-250: —, DNS: ○

The results obtained for $Pr = 200$ suggest that the Reynolds Analogy is not playing an integral part to model sub-grid thermal effects. This analogy fails to feature basic property of an appropriate sgs-model in a mesh with a coarser resolution than DNS, i.e. there is basically no modeled part for temperature variance and entropy. Therefore, application of this analogy to capture near-wall thermal phenomena in complex high Prandtl number flows where providing high enough resolution is not feasible, might lead to significant inaccuracies.

However, despite the issue discussed, the total entropy generation obtained from both mechanisms confirm the finding of RANS simulation that most irreversibly of process dealing with high Pr number fluids stem from thermal phenomena.

3.6 Conclusions and Outlook

In this study, predictive capabilities of the Reynolds Analogy to determine entropy production mainly through heat transfer has been thoroughly assessed. This includes application of this analogy to turbulent wall-bounded shear flows at different Reynolds and Prandtl numbers within steady and unsteady state calculations. In case of steady state calculations, the Reynolds Analogy is able to provide acceptable results for mean and fluctuating entropy generation for Prandtl numbers around unity. Departing away from these Prandtl numbers, the Reynolds Analogy is still capable of predicting the mean entropy production in good agreement with DNS data. However, the fluctuating production fails particularly in near-wall region, mainly due to the misprediction of the dissipation of kinetic energy.

Concerning unsteady calculations, it was shown that the Reynolds Analogy fails to feature basic properties of an appropriate sub-grid scale model, mainly due to inappropriate response to mesh resolution. Further, the mean entropy generation is well predicted for all investigated Prandtl numbers. Concerning the sub-grid model properties, the model pushes the simulations towards direct numerical simulation on any grid resolution, leading to misprediction of sub-grid values such as sub-grid entropy production particularly for low and high Prandtl numbers. This could lead to significant error

when near-wall phenomena and/or fluctuations are of great importance and thus, the Reynolds Analogy may not be considered as reliable sub-grid scale modeling strategy. Moreover, results suggest that optimization efforts need to be put on minimizing viscous dissipation for processes involving low Prandtl number fluids, while efficient heat transfer is the key to reduce irreversibility of a process dealing with high Prandtl number fluids. Further, it turns out that both mechanisms for entropy generation are equally important concerning fluids with Prandtl number around unity, suggesting necessity of concurrent optimization to reduce viscous dissipation while making heat transfer more efficient. This clearly makes the optimization a more challenging task.

The obtained results confirm that using zero-equation approach (the Reynolds Analogy) cannot be deemed as an appropriate tool for design and optimization purposes, especially when relying on entropy generation/optimization strategies and working fluids with non-unity Prandtl number. This strongly suggests moving toward development of more advanced turbulent heat transfer models consistent with thermodynamics laws, which requires application of one-equation or algebraic models to model heat transfer phenomena [109], in conjunction with advanced turbulence models capable of capturing complex and nonlinear wall effects.

Addendum

Funding This research received no external funding and was supported using start-up funds from the University of Missouri-Kansas City.

Acknowledgment The corresponding author gratefully acknowledges fruitful discussions with Prof. Sadiki's research group within the CRC/Transregio 150 "Turbulent, chemically reactive, multi-phase flows near wall" program founded by DFG.

Conflict of interest The authors declare no conflict of interest.

3.6.1 Nomenclature

	Name
c_p	specific heat capacity at constant pressure
f	elliptic relaxation
k	kinetic energy
r	grid stretching factor in y-direction
s	entropy density
u_i	velocity fluctuations
$\overline{u}_i$	mean velocity
q_i	heat flux density vector
q_w	wall heat flux
y^+	yPlus
Pr	Prandtl
$\mathcal{R} = \tau_\theta/\tau_m$	mechanical to thermal time scale ratio
$Re_\tau = U_\tau \delta/\nu$	turbulent Reynolds number
$S_\tau = \nu\alpha(T_w/\mathrm{T}_\tau)^2/U_\tau\lambda$	friction entropy production rate
S_T	source terms in internal temperature equation
T	mean temperature
$T_\tau = \rho/c_p q_w U_\tau$	friction temperature
T_w	wall temperature
$U_\tau = Re_\tau \nu/\delta = \sqrt{\tau_w/\delta}$	friction velocity
$U_i = \overline{u}_i + u_i$	total velocity
$\alpha = \lambda/\rho c_p$	thermal diffusivity
δ	channel half height
ϵ	dissipation of kinetic energy
ε_θ	dissipation of the variance of temperature fluctuations
$\zeta = \overline{v^2}/k$	velocity scale ratio
θ	temperature fluctuations
$\overline{\theta u_i}$	turbulent heat flux
θ_{rms}	rms value of temperature fluctuations
$\overline{\theta^2}$	temperature variance
$\Theta = T + \theta$	total temperature
ω	dissipation rate of kinetic energy
λ	thermal conductivity
μ	dynamic viscosity
ν	kinematic viscosity
ν_t	turbulent kinematic viscosity
Π	entropy production
ρ	density
σ_t	turbulent Prandtl number
$\tau_m = k/\varepsilon$	mechanical time scale
$\tau_\theta = \overline{\theta^2}/2\varepsilon_\theta$	thermal time scale
τ_w	wall shear stress
$(\,)^{sgs}$	sub-grid component
$(\,)^{res}$	resolved component
$(\,)^{tot}$	total
$\overline{(\,)}$	mean value
$\langle(\,)\rangle$	spatial and time averaged

$( )'$	fluctuating component
$( )^+$	normalized by wall variables

CHAPTER 4

AN ASSESSMENT OF THE REYNOLDS ANALOGY IN PREDICTING HEAT TRANSFER IN TURBULENT FLOWS OF LOW PRANDTL NUMBERS

The conference presentation was held by Matthias Ziefuss[1] and supervised by Amirfahrhang Mehdizadeh[1] at the 72nd Annual Meeting of the APS Division of Fluid Dynamics.

[1] Civil and Mechanical Engineering Department, School of Computing and Engineering, University of Missouri-Kansas City, Kansas City, MO 64110, USA

APS Division of Fluid Dynamics (Fall) 2019, abstract id.Q13.006; 2019APS..DFDQ13006Z

4.1 **Abstract**

Heat transfer modeling plays a major role in design and optimization of modern and efficient cooling systems. However, currently available models suffer from a fundamental shortcoming: their development is based on the general notion that an accurate prediction of the flow field will guarantee an appropriate prediction of the thermal field, known as the Reynolds Analogy. This analogy works reasonably well when applied to fluids with a Prandtl number around unity to obtain first order statistics. Concerning fluids with non-unity Prandtl number, there is no comprehensive assessment available. Thus, this investigation presents an introductory assessment of the capability of the Reynolds Analogy when applied to turbulent shear flows of fluids with small Prandtl number. The assessment includes steady and unsteady state simulations. In case of steady state simulations, it turns out that the Reynolds Analogy is not able to predict the mean temperature at an acceptable level of accuracy, while second order statistics are severely mispredicted. In case of unsteady simulations, it is shown that the Reynolds Analogy cannot be considered as an appropriate sub-grid scale model as it fails to feature basic properties of a reliable sub-grid scale model.

CHAPTER 5

A WALL-ADAPTED ANISOTROPIC HEAT FLUX MODEL FOR LARGE EDDY SIMULATIONS OF COMPLEX TURBULENT THERMAL FLOWS

The paper is published in *Flow, Turbulence and Combustion* and written by Florian Ries[1]*, Yongxiang Li[1], Louis Dressler[1], Matthias Ziefuss[2], Amirfarhang Mehdizadeh[2], Christian Hesse [3] and Amsini Sadiki[1]

[1] Department of Reactive Flows and Diagnostics, Technische Universität Darmstadt, 64289 Darmstadt, Germany
[2] Civil and Mechanical Engineering Department, School of Computing and Engineering, University of Missouri-Kansas City, Kansas City, MO 64110, USA
[3] Department of Simulation of Reactive Thermo-Fluid Systems, Technische Universität Darmstadt, 64289 Darmstadt, Germany
* Corresponding author: ries@ekt.tu-darmstadt.de

Flow, Turbulence and Combustion, 14 August 2020; https://doi.org/10.1007/s10494-020-00201-6

5.1 **Abstract**

In this paper, a wall-adapted anisotropic heat flux model for large eddy simulations of complex engineering applications is proposed. First, the accuracy and physical consistency of the novel heat flux model are testified for turbulent heated channel flows with different fluid properties by comparing with conventional isotropic models. Then, the performance of the model is evaluated in case of more complex heat and fluid flow situations that are in particular relevant for internal combustion engines and engine exhaust systems. For this purpose large eddy simulations of a strongly heated pipe flow, a turbulent inclined jet impinging on a heated solid surface and a backward-facing step flow with heated walls were carried out. It turned out that the proposed heat flux model has the following advantages over existing model formulations: (1) it accounts for variable fluid properties and anisotropic effects in the unresolved temperature scales, (2) no ad-hoc treatments or dynamic procedure are required to obtain the correct near-wall behavior, (3) the formulation is consistent with the second law of thermodynamics, and

(4) the model has a similar prediction accuracy and computational effort than conventional isotropic models. In particular, it is shown that the proposed heat flux model is the only model under consideration that is able to predict the direction of subgrid-scale heat fluxes correctly, also under realistic heat and fluid flow conditions in complex engineering applications.

5.2 Introduction

Many energy systems, such as internal combustion engines or exhaust after treatment devices, are confined by solid walls. Thereby, combustion and other energy conversion processes lead to an intensive heat transfer through the solid walls along with complex unsteady mixing dynamics that determine the lifetime and overall thermodynamic performance of thermo-fluid systems. These complex heat and fluid flow phenomena make a description and optimization of such energy systems very challenging and require accurate and viable tools for their engineering design.

On the numerical side, LES technique has proved to be a promising approach to predict complex heat and fluid flow phenomena in many thermo-fluid systems, likewise in automotive applications [69, 29, 68, 21, 97, 20]. In LES, the large three-dimensional unsteady turbulent motions are explicitly computed, whilst a turbulence closure model accounts for the influence of the unresolved more universal scales [48, 100, 85]. The benefit of such an approach is quite obvious. First, the computational expense of LES is significantly lower than in fully resolved LES. Secondly, only small scale turbulent structures with a small amount of turbulent energy have to be modeled, which are believed to be universal, homogeneous and isotropic. This simplifies the turbulence modeling, improves the predictive capability compared to approaches based on the solution of the RANS and makes LES valid for a broad range of flow situations with complex physics.

In principle, most strategies that are used to close the LES momentum equation can be also applied to deal with the unresolved subgrid-scale heat flux vector in the energy equation [100]. However, based on turbulence theory, the rationale behind

LES is less obvious when dealing with turbulent heat transport. The main reason is that the temperature variance spectrum as well as the dynamics of small temperature scales have a less universal character than the kinetic energy spectrum and velocity scales. As a consequence, the spectral scalar transfer across the LES cutoff can strongly depend on the physical regime in which it is located [100]. Moreover, small temperature scales are also influenced by the interaction of the velocity gradient and the scalar fluctuations, which causes anisotropic behavior even at smallest temperature scales. Consequently, more advanced subgrid-scale models are required in the case of turbulent heat transport in order to justify the cut off and modeling of the unresolved temperature scales. However, despite of the anisotropic behavior of small turbulent thermal structures, isotropic models are most often employed in LES of turbulent heat transport. Thereby, the subgrid-scale thermal diffusivity is traditionally represented based on the Reynolds analogy and the concept of turbulent Prandtl number. Many researchers intended to improve this simple approach by using a dynamic procedure to calculate the turbulent Prandtl number [58, 63], including buoyancy effects [17], using a definition of the thermal diffusivity based on Kolmogorov scaling [123] or including the effects of local fluid properties in the subgrid-scale model [75].

As implied by the discussion above, a better representation of the subgrid-scale heat flux vector for complex heat and fluid flow situations can be obtained by accounting for the anisotropic behavior of small temperature scales and introducing a tensor subgrid-scale thermal diffusivity. Some of these models were derived in analogy to the general gradient diffusion hypothesis [14] as it is often applied in the RANS context. In the approach of Peng and Davidson [82], the authors developed a non-linear subgrid-scale heat flux model based on considerations of the transport equation of the subgrid-scale heat flux. Wang et al. [117, 116, 118] proposed a series of models which includes the resolved strain-rate tensor S_{ij}, rotation rate tensor Ω_{ij} and the temperature gradient $\partial T/\partial x_i$. Similar, Rasam et al. [87] proposed an anisotropic scalar flux model that is based on the modeled transport equation of the subgrid-scale scalar flux and depends also on S_{ij}, Ω_{ij} and $\partial T/\partial x_i$. In contrast to these model formulations, the anisotropic

model by Huai and Sadiki [31, 79] is based on the second law of thermodynamics in conjunction with the invariant theory. In this way, the irreversibility requirements of the second law of thermodynamics are automatically fulfilled by the model formulation. Besides, scale similarity and mixed models were also proposed in the literature, e.g. [35, 86, 102].

From this brief literature review it appears that only a few advanced anisotropic heat flux models exist in the literature and they are almost never used in LES practice. Most of these models are relatively complex, do not account for the effects of local fluid properties and do not provide the correct asymptotic near-wall behavior. To overcome these limitations, a novel wall-adapted anisotropic heat flux model for LES is proposed in this chapter. The main features of the novel model are that (1) it accounts for variable fluid properties and anisotropic effects in the unresolved temperature scales, (2) no ad-hoc treatments or dynamic procedure are required to obtain the correct near-wall behavior, and (3) the formulation is consistent with the second law of thermodynamics. First, the prediction accuracy and computational cost of the novel heat flux model are evaluated in the present work for a turbulent heated channel flow with different Prandtl numbers. Then, the performance of the proposed heat flux model is demonstrated for complex heat and fluid flow situations.

The present chapter is organized as follows: First, the applied LES approach and the novel anisotropic heat flux model are introduced (Section 5.3). Then, the accuracy and consistency of the proposed model is evaluated for turbulent heated channel flows at different Prandtl numbers (Section 5.4). Thereby comparison with available DNS data and with achievements obtained by means of conventional isotropic models are presented and discussed. Subsequently, the model is applied to more complex heat and fluid flow situations that are in particular relevant to internal combustion engines and exhaust gas systems, namely, a strongly heated pipe flow, a turbulent inclined jet impinging on a heated surface and a backward-facing step flow with heated walls (Section 5.5). Finally, some concluding remarks are provided at the end (Section 5.6).

5.3 Model Description and Numerical Treatment

In the case of LES with implicit filtering of an incompressible fluid flow with variable physical properties, the transport equations of mass, momentum and enthalpy can be formulated as [100]

$$\frac{\partial \overline{\rho}}{\partial t} + \frac{\partial \overline{\rho} U \widetilde{U}_i}{\partial x_i} = 0, \tag{5.1}$$

$$\frac{\partial \overline{\rho} U \widetilde{U}_i}{\partial t} + \frac{\partial \overline{\rho} U \widetilde{U}_i U \widetilde{U}_j}{\partial x_j} = \frac{\partial \overline{\sigma}_{ij}}{\partial x_j} - \frac{\partial \overline{\rho} \tau_{ij}^{sgs}}{\partial x_j}, \tag{5.2}$$

$$\frac{\partial \overline{\rho} h \widetilde{h}}{\partial t} + \frac{\partial \overline{\rho} U \widetilde{U}_j h \widetilde{h}}{\partial x_j} = -\frac{\partial \overline{q}_j}{\partial x_j} + \overline{\sigma}_{<ij>} \frac{\partial U \widetilde{U}_i}{\partial x_j} - \frac{\partial \overline{\rho} q_j^{sgs}}{\partial x_j}, \tag{5.3}$$

where $\overline{(.)}$ are spatially filtered quantities, $(.)\widetilde{(.)}$ Favre-filtered quantities and $(.)^{sgs}$ denotes the subgrid-scale quantities. ρ is the mass density, U_i the velocity, h the sensible enthalpy, σ_{ij} the stress tensor, τ_{ij}^{sgs} the subgrid-scale stress tensor, and q_j^{sgs} the unresolved heat flux. In the case of a Navier-Stokes-Fourier fluid, the stress tensor is described as

$$\overline{\sigma}_{ij} = \overline{\sigma}_{<ij>} - \overline{p}\delta_{ij} = \overline{\mu}\left(\frac{\partial U \widetilde{U}_i}{\partial x_j} + \frac{\partial U \widetilde{U}_j}{\partial x_i} - \frac{2}{3}\frac{\partial U \widetilde{U}_k}{\partial x_k}\delta_{ij}\right) - \overline{p}\delta_{ij}, \tag{5.4}$$

where μ is the molecular viscosity and p is the pressure. The resolved heat flux is expressed by means of Fourier's law for incompressible flow as

$$\overline{q}_j = -\overline{\lambda}\frac{\partial T \widetilde{T}}{\partial x_j} = -\frac{\overline{\lambda}}{\overline{c}_p}\frac{\partial h \widetilde{h}}{\partial x_j}, \tag{5.5}$$

where λ is the thermal conductivity and c_p the isobaric heat capacity. The gravitational force and the radiation are not considered in equations 5.2 and 5.3. Furthermore, the unsteady pressure term in the enthalpy equation is usually assumed to be small in incompressible flows [84]. It is therefore neglected in this work.

In order to close the filtered momentum and energy transport equations, the subgrid-scale stress tensor $\tau_{ij}^{sgs} = \left(U_i U_j \widetilde{U_i U_j} - U\widetilde{U}_i U\widetilde{U}_j\right)$ and the subgrid-scale heat

flux vector $q_i^{sgs} = \left(U_i h\widetilde{U_i h} - U\widetilde{U}_i h\widetilde{h}\right)$ have to be postulated by being related to the resolved velocity and temperature fields, respectively, in terms of subgrid-scale models.

5.3.1 Modeling of the subgrid-scale momentum transport

In this work, the eddy viscosity approach is applied to model the subgrid-scale transport of momentum. Thereby, the isotropic part of τ_{ij}^{sgs} is included into the modified filtered pressure

$$\overline{P} = \overline{p} + \frac{1}{3}\tau_{kk}^{sgs} \tag{5.6}$$

and the remaining deviatoric part is expressed using the eddy viscosity ν_{sgs} and the Boussinesq approximation as

$$\tau_{\langle ij\rangle}^{sgs} = \tau_{ij}^{sgs} - \frac{1}{3}\tau_{kk}^{sgs}\delta_{ij} = -2\nu_{sgs}\left(S\widetilde{S}_{ij} - \frac{1}{3}S\widetilde{S}_{kk}\delta_{ij}\right), \tag{5.7}$$

where $S\widetilde{S}_{ij} = 1/2\left(\partial U\widetilde{U}_i/\partial x_j + \partial U\widetilde{U}_j/\partial x_i\right)$ is the strain-rate tensor. The eddy viscosity is represented by means of the SIGMA-model [67] with standard model coefficient $C_\sigma = 1.5$.

5.3.2 Modeling of the subgrid-scale heat transport

Because turbulent flows are thermodynamic processes and the directions of all such processes are restricted by the second law of thermodynamics, it is recommendable to take account of this fact at every level and kind of closure formulations. In analogy to the anisotropic scalar flux model of Huai and Sadiki [31, 79], the explicit algebraic anisotropic heat flux model proposed here is based on the second law of thermodynamics in conjunction with the invariant theory. From this formalism, a general expression for the subgrid-scale heat flux vector in non-rotating observer system can be written as (see [31, 79]):

$$q_i^{sgs} = -\alpha_{ij}^{sgs}\frac{\partial h\widetilde{h}}{\partial x_j} = \left(\beta_1\delta_{ij} + \beta_5\tau_{ij}^{sgs} + \beta_8\left(\frac{\partial T\widetilde{T}}{\partial x_k}\frac{\partial T\widetilde{T}}{\partial x_k}\right)\delta_{ij}\right)\frac{\partial h\widetilde{h}}{\partial x_j}, \tag{5.8}$$

where the first term on the right-hand side represents the contribution by linear diffusion, the second term expresses the influence of the subgrid-scale flow fluctuations acting on the resolved enthalpy gradient and the last term is associated with production/dissipation of subgrid-scale variance. For more details on the derivation of equation 5.8 the reader is referred to [5, 98].

Restricting ourselves to linear subgrid-scale viscosity models for the velocity field in equation 5.8 to represent τ_{ij}^{sgs} and by means of dimensional analysis, equation 5.8 can be reformulated as

$$\begin{aligned} q_i^{sgs} = & \Bigg(- C_1 \tau_c k_{sgs} \delta_{ij} - C_5 \tau_c \frac{2}{3} k_{sgs} \delta_{ij} + C_5 \tau_c 2 \nu_{sgs} \left(S\widetilde{S}_{ij} - \frac{1}{3} S\widetilde{S}_{kk} \delta_{ij} \right) \\ & - C_8 \tau_c \frac{k_{sgs}^2}{\epsilon_{\theta_{sgs}} \epsilon_{k_{sgs}}} \delta_{ij} \left(\frac{\partial T\widetilde{T}}{\partial x_k} \frac{\partial T\widetilde{T}}{\partial x_k} \right) \Bigg) \frac{\partial h\widetilde{h}}{\partial x_j}, \end{aligned} \tag{5.9}$$

where k_{sgs} is the unresolved turbulent kinetic energy, $\epsilon_{k_{sgs}}$ the dissipation rate of k_{sgs}, θ_{sgs} the subgrid-scale temperature variance and $\epsilon_{\theta_{sgs}}$ its dissipation rate. τ_c is a characteristic subgrid-scale time scale that can be either represented by means of a mechanical $\tau_c = k_{sgs}/\epsilon_{k_{sgs}}$, a thermal $\tau_c = \theta_{sgs}/\epsilon_{\theta_{sgs}}$ or a mixed subgrid-scale time scale $\tau_c = \sqrt{\frac{\theta_{sgs} k_{sgs}}{\epsilon_{k_{sgs}} \epsilon_{\theta_{sgs}}}}$. The latter one was used for example in the model formulation proposed by the first author in [91]. As shown by DNS [40], the time scale ratio between thermal and mechanical time scales behaves proportionally to $\sim \sqrt{Pr}$ for turbulent fluid flows with a wide range of molecular Prandtl numbers. In order to account for fluid flows with variable molecular Prandtl numbers, the same behavior is assumed for the characteristic subgrid-scale time scale in the present model formulation leading to $\tau_c \sim \sqrt{Pr} \frac{k_{sgs}}{\epsilon_{k_{sgs}}}$.

At this stage, it is obvious that closure relation for k_{sgs}, $\epsilon_{k_{sgs}}$, θ_{sgs} and $\epsilon_{\theta_{sgs}}$ are required to close the model formulation in equation 5.9. However, by applying the inertial-convective subrange theory [72, 13, 105] and combining all isotropic terms on the right-hand side, equation 5.9 can be rewritten in a fully algebraic form as

$$q_i^{sgs} = -C_I \sqrt{Pr}\, \nu_{sgs} \frac{\partial h\widetilde{h}}{\partial x_i} + C_{II} \sqrt{Pr}\, \Delta^2 \left(S\widetilde{S}_{ij} - \frac{1}{3} S\widetilde{S}_{kk} \delta_{ij} \right) \frac{\partial h\widetilde{h}}{\partial x_j}, \tag{5.10}$$

where the coefficients C_I and C_{II} are determined in analogy to the generalized gradient diffusion hypothesis [14] and in accordance with the inertial-convective subrange theory [72, 13, 105] as $C_I = 2.381$ and $C_{II} = 0.081$.

Finally, in order to obtain the correct asymptotic behavior of $q_i^{sgs} \sim \mathcal{O}(y^3)$ in the vicinity of the wall, a damping factor f_q is added to the second term on the right-hand side of equation 5.10. This leads to the final formulation of the present explicit algebraic anisotropic heat flux model as

$$q_i^{sgs} = -C_I\sqrt{Pr}\,\nu_{sgs}\frac{\partial h\widetilde{h}}{\partial x_i} + C_{II}\sqrt{Pr}\,\Delta^2\left(S\widetilde{S}_{ij} - \frac{1}{3}S\widetilde{S}_{kk}\delta_{ij}\right)f_q\frac{\partial h\widetilde{h}}{\partial x_j}, \tag{5.11}$$

where f_q is defined as

$$f_q = min\left[\frac{C_\epsilon^{1/2}\nu_{sgs}}{C_k^{3/2}\Delta^2\sqrt{2\overline{S}_{ij}\overline{S}_{ij}}}, 1\right], \tag{5.12}$$

which accounts for shear damping effects in the near-wall region. From scaling analysis, it appears that $f_q \sim \mathcal{O}(y^3)$ leads to the correct asymptotic behavior of $q_i^{sgs} \sim \mathcal{O}(y^3)$ for $y \to 0$ in the case that $\nu_{sgs} \sim \mathcal{O}(y^3)$. Notice that the asymptotic behavior of ν_{sgs} switches from cubic to quadratic when density fluctuations are present at the wall, which is correctly represented by the SIGMA-model [67]. This holds also for q_i^{sgs} in case the SIGMA-model is used as subgrid-scale closure for the flow field. The coefficients of the novel model are summarized as $C_I = 2.381$, $C_{II} = 0.081$, $C_k = 0.094$ and $C_\epsilon = 1.048$. A detailed derivation of the model can be found in [91]. An analysis of the asymptotic behavior of the proposed model for different spatial resolutions is provided in the Appendix.

5.3.3 Numerical Treatment

All simulations were carried out using OpenFOAM 2.4.0 [22]. Thereby, a low Mach-number approach was employed that is suitable for flows under incompressible conditions ($Ma < 0.3$). This consists of a merged PISO[34]-SIMPLE[81] algo-

rithm for the pressure-velocity coupling along with a second-order implicit backward-differencing scheme for time integration. The solution procedure was applied with a low-dissipative second-order flux-limiting differencing scheme for the convection terms and a conservative scheme for the Laplacian and gradient terms. A detailed description, verification and validation of the code employed in this study can be found in [94, 91].

5.4 Model Evaluation

The evaluation study of the proposed anisotropic heat flux model (see equation 5.11) is divided into three parts. First, the physical consistency of the model is testified for turbulent heated channel flow at $Re_\tau = 395$ and $Pr = 0.71$. For comparison purpose, the DNS dataset of Kawamura et al. [39] is utilized. Additionally, results of the linear thermal diffusivity model with a constant subgrid-scale Prandtl number of $Pr_{sgs} = 0.7$ and with a dynamic procedure to calculate Pr_{sgs} are also provided. In the second part, the influence of the fluid properties on the prediction accuracy of the heat flux models is analyzed. For this purpose LES of turbulent heated channel flow at different molecular Prandtl numbers were carried out and predictions are compared and assessed with the reference DNS dataset of Abe et al. [1]. Finally, in the last part of the model evaluation study, the prediction accuracy and computational cost of the proposed heat flux model are quantified and compared with those of isotropic heat flux models.

An illustration of the computational domain employed in the present evaluation studies is depicted in figure 5.1, where δ denotes half the height of the channel and $N_{1,2,3}$ is the number of grid points in x-, y- and z-direction.

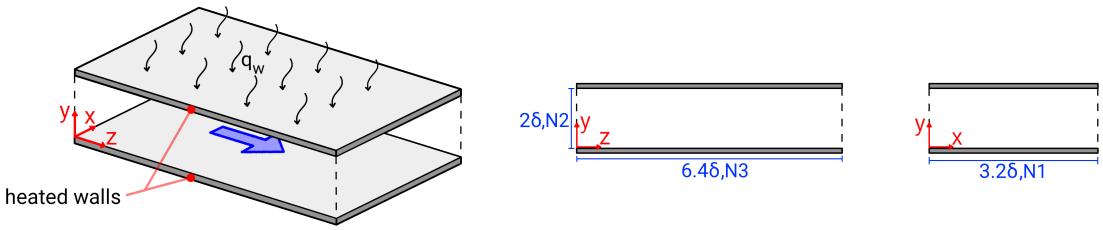

Figure 5.1: Computational domain for the LES study of heated channel flow. $N_{1,2,3}$ represents the number of grid points

Three numerical grids with $(N_1 \times N_2 \times N_3) = (81 \times 91 \times 81)$, $(97 \times 111 \times 97)$, and $(121 \times 137 \times 121)$ cells, denoted here as grid no. 1, 2, 3, respectively, are used in the evaluation study. Thereby, all grids are refined towards the near wall region to ensure a non-dimensional wall distance much smaller than one.

5.4.1 Physical Consistency

Figure 5.2 shows non-dimensional mean and rms temperature profiles predicted by the different heat flux models in comparison with DNS data. Thereby, the non-dimensional temperature is defined as $\Theta^+ = (T_w - T)/T_\tau$, where $T_\tau = q_w/(\rho c_p u_\tau)$ is the friction temperature taken from the DNS. As focus is put on thermal quantities only, velocity fields are not shown.

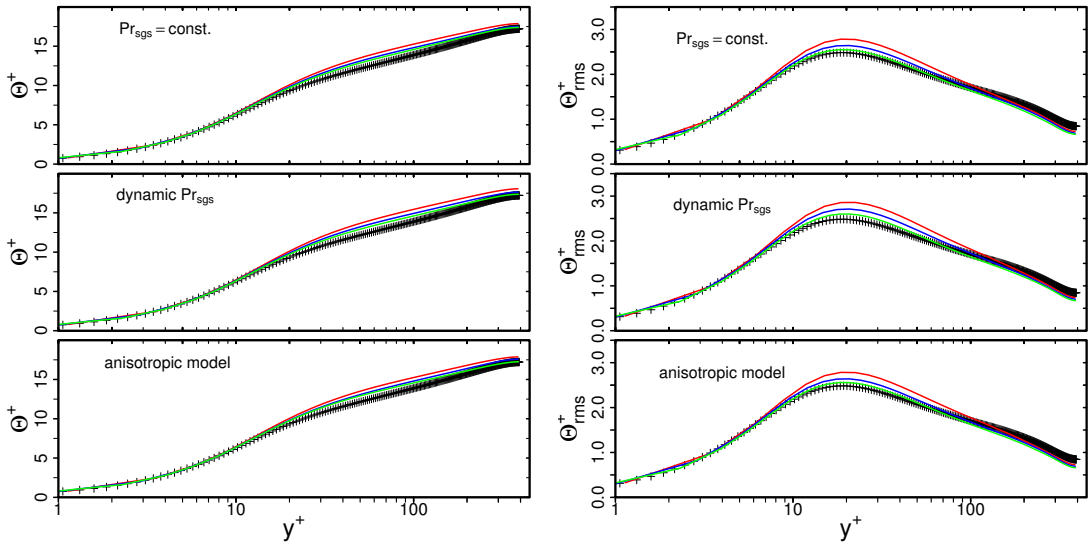

Figure 5.2: Predicted mean (a) and rms (b) temperature profiles for different spatial resolutions. Grid no. 1 (—), grid no. 2 (—), grid no. 3 (—). Comparison with DNS data (+) of [39]

As it is expected, predictions of mean and rms temperature profiles become more accurate with increasing spatial resolution. This holds true for all heat flux models under consideration. Thereby, LES results of the different models are very close to each other which indicates a similar prediction accuracy of the models.

Next the physical consistency of predicted subgrid-scale heat fluxes are analyzed. For this purpose, figure 5.3 shows predicted wall-normal (a) and axial (b) tur-

bulent heat fluxes in comparison with the DNS data. Solid lines denote resolved heat fluxes, while dashed lines represent subgrid-scale heat fluxes. Thereby, in case of turbulent heated channel flow, axial velocity u and temperature θ are always greater than or equal to zero. From this reason and by using the Steiner translation theorem, it follows directly that resolved and subgrid-scale axial heat fluxes should be also greater than or equal to zero.

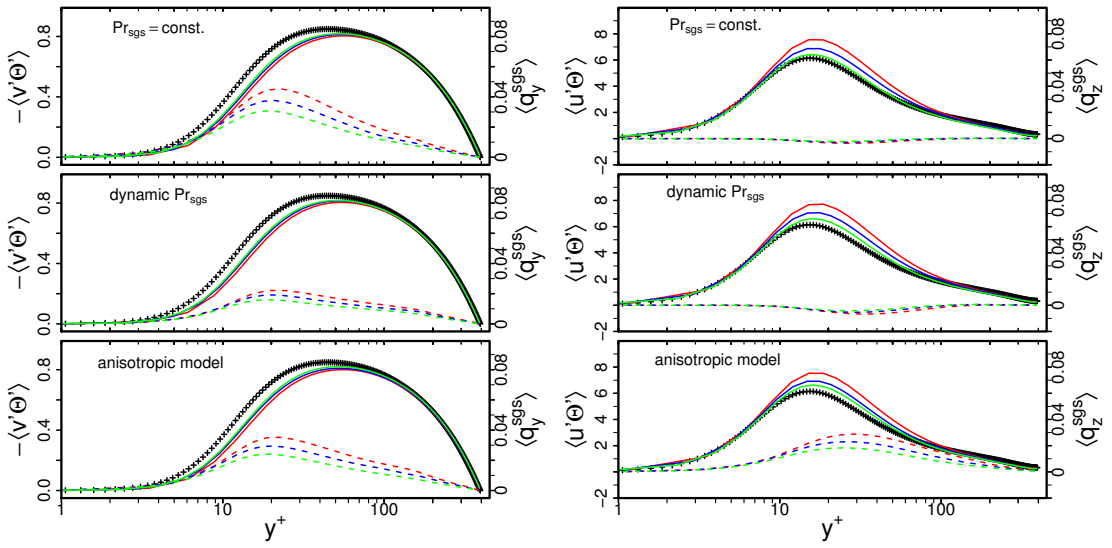

Figure 5.3: Predicted wall-normal (a) and axial (b) turbulent heat fluxes. Solid lines represent resolved heat fluxes and dashed lines are subgrid-scale heat fluxes. (see figure 5.2 for legend)

Regarding wall-normal heat fluxes as depicted in figure 5.3 (a), it can be clearly seen that predictions of all subgrid-scale heat flux models are quite similar. In contrast, resolved and subgrid-scale axial heat fluxes have only same positive sign in case of the anisotropic heat flux model (see figure 5.3 (b)). This reflects the physical consistency of the proposed anisotropic heat flux model. Considering the isotropic models, both, the standard and dynamic thermal diffusivity models are unable to reproduce the direction of axial subgrid-scale heat flux correctly. Nevertheless, although the resolved and subgrid-scale axial heat fluxes are not correctly predicted by means of the isotropic models, the additional anisotropic contribution appears quite small, which might explain that the overall prediction accuracy of thermal statistics with such isotropic models is often comparable to anisotropic model. This will be quantified in subsection 5.4.3.

5.4.2 Influence of the Molecular Prandtl Number

The influence of the fluid properties on the prediction accuracy of the subgrid-scale heat flux models is analyzed next. For this purpose, figure 5.4 shows LES results of a turbulent heated channel flow at $Re_\tau = 395$ and molecular Prandtl numbers of Pr=0.025, 0.71 and 10. Thereby, predictions of the proposed anisotropic heat flux model, the isotropic heat flux model with $Pr_{sgs} = 0.7$ and the isotropic heat flux model using a dynamic procedure to calculate Pr_{sgs} are compared to DNS data of [39]. In addition, results of the anisotropic heat flux model without the anisotropic term ($C_{II} = 0$ in equation 5.11) are provided in figure 5.4 in order to assess the advantage of the proposed $\sqrt{Pr}$ dependency of the model. Figure 5.4 (a) depicts predicted mean temperature profiles and figure 5.4 (b) shows rms temperature profiles as a function of non-dimensional wall distance. Thereby, only LES results of grid no. 1 are presented. Similar results are obtained for grid no. 2 and 3, and are therefore simply omitted for the sake of clarity.

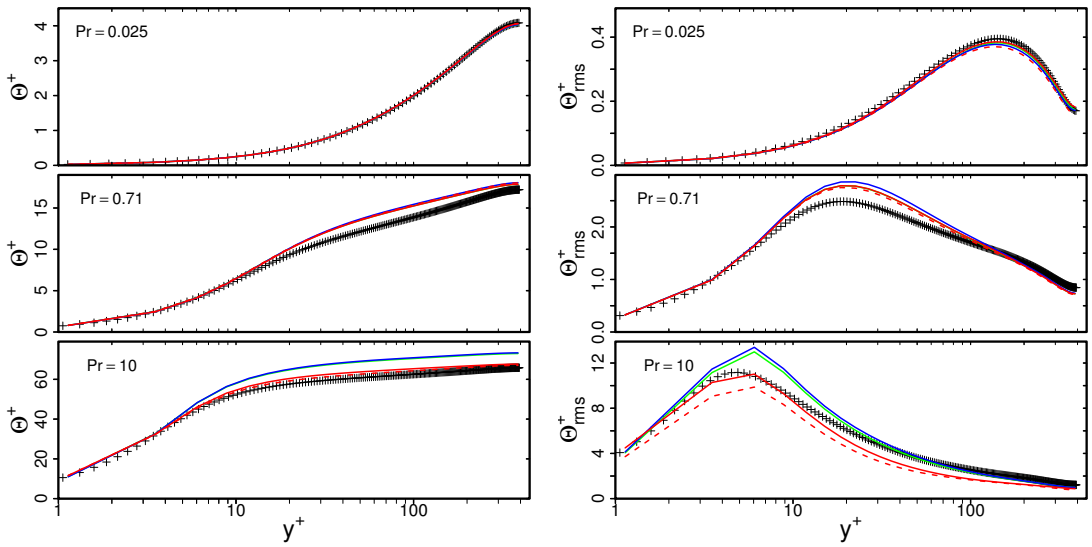

Figure 5.4: Predicted mean (a) and rms (b) temperature profiles for different molecular Prandtl numbers. Anisotropic heat flux model (—), isotropic heat flux model with $Pr_{sgs} = 0.7$ (—), isotropic heat flux model with dynamic procedure (—), anisotropic heat flux model with $C_{II} = 0$ (- -). Comparison with reference DNS data (+) of [39]

As it can be clearly seen in figure 5.4, the physics of turbulent heat transfer in channel flow differs significantly for different Prandtl numbers. Non-dimensional

mean and rms temperatures (Θ^+ and Θ^+_{rms}) increase with increasing molecular Prandtl number and peak values of Θ^+_{rms} are shifted towards the wall. This tendency is well retrieved by all tested subgrid-scale heat flux models, and, just as in the case of $Pr = 0.71$, predictions of the different models are also quite similar. However, it can be seen that predicted mean temperature profiles and peak values of Θ^+_{rms} at $Pr = 0.025$ and $Pr = 10$ are closer to the reference DNS data when the proposed anisotropic model is applied in comparison to cases conventional isotropic models are used. Similar results are obtained by using the proposed heat flux model without the anisotropic contribution term ($C_{II} = 0$). This suggests that mainly the $\sqrt{Pr}$ dependency, that reduces the residual contribution in case of fluid flows with Prandtl numbers smaller than one and increases the modeling contribution regarding fluid flows with Prandtl numbers higher than one, leads to a better prediction of flows with variable fluid properties.

5.4.3 Prediction Accuracy and Computational Cost

It appears that LES predictions of first and second order thermal statistics in turbulent heated channel flows are very similar for anisotropic and isotropic heat flux models. This is quantified next by means of an error analysis. Thereby, a turbulent heated channel flow test case at $Re_\tau = 395$ and $Pr = 0.71$ is selected for the error analysis and the DNS dataset of Kawamura et al. [39] is utilized as reference. The normalized relative error of the mean (e_{θ^+}) and rms ($e_{\theta^+_{rms}}$) temperatures with respect to the non-dimensional wall distance y^+ are shown in figure 5.5. Results are shown for grid no. 1. Similar error characteristics are obtained for the other spatial resolutions. Notice that the relative error is normalized in this study by means of the difference between the maximal and minimal value of the reference data, following the error analysis procedure for LES described in [92].

It is visible in figure 5.5 that errors are small in the near-wall region, increase rapidly in the buffer layer and finally decrease in the outer region. This trend is similar for all tested LES heat flux models and also for both thermal statistics, mean and rms temperatures. Especially in regard to $e_{\theta^+_{rms}}$, it is interesting to observe that the isotropic

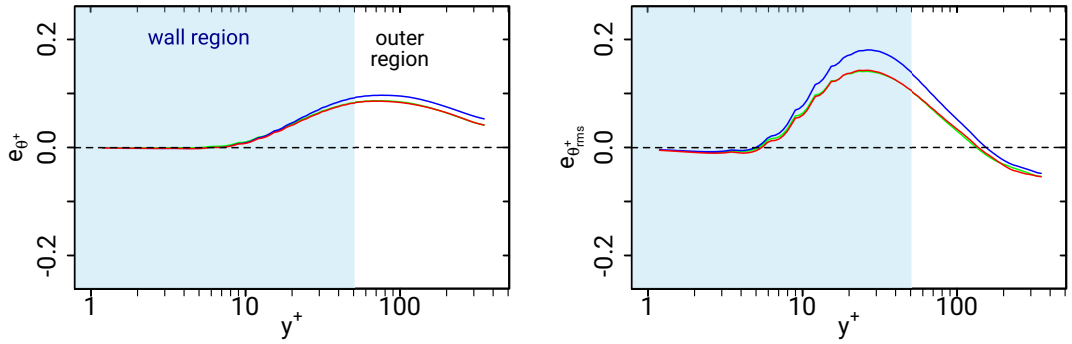

(a) (b)

Figure 5.5: Normalized error of predicted mean and rms temperatures of different subgrid-scale heat flux models as a function of non-dimensional wall distance. Anisotropic heat flux model (—), isotropic heat flux model with $Pr_{sgs} = 0.7$ (—), isotropic heat flux model with dynamic procedure (—)

model with $Pr_{sgs} = 0.7$ and in particular the proposed anisotropic heat flux model are more accurate in the near-wall region than the isotropic heat flux model with dynamic procedure. Further away from the wall, in the outer region, the error contribution is similar for all models. As shown by the authors in [92], localized dynamic procedures can produce a non-physical amount of residual contribution in the near-wall region when the dynamic procedure is not applied over homogeneous planes parallel to the walls. Such a procedure is generally not feasible in complex geometries and therefore not applied in this study. Thus, it seems to be likely, that this physical inconsistency of the dynamic procedure is responsible for the higher errors of the dynamic model in the near-wall region.

After analyzing the error characteristics of the different heat flux models for a given spatial resolution, the overall prediction accuracy of the models is now examined with respect to spatial resolution. Following the procedure described in [92], the normalized mean absolute error (nMAE) is employed as global error metric to quantify the overall prediction accuracy of each model. Thereby, the locations at which the nMAEs are computed are logarithmically distributed along the channel height in order to obtain an approximately equal number of sampling points in each flow regime. Results with respect to the spatial averaged ratio of Kolmogorov length scale η_K and grid width Δ_{grid} are depicted in figure 5.6.

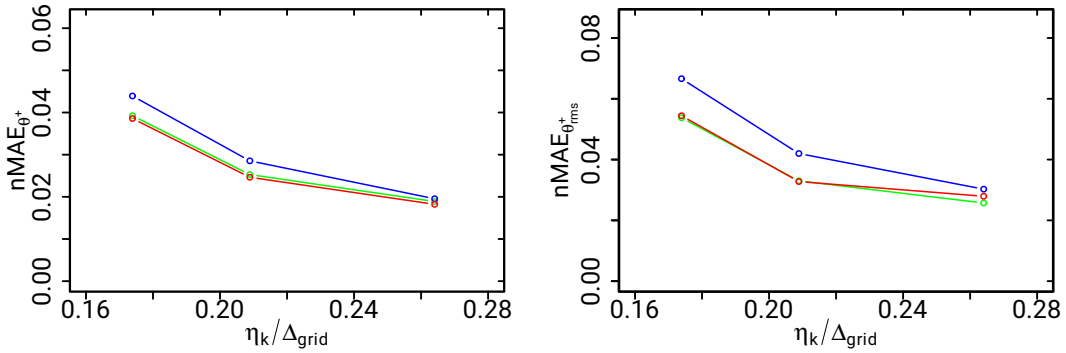

(a) (b)

Figure 5.6: Normalized mean absolute error (nMAE) of predicted mean and rms temperatures with respect to spatial resolutions. (legend see figure 5.5)

As it is expected the nMAEs decrease with increasing spatial resolution ($\eta_K/\Delta_{grid} \uparrow$). This holds true for all tested heat flux models and also for both statistics, which confirms the consistency of all these modeling approaches in terms of LES. Thereby, in particular the anisotropic heat flux model and the isotropic model with constant Pr_{sgs} have lowest values of nMAEs, reflecting a smaller modeling error and therefore best prediction accuracy. However, deviations are small, and it can be concluded that all the tested models have a comparable prediction accuracy, at least for the turbulent heated channel flow test case at $Re_\tau = 395$ and $Pr = 0.71$.

Finally, the required computational cost of the subgrid-scale heat flux models is analyzed. Following the procedure described in [92], the relative computational cost of a subgrid-scale model $CPUh^*$ can be defined as the ratio of the CPU time spent for the calculation of the subgrid-scale model and the total computation time of the simulation. Regarding the selected subgrid-scale heat flux models in this study, it is found that the eddy diffusivity model with constant Pr_{sgs} has the lowest relative computational cost ($CPUh^* \sim 0.25\%$), whereas the eddy diffusivity model using a dynamic procedure to calculate Pr_{sgs} is the most expensive one ($CPUh^* \sim 3\%$). The proposed anisotropic heat flux model is also quite inexpensive ($CPUh^* \sim 0.5\%$) since it is fully algebraic and does not use any dynamic procedure. Nevertheless, the CPU time spent for the calculation of all subgrid-scale heat flux models under consideration is fairly small compared to the total computation time of the simulations.

Considering the present evaluation study for turbulent heated channel flow, it turned out that the proposed anisotropic subgrid-scale heat flux model as well as isotropic models are able to predict first and second order thermal statistics accurately for this test case, regardless a dynamic procedure is used or not. However, only the proposed anisotropic model is able to reproduce the correct direction of the axial subgrid-scale heat flux, accounts for variable fluid properties and exhibits the proper near-wall behavior. This reflects the physical consistency of the proposed model. Furthermore, it is shown that the anisotropic heat flux model has not major impact on computational cost. Its prediction capability in complex flows is therefore demonstrated in the following section.

5.5 Application to Flow Configurations Relevant to Internal Combustion Engines and Exhaust Gas Systems

Among various energy systems, internal combustion (IC) engines features very complex heat and fluid flow situations. Besides being confined by solid walls, the IC engine motor is connected to an exhaust gas system. All together includes processes like (1) thermo-viscous boundary layer flows, (2) impinging cooling/heating, (3) recirculation, (4) flow separation and many more. Thus, given the complexity of heat and fluid flows in IC-engines and exhaust gas systems, it is useful to divide the evolving flow and mixing phenomena into different canonical flow situations that represents the most of the physical processes relevant to such applications. This allows to evaluate a modeling approach for such complex engineering systems in generality by considering only process relevant unit problems.

After analyzing the performance of the proposed anisotropic heat flux model for turbulent heated channel flow and different fluid properties, the novel approach is now applied to more complex heat and fluid flow situations, namely a strongly heated turbulent air flow in a pipe, a turbulent inclined jet impinging on a heated surface, and a backward-facing step flow with heated walls. These test cases are selected since they feature essential heat and fluid flow situations that are in particular relevant for internal combustion engines and exhaust gas systems. An illustration of the generic test cases

and the location where such flow situations can be found in automotive technologies is shown in figure 5.7. A short description of each test case and the obtained LES results are presented and discussed in the following.

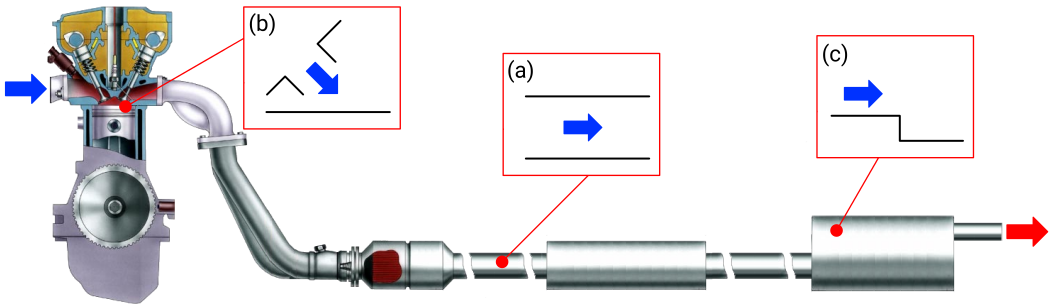

Figure 5.7: Illustration of an internal combustion engine with exhaust gas system. Characteristic heat and fluid flow situations: (a) thermal boundary layer flow, (b) impinging cooling/heating, (c) recirculation and reattachment

5.5.1 Strongly Heated Turbulent Air Flow in a Pipe

In exhaust gas systems and many other engineering applications, large temperature differences occur that leads to strongly varying thermo-fluid properties. In order to establish the validity of the present anisotropic heat flux model for such extreme operating conditions, LES of a strongly heated air flow in a vertical pipe with constant heat flux have been carried out and simulation results are compared with measurements of Shehata and McEligot [108] and DNS data of Bae et al. [6]. In addition, LES results using the isotropic linear thermal diffusivity model with $Pr_{sgs} = 0.7$ are also provided for comparison purpose. An illustration of the strongly heated pipe flow configuration is shown in figure 5.8, where D denotes the inner diameter of the pipe.

In the test section, a fully developed turbulent flow of dry air ($Re = 6000$, $T_0 = 298.15K$, $p = 0.1MPa$) enters a DN-25 pipe ($D = 0.0272m$, $L = 30D$) and is heated up after an entrance length of $5D$. The heated pipe region has a length of $25D$ with a constant wall heat flux of $q_w = 4.11kW/m^2$. In line with the DNS study of [6], air is treated in the current LES study as an ideal gas using the ideal gas equation. Other thermo-physical properties are obtained by means of power laws in the temperature as described in [6].

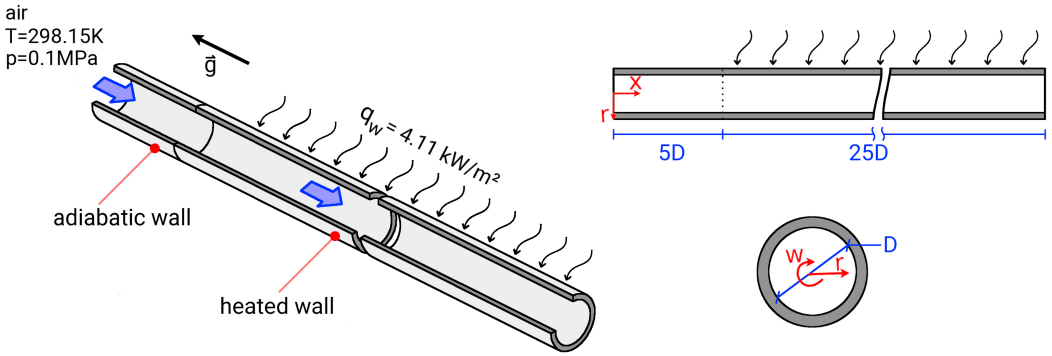

Figure 5.8: Illustration of the heated pipe flow domain. Isometric view (left); view along x-axis (top right); view along r-axis (down right). D denotes the inner diameter of the pipe.

A block-structured numerical grid with 649536 control volumes is used to discretize the pipe flow domain. Thereby, the near-wall region is refined in order to fully resolve the small turbulence scales in the vicinity of the wall. At the pipe wall, a no-slip condition is set for the velocity and a zero Neumann conditions for the pressure. A constant wall heat flux of $q_w = \frac{\lambda}{c_p}\frac{\partial h}{\partial r}|_{r=R} = 4.11 kW/m^2$ is imposed at the heated wall while a zero temperature gradient condition is set at the adiabatic wall. In order to obtain realistic inflow turbulence, the velocity field is extracted for each time step at the $x = 5D$ plane downstream of the inlet and used to prescribe the velocity field at the inflow plane. At the outlet, a convective boundary condition is used for the velocity to maintain the overall mass conservation, while the pressure is set to a constant value. Figure 5.9 (a) shows predicted mean wall temperature and Nusselt number as a function of axial distance, where heating starts at a axial position of $x/D = 5$.

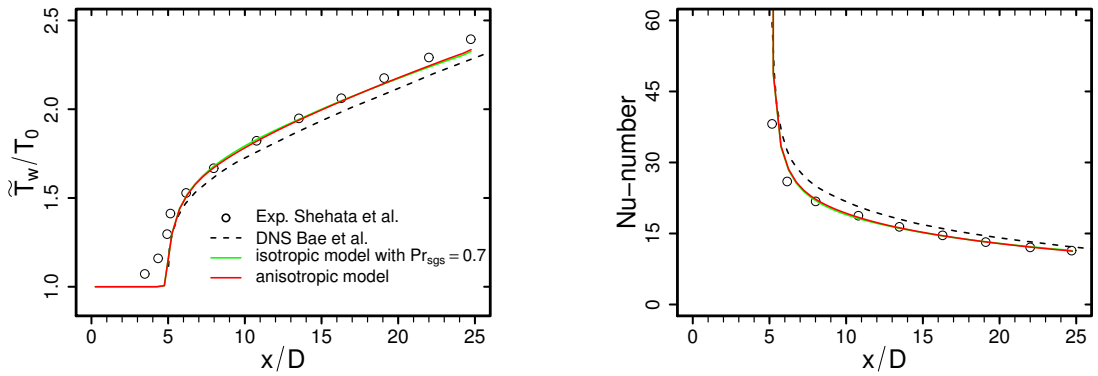

(a) (b)

Figure 5.9: Predicted mean wall temperature (a) and Nusselt number (b) as a function of axial distance.

As it can be seen in figure 5.9, both, the anisotropic heat flux model as well as the isotropic model with $Pr_{sgs} = 0.7$ show excellent agreement with the experiment [108] and also with the reference DNS [6] in case of streamwise distribution of the wall temperature and Nusselt number. Furthermore, LES results are very similar to each other, which suggests that both models are well suited to predict such a strongly heated turbulent air flow in a pipe with variable thermo-physical properties, at least in case of mean wall temperatures and Nusselt number.

5.5.2 Turbulent Inclined Jet Impinging on a Heated Solid Surface

Several canonical mixing and fluid flow situations that occur in internal combustion engines and exhaust gas systems can be also found in impinging jet flows. These complex phenomena include (1) thermo-viscous boundary layers, (2) impinging heating/cooling, (3) wall-jets, (4) recirculation and (5) separation. In order to establish the validity of the novel anisotropic heat flux model under such flow conditions, the second application test case consists of a turbulent square jet impinging on a heated solid surface. The heat and fluid flows within this configuration were investigated numerically using DNS technique (see [90, 93]). A schematic of the impinging jet configuration used in the LES study is provided in figure 5.10.

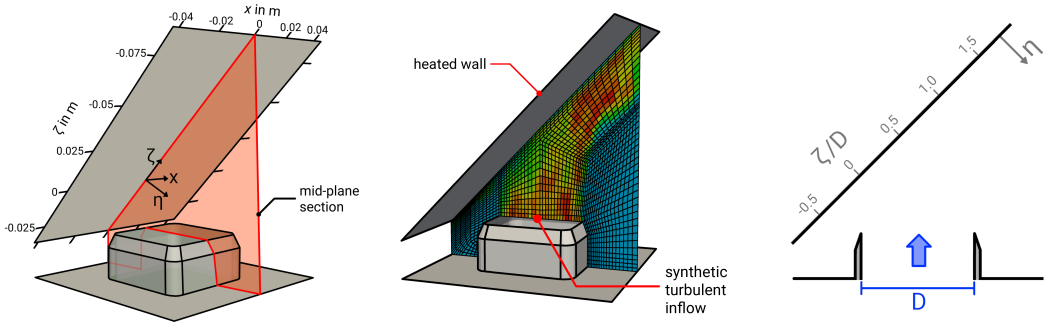

Figure 5.10: Computational domain, slice through the numerical grid at mid-plane section, and description of the coordinate system of the impinging jet configuration [91]

In accordance with the reference DNS, a turbulent jet of dry air ($T_{inlet} = 290K$, $p = 1atm$) leaves a square nozzle ($D = 40mm$) and impinges on a heated flat plate. The heated wall has a constant wall temperature of $T_w = 330K$, a jet-to-plate distance of $H/D = 1$, and an inclination angle of $\alpha = 45°$. At the impinged wall, the jet

is divided into two opposed wall-jets directed outward along the solid wall and gets heated up.

A block-structured numerical grid with 1699375 control volumes is employed in the LES study, that is refined in the near-wall region to ensure a non-dimensional wall distance smaller than one. Regarding the inflow, synthetic turbulent inlet condition is employed at the nozzle exit section. Thereby, realistic turbulence is generated using the digital filter approach proposed by Klein et al. [49], while the mean velocity profile is taken from the DNS study.

Figure 5.11 (a) shows LES predictions of the distribution of the local Nusselt number along the ζ-axis at $x = \eta = 0$ in comparison with the DNS data. Thereby, the local Nusselt number is defined as $Nu = h_t D/\lambda$, where h_t denotes the local heat transfer coefficient and λ the thermal conductivity. Figure 5.11 (b) depicts the turbulent wall-parallel heat flux as a function η at $\zeta/D = -0.15$. At this location, the Nusselt number is maximal, heat is transported counter to the temperature gradient and heat fluxes appear highly anisotropic (see [93]). In figure 5.11 (b) solid lines denote resolved heat fluxes and dashed lines represent modeled subgrid-scale heat fluxes. LES results of the proposed anisotropic heat flux model and the isotropic heat flux model with $Pr_{sgs} = 0.7$ are presented.

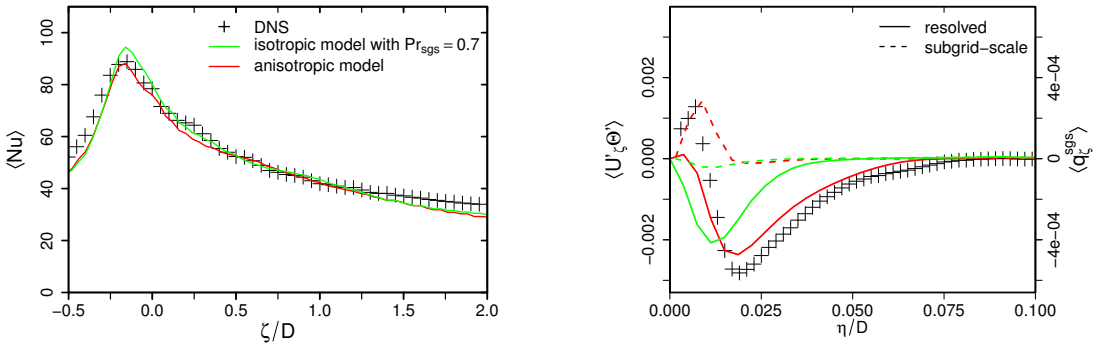

(a) (b)

Figure 5.11: LES results of local Nusselt Number along the wall-parallel direction (a) and turbulent wall-parallel heat flux at $\zeta/D = -0.15$ (b). Comparison with DNS data of [90, 93]

Examining figure 5.11, a clear peak in the Nusselt number can be observed at $\zeta/D = -0.15$. Additionally, the higher values perceived around the stagnation point

rapidly decrease away from this location. This tendency is well reproduced by both heat flux models under consideration. Regarding turbulent wall-parallel heat fluxes $< U'_\zeta \Theta' >$ at $\zeta/D = -0.15$ shown in figure 5.11 (b), it can be clearly seen that the direction of $< U'_\zeta \Theta' >$ changes close to the wall in the DNS data. This trend is only reproduced correctly by means of the proposed anisotropic heat flux model. Furthermore, predictions of $< U'_\zeta \Theta' >$ using the proposed anisotropic heat flux model compare much better to the reference DNS than heat fluxes obtained by using the standard isotropic model. This confirms that only the proposed heat flux model is able to predict resolved and subgrid-scale heat fluxes in a physically consistent way for such a complex heat and fluid flow situation, while standard isotropic models fail.

5.5.3 Backward-Facing Step Flow with Heated Walls

The last test case in the evaluation study deals with a backward-facing step flow with a constant heated surface behind a sudden expansion. This generic test case features complex flow situations such as recirculation and flow separation and is therefore an excellent benchmark flow for exhaust gas systems, in particular to mimic heat and fluid flow phenomena within exhaust silencer devices. The backward-facing step flow with heated walls was investigated experimentally by Vogel and Eaton [115]. A representation of the computational domain used in the LES study is shown in figure 5.12.

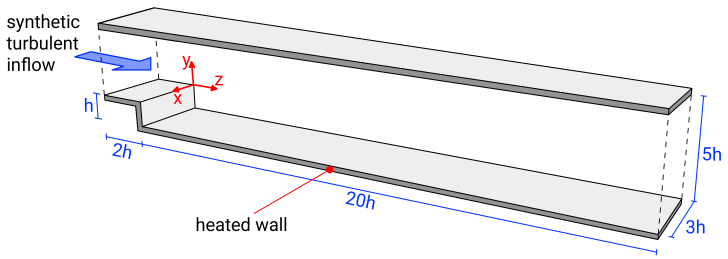

Figure 5.12: Computational domain of the backward-facing step configuration

In the backward-facing step test case, a turbulent stream of dry air ($T = 298K$, $Pr = 0.71$) enters a wind tunnel, expands suddenly after $2h$ and is finally heated up with a constant heat flux of $q_w = 270W/m^2$ behind the sudden expansion. The channel

expansion ratio is 1.25 with a Reynolds number of $Re = 28000$ (based on the freestream velocity and step height, h).

A block-structured numerical grid with 2745504 control volumes is employed in the LES study, that is refined in the near-wall region to ensure a non-dimensional wall distance smaller than one. Realistic inflow turbulence is generated using the digital filter approach proposed in [49], while the mean velocity profile equals a boundary layer flow profile with a boundary layer thickness of $\delta_{99} = 1.07h$.

Figure 5.8 depicts (a) temperature profiles at different axial positions and (b) the distribution of the Stanton number along the axial direction at the heated lower wall behind the expansion. Thereby, the Stanton number is defined as $St = q_w/(U_\infty \rho c_p (T - T_w))$, where U_∞ is the freestream velocity, c_p the specific heat capacity of the fluid, ρ the fluid density and T_w the wall temperature.

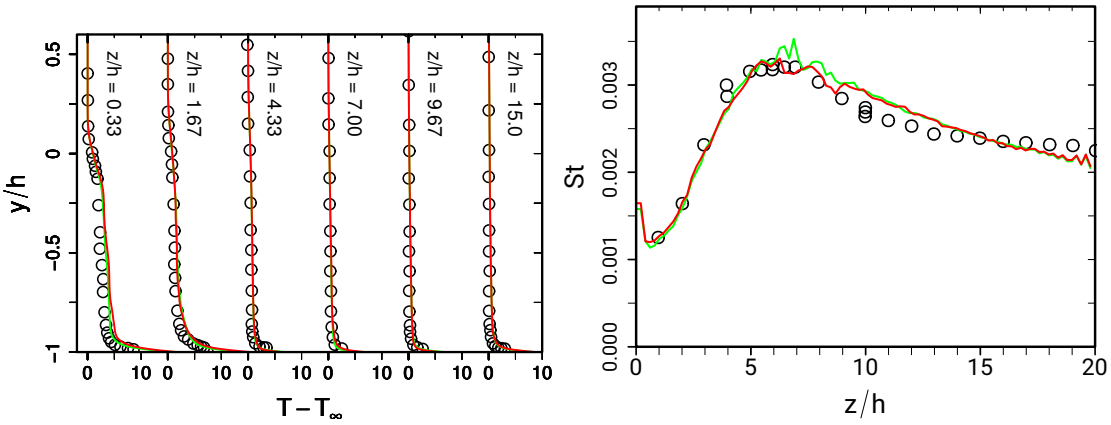

(a) (b)

Figure 5.13: Temperature profiles at different axial positions (a) and Stanton number at the heated wall as a function of axial position (b). (—): anisotropic heat flux model; (—): isotropic heat flux model with $Pr_{sgs} = 0.7$; ○: experimental data of Vogel and Eaton [115].

As it can be observed in figure 5.13, there is excellent agreement between LES predictions and the experiment. Mean temperature profiles are very close to the experimental data and peak values in the computed profiles of St compare qualitatively and quantitatively very well with the experiment. This holds true for the anisotropic heat flux model as well as for the isotropic model with $Pr_{sgs} = 0.7$. A significant improvement in using an anisotropic heat flux model cannot be determined.

5.6 Conclusion and Outlook

A novel anisotropic heat flux model for large eddy simulations of complex engineering applications have been proposed and evaluated. The prominent features of the proposed model are that (1) it accounts for variable fluid properties and anisotropic effects in the unresolved temperature scales, (2) no ad-hoc treatments or dynamic procedure are required to obtain the correct near-wall behavior, and (3) the formulation is consistent with the second law of thermodynamics. It is shown in this work that only the proposed anisotropic model from the tested ones is able to predict subgrid-scale heat fluxes in a physically consistent way, while both, the standard and dynamic thermal diffusivity models are unable to reproduce the direction of subgrid-scale heat flux correctly. However, the proposed anisotropic heat flux model has a similar prediction accuracy and computational expense than conventional isotropic models. This was confirmed by comparison with DNS and experimental data from the literature for several test cases that are relevant for internal combustion engines and exhaust gas systems, namely, a turbulent heated channel flow, a strongly heated air flow in a vertical pipe, a turbulent inclined jet impinging on a heated solid surface and a backward facing step flow with heated walls.

Addendum

Conflict of interest The authors declare that they have no conflict of interest.

Acknowledgment Open Access funding provided by Projekt DEAL. The authors gratefully acknowledge the fnancial support of the DFG (German Research Council) SFB-TRR 150 and the support of the numerical simulations on the Lichtenberg High Performance Computer (HHLR) at the Techische Universität Darmstadt.

[

Appendix]**Appendix** Similar to the subgrid-scale viscosity, a correct asymptotic behavior of the subgrid-scale thermal diffusivity α_{ij}^{sgs} is an important factor in dealing with wall-resolved LES of turbulent flows with heat transport. In order to an-

alyze the asymptotic behavior of the proposed heat flux models near solid walls, figure 5.14 presents the scaled wall-normal subgrid-scale thermal diffusivity component α_{yy}^{sgs} as a function of dimensionless wall distance y^+ in a turbulent heated channel flow at $Re_\tau = 395$ and $Pr = 0.71$. LES results of three different numerical grids with $(N_1 \times N_2 \times N_3) = (81 \times 91 \times 81)$, $(97 \times 111 \times 97)$, and $(121 \times 137 \times 121)$ control volumes are shown. It is visible in figure 5.14 that the theoretical behavior of $\alpha_{yy}^{sgs} \sim \mathcal{O}\left(y^3\right)$ is well retrieved numerically. This holds true for all grid resolutions under consideration, which confirms the proper asymptotic behavior of the proposed heat flux models near solid walls.

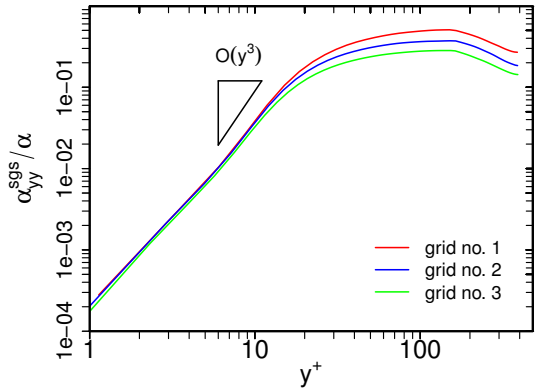

Figure 5.14: Scaled wall-normal subgrid-scale thermal diffusivity component α_{yy}^{sgs} as a function of dimensionless wall distance y^+ in a turbulent heated channel flow at $Re_\tau = 395$ and $Pr = 0.71$

CHAPTER 6

TOWARDS IDENTIFICATION AND DEVELOPMENT OF A RELIABLE FRAMEWORK TO PREDICT THE THERMAL FIELD IN TURBULENT WALL-BOUNDED SHEAR FLOWS

The paper was under preparation and not published by the time the dissertation was finished. Thus, differences to the upcoming publication are possible. It is very likely that a modified and shorter version of the current manuscript will be submitted due to limitations on "number of pages" existing in journals that are considered. It is written by Matthias Ziefuss[1], Nader Karimi[2] and Amirfarhang Mehdizadeh[1]*.

[1] Civil and Mechanical Engineering Department, School of Computing and Engineering, University of Missouri-Kansas City, Kansas City, MO 64110, USA [2] Department of Chemical and Biological Engineering, University of Colorado, 596 UCB, Boulder, CO 80309, United States

[3] School of Engineering and Materials Science, Queen Mary University of London, London E1 4NS, United Kingdom

* Corresponding author: mehdizadeha@umkc.edu

6.1 **Abstract**

Heat transfer modeling plays an integral role in design and optimization of traditional, as well as modern emerging thermal-fluid systems. However, currently available models suffer from a fundamental shortcoming: their development is mainly based on the general notion that accurate prediction of the flow field will guarantee an appropriate prediction of the thermal field, known as eddy diffusivity models based on the Reynolds Analogy concept. In particular, these models face serious challenges in prediction of second order statistics such as heat fluxes in homogeneous directions and temperature variance. Additionally, these models are developed targeting fluids with Prandtl (Pr) number around unity and thus, incapable of capturing thermal fields of working fluid with Pr numbers significantly different than unity. In an attempt to address the existing shortcomings of such models, this investigation aims to identify a reliable framework to predict the thermal field in wall-bounded shear flows. Towards this, most advanced models, i.e. implicit and explicit algebraic turbulent heat flux models have been applied

to a turbulent attached boundary layer of various working fluids with significantly different Prandtl numbers. It turns out that the explicit framework is potentially capable of dealing with complex turbulent thermal fields and to address longstanding shortcomings of currently available models if the flow field is predicted accurately. Moreover, it has been shown that thermal time scale plays an integral role to predict thermal phenomena, particularly those of fluids with low/high Pr numbers.

6.2 Introduction

The passive transport of heat in a turbulent environment plays an integral role in development and optimization in various advanced and emerging systems. These include cooling systems for nuclear power plants, where liquid metal is used as coolant [71, 12], boiler systems for biomass combustion [50], and heat exchange devices in the petroleum/petrochemical industry [78], to name only a few. The design and optimization of such systems rely heavily on computational modeling and simulation as experimental investigations are either not possible or prohibitively expensive [106].

Development and optimization of such systems require insight into complex dynamics of heat and mass transfer inside the system, which necessitates the application of reliable models. Furthermore, the above mentioned applications impose an additional challenge for models in predicting the heat transport at an acceptable level of accuracy when the Prandtl (denoted as Pr) number of the working fluid is significantly different than unity [25, 8, 125], i.e. ranges from Pr $<<$ 1 for liquid metal to a few thousands for crude oils. Thus, understanding and correct modeling of heat transport have introduced a major challenge in the past decades [24]. One of the underlying challenges is the strong dependency of the thermal field (temperature) on the flow field, which often is highly turbulent. As a direct consequence, an appropriate model for the momentum transport is an indispensable necessity and therefore, the main focus of modeling in the past few decades has been placed on turbulent flow field modeling [107]. The intuitive assumption is that a better prediction of momentum quantities leads to a better prediction of thermal quantities. Moreover, it was assumed that the heat transport could solely

be predicted by knowledge of the momentum transport. That has led to the formulation of the simplest model for turbulent heat fluxes, i.e. the on the eddy diffusivity approach based Reynolds Analogy. While this approach is a drastic simplification of the physical mechanisms, it has been applied successfully to predict first order statistics such as the mean temperature in a large number of industrial applications using CFD technique. It is worth noting that these applications mostly deal with working fluids with Pr number around unity [7]. It was shown in [126, 125] that the eddy diffusivity approach (e.g. the Reynolds Analogy) suffers from serious shortcomings when applied to predict second order statistics or thermal field of fluids with Pr number different than unity. Further, due to the mathematical formulation of the Reynolds Analogy—the heat flux is proportional to the mean temperature gradient [44]—a non-existing temperature gradient leads to a non-existing heat flux, which leads to inaccurate prediction of turbulent heat fluxes in homogeneous direction in turbulent shear flows [125].

In order to address the shortcomings of the Reynolds analogy based models, several approaches, with different levels of complexity, have been proposed based on the concept of cross-streamwise mixing, which is known to be the major underlying mechanism for both momentum and heat transfer [107]. These include, the GGDH, which includes time scales for the momentum or temperature field [14, 33], and AFM, which introduce additional correlations to predict the heat flux [62, 55, 44, 124, 64]. However, these approaches have never been extensively investigated and there is only limited information on prediction capabilities of these methods in the literature [76, 25]. Nevertheless, it should be noted that algebraic heat flux models may offer promising potential to overcome shortcomings of the Reynolds Analogy, based on limited information in the literature [25, 124, 42]. Therefore, this study centers these models and aims to provide a comprehensive assessment of these methods when applied to a fully attached turbulent boundary layer using different working fluids.

There are two major variants of the AFM distinguished by two fundamental different approaches: implicit and explicit models. The former is a result of truncating the exact heat flux equation [42, 27], while the latter is derived based on the representation

theorem [124, 64]. There are few recent efforts on applications of implicit methods to predict thermal behavior of low Pr number fluids in turbulent wall bounded channel flow [107, 96], which will be discussed in section 6.3.3.3. Although some improvement were achieved compared to the classical methods, these studies do not provide some relevant statistical quantities such as the heat fluxes and dissipation of temperature variance. Additionally, these studies mainly target fluids with Pr numbers less than unity, i.e. the implicit models were calibrated/tuned for low Pr number fluids, which limits the application of the models.

In contrast, there is only one study that uses the explicit model to predict the temperature field in a turbulent channel flow [64]. This study shows clear improvements as compared to the classical approach based on the Reynolds Analogy. However, detailed results are only presented for a turbulent rotating channel flow with main emphasis on temperature first order statistics.

The current study presents a comprehensive assessment of the predictive capabilities of the implicit and explicit turbulent heat flux models for first and second order statistics when applied to 3D wall-bounded shear flow using different working fluids. Additionally, the assessment includes sensitivity analysis with respect to the turbulence model used to describe the flow field.

Moreover, both implicit and explicit models considered here use only mechanical time scale in their formulations, as will be discussed in the following sections. As a result of this, relevance and effects of thermal time scale in prediction capability of heat flux models remains unclear. This investigation aims to study the effects of thermal time scale on the predictive capabilities of both models. Therefore, the existing mechanical time scale is modified by including the thermal time scale in both models as will be shown in section 6.3.3. However, it should be noted that the goal here is only to study model sensitivity to the inclusion of thermal time scale and therefore, no additional model calibrations/tuning have been performed after inclusion of the thermal time scale into the model.

The chapter is organized as follows: in Section 6.3, the governing equations including employed turbulence and heat flux models will be presented and discussed. In Section 6.4, an overview of test cases and the numerical approach is provided. Results obtained from simulations are presented and discussed in Section 6.5. The chapter concludes with a summary and conclusion in Section 6.6.

6.3 Governing Equations and Model Description

The current study aims to provide a comprehensive assessment and comparison of the prediction capabilities of the implicit and explicit heat flux models when applied to turbulent attached boundary layer (channel flow) using working fluids with different Pr numbers. Moreover, sensitivity of both modeling approaches towards to turbulence models used to describe the flow field will be studied.

Two different turbulence models, including Launder-Sharma's $k-\varepsilon$ model [56] and Lien-Abe's $k-\varepsilon$ model, will be used. The major difference between these models is that Launder-Sharma's model is a linear eddy viscosity model, while Lien-Abe's is a non-linear eddy viscosity model. This model is based on Lien's $k-\varepsilon$ model [57], modified with the non-linear term proposed by Abe [2]. As it will be shown and discussed later, the non-linear model is capable of predicting the Reynolds Stress tensor with a remarkably higher accuracy compared to the linear model, which should lead to more accurate predictions of thermal quantities.

6.3.1 Turbulence Models

6.3.1.1 Launder and Sharma's $k-\varepsilon$ model

The Launder-Sharma $k-\varepsilon$ [56] model is one of the most commonly used linear models. Henceforth, this model **will be denoted as *LS***. It employs two transport equa-

tions, one for turbulent kinetic energy k, and one for the dissipation rate ε. The model equations read:

$$\frac{Dk}{Dt} = \frac{\partial}{\partial x_i}\left[\left(\nu + \frac{\nu_t}{\sigma_k}\right)\frac{\partial k}{\partial x_i}\right] + P_k - \varepsilon, \tag{6.1}$$

$$\frac{D\tilde{\varepsilon}}{Dt} = \frac{\partial}{\partial x_i}\left[\left(\nu + \frac{\nu_t}{\sigma_\varepsilon}\right)\frac{\partial \tilde{\varepsilon}}{\partial x_i}\right] + C_1 P_k \frac{\tilde{\varepsilon}}{k} - C_2 f_2 \frac{\tilde{\varepsilon}^2}{k} + E. \tag{6.2}$$

Where

$$P_k = -\overline{u_i u_j}\frac{\partial U_i}{\partial x_j}, \quad E = 2\nu\nu_t\left(\frac{\partial^2 U_i}{\partial x_j \partial x_k}\right)^2, \quad \tilde{\varepsilon} = \varepsilon - 2\nu\left(\frac{\partial \sqrt{k}}{\partial x_k}\right)^2,$$
$$\nu_t = C_\mu f_\mu \frac{k^2}{\tilde{\varepsilon}}, \quad f_\mu = \exp\left[\frac{-3.4}{1 + \frac{\mathrm{Re}_t}{50}}\right],$$

and

$$-\overline{u_i u_j} = b_{ij} - \frac{2}{3}\delta_{ij}k. \tag{6.3}$$

Here, b_{ij} is the Reynolds stress anisotropy tensor and since this is a linear model, b_{ij} holds only a linear term (denoted as ${}^l b_{ij}$):

$$b_{ij} = {}^l b_{ij} = S_{ij} = \nu_t\left(\frac{\partial U_i}{\partial x_j} + \frac{\partial U_j}{\partial x_i}\right). \tag{6.4}$$

Further details on model constants and functions, i.e. $C_1, C_2, C_\mu, \sigma_k, \sigma_\varepsilon, f_2$, are provided in [56].

6.3.1.2 Lien-Abe's $k-\varepsilon$ model

As previously mentioned, the Lien-Abe model is based on the linear part of the $k-\varepsilon$ model proposed in [57] and employs the non-linear term introduced by Abe et. al

[2]. This model **will be denoted as *LA*** in the current study, and below is a summary of the model equations:

$$\frac{Dk}{Dt} = \frac{\partial}{\partial x_i}\left[\left(\nu + \frac{\nu_t}{\sigma_k}\right)\frac{\partial k}{\partial x_i}\right] + P_k - \varepsilon, \tag{6.5}$$

$$\frac{D\varepsilon}{Dt} = \frac{\partial}{\partial x_i}\left[\left(\nu + \frac{\nu_t}{\sigma_\varepsilon}\right)\frac{\partial \varepsilon}{\partial x_i}\right] + C_{\varepsilon 1}P_k\frac{\varepsilon}{k} - C_{\varepsilon 2}f_2\frac{\varepsilon^2}{k} + E(f_2), \tag{6.6}$$

where

$$P_k = -\overline{u_i u_j}\frac{\partial U_i}{\partial x_j}, \quad E(f_2) = C_{\varepsilon_2}C_\mu^{0.75}f_2\sqrt{k}\frac{\varepsilon}{l_e}\exp\left[-A_E y^{*2}\right], \quad l_e = \frac{\kappa y^*}{1 + \frac{2\kappa y^*}{C_\mu^{0.75}}}.$$

The term $\overline{u_i u_j}$ is defined as in Eq. 6.3 but b_{ij} holds in addition to the linear term ($^l b_{ij}$) two further non-linear terms ($^2 b_{ij}$ and $^s b_{ij}$):

$$b_{ij} = {}^l b_{ij} + {}^2 b_{ij} + {}^s b_{ij}. \tag{6.7}$$

These two additional terms are rather complex and further details are provided in [2] while details on model constants for the $k - \varepsilon$ equations and functions, i.e. $A_E, C_{\varepsilon 1}, C_{\varepsilon 2}, C_\mu, \kappa, y^*, \sigma_k, \sigma_\varepsilon, f_2$, are provided in [57] and [32].

6.3.2 Internal Energy Equation

The Reynolds-averaged internal energy equation reads as [27]:

$$\rho c_p \frac{DT}{Dt} = S_T + \frac{\partial}{\partial x_i}\Big[\Big(\lambda\frac{\partial T}{\partial x_i}\Big) - \rho c_p\overline{\theta u_i}\Big]. \tag{6.8}$$

Assuming incompressible flow, constant physical properties and neglecting additional source terms (such as radiation), the equation can be written as below:

$$\frac{DT}{Dt} = \frac{\partial}{\partial x_i}\Big[\Big(\frac{\nu}{Pr}\frac{\partial T}{\partial x_i}\Big) - \overline{\theta u_i}\Big]. \tag{6.9}$$

The quantity $\overline{\theta u_i}$ on the right hand side is called turbulent heat flux and is the Reynolds-averaged fluctuating velocity-temperature correlation. This quantity needs to be modeled in order to close the equation.

6.3.3 Turbulent Heat Flux

As previously mentioned, the heat flux must be determined to close the energy equation. The exact transport equation for $\overline{\theta u_i}$ for incompressible non-buoyant flows in the RANS-framework reads as below [42]:

$$\frac{D\overline{\theta u_i}}{\partial t} = \underbrace{\frac{\partial}{\partial x_i}\left(-\overline{\theta u_i u_j} + \frac{\overline{\theta p}}{\rho}\delta_{ij} + \nu\theta\overline{\frac{\partial u_i}{\partial x_j}} + \alpha\overline{u_i\frac{\partial \theta}{\partial x_j}}\right)}_{D_{\theta i}} + \underbrace{\overline{\frac{p}{\rho}\frac{\partial \theta}{\partial x_i}}}_{\Phi_{\theta i}} - \underbrace{\left(\overline{u_i u_j}\frac{\partial T}{\partial x_j} + \overline{\theta u_j}\frac{\partial U_i}{\partial x_j}\right)}_{P_{\theta i}} - \underbrace{(\nu+\alpha)\overline{\frac{\partial u_i}{\partial x_j}\frac{\partial \theta}{\partial x_j}}}_{\varepsilon_{\theta i}}, \quad (6.10)$$

where $D_{\theta i}$ is the diffusive transport, $\Phi_{\theta i}$ is the pressure-temperature correlation, $P_{\theta i}$ is the production due to combined actions of mean velocity and mean temperature gradient, and $\varepsilon_{\theta i}$ is the dissipative correlation/destruction term. The direct application of this equation to predict the heat flux is not possible due to existing of several terms that are not know ($D_{\theta i}$, $\Phi_{\theta i}$ and $\varepsilon_{\theta i}$), and need to be modeled. Explicit and implicit algebraic methods are among strategies to model this equation and will be discussed in detail in this study. Thereby, it will be explained how the unknown terms are treated and modeled.

6.3.3.1 Thermal Dissipation and Temperature Variance

Among unclosed terms in the heat flux equation, thermal dissipation ε_θ has attracted more attention and there are a few models for ε_θ in the literature [66, 44, 60, 76]. Following same assumptions and analogy as for the flow field, i.e. high Reynolds

number and small scale being locally isotropic, the exact transport equation for thermal dissipation ε_θ reads as follow [27]:

$$\frac{D\varepsilon_\theta}{\partial t} = \Bigg[\underbrace{-\frac{\partial\overline{\varepsilon_\theta u_i}}{\partial x_i}}_{T_{\varepsilon\theta}} + \underbrace{\alpha\frac{\partial^2\varepsilon_\theta}{\partial x_i\partial x_i}}_{D_{\varepsilon\theta}}\Bigg] - \underbrace{2\alpha\overline{\frac{\partial u_i}{\partial x_j}\frac{\partial\theta}{\partial x_j}\frac{\partial\theta}{\partial x_i}}}_{P_{\varepsilon\theta4}}$$
$$\underbrace{-2\alpha\left(\overline{\frac{\partial\theta u_i}{\partial x_j}\frac{\partial\theta}{\partial x_j}}\frac{\partial T}{\partial x_i} + \overline{\frac{\partial\theta}{\partial x_i}\frac{\partial\theta}{\partial x_j}}\frac{\partial U_k}{\partial x_j} + \overline{u_k\frac{\partial\theta}{\partial x_j}}\frac{\partial^2 T}{\partial x_i\partial x_j}\right)}_{P_{\varepsilon\theta1}+P_{\varepsilon\theta2}+P_{\varepsilon\theta3}} \underbrace{-2\left(\overline{\alpha\frac{\partial^2\theta}{\partial x_i\partial x_j}}\right)^2}_{Y_{\varepsilon\theta}}, \quad (6.11)$$

where $T_{\theta\varepsilon}$ is the turbulent diffusive transport, $D_{\theta\varepsilon}$ is the molecular diffusive transport, $P_{\varepsilon\theta1} + P_{\varepsilon\theta2} + P_{\varepsilon\theta3}$ are production due to gradient of mean quantities. $P_{\varepsilon\theta4}$ is the turbulent production, and Y_ε is the destruction at small scales.

Closing this equation is more complex compared to closing the equation for the dissipation of turbulent kinetic energy ε. As stated in [107, 54, 110, 76, 25, 60], twice as many free parameters need to be determined. Several models have been proposed [66, 44, 60, 76] which follow the same modeling methodology as for ε. This leads to the following general form for the transport equation for ε_θ [44]:

$$\frac{D\tilde{\varepsilon}_\theta}{Dt} = \mathcal{D}_{\varepsilon_\theta} + C^\theta_{\varepsilon1}P_\theta\frac{\tilde{\varepsilon}_\theta}{\overline{\theta^2}} + C^\theta_{\varepsilon3}P\frac{\tilde{\varepsilon}_\theta}{k} - C^\theta_{\varepsilon4}\frac{\tilde{\varepsilon}^2_\theta}{\overline{\theta^2}} - C^\theta_{\varepsilon5}f_{\varepsilon\theta}\frac{\tilde{\varepsilon}_\theta\tilde{\varepsilon}}{k} + \underbrace{E_\theta}_{\substack{\text{near-wall}\\ \text{correction}}}, \quad (6.12)$$

where

$$P_k = -\overline{u_iu_j}\frac{\partial U_i}{\partial x_j}, \quad P_\theta = -\overline{\theta u_i}\frac{\partial T}{\partial x_i}, \quad E_\theta = 2\alpha\alpha_t\left(\frac{\partial^2 T}{\partial x_j\partial x_k}\right)^2, \quad \tilde{\varepsilon}_\theta = \varepsilon_\theta - \underbrace{\alpha\left(\frac{\partial\sqrt{\overline{\theta^2}}}{\partial x_k}\right)^2}_{\substack{\varepsilon_\theta \text{ at}\\ \text{the wall}}}.$$

Note that the model differs in near-wall correction and ε_θ at the wall. The model proposed in [44] will be used in this study with E_θ and $\tilde{\varepsilon}_\theta$ as defined above.

Modeling of the equation for temperature variance $\overline{\theta^2}$ is relatively straightforward and the modeled equation reads as below [107]:

$$\frac{D\overline{\theta^2}}{Dt} = 2P_\theta - 2\varepsilon_\theta + \frac{\partial}{\partial x_i}\Big[\Big(\frac{\nu}{Pr} + \frac{\nu_t}{\sigma_t}\Big)\frac{\partial\overline{\theta^2}}{\partial x_i}\Big], \tag{6.13}$$

where $P_\theta = -\overline{\theta u_i}\partial T/\partial x_i$ is the production of temperature variance. Details on model constants are provided in [107]. As will be discussed in the following, the quantities, $\overline{\theta^2}$ and ε_θ, are necessary to determine the thermal time scale.

6.3.3.2 Mechanical and Thermal Time Scales

There are three time scales that may play integral roles to predict the thermal field at an acceptable level of accuracy and fidelity. They are the mechanical, the thermal, and a combination out of the mechanical and thermal, referred to as mixed time scale. The mechanical time scale is defined as the ratio of the turbulent kinetic energy k and its dissipation ε:

$$\tau_m = \frac{k}{\varepsilon}. \tag{6.14}$$

The thermal time scale follows the same principle and is represented by the ratio of the temperature variance $\overline{\theta^2}$ and its dissipation ε_θ:

$$\tau_\theta = \frac{\overline{\theta^2}}{2\varepsilon_\theta}. \tag{6.15}$$

However, in contrast to the mechanical time scale, this quantity cannot be obtained directly from the flow field and requires data on $\overline{\theta^2}$ and ε_θ to be obtained from corresponding transport equations discussed in Section 6.3.3.1.

The combined time scale τ, which plays an integral role in the modeling of the heat flux, is a combination of both time scales:

$$\tau = \sqrt{\frac{k}{\varepsilon}\frac{\overline{\theta^2}}{\varepsilon_\theta}}. \tag{6.16}$$

As mentioned above, two more transport equations for $\overline{\theta^2}$ and ε_θ are necessary to calculate this time scale. However, often an overly simplistic assumption that avoids an additional transport equation for ε_θ is used. This approach assumes a constant thermal to mechanical time scale ratio, denoted as $\mathcal{R} = \tau_\theta/\tau_m$, to provide information on the thermal time scale. With the typical value of $\mathcal{R} = 0.5$ [107, 43], it results in an algebraic expression for ε_θ:

$$\varepsilon_\theta = \frac{\varepsilon\overline{\theta^2}}{k}. \tag{6.17}$$

Moreover, applying this simplification into the mixed time-scale, Eq. 6.16, leads to the mechanical time scale:

$$\tau = \sqrt{\frac{k}{\varepsilon}\frac{\overline{\theta^2}}{\varepsilon_\theta}} \overset{\text{Eq. 6.17}}{=} \frac{k}{\varepsilon}. \tag{6.18}$$

Several studies [45, 109, 44] have shown that this assumption is appropriate for fluids with Pr number around unity, but fails when used for non-unity Pr numbers [125, 77]. Fig. 6.1 depicts dynamics of $\mathcal{R}$ in a turbulent channel flow for different Pr numbers based on DNS data. It clearly shows that this assumption is appropriate away from solid surfaces and only for fluids with Pr number around unity.

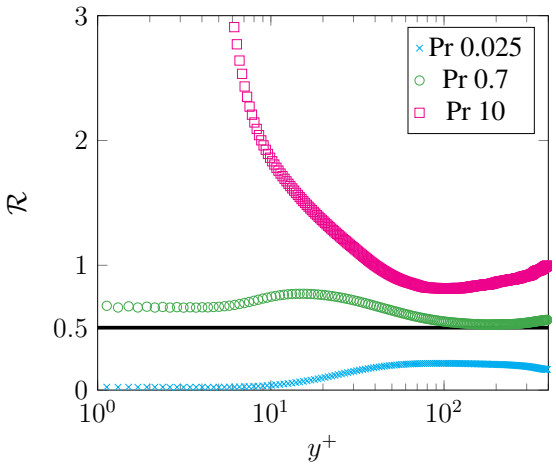

Figure 6.1: Ratio of thermal to mechanical time scale in turbulent channel flow for different Prandtl numbers obtained from DNS data [39]

6.3.3.3 Implicit Heat Flux Model

The implicit heat flux model takes advantage of existing known terms (particularly the production term $P_{\theta i}$) in the transport equation for the heat flux (Eq. 6.10). Application of the weak equilibrium hypothesis [95, 26] along with neglecting the destruction term $\varepsilon_{\theta i}$, leaves only the pressure scrambling term $\Phi_{\theta i}$ to model. The most common method to model this term is proposed in [18, 42]:

$$\Phi_{\theta i} = -\frac{1}{\tau}\left[\frac{1}{C_{t0}}\overline{\theta u_i} + C_{t4}a_{ij}\overline{\theta u_j}\right], \tag{6.19}$$

where $a_{ij} = \overline{u_i u_j}/k - 2/3\delta_{ij}$. The above model for $\Phi_{\theta i}$ results in the following form for implicit algebraic turbulent heat flux model:

$$\overline{\theta u_i} = -C_{t0}\tau\left[C_{t1}\overline{u_i u_j}\frac{\partial T}{\partial x_j} + C_{t2}\overline{\theta u_j}\frac{\partial U_i}{\partial x_j}\right] + C_{t4}C_{t0}a_{ij}\overline{\theta u_j}. \tag{6.20}$$

As mentioned before, the time scale τ is the mixed time scale that requires information of $\overline{\theta^2}$ and ε_θ. However, investigations concerning turbulent wall-bounded shear flows [107, 96, 43] use a simplified version of the model based on the constant thermal to mechanical time scale assumption with $\mathcal{R} = 0.5$. The simplified form of the model reads as follows:

$$\overline{\theta u_i} = -C_{t0}\frac{k}{\varepsilon}\left[C_{t1}\overline{u_i u_j}\frac{\partial T}{\partial x_j} + C_{t2}\overline{\theta u_j}\frac{\partial U_i}{\partial x_j}\right] + C_{t4}C_{t0}a_{ij}\overline{\theta u_j}. \tag{6.21}$$

Further, it was shown [107] that the model constants need to be modified to reach an acceptable level of accuracy for differnt Pr numbers, leading to a correlation for C_{t1}. This resulting model is referred to as *AHFM-NRG*, and will be used in this investigation. Model coefficients are summarized in Tab. 6.1.

Table 6.1: Coefficients for the implicit heat flux model *AHFM-NRG* as given by [107]

C_{t0}	C_{t1}	C_{t0}	C_{t4}
0.2	0.053 ln $(RePr)$-0.27	0.6	0.0

It should be noted that all before mentioned studies that use the *AHFM-NRG* model are limited to fluids with Pr numbers around or less than unity and do not provide data on some relevant statistical quantities such as the heat fluxes. Moreover, they do not address the sensitivity of the heat flux model with respect to the turbulence model used to described the flow field.

In this study, the *AHFM-NRG* model will be assessed extensively when applied to turbulent (attached) wall-bounded shear flows of different working fluid. Additionally, the *AHFM-NRG* model will be modified by incorporating the thermal time scale into the model, i.e. the mechanical time scale will be replaced by the mixed time scale. This will allow to identify relevance of the thermal time scale, as well as, if/how the implicit modeling methodology responds to the inclusion the thermal time scale.

6.3.3.4 Explicit Heat Flux Model

An explicit model for turbulent heat flux can be constructed based on the representation theorem. Assuming an incompressible, non-buoyant flow at high Reynolds numbers, the functional relationship for the turbulent heat flux is given as below [124]:

$$\overline{\theta u_i} = -f_i\left(\overline{u_i u_j}, S_{ij}, W_{ij}, T_{,j}, T, \varepsilon, \overline{\theta^2}\right), \tag{6.22}$$

where S_{ij} is the mean rate of strain and W_{ij} is the mean vorticity tensor.

For the determination of the model, it is assumed that anisotropies and turbulent time-scales are sufficiently small and that an equal balance between the effects of rotational and irrotational strain rates exists. Further details including a detailed derivation of the model are provided in [124]. The model reads as follows:

$$\overline{\theta u_i} = -\left[C_1\tau k\frac{\partial T}{\partial x_i} + C_2\tau\overline{u_i u_j}\frac{\partial T}{\partial x_j} + C_3\tau^2 k\frac{\partial U_i}{\partial x_j}\frac{\partial T}{\partial x_j} + C_4\tau^2\left(\overline{u_i u_k}\frac{\partial U_j}{\partial x_k} + \overline{u_j u_k}\frac{\partial U_i}{\partial x_k}\right)\frac{\partial T}{\partial x_j}\right]. \tag{6.23}$$

Here, τ can represent either the mechanical or thermal or mixed time scale. Choosing the mechanical time scale (following the same assumption as for the implicit

flux model, a constant ratio between mechanical and thermal time scale with $\mathcal{R} = 0.5$) leads to the proposed model in Younis et al. [124]:

$$\overline{\theta u_i} = -\left[C_1 \frac{k^2}{\varepsilon} \frac{\partial T}{\partial x_i} + C_2 \frac{k}{\varepsilon} \overline{u_i u_j} \frac{\partial T}{\partial x_j} + C_3 \frac{k^3}{\varepsilon^2} \frac{\partial U_i}{\partial x_j} \frac{\partial T}{\partial x_j} + C_4 \frac{k^2}{\varepsilon^2} \left(\overline{u_i u_k} \frac{\partial U_j}{\partial x_k} + \overline{u_j u_k} \frac{\partial U_i}{\partial x_k} \right) \frac{\partial T}{\partial x_j} \right]. \tag{6.24}$$

This model has not been tested in fully attached turbulent boundary layers. However, there is a recent investigation [64] that employs a slightly modified version to study non-isothermal rotating and non-rotating turbulent channel flow. The modified model reads as follows:

$$\overline{\theta u_i} = -\left[C_1 \frac{k^2}{\varepsilon} \frac{\partial T}{\partial x_i} + C_2 \frac{k}{\varepsilon} \overline{u_i u_j} \frac{\partial T}{\partial x_j} + C_4 \frac{k^2}{\varepsilon^2} \left(\overline{u_i u_k} \frac{\partial U_j}{\partial x_k} - \overline{u_j u_k} \frac{\partial U_i}{\partial x_k} \right) \frac{\partial T}{\partial x_j} \right]. \tag{6.25}$$

While this model offers remarkable improvements compared to the classical Reynolds Analogy based model, it is worth noting that only the mechanical time scale was included as well as only working fluids with Pr around unity were tested. This modified model will be used in this study and the model coefficients are given in Tab. 6.2.

Table 6.2: Coefficients for the explicit heat flux model as given by [64]

C_1	C_2	C_3	C_4
0.03	0.21	0.0	-0.105

Moreover, similar to the implicit heat flux model, sensitivity of the model with respect to the turbulence model and effect of considering the thermal time scale will be investigated. Inclusion of the thermal time scale into the model and using the mixed time scale will result in the following form of the model:

$$\overline{\theta u_i} = -\left[C_1 \tau k \frac{\partial T}{\partial x_i} + C_2 \tau \overline{u_i u_j} \frac{\partial T}{\partial x_j} + C_4 \tau^2 k \left(\overline{u_i u_k} \frac{\partial U_j}{\partial x_k} - \overline{u_j u_k} \frac{\partial U_i}{\partial x_k} \right) \frac{\partial T}{\partial x_j} \right]. \tag{6.26}$$

It should be noted that the model constants remain same after modifying the time scale, as discussed in the introduction.

6.4 Numerical Setup

6.4.1 Flow Configuration

The configuration is a fully developed turbulent channel flow as shown in Fig. 6.2. The size of the computational domain is $2\pi\delta, 2\delta, \pi\delta$, where δ is the channel half height. Different Prandtl numbers (0.025, 0.71, 10) have been considered based on the availability of reference (DNS) data. The details of all simulations are summarized in table 6.3.

Different mesh designs have been used for different Prandlt numbers and in particular, a different spacing in wall-normal direction is required to achieve appropriate distribution according to the findings in [125]. A simple-gradient spacing is used to create suitable distributions in the wall-normal direction, see [74] for details.

Note that the Reynolds number $Re_\tau = U_\tau\delta/\nu$ is defined based on the friction velocity at wall (U_τ) and channel half height δ. A constant pressure gradient is applied via an additional source term in the momentum equation to drive the flow to the targeted Reynolds number.

Periodic boundary conditions are imposed in the streamwise and spanwise directions, and no-slip condition is used at both walls. For the temperature field, a mean uniform heat flux at the walls, and periodic boundary conditions in the streamwise and the spanwise directions have been applied. Further, it is important to mention that the temperature variance and its dissipation are set to zero at the wall, i.e. $\overline{\theta^2}|_w$ and $\varepsilon_\theta|_w = 0$. The results are normalized by the δ, U_τ, the kinematic viscosity ν, the density ρ, and the friction temperature T_τ.

Three different model categories for the thermal field will be applied and assessed in this investigation. These include *TV-R*, *TV-E* and *TV-M*. *TV-R* uses solely the mechanical time scale along with the transport equation for $\overline{\theta^2}$, (Eq. 6.13), and the algebraic expression to determine ε_θ, (Eq. 6.17), for both the implicit and explicit heat

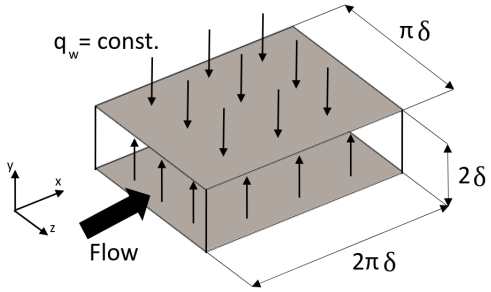

Figure 6.2: Sketch of horizontal channel flow configuration

flux model. *TV-E* makes use of the transport equation for ε_θ, (Eq. 6.12), to provide information for thermal dissipation while using only the mechanical time scale similar to category *TV-R*. The last category (*TV-M*) takes leverage of the mixed time scale τ defined by Eq. 6.16 in both turbulent heat flux models. All three categories along with corresponding equations are summarized in Tab. 6.4.

Table 6.3: Overview of flow variations

Re_τ	Pr	Reference Data	Resolution
395	0.025	Kawamura et al. [38]	$48 \times 36 \times 6$
395	0.71	Kawamura et al. [38]	$48 \times 36 \times 6$
395	10	Kawamura et al. [38]	$48 \times 36 \times 6$

Table 6.4: Overview of model categories

category	$\overline{\theta u_i}$-Equation		time scale	$\overline{\theta^2}$-Equation	ε_θ-Equation
	Implicit	Explicit			
TV-R	Eq. 6.21	Eq. 6.25	$\frac{k}{\varepsilon}$	Eq. 6.13	Eq. 6.17
TV-E	Eq. 6.21	Eq. 6.25	$\frac{k}{\varepsilon}$	Eq. 6.13	Eq. 6.12
TV-M	Eq. 6.20	Eq. 6.26	$\sqrt{\frac{k}{\varepsilon}\frac{\overline{\theta^2}}{\varepsilon_\theta}}$	Eq. 6.13	Eq. 6.12

6.4.2 Code Description

All numerical simulations presented in this chapter are performed using OpenFOAM-v2.2.2 with necessary modifications. The PISO-algorithm has been used

and second order schemes have been applied for velocity, turbulence and thermal quantities.

6.4.3 Verification and Comparison of Turbulence Models

In this section, the two turbulence models used in this investigation will be assessed and compared when applied to a fully developed turbulent channel flow. Mean velocity, turbulent kinetic energy and its dissipation are shown in Fig. 6.3. It can be seen, that the velocity is well predicted by both models. Turbulent kinetic energy k is slightly better predicted by *LA* model, while both models predict the dissipation with the same accuracy.

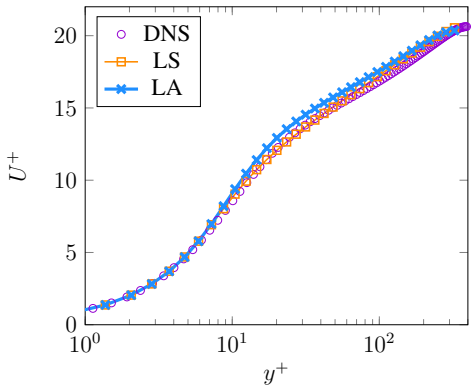

(a) Mean velocity

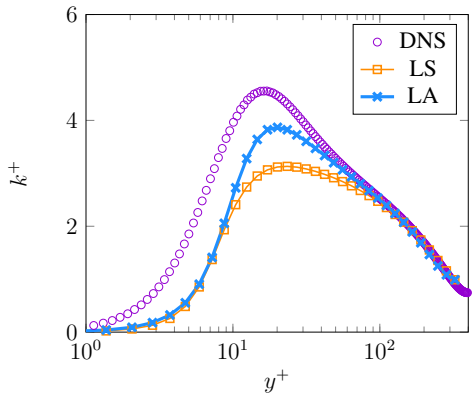

(b) Turbulent kinetic energy

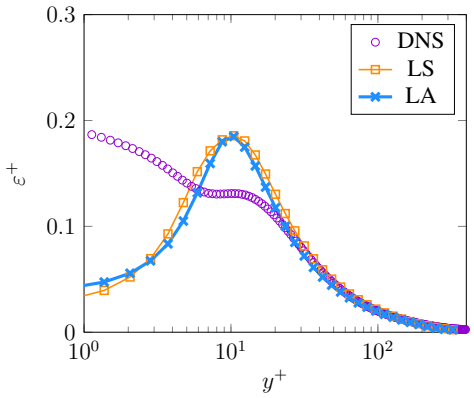

(c) Dissipation of turbulent kinetic energy

Figure 6.3: Re_τ= 395. Several momentum quantities

The Reynolds stresses play integral roles in prediction of the turbulent heat fluxes, as can be deduced from the governing equations (Eqs. 6.20 and 6.26).

Fig. 6.4 demonstrates the Reynolds stresses obtained from the two turbulence models. It can be observed that the normal stresses ($\overline{uu}, \overline{vv}, \overline{ww}$) are remarkably better predicted by the non-linear model (*LA*) and its impact on the heat flux prediction for both implicit and explicit methods will be investigated.

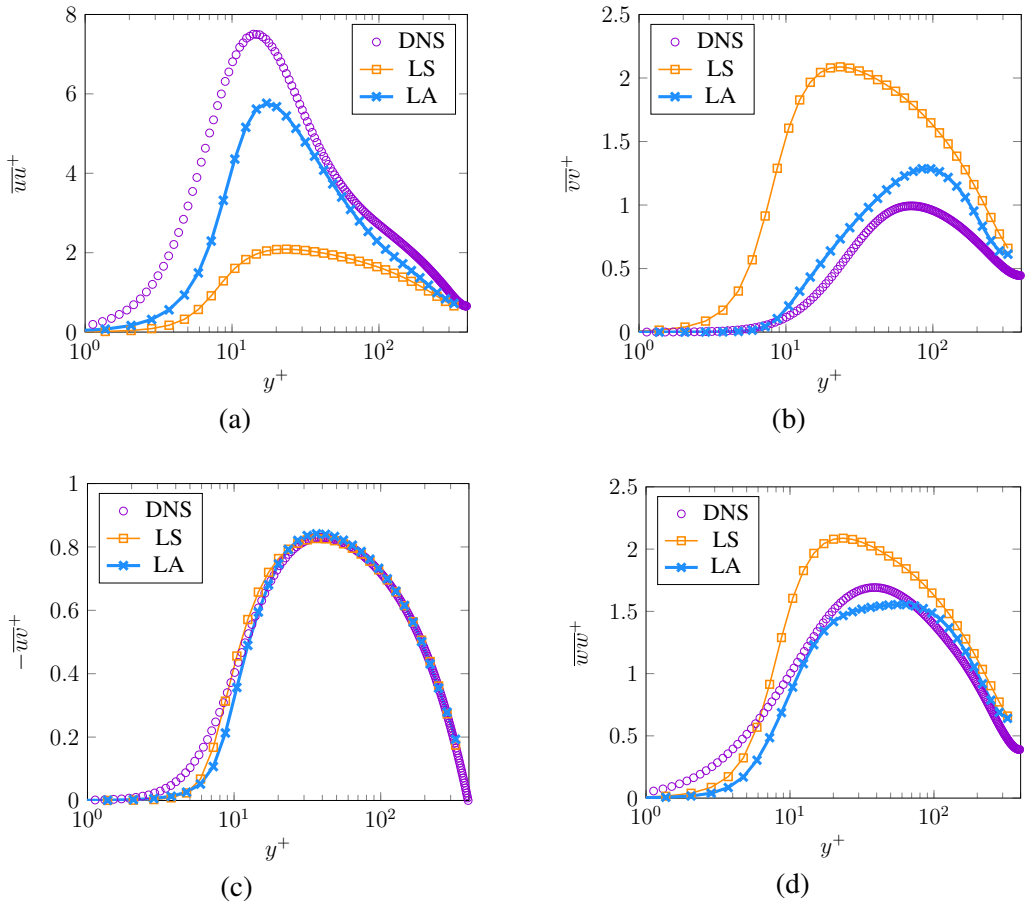

Figure 6.4: Re_τ= 395. Reynolds Stresses

6.5 Results and Discussion

In the current study, prediction capabilities of the implicit and explicit heat flux models for first and second order statistics for different Prandtl numbers are investigated, as described in Table 6.4. This covers a wide range of Pr numbers ($O(0.01)$, $O(1)$ and $O(10)$) when dynamics of heat transfer are significantly different. The main goal here is to provide a comprehensive comparison and analysis between the implicit and explicit methods to identify a reliable framework to capture the thermal field in turbulent wall-bounded shear flows.

All simulations have been conducted in steady state fashion using RANS based turbulence models described in section 6.3.1. Further, mesh convergence studies have been done for all simulations and only mesh independent results are presented.

6.5.1 Pr= 0.71

Pr= 0.71 differs strongly in its behavior compared to high and low Pr numbers. For this particular Pr number, the thermal and momentum boundary layers overlay and thus, it is expected that a constant value (usually 0.5) for the ratio of mechanical to thermal time scale works reasonably well, as also shown in [45, 109, 44]. It follows that results from all three model categories (*TV-R*, *TV-E* and *TV-M*) should share a lot of similarity, which will be investigated here.

6.5.1.1 Implicit Heat Flux Model

6.5.1.1.1 Mean Temperature

Fig. 6.5a presents mean temperatures obtained for Pr = 0.71 at Re_τ = 395 for *TV-R* and *TV-E*. It should be noted that both models result in the same temperature profile, since the temperature equation is independent of $\overline{\theta^2}$ and ε_θ, see section 6.3.3.3 for details. The mean temperature is not well captured irrespective of the turbulence model used to capture the flow field. It appears that the implicit model does not respond in a consistent manner to improvements of flow field quantities, provided by the non-linear turbulence model *LA*. This inconsistent behavior is also presented in Fig. 6.6, where accuracy of mean temperature varies significantly, even if turbulence models with similar prediction capabilities are used to predict the flow field. Results shown in Fig. 6.6 are obtained with three different linear-eddy viscosity turbulence models, i.e. *LS*, $k-\omega-SST$ [61] (denoted as *kO*) and Lam and Bremhorst's $k-\epsilon$ model [53] (denoted as *LB*). Although all three models predict the flow quantities at comparable level of accuracy, there is remarkable differences in mean temperature. Therefore, it is possible to find some turbulence models such that mean temperature matches the DNS data, similar to one proposed in [107]. In fact, this analysis demonstrates that the

implicit formulation for the turbulent heat flux fails to establish a consistent coupling with the flow field.

6.5.1.1.1.1 Effects of Mixed Time Scale

Fig. 6.5b presents mean temperatures for Pr = 0.71 at Re_τ = 395 obtained by *TV-M* with both turbulence models. Including the thermal time scale into the heat flux equation modifies the prediction of the linear turbulence model (*LS*) (however, not in a consistent manner), while results obtained using the non-linear turbulence model (*LA*) remain unaffected, which is a somehow expected behavior since mechanical and thermal time scale show similar behaviors. Thus, it suggests that an appropriate and consistent response to the inclusion of the thermal time scale may require advanced turbulence models to provide accurate prediction for the Reynolds stress tensor.

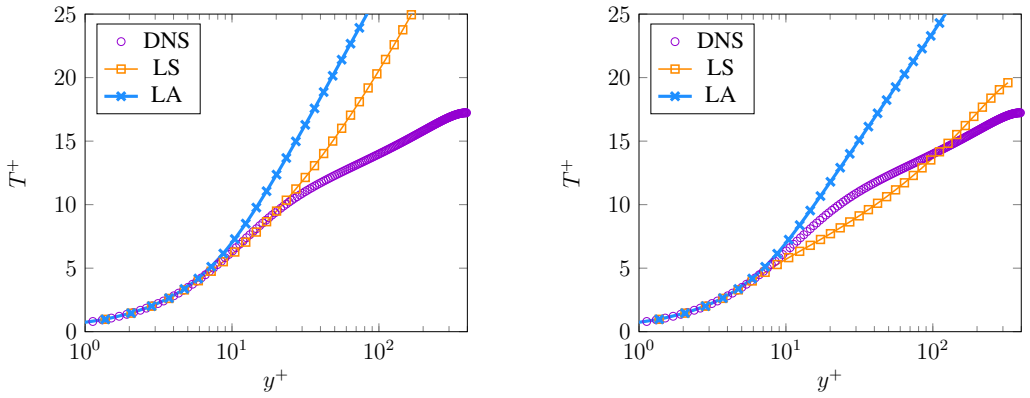

(a) *TV-R* and *TV-E* (b) *TV-M*

Figure 6.5: Mean temperature obtained by *TV-R*, *TV-E* and *TV-M* for Pr= 0.71 at Re_τ= 395 with the implicit heat flux model

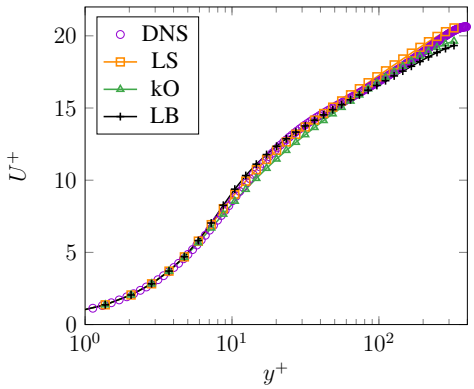

(a) Mean velocity

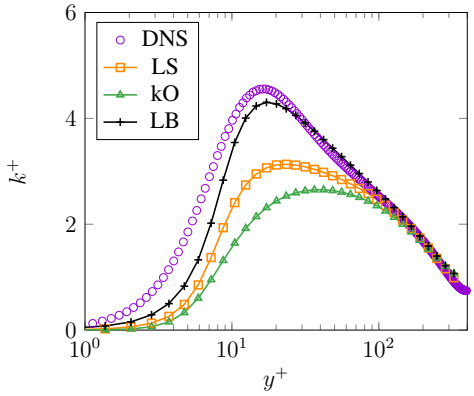

(b) Turbulent kinetic energy

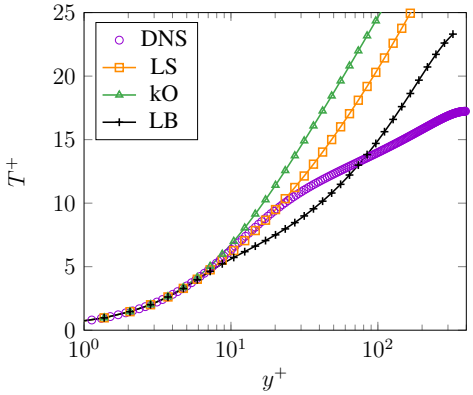

(c) Mean temperature

Figure 6.6: Mean velocity, turbulent kinetic energy and mean temperature obtained by *TV-R* for Pr= 0.71 at Re_τ= 395 with the implicit heat flux model

6.5.1.1.2 Temperature Variance

Unlike the mean temperature, there are some differences in results obtained by *TV-E* and *TV-R* for temperature variance (equivalently, the rms value of temperature fluctuations denoted as θ_{rms}), see Section 6.4. Regarding *TV-R*, it should be noted that irrespective of the turbulence model, the implicit heat flux model fails to capture the general behavior of θ_{rms}, see Fig. 6.7a. In particular, the peak around $y^+ \approx 10$ is mispredicted and followed by a wrong tendency towards channel center. Furthermore, using an extra transport equation for the thermal dissipation ε_θ (*TV-E*) only provides marginal improvements in the near-wall region ($y^+ < 10$), compared to *TV-R*, while exacerbates the situation in the core region. The discrepancies mainly trace back to the misprediction of the mean temperature (shown in Fig. 6.5a), since mean temperature gradient is a main contributor in production of $\overline{\theta^2}$, as shown in Eq. 6.13. Moreover, it

appears that application of the more advanced turbulence model (*LA*) does not improve the prediction accuracy for temperature variance significantly. The results may be indicative of some fundamental issues in the implicit model for turbulent heat flux in its current form (*AHFM-NRG*) to capture the second order statistics at an acceptable level of accuracy.

6.5.1.1.2.1 Effects of Mixed Time Scale

In order to investigate effect of mixed time scale on the model prediction capability of temperature variance, the mixed time scale was included into the implicit heat flux model, i.e. *TV-M* approach was used to capture the temperature variance. As expected for fluids with Pr around unity, no significant improvements (sensitivity) was observed, Fig. 6.7c.

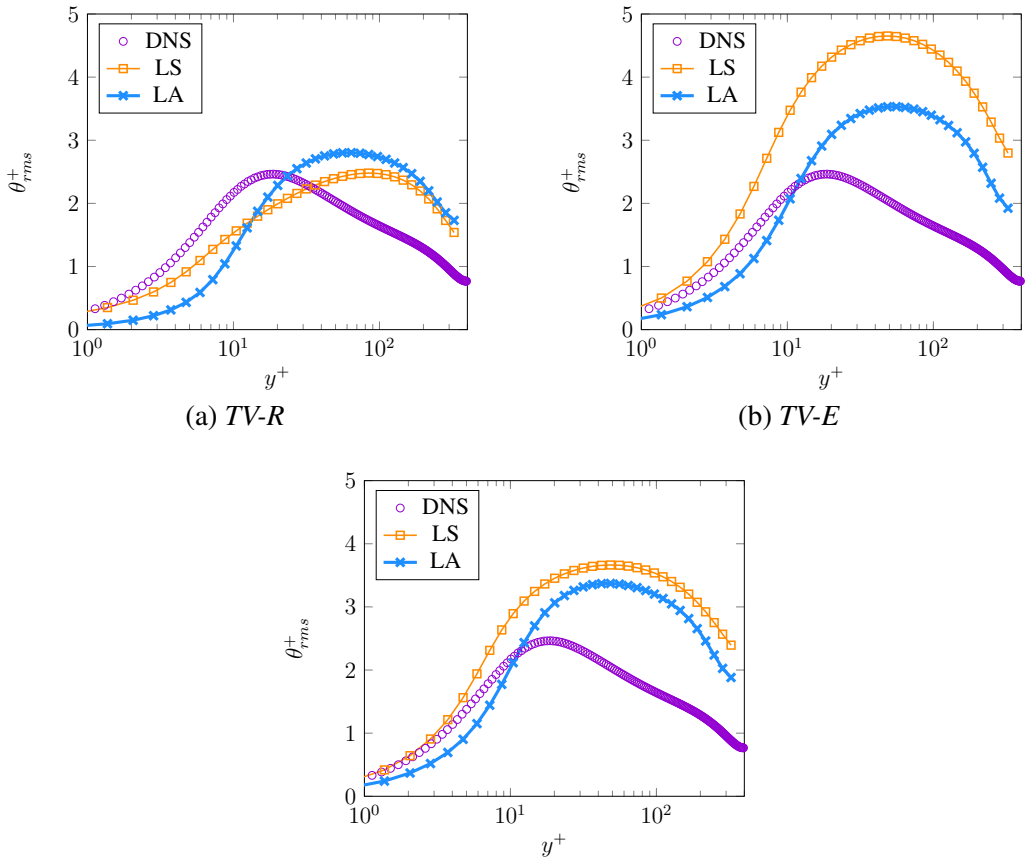

(a) *TV-R* (b) *TV-E*

(c) *TV-M*

Figure 6.7: Temperature variance obtained by *TV-R*, *TV-E* and *TV-M* for Pr= 0.71 at Re_τ= 395 with the implicit heat flux model

6.5.1.1.3 Dissipation of Temperature Variance

Results for the dissipation of temperature variance ε_θ under the assumption of a constant time scale ratio ($\mathcal{R} = 0.5$) are presented in Fig. 6.8a. The thermal dissipation rate is mispredicted, particularly in the near-wall region because of the assumption of a constant thermal to mechanical timescale ratio ($\mathcal{R} = 0.5$). This assumption describes ε_θ based on ε, which leads to a misprediction of ε_θ in near-wall region, similar to ε.

Including the transport equation for ε_θ (*TV-E*) leads to some degree of improvement in the near-wall region, most notably when the non-linear turbulence model (*LA*) was used, Fig. 6.8b.

6.5.1.1.3.1 Effects of Mixed Time Scale

Results obtained for ε_θ using the mixed time scale in the implicit heat flux model (*TV-M*) are shown in Fig. 6.8c. As expected, for fluids with Pr number around unity, inclusion of the mixed time does not provide remarkable improvements.

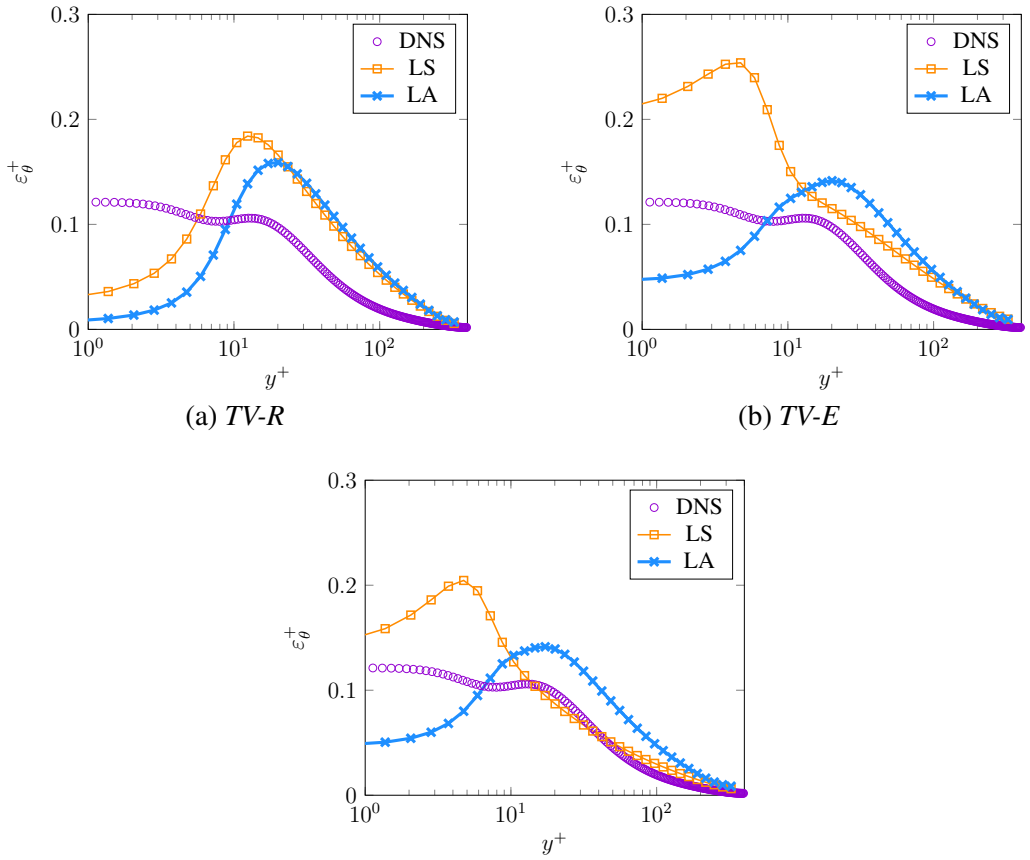

(a) *TV-R* (b) *TV-E*

(c) *TV-M*

Figure 6.8: Thermal dissipation obtained by *TV-R*, *TV-E* and *TV-M* for Pr= 0.71 at Re_τ= 395 with the implicit heat Flux model

6.5.1.1.4 Streamwise Heat Flux

The streamwise heat fluxes obtained by *TV-R* and *TV-E* approaches are shown in Fig. 6.9a. Similar to mean temperature, the heat fluxes are independent of temperature variance and its dissipation. Therefore, there is no difference between results obtained by *TV-R* and *TV-E* models. The streamwise heat flux is strongly mispredicted by the implicit heat flux model regardless of the turbulence model used to provide flow field quantities. In fact, it appears that the implicit heat flux model shows only a little sensitivity to the heat flux in the homogeneous direction.

6.5.1.1.4.1 Effects of Mixed Time Scale

Results obtained for the streamwise heat flux after inclusion of the mixed time scale are presented in Fig. 6.9b, which show very marginal improvements. These results

might suggest that the implicit formulation suffers from a significant shortcoming in predicting the heat flux in homogeneous directions.

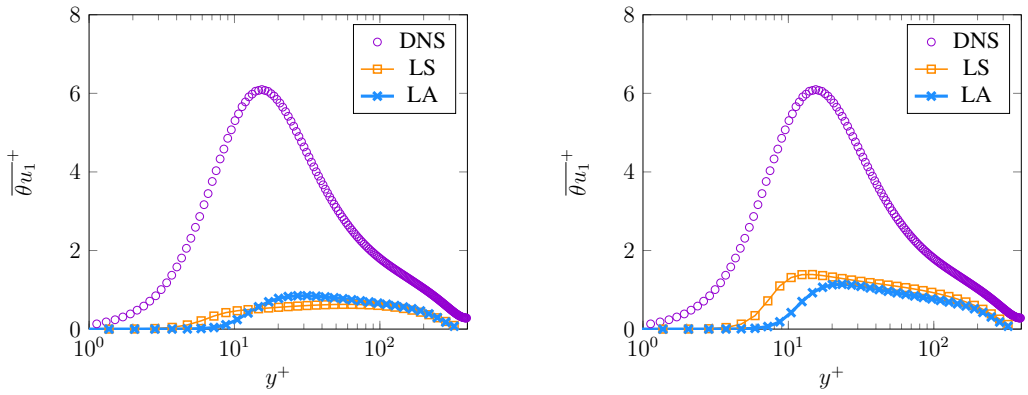

(a) *TV-R* and *TV-E* (b) *TV-M*

Figure 6.9: Streamwise heat flux obtained by *TV-R*, *TV-E* and *TV-M* for Pr= 0.71 at Re_τ= 395 with the implicit heat flux model

6.5.1.1.5 Wall-Normal Heat Flux

Wall-normal heat fluxes obtained by *TV-R* and *TV-E* approaches are shown in Fig. 6.10a. As shown, the implicit model is capable of capturing the wall-normal heat flux behavior correctly. It is worth noting that it seems that the near-wall region is better predicted with the linear turbulence model. However, this superiority is deemed to be an accident, given the lower quality provided by the linear model for flow field quantities.

6.5.1.1.5.1 Effects of Mixed Time Scale

Inclusion of the mixed time scale (*TV-M*) appears to provide slight improvements, when the non-linear turbulence model was used, see Fig. 6.10b. This is very much expected as the thermal and mechanical time scales exhibit very similar dynamics for fluids with Pr around unity. In contrast, the inclusion modifies the heat flux obtained when the linear turbulence model is used, which might suggest an inconsistent feature of the implicit formulation, confirming the previous finding regarding mean temperature, i.e. a consistent response from the implicit heat flux model requires advanced turbulence models to provide accurate prediction of the flow field.

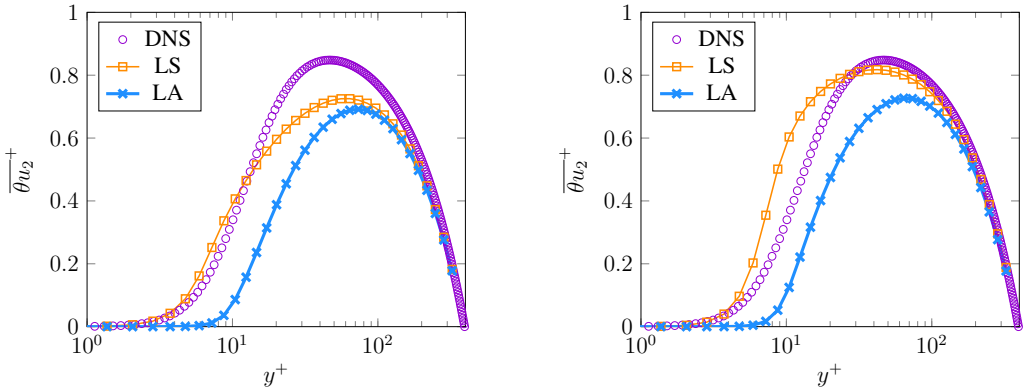

(a) *TV-R* and *TV-E* (b) *TV-M*

Figure 6.10: Wall-normal heat flux obtained by *TV-R*, *TV-E* and *TV-M* for Pr= 0.71 at Re_τ= 395 with the implicit heat flux model

6.5.1.1.6 Thermal to Mechanical Time Scale

Fig. 6.11 demonstrates the ratio of thermal to mechanical time scale ($\mathcal{R}$) obtained by different approaches (*TV-E* and *TV-M*). As can be seen, there is no change in the model prediction after inclusion of the mixed time scale when the non-linear turbulence model is used to describe the flow field, i.e. the model responds consistently to inclusion of the thermal time scale for fluids with Pr number around unity. Additionally, results suggest that an additional transport equation might be necessary to predict the thermal time scale more accurately when compared to the traditional assumption of a constant thermal to mechanical time ratio, even for fluids with Pr numbers around unity, however, in conjunction with an advanced turbulence model.

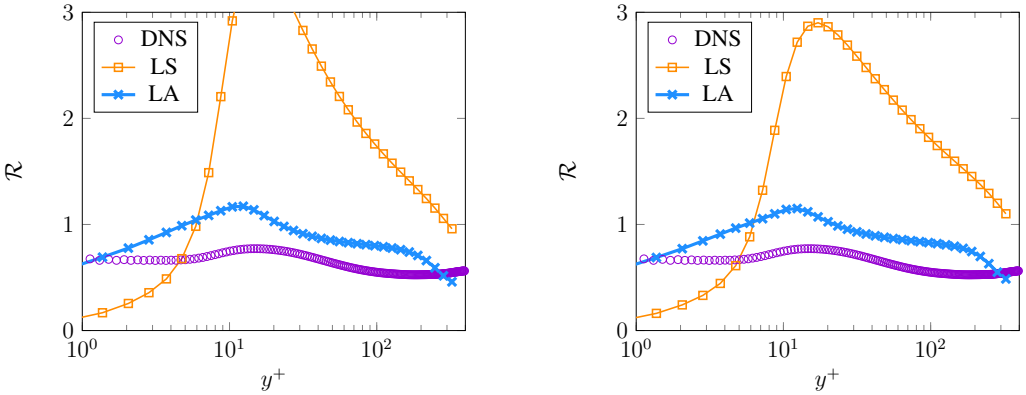

(a) *TV-E* (b) *TV-M*

Figure 6.11: Ratio of thermal to mechanical time scale obtained by *TV-R*, *TV-E* and *TV-M* for Pr= 0.71 at Re_τ= 395 with the implicit heat Flux model

6.5.1.2 Explicit Heat Flux Model

6.5.1.2.1 Mean Temperature

In Fig. 6.12a, the mean temperatures obtained by the explicit heat flux model using both turbulence models within *TV-R* and *TV-E* approaches are shown. The result using the linear turbulence model (*LS*) underestimate the profile strongly, while the result using the non-linear turbulence model (*LA*) is in good agreement with the reference data. More importantly, in comparison to the implicit heat flux model, the explicit heat flux model shows a consistent sensitivity to the turbulence model, i.e. the more accurate the flow field, the more accurate the thermal field.

6.5.1.2.1.1 Effects of Mixed Time Scale

Introducing the thermal time scale into the explicit heat flux model (*TV-M*) does not seem to have a remarkable effect, which is expected for fluids with Pr number around unity (Fig. 6.12b).

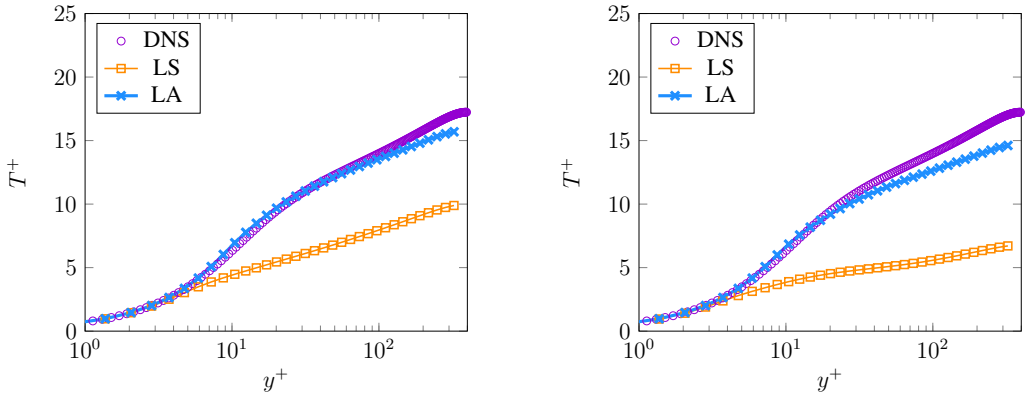

(a) *TV-R* and *TV-E* (b) *TV-M*

Figure 6.12: Mean temperature obtained by *TV-R*, *TV-E* and *TV-M* for Pr= 0.71 at Re_τ= 395 with the explicit heat flux model

6.5.1.2.2 Temperature Variance

Temperature variances (θ_{rms}) obtained by *TV-R* and the explicit heat flux model are shown in Fig. 6.13a. As can be seen, the explicit model shows sensitivity to the accuracy of the flow field and captures the trend of θ_{rms} accurately when the non-

linear turbulence model (*LA*) was used, while using the linear model (*LS*) leads to a misprediction of θ_{rms}. Inclusion of an extra transport equation for ε_θ (*TV-E*) seems to affect the results obtained with the linear turbulence model. While some improvement can be observed, the tendency of θ_{rms} is not well captured, particularly in the core region, see Fig. 6.13b.

6.5.1.2.2.1 Effects of Mixed Time Scale

Inclusion of the mixed time scale, shows only slightly improvements in near-wall region, when the non-linear turbulence model was applied. However, it appears that the explicit heat flux model is very sensitive to the turbulence model used to capture the flow field and responses inappropriately to the inclusion of the mixed time scale when the linear turbulence model is used.

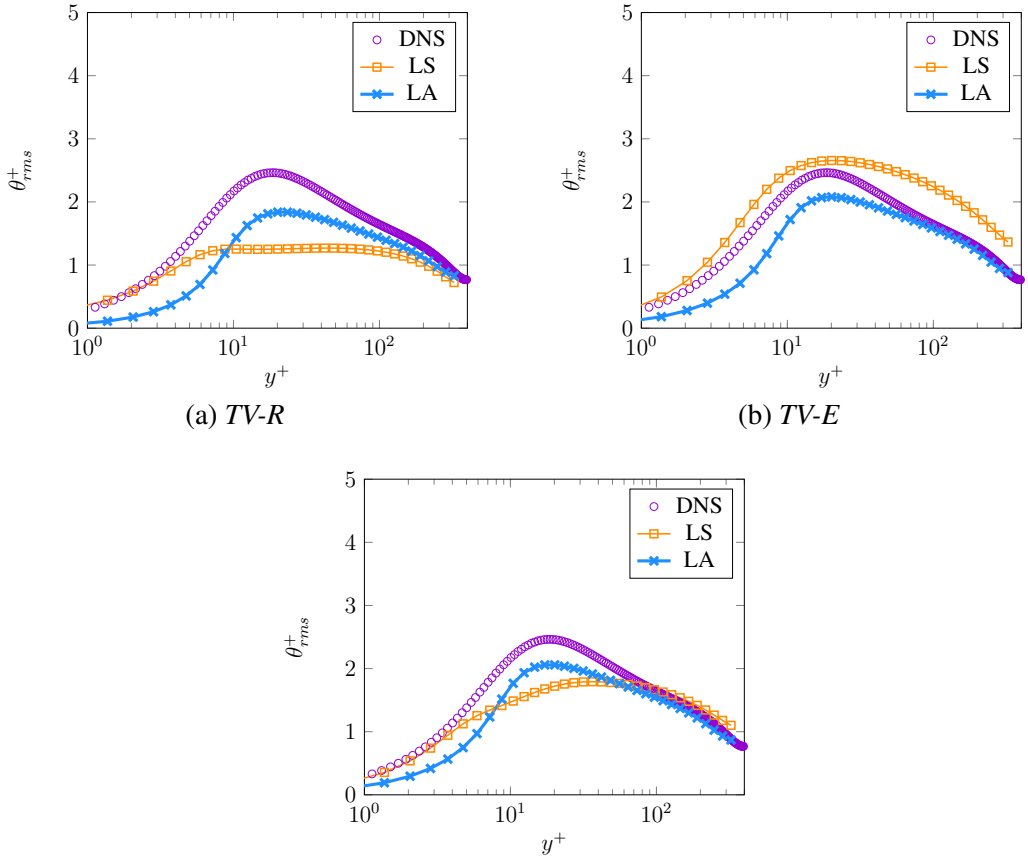

(a) *TV-R* (b) *TV-E*

(c) *TV-M*

Figure 6.13: Temperature rms obtained by *TV-R*, *TV-E* and *TV-M* for Pr= 0.71 at Re_τ= 395 with the explicit heat flux model

6.5.1.2.3 Dissipation of Temperature Variance

Results for the dissipation of temperature variance obtained by *TV-R* and *TV-E* are presented in Fig. 6.14a and 6.14b. There is similar behavior in the wall region ($y^+ < 10$), irrespective of the approach, while some improvement can be seen in the core region, when an additional transport equation for ε_θ is solved (*TV-E*).

6.5.1.2.3.1 Effects of Mixed Time Scale

As expected for fluids with Pr number around unity, the explicit model does not provide any improvement (sensitivity) when the mixed time scale is used with the non-linear turbulence model. However, the opposite is true when the linear model is used (Fig. 6.14c) leading to a worse prediction.

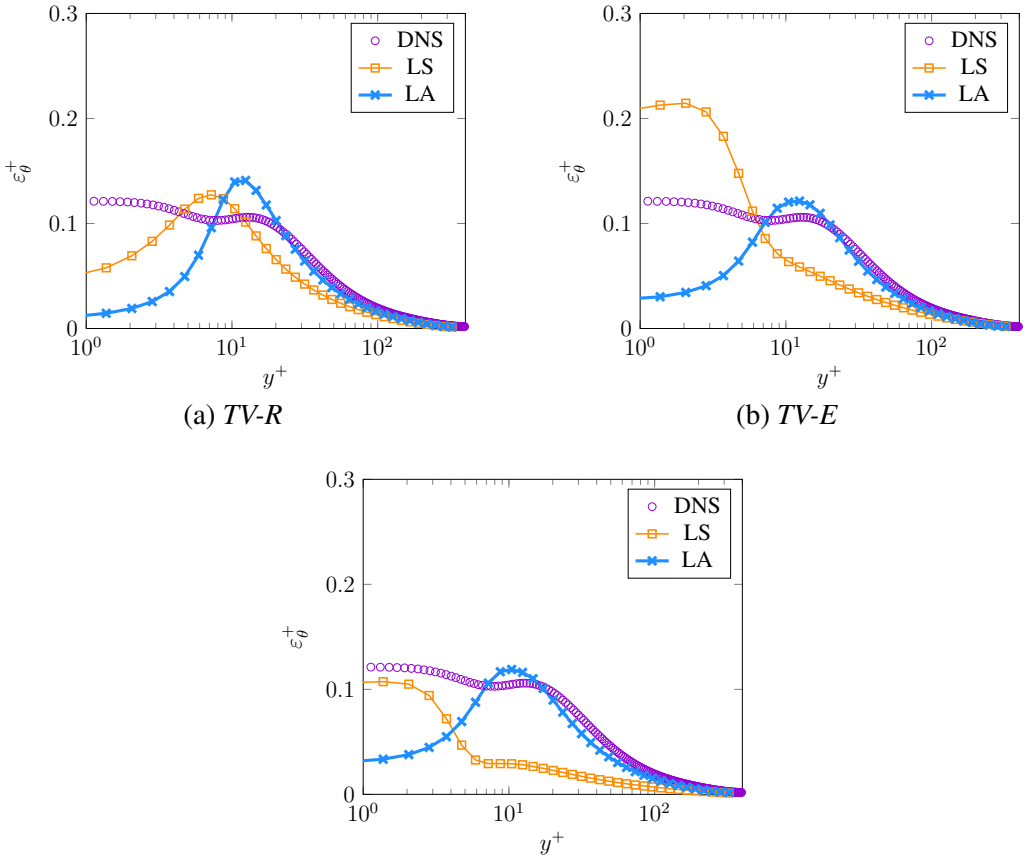

(a) *TV-R* (b) *TV-E*

(c) *TV-M*

Figure 6.14: Dissipation of temperature variance obtained by *TV-R*, *TV-E* and *TV-M* for Pr= 0.71 at Re_τ= 395 with the explicit heat flux model

6.5.1.2.4 Streamwise Heat Flux

Fig. 6.15a shows the streamwise heat fluxes obtained by *TV-R* and *TV-E*. In contrast to the implicit model (Fig. 6.9a), the explicit heat flux model demonstrates potential capability to capture the streamwise heat flux. In particular, the model shows a decent capability, when the non-linear turbulence is used. This may suggest that an accurate prediction of the flow field along with an appropriate model for the heat flux are essential to address the longstanding shortcoming of heat flux models in predicting heat fluxes in homogeneous directions.

6.5.1.2.4.1 Effects of Mixed Time Scale

Using the mixed time scale in the explicit heat flux model (*TV-M*) does offer marginal improvements (Fig. 6.15b). In particular, the model shows some potential capability, when the non-linear turbulence is used along with the mixed time scale. Again, the opposite is true for the linear turbulence model, leading to a much worse prediction.

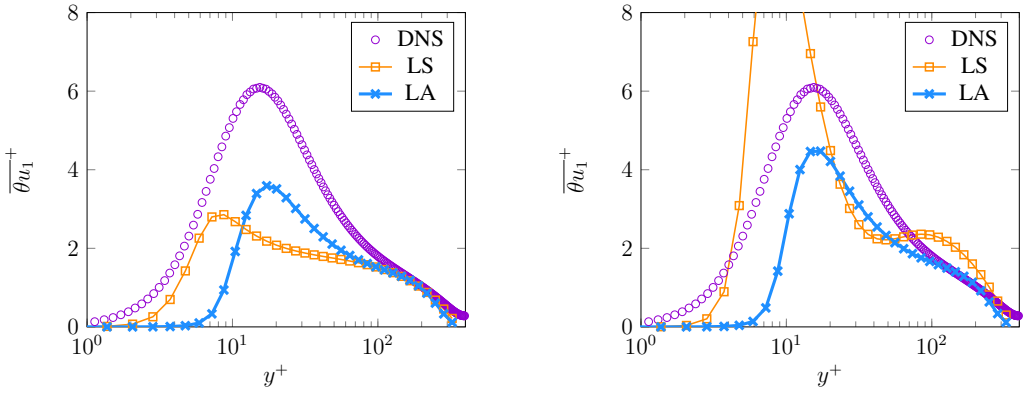

(a) *TV-R* (b) *TV-M*

Figure 6.15: Streamwise heat flux obtained by *TV-R*, *TV-E* and *TV-M* for Pr= 0.71 at Re_τ= 395 with the explicit heat flux model

6.5.1.2.5 Wall-Normal Heat Flux

Fig. 6.16a depicts the wall-normal heat fluxes obtained by *TV-R* and *TV-E*. It can be observed that the wall-normal heat flux can be accurately predicted, if the flow field is accurately captured, i.e. the non-linear turbulence model (*LA*) is used.

6.5.1.2.5.1 Effects of Mixed Time Scale

As expected for fluids with Pr number around unity, using the mixed time scale does not provide any improvements. This consistent behavior is very much expected. However, it should be noted that if the flow field is not predicted at an acceptable level of accuracy, the heat flux model could potentially deliver a remarkable discrepancy as shown in Fig. 6.15b, as demonstrated by the linear turbulence model (*LS*).

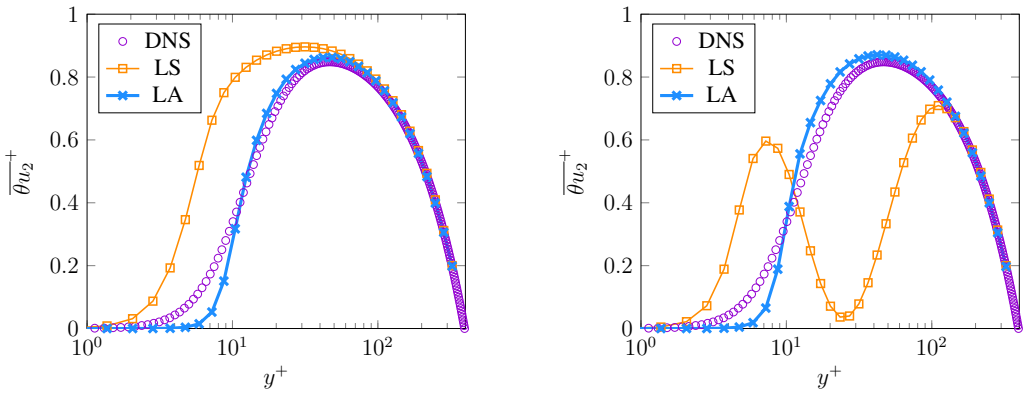

(a) *TV-R* and *TV-E* (b) *TV-M*

Figure 6.16: Wall-normal heat flux obtained by *TV-R*, *TV-E* and *TV-M* for Pr= 0.71 at Re_τ= 395 with the explicit heat flux model

6.5.1.2.6 Thermal to Mechanical Time Scale

Fig. 6.17 shows the ratios of thermal to mechanical time scale obtained by different approaches, *TV-E* and *TV-M*. It clearly can be deduced that the explicit heat flux model has the capability to provide accurate results if the flow field is accurately captured, and reliable information (via an additional transport equation for ε_θ) for thermal time scale is provided.

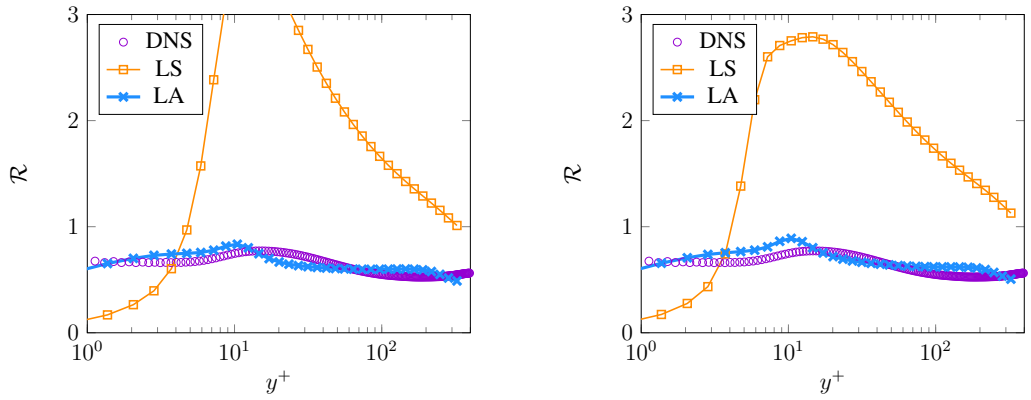

(a) *TV-E* (b) *TV-M*

Figure 6.17: Ratio of thermal to mechanical time scale obtained by *TV-R*, *TV-E* and *TV-M* for Pr= 0.71 at Re_τ= 395 with the explicit heat flux model

6.5.2 Pr= 0.025

In contrast to fluids with Pr numbers around unity, thermal boundary layers of fluids with Pr numbers substantially less than unity show different characteristics compared to the velocity (hydrodynamics) boundary layer. In particular, thermal boundary layers of low Pr number fluids are thicker than hydrodynamic boundary layers, leading to much smaller thermal time scales. Therefore, as expected and confirmed in [126, 125], the classical Reynolds Analogy based models face severe challenges in predicting the turbulent thermal field of low Pr number fluids.

In this study, the most recent version of the implicit heat flux model [107] (modified particularly to deal with low Pr number fluids), along with the explicit heat flux model proposed in [64] are applied to assess their capabilities in predicting thermal field of low Pr number fluids in turbulent wall-bounded shear flows.

6.5.2.1 Implicit Heat Flux Model

6.5.2.1.1 Mean Temperature

Fig. 6.18a presents the mean temperatures obtained for Pr = 0.025 and Re_τ = 395 by *TV-R* and *TV-E*. The mean temperature is overpredicted similarly, irrespective of turbulence model. Note that there is no difference between *TV-R* and *TV-E* for mean temperature due to their mathematical formulation. Furthermore, it can be observed

that improving the prediction accuracy for the flow field, offered by the non-linear turbulence model (*LA*), does not lead to any improvement for the mean temperature. This can be explained by inspecting the transport equation for the mean temperature in a dimensionless form:

$$\underbrace{\frac{DT^*}{Dt}}_{M_D} = \frac{\partial}{\partial x_i^*}\Big[\Big(\underbrace{\frac{1}{PrRe_\tau}\frac{\partial T^*}{\partial x_i^*}}_{D_T}\Big) - \underbrace{\frac{1}{Re_\tau}\overline{\theta u_i}^*}_{H_F}\Big], \tag{6.27}$$

where M_D is the material derivative, D_T the molecular thermal diffusion, and H_F the turbulent heat flux.

For low Pr number fluids the molecular diffusion term dominates the turbulent thermal diffusivity ($D_T >> H_F$); except for very high Reynolds number flows, which is not the case here. This leads to the conclusion that the mean temperature prediction accuracy is somehow independent of how the turbulent heat flux is modeled.

6.5.2.1.1.1 Effect of Mixed Time Scale

Results for the mean temperature using the mixed time scale (*TV-M*) in the implicit heat flux model are shown in Fig. 6.18b. The inclusion of the thermal time scale does not modify the results. As discussed before, this is a somehow expected behavior since the turbulent heat flux is not playing a major role to predict the mean temperature.

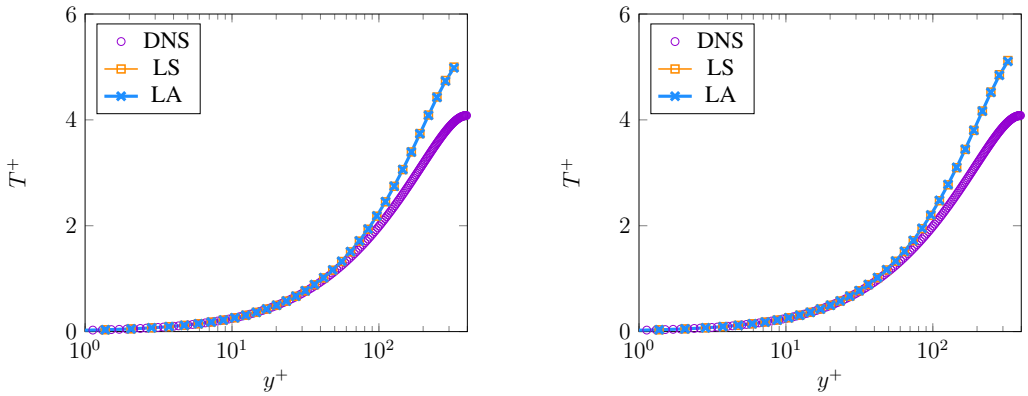

(a) *TV-R* and *TV-E* (b) *TV-M*

Figure 6.18: Mean temperature obtained by *TV-R*, *TV-E* and *TV-M* for Pr= 0.025 at Re_τ= 395 with the implicit heat flux model

6.5.2.1.2 Temperature Variance

Fig. 6.19a presents θ_{rms} obtained for Pr = 0.025 and Re_τ = 395 by *TV-R* approach using both turbulence models. The profile is underpredicted in the core region. Using an extra transport equation for ε_θ to provide more accurate data for thermal time scale (*TV-E*) leads to a decrease in prediction accuracy, Fig. 6.19b. This may suggest that the implicit heat flux model in its current formulation might not be able to capture second order thermal statistics at an acceptable level of accuracy. The discrepancies mainly trace back to the misprediction of the heat fluxes (shown in Fig. 6.21a and 6.22a), since the fluxes are main contributors in production of $\overline{\theta^2}$, as shown in Eq. 6.13.

6.5.2.1.2.1 Effect of Mixed Time Scale

As can be seen in Fig. 6.19c, there is no remarkable sensitivity to the inclusion of the thermal time scale; very similar to what observed for the mean temperature. This again traces back to the inaccurate prediction of heat fluxes (Fig. 6.21 and 6.21).

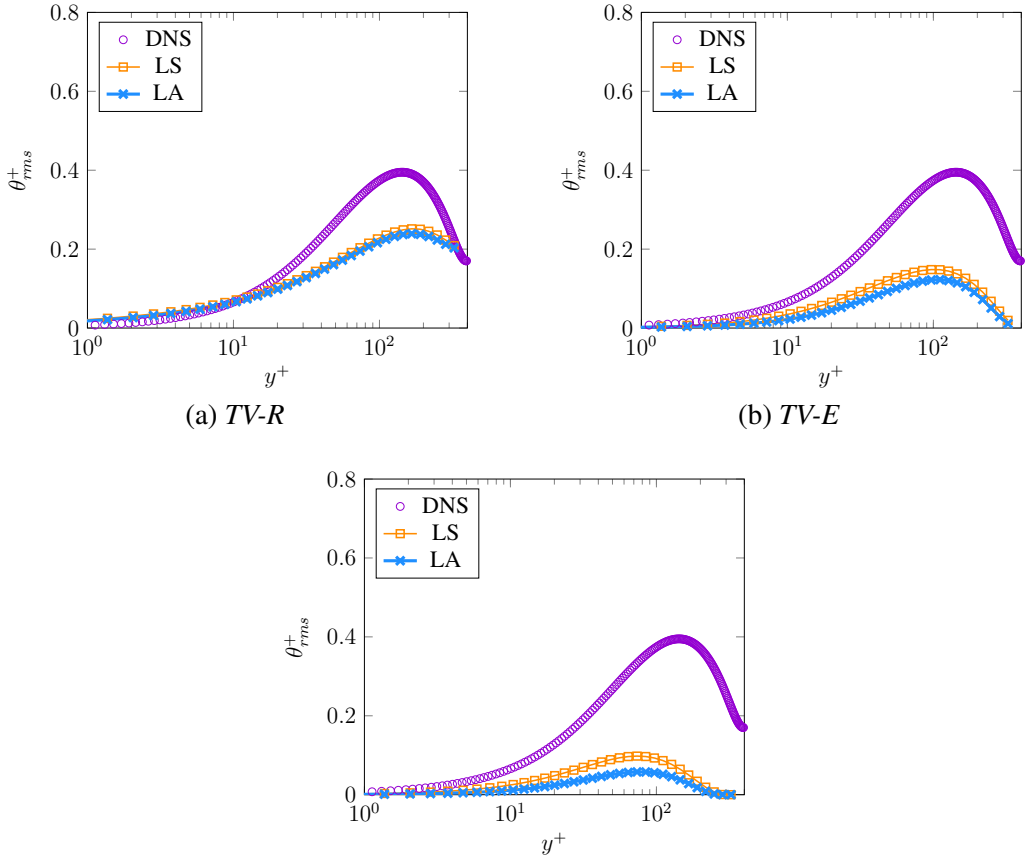

(a) *TV-R* (b) *TV-E*

(c) *TV-M*

Figure 6.19: Temperature rms obtained by *TV-R*, *TV-E* and *TV-M* for Pr= 0.025 at Re_τ= 395 with the implicit heat flux model

6.5.2.1.3 Dissipation of Temperature Variance

Results for the dissipation of temperature variance under the assumption of a constant time scale ratio (*TV-R*) are presented in Fig. 6.20a. The thermal dissipation rate ε_θ is mispredicted over the whole domain, indicating an inaccuracy of the assumption of a constant thermal to mechanical timescale ratio ($\mathcal{R} = 0.5$). Including the transport equation for ε_θ (*TV-E*), Fig. 6.20b, does not lead to any improvement and in fact, there is no sensitivity observed. This is mainly due to the inability of the implicit model to capture heat fluxes (discussed in the following), since interaction between the heat flux and mean temperature gradient is a major production mechanism (Eq. 2.11).

6.5.2.1.3.1 Effect of Mixed Time Scale

Results obtained for ε_θ using the mixed time scale in the implicit heat flux model are shown in Fig. 6.20c. As expected, inclusion of the mixed time scale does not provide any improvements with the current form of the implicit model, given inability of the model capturing the heat fluxes.

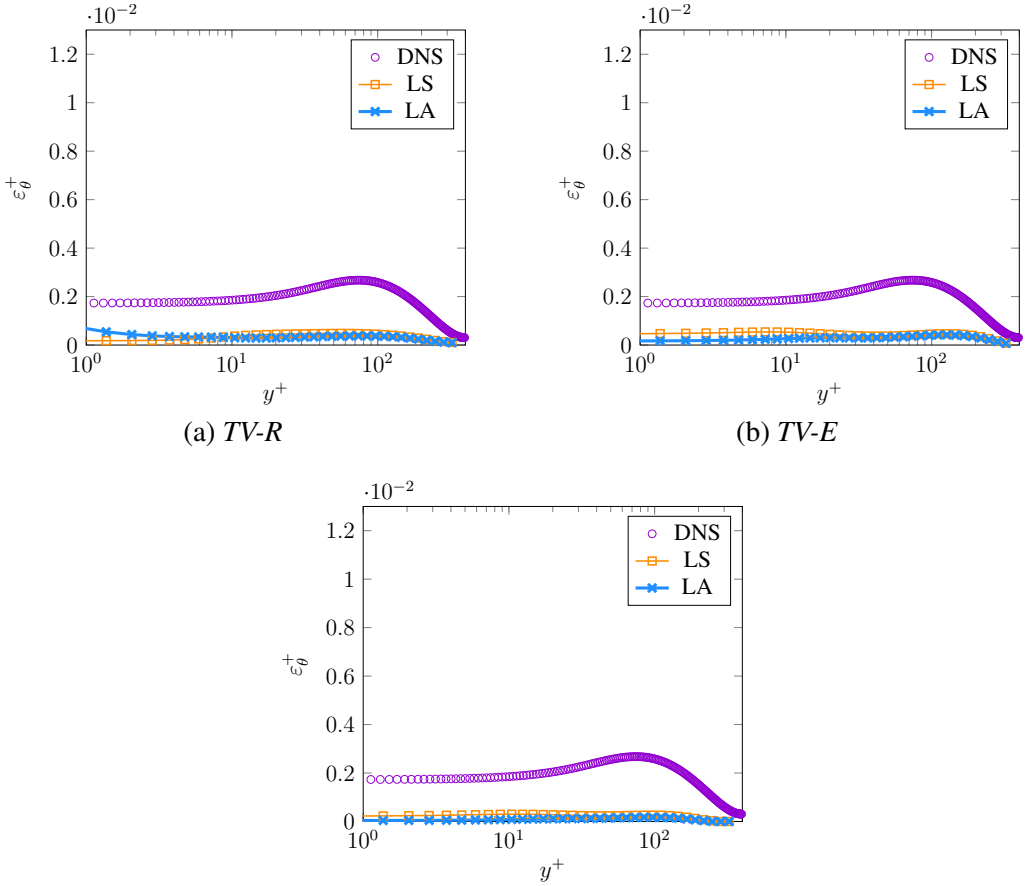

(a) *TV-R* (b) *TV-E*

(c) *TV-M*

Figure 6.20: Dissipation of temperature variance obtained by *TV-R*, *TV-E* and *TV-M* for Pr= 0.025 at Re_τ= 395 with the implicit heat flux model

6.5.2.1.4 Streamwise Heat Flux

The streamwise heat fluxes obtained by *TV-R* and *TV-E* are shown in Fig. 6.21a. Similar to calculations for Pr = 0.71, the streamwise heat flux is strongly mispredicted by the implicit heat flux model, regardless of the turbulence model. The implicit flux model shows no sensitivity towards the heat flux in homogeneous direction.

6.5.2.1.4.1 Effect of Mixed Time Scale

Results obtained for the streamwise heat flux after inclusion of the mixed time scale (*TV-M*) are presented in Fig. 6.21b, which show no improvement. The results obtained for the streamwise heat flux strongly point to a fundamental shortcoming of the implicit formulation as used here.

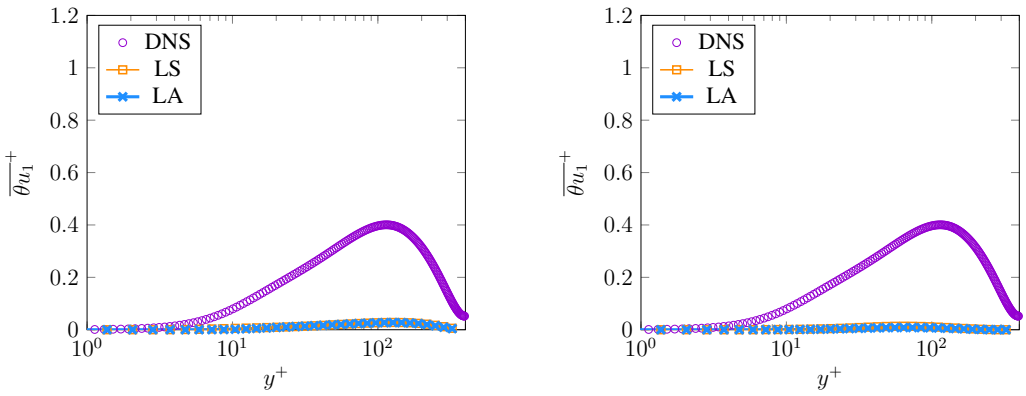

(a) *TV-R* and *TV-E* (b) *TV-M*

Figure 6.21: Streamwise heat flux obtained by *TV-R*, *TV-E* and *TV-M* for Pr= 0.025 at Re_τ= 395 with the implicit heat flux model

6.5.2.1.5 Wall-Normal Heat Flux

Wall-normal heat fluxes obtained by *TV-R* and *TV-E* are shown in Fig. 6.22. In contrast to Pr = 0.71, the model is not capable of capturing the wall-normal heat flux behavior correctly. This may suggest that the *AHFM-NRG*-model proposed in [107] has been designed to predict the first order statistics (mean temperature) using a particular turbulence model.

As discussed before, incapability of the implicit model to capture turbulent heat flux leads to significant inaccuracy of other thermal quantities such as ε_θ and θ_{rms}. In particular, the heat fluxes are major contributors to production of $\overline{\theta^2}$ (Eq. 6.12) and ε_θ (Eq. 6.12) and thus, a inability to predict heat fluxes leads to misprediction of other thermal quantities.

6.5.2.1.5.1 Effect of Mixed Time Scale

Inclusion of the mixed time scale (*TV-M*) does not appear to provide any improvements obtained with both turbulence models, Fig. 6.22b. This is very much expected since the model does not present any capability to predict the heat flux in the first place.

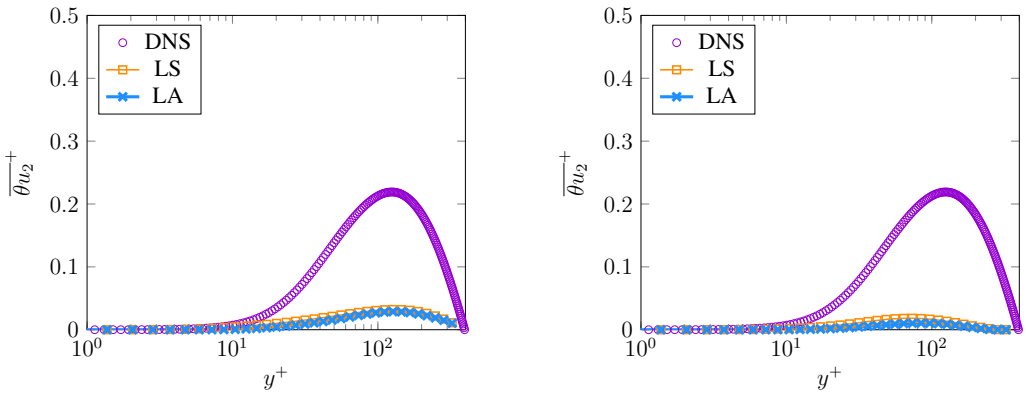

(a) *TV-R* and *TV-E* (b) *TV-M*

Figure 6.22: Wall-normal heat flux obtained by *TV-R*, *TV-E* and *TV-M* for Pr= 0.025 at Re_τ= 395 with the implicit heat flux model

6.5.2.1.6 Thermal to Mechanical Time Scale

Fig. 6.23 demonstrates the ratios of thermal to mechanical time scale ($\mathcal{R}$) obtained from different models, *TV-E* and *TV-M*. Although the thermal quantities used to calculate the ratio (i.e. $\overline{\theta^2}$ and ε_θ) are underpredicted, their ratio shows a consistent sensitivity with respect to the flow field prediction accuracy (Fig. 6.23a and 6.23b). Moreover, the assumption of a constant ratio with $\mathcal{R} = 0.5$ fails completely and results suggest that an additional transport equation is necessary to predict the thermal time scale at an acceptable level of accuracy.

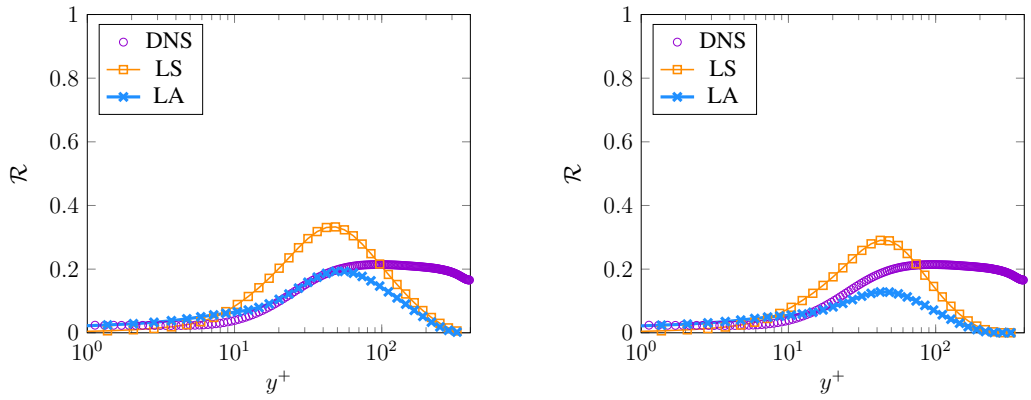

(a) *TV-E* (b) *TV-M*

Figure 6.23: Ratio of thermal to mechanical time scale obtained by *TV-E* and *TV-M* for Pr= 0.025 at Re_τ= 395 with the implicit heat flux model

6.5.2.2 Explicit Heat Flux Model

6.5.2.2.1 Mean Temperature

The mean temperatures obtained with both turbulence models using the explicit heat flux model within *TV-R* and *TV-E* approaches are shown in Fig. 6.24a. The results obtained with both turbulence models underestimate the profile. However, the prediction with the non-linear turbulence model (*LA*) is slightly better. More importantly, in comparison to the implicit heat flux model, the explicit model shows a consistent response to the turbulence model, i.e. the more accurate the flow field, the more accurate the thermal field.

6.5.2.2.1.1 Effect of Mixed Time Scale

Introducing the thermal time scale into the explicit heat flux model (*TV-M*), shows only improvement for the profile obtained with the non-linear turbulence model, Fig. 6.24b. Similar to previously obtained results for Pr = 0.71, the explicit heat flux model presents a consistent behavior to the prediction quality of the flow field.

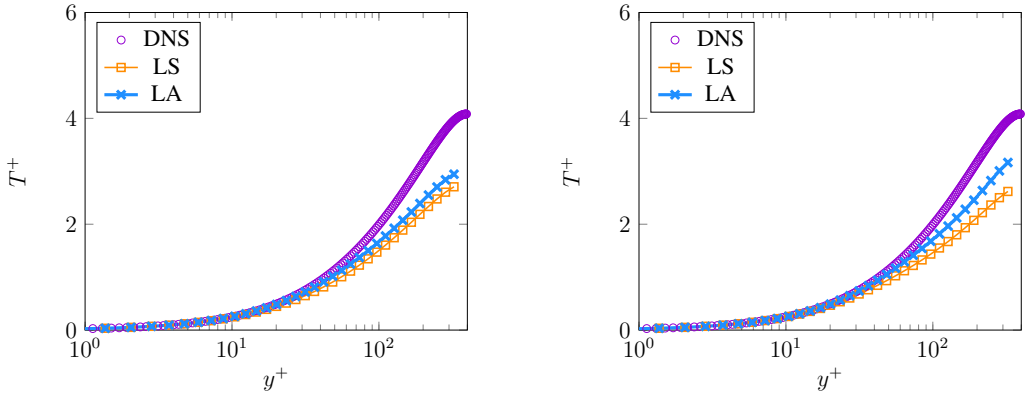

(a) *TV-R* (b) *TV-M*

Figure 6.24: Mean temperature obtained by *TV-R*, *TV-E* and *TV-M* for Pr= 0.025 at Re_τ= 395 with the explicit heat flux model

6.5.2.2.2 Temperature Variance

Temperature variances (θ_{rms}) obtained by *TV-R* and the explicit heat flux model are shown in Fig. 6.25a. As can be seen, the explicit model shows no sensitivity to the accuracy of the flow field but captures the trend of θ_{rms} accurately. Inclusion of an extra transport equation for ε_θ (*TV-E*) seems to affect the results obtained with both turbulence models, most notably when the flow field is predicted at a higher level of accuracy, Fig. 6.25b.

6.5.2.2.2.1 Effect of Mixed Time Scale

Inclusion of the mixed time scale shows only slight improvements close to the channel core when the non-linear turbulence model was applied, see Fig. 6.25c. It appears that the explicit heat flux model is sensitive to the turbulence model used to capture the flow field, in addition to appropriately respond to the inclusion of the mixed time scale.

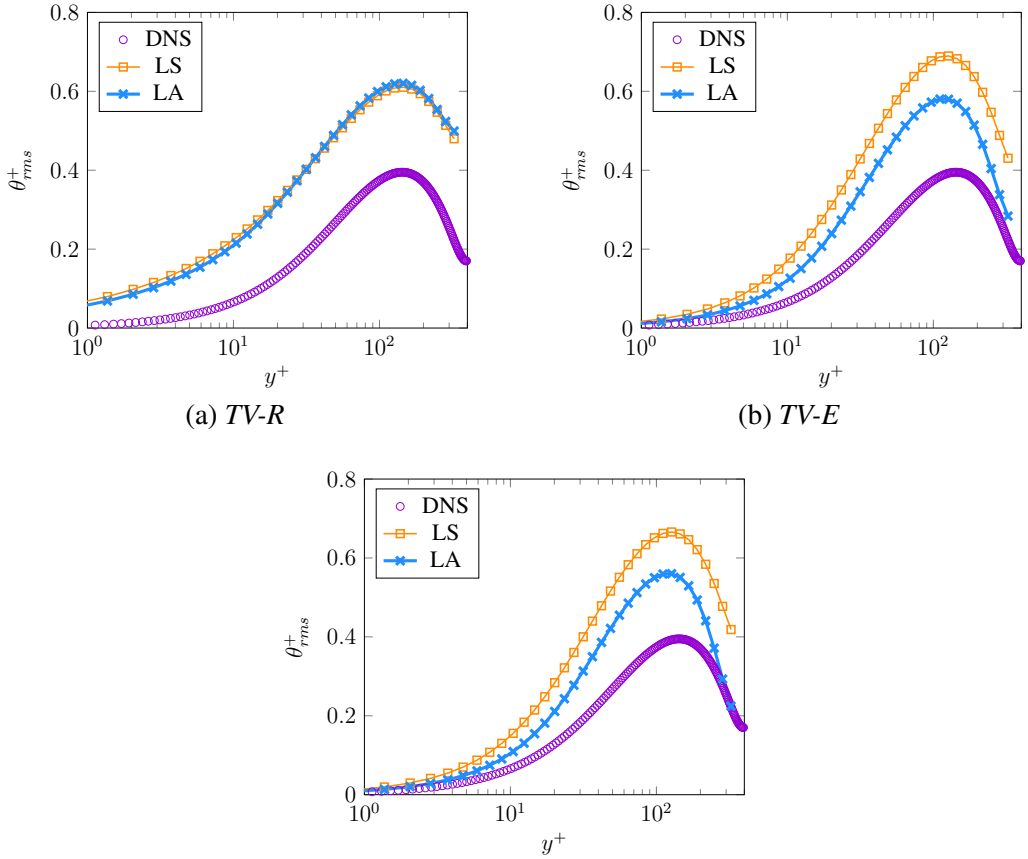

(a) *TV-R* (b) *TV-E*

(c) *TV-M*

Figure 6.25: Temperature Variance obtained by *TV-R*, *TV-E* and *TV-M* for Pr= 0.025 at Re_τ= 395 with the explicit heat flux model

6.5.2.2.3 Dissipation of Temperature Variance

Results for the dissipation of temperature variance obtained for *TV-R* are presented in Fig. 6.26a. The profiles obtained with both turbulence model mostly differ in near-wall region ($y^+ < 100$), while fail to capture the plateau behavior. Some improvement regarding the general tendency of ε_θ can be observed, when an additional transport equation for ε_θ (*TV-E*) is used, most notably using the non-linear turbulence model, Fig. 6.26b.

6.5.2.2.3.1 Effect of Mixed Time Scale

Inclusion of the mixed time scale (*TV-M*) shows improvements regarding the magnitude of the captured plateau obtained with both turbulence model, Fig. 6.26c. In contrast to the implicit heat flux model, the explicit model shows consistent sensitivity

to the turbulence model, as well as to the inclusion of the mixed time scale. However, it should be noted that although some improvement regarding the overall behavior has been achieved, there are still significant deviation from the reference data. In particular, the location of the peak is very much mispredicted and has not been improved after inclusion of the mixed time scale. This may suggest that ε_θ, in case of low Pr number fluids, should not be modeled solely based on similar assumptions made to model the dissipation of turbulent kinetic energy (ϵ), see Section 6.3.3.1 for details about the modeling.

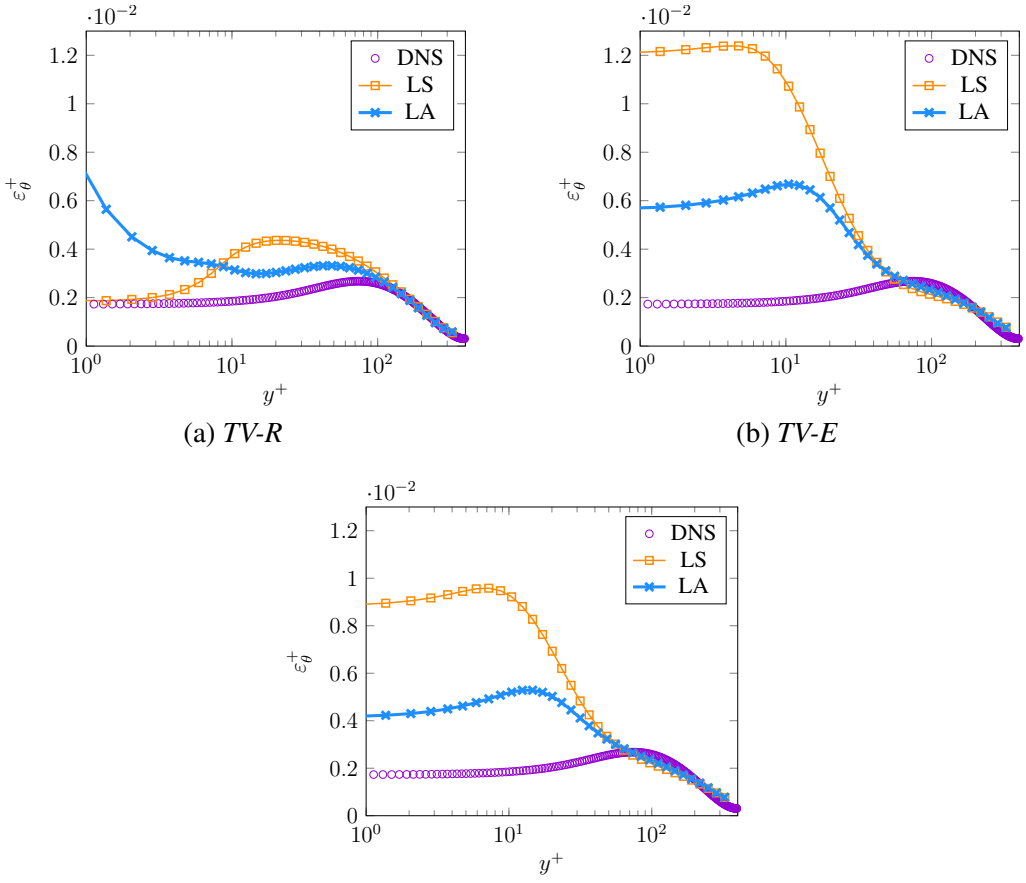

(a) *TV-R* (b) *TV-E*

(c) *TV-M*

Figure 6.26: Dissipation of temperature variance obtained by *TV-R*, *TV-E* and *TV-M* for Pr= 0.025 at Re_τ= 395 with the explicit heat flux model

6.5.2.2.4 Streamwise Heat Flux

Fig. 6.27a shows the streamwise heat fluxes obtained by *TV-R* and *TV-E* using both turbulence models. In contrast to the implicit model (Fig. 6.21a), the explicit heat flux model demonstrates potential capability to capture the streamwise heat flux.

6.5.2.2.4.1 Effect of Mixed Time Scale

As expected and similar to previous results, including the mixed time scale (*TV-M*) offers somehow improvements to capture the general behavior of the heat flux (Fig. 6.27b), demonstrating promising potential of explicit framework for reliable prediction of thermal quantities. In particular, results are indicative of relevance of thermal time scale to capture dynamics of thermal field for fluids with Pr numbers other than unity. However, there are still remarkable deviations from reference data that need more in-depth investigations, which is not scope of this study. Nevertheless, it is worth noting that the explicit model demonstrates a consistent sensitivity regarding the turbulence model.

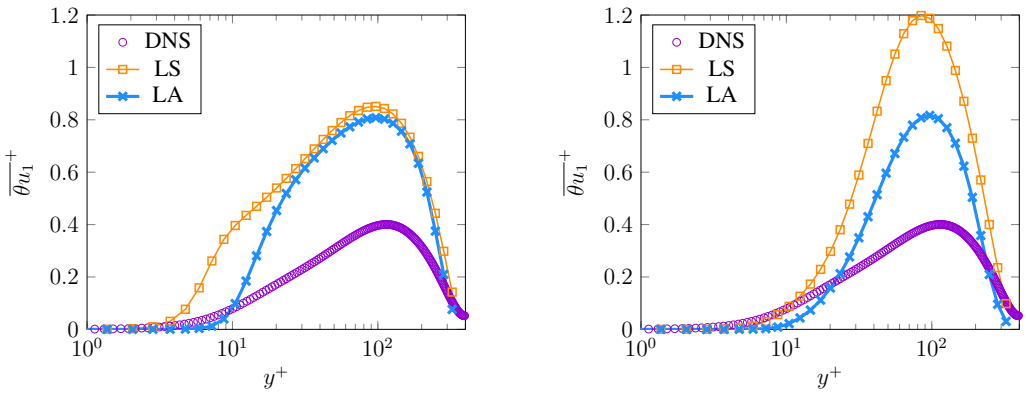

(a) *TV-R* and *TV-E* (b) *TV-M*

Figure 6.27: Streamwise heat flux obtained by *TV-R*, *TV-E* and *TV-M* for Pr= 0.025 at Re_τ= 395 with the explicit heat flux model

6.5.2.2.5 Wall-Normal Heat Flux

Fig. 6.28a depicts the wall-normal heat fluxes obtained from *TV-R* and *TV-E*. Both approaches fail to predict the heat flux at an acceptable level of accuracy. However,

the general trend is predicted, particularly when the non-linear turbulence model was used.

6.5.2.2.5.1 Effect of Mixed Time Scale

Inclusion of the mixed time scale shows no remarkable improvements, as shown in Fig. 6.27b. As previously discussed and although incremental, the better the flow field prediction the more accurate the wall-normal heat flux is predicted.

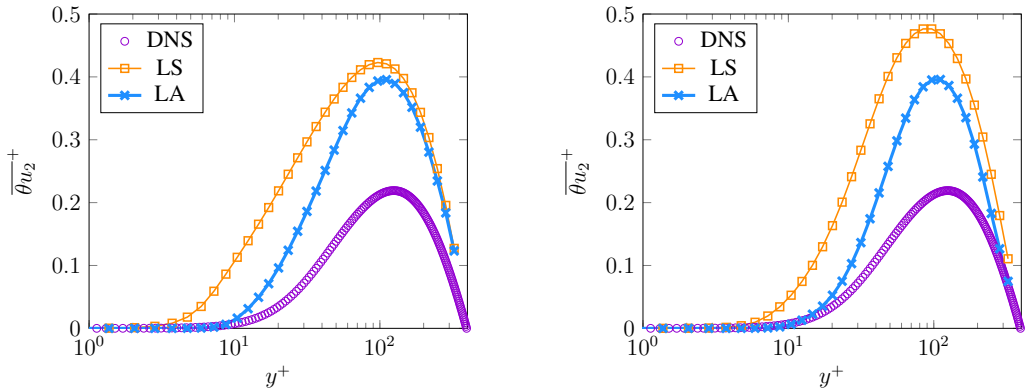

(a) *TV-R* and *TV-E* (b) *TV-M*

Figure 6.28: Wall-normal heat flux obtained by *TV-R*, *TV-E* and *TV-M* for Pr= 0.025 at Re_τ= 395 with the explicit heat flux model

6.5.2.2.6 Thermal to Mechanical Time Scale

Fig. 6.29 shows the ratios of thermal to mechanical time scale obtained from different approaches, *TV-E* and *TV-M*. The explicit model is capable to predict the near-wall behavior correctly (Fig. 6.29a and 6.29b). However, the prediction accuracy decreases towards channel center, similar to results obtained using the implicit model. It is worth noting here that neither implicit nor explicit model is able to predict the correct behavior of the ratio in the core region of the channel. This is thought to trace back mainly to the inaccurate prediction of the thermal dissipation suggesting necessity to revisit its derivation concept.

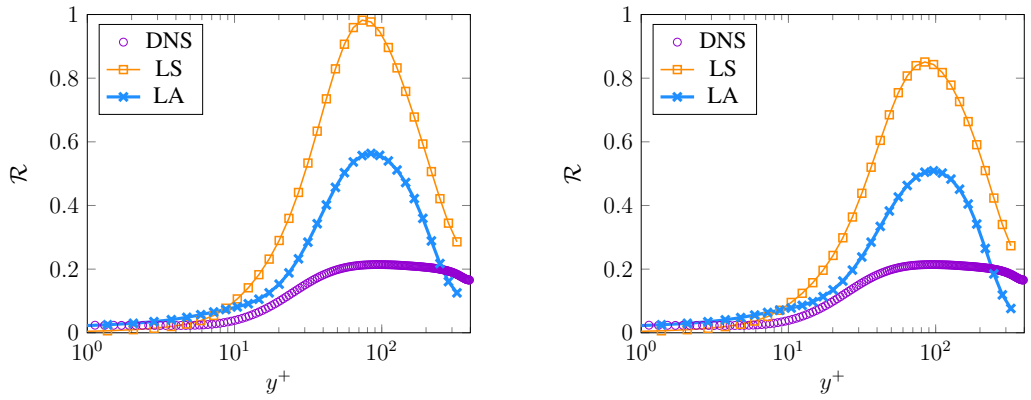

(a) *TV-E* (b) *TV-M*

Figure 6.29: Ratio of thermal to mechanical time scale obtained by *TV-E* and *TV-M* for Pr= 0.025 at Re_τ= 395 with the explicit heat flux model

6.5.3 Pr= 10

In contrast to low Prandtl number fluids, the thermal boundary layer for high Pr number fluids is much thinner than the velocity boundary layer. This requires a different mesh design to capture dynamics of the thermal boundary layer accurately. In particular, much finer resolution is necessary in near-wall region as discussed in [125].

6.5.3.1 Implicit Heat Flux Model

6.5.3.1.1 Mean Temperature

Fig. 6.30a presents mean temperatures obtained for Pr = 10 and Re_τ = 395 with the implicit heat flux model for *TV-R* and *TV-E*. The mean temperature is not well captured irrespective of the turbulence model used to predict the flow field. It is worth noting that the more accurate prediction obtained using the linear turbulence model for flow field is deemed accidental, given the lower prediction capability provided by the linear model.

6.5.3.1.1.1 Effect of Mixed Time Scale

Fig. 6.30b presents mean temperatures for Pr = 10 at Re_τ = 395 obtained by *TV-M* with both turbulence models. Including the thermal time scale into the heat flux equation improves the prediction obtained when the non-linear turbulence is used.

Moreover, it seems that the implicit heat flux model responds appropriately to the choice of turbulence model, although thse improvement is only limited to the general trend of the mean temperature. Additionally, the improvement in the mean temperature may be indicative of the relevance of the thermal time scale when dealing with fluids with Pr numbers significantly higher than unity.

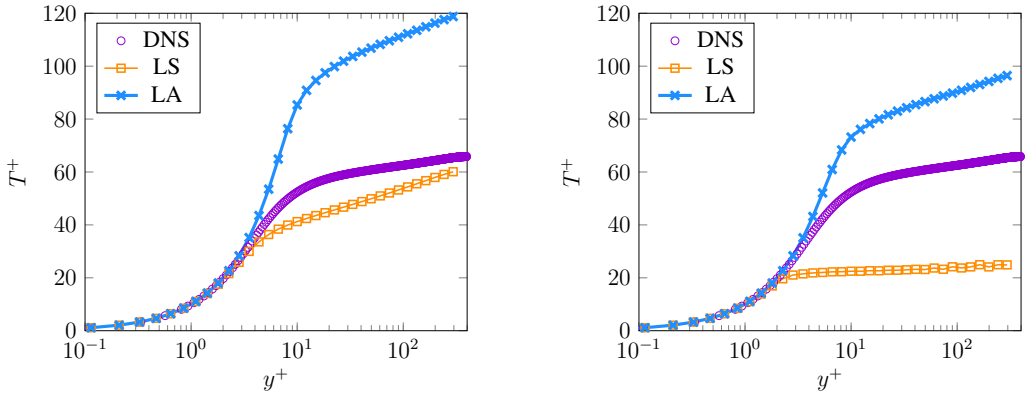

(a) *TV-R* and *TV-E* (b) *TV-M*

Figure 6.30: Mean temperature obtained by *TV-R*, *TV-E* and *TV-M* for Pr= 10 at Re_τ= 395 with the implicit heat flux model

6.5.3.1.2 Temperature Variance

Temperature variances (θ_{rms} equivalently) obtained by TV-R are shown in Fig. 6.31a. The implicit mode captures the general behavior. Using an additional transport equation for ε_θ (*TV-E*) to provide information on thermal time scale, improves the results significantly, Fig. 6.31b, which confirms that the assumption of a constant thermal to mechanical time scale ratio is fundamentally wrong for high Pr numbers.

6.5.3.1.2.1 Effect of Mixed Time Scale

In order to investigate the effect of mixed time scale on the model prediction capability, *TV-M* approach was used to predict the temperature variance. As expected for high Pr numbers, the prediction improves remarkably, if the flow field is captured accurately, i.e. the non-linear turbulence model is used, Fig. 6.31c. It should be noted that the production term in the transport equation for *TV-M* includes the mean temper-

ature gradient, which is fairly well predicted by *TV-M* approach (general behavior is captured) using the non-linear turbulence model.

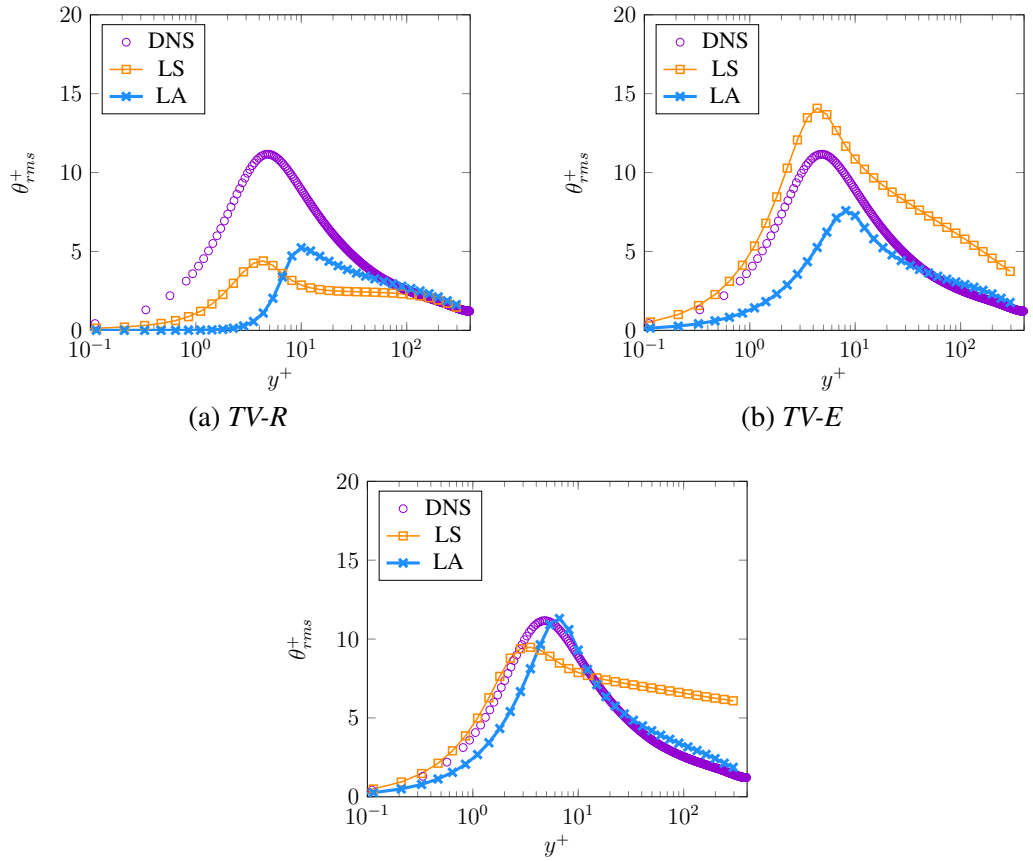

(a) *TV-R* (b) *TV-E*

(c) *TV-M*

Figure 6.31: Temperature variance obtained by *TV-R*, *TV-E* and *TV-M* for Pr= 10 at Re_τ= 395 with the implicit heat flux model

6.5.3.1.3 Dissipation of Temperature Variance

Results for the dissipation of temperature variance under the assumption of a constant time scale ratio ($\mathcal{R} = 0.5$) are presented in Fig. 6.32a. Similar to previously discussed Pr numbers, the thermal dissipation rate ε_θ is mispredicted particularly in the near-wall region. This is due to the assumption of a constant time scale ratio, which reflects misprediction of ε in near-wall region. Including the transport equation for ε_θ (*TV-E*) leads to improvements in the near-wall region, as shown in Fig. 6.32b.

6.5.3.1.3.1 Effect of Mixed Time Scale

Results obtained for ε_θ using the mixed time scale in the implicit heat flux model are shown in Fig. 6.32c. As expected, for fluids with high Pr numbers, inclusion of the mixed time scale leads to improvements. More importantly, in contrast to previously discussed results obtained with the implicit heat flux model for low and unity Pr numbers ($Pr << 1$ and $Pr \approx 1$), the implicit heat flux model shows a consistent response to the turbulence model, i.e. the more accurate the flow field, the more accurate the thermal field.

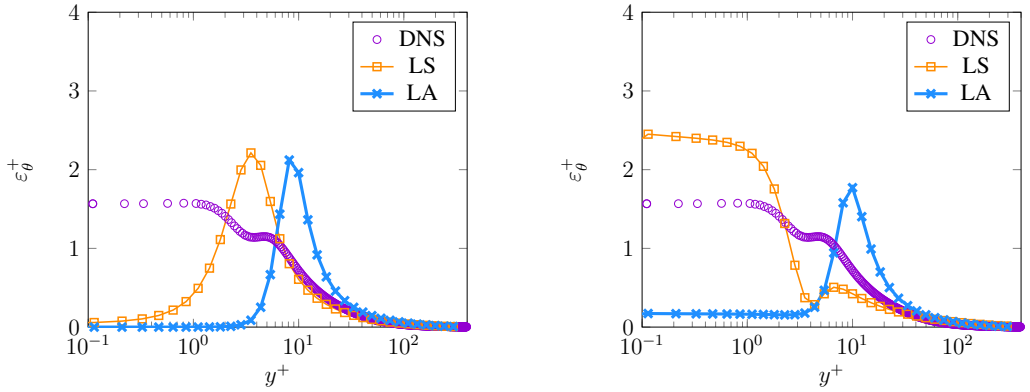

(a) *TV-R* (b) *TV-E*

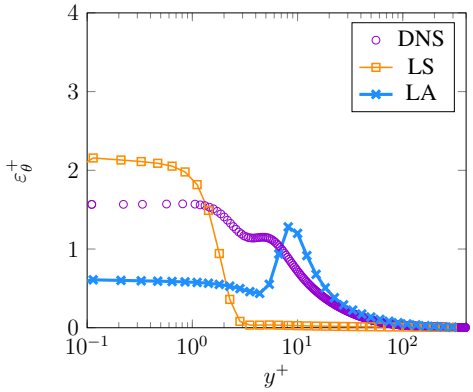

(c) *TV-M*

Figure 6.32: Dissipation of temperature variance obtained by *TV-R*, *TV-E* and *TV-M* for Pr= 10 at Re_τ= 395 with the implicit heat flux model

6.5.3.1.4 Streamwise Heat Flux

The streamwise heat fluxes obtained by *TV-R* and *TV-E* are shown in Fig. 6.33a. Similar to previously discussed cases, the streamwise heat flux is strongly mispredicted,

regardless of the turbulence model used to capture the flow field. In fact, there is only little sensitivity to the heat flux in homogeneous direction.

6.5.3.1.4.1 Effect of Mixed Time Scale

Results obtained for the streamwise heat fluxes after inclusion of the mixed time scale (*TV-M*) are presented in Fig. 6.33b. It appears that inclusion of thermal time scale increases the sensitivity of the model, however marginally. It should be noted that using the linear turbulence model leads to numerical instabilities and thus, only the result obtained using the non-linear model is presented.

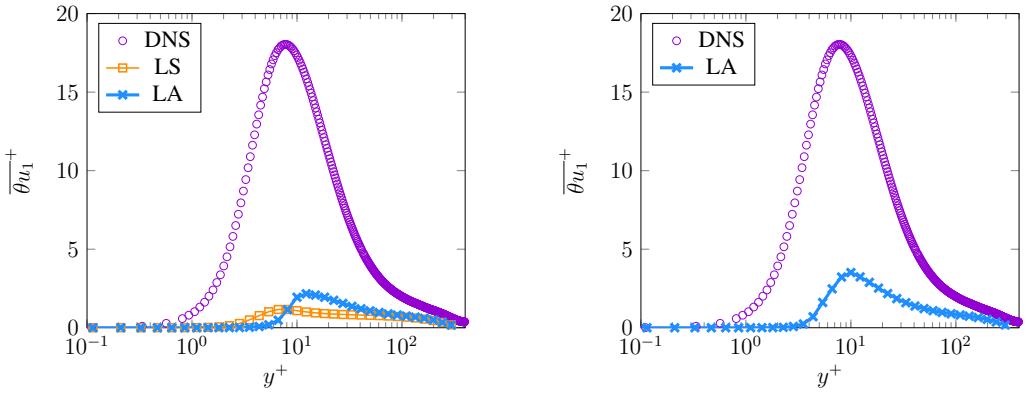

(a) *TV-R* and *TV-E* (b) *TV-M*

Figure 6.33: Streamwise heat flux obtained by *TV-R*, *TV-E* and *TV-M* for Pr= 10 at Re_τ= 395 with the implicit heat flux model

6.5.3.1.5 Wall-Normal Heat Flux

Wall-normal heat fluxes obtained for *TV-R* and *TV-E* are shown in Fig. 6.33a. As shown, the model is capable of capturing the wall-normal heat flux behavior correctly. Similar to $Pr = 0.71$, it seems that the near-wall region is better predicted with the linear turbulence model. Again, this superiority is deemed to be an accident, given the lower quality provided by the linear model for the flow field.

6.5.3.1.5.1 Effect of Mixed Time Scale

Inclusion of the mixed time scale does not appear to provide any remarkable improvements, when the non-linear turbulence model is used, see Fig. 6.33b. Moreover,

the prediction using the linear turbulence model experiences numerical instability and thus, is not shown here.

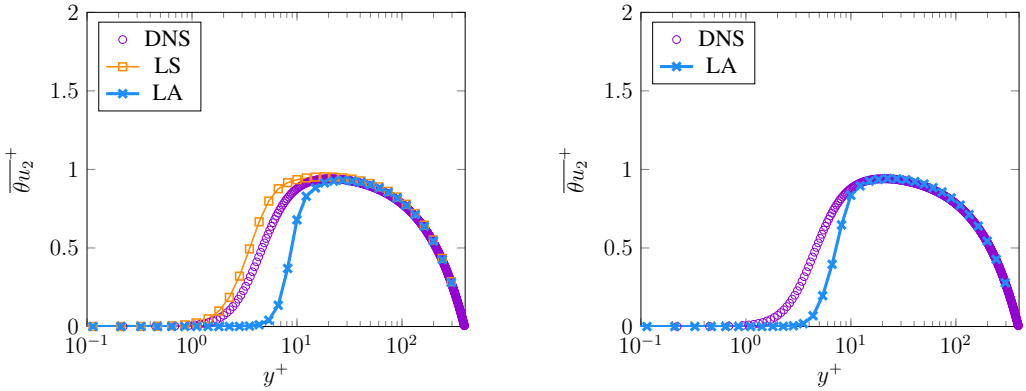

(a) *TV-R* and *TV-E* (b) *TV-M*

Figure 6.34: Wall-normal heat flux obtained by *TV-R*, *TV-E* and *TV-M* for Pr= 10 at Re_τ= 395 with the implicit heat flux model

6.5.3.1.6 Thermal to Mechanical Time Scale

Fig. 6.35 demonstrates the ratios of thermal to mechanical time scale ($\mathcal{R}$) obtained by *TV-E* and *TV-M*. A consistent sensitivity with respect to the flow field prediction accuracy can be clearly observed (Fig. 6.35a and 6.35b). Additionally, it turns out that the inclusion of the thermal time scale in the heat flux model is necessary to accurately predict the thermal field, particularly close to solid surfaces. Moreover, these results suggest that an additional transport equation is necessary to predict the thermal time scale more accurately since the assumption of a constant thermal to mechanical time scale faces serious challenges dealing with high Pr number fluids, particularly in near-wall region.

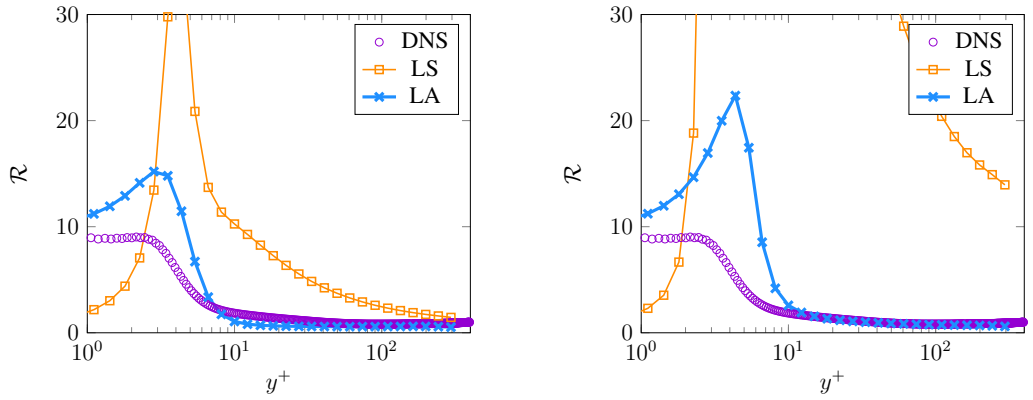

(a) *TV-E* (b) *TV-M*

Figure 6.35: Ratio of thermal to mechanical time scale obtained by *TV-E* and *TV-M* for Pr= 10 at Re_τ= 395 with the implicit heat flux model

6.5.3.2 Explicit Heat Flux Model

6.5.3.2.1 Mean Temperature

The mean temperatures obtained using both turbulence models using the explicit heat flux model within *TV-R* and *TV-E* approaches are shown in Fig. 6.36a. The result obtained with the linear turbulence model (*LS*) underestimates the profile, while using the non-linear turbulence model (*LA*) leads to an overprediction of the mean temperature.

6.5.3.2.1.1 Effect of Mixed Time Scale

Introducing the thermal time scale into the explicit heat flux model has a remarkable effect on the prediction when the non-linear turbulence model is used, Fig. 6.36b, leading to a profile that is in good agreement with the reference data. This indicates the relevance of the thermal time scale, as well as, accuracy of the flow field when dealing with high Pr number fluids.

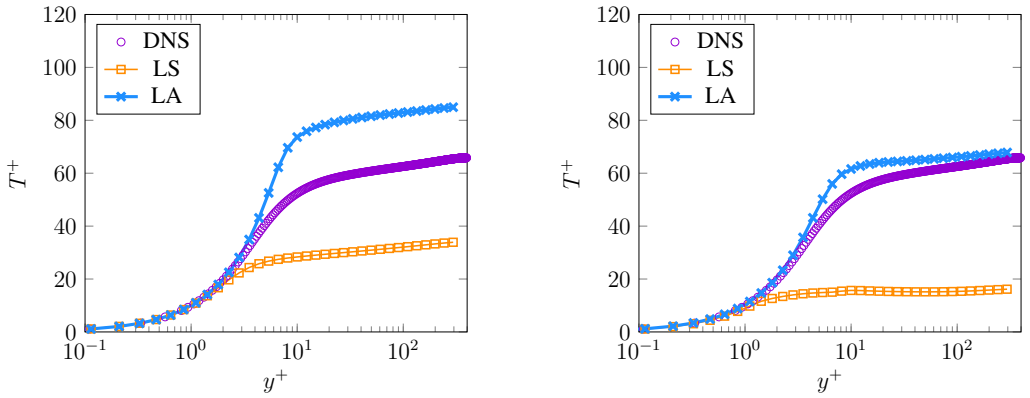

(a) *TV-R* and *TV-E* (b) *TV-M*

Figure 6.36: Mean temperature obtained by *TV-R*, *TV-E* and *TV-M* for Pr= 10 at Re_τ= 395 with the explicit heat flux model

6.5.3.2.2 Temperature Variance

Temperature variances (θ_{rms}) obtained by *TV-R* and the explicit heat flux model are shown in Fig. 6.37a. Similar to the prediction with the implicit model, the explicit model captures the general behavior with both turbulence models, however, with a significant deviation from reference data. Moreover, using an extra transport equation for ε_θ (*TV-E*) provides improvement (Fig. 6.37b), pointing to the different dynamics of thermal time scale compared to mechanical time scale.

6.5.3.2.2.1 Effect of Mixed Time Scale

Fig. 6.37c presents θ_{rms} obtained with the mixed time scale. As expected, inclusion of the mixed time scale (*TV-M*) affects the results obtained with both turbulence models. While remarkable improvements can be observed for the prediction with the non-linear turbulence model, θ_{rms} predicted with the linear turbulence model demonstrates notable discrepancy. Hence, it might be concluded that inclusion of the thermal time scale into the heat flux models seems to be essential to predict the thermal field accurately. However, this must be in conjunction with advanced turbulence models capable to predicting the flow field accurately.

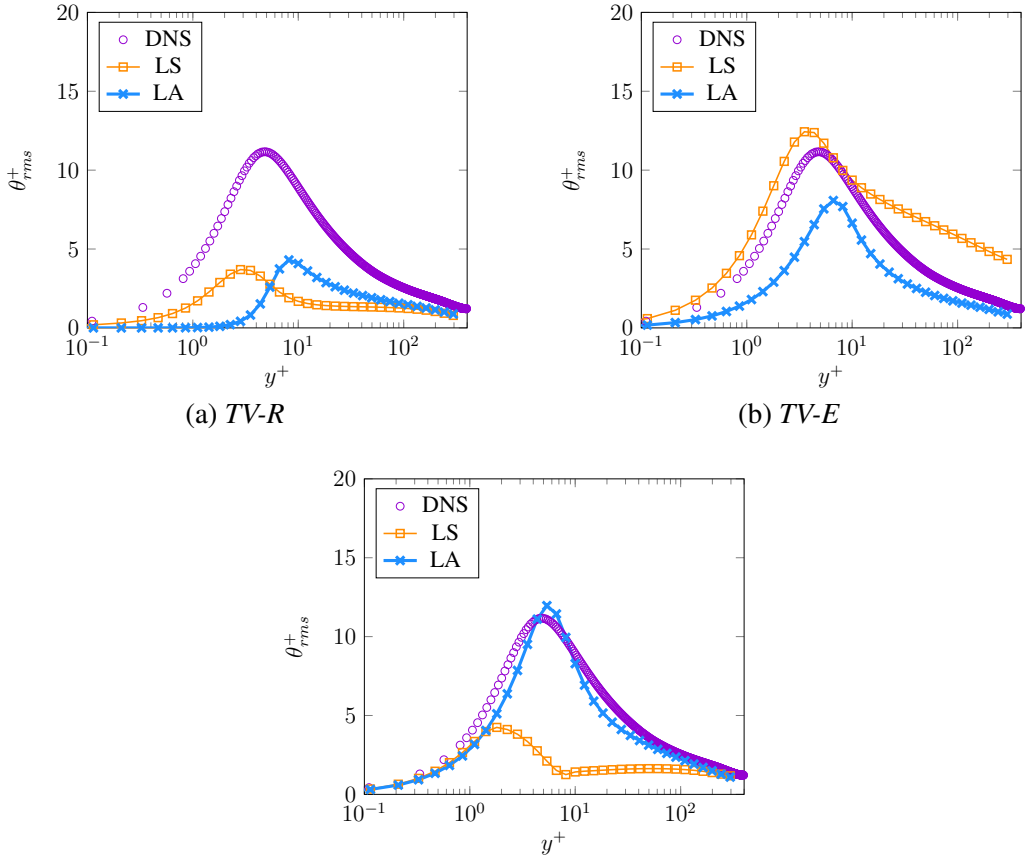

(a) *TV-R* (b) *TV-E*

(c) *TV-M*

Figure 6.37: Temperature variance obtained by *TV-R*, *TV-E* and *TV-M* for Pr= 10 at Re_τ= 395 with the explicit heat flux model

6.5.3.2.3 Dissipation of Temperature Variance

Fig. 6.38a presents ε_θ obtained using the explicit heat flux model and the algebraic expression for ε_θ (*TV-E* and Eq. 6.17). Similar to previous results, the thermal dissipation rate ε_θ is mispredicted, particularly in the near-wall region. Including the transport equation for ε_θ leads to particular improvements in the near-wall region, Fig. 6.38b. Moreover, the prediction with the explicit heat flux model resembles the prediction obtained with the implicit model, Fig. 6.32b.

6.5.3.2.3.1 Effect of Mixed Time Scale

As expected for high Pr numbers, the explicit heat flux model provides improvements when the mixed time scale is used in conjunction with the non-linear tur-

bulence model, consistent with other thermal quantities. However, the opposite is true for the linear turbulence model, Fig. 6.38c.

It follows that currently available models for the thermal dissipation within the explicit framework are capable to deal with high Pr number fluids, if the flow field is accurately predicted.

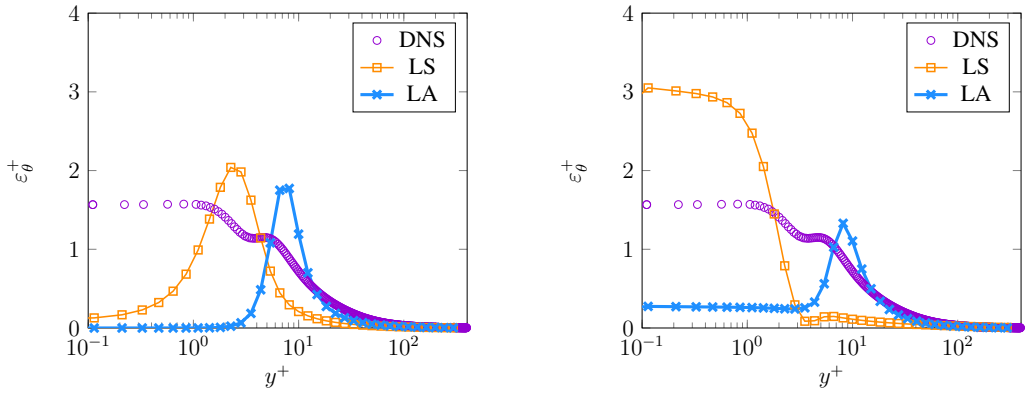

(a) *TV-R* (b) *TV-E*

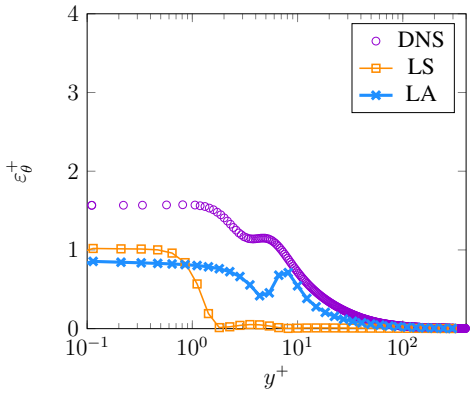

(c) *TV-M*

Figure 6.38: Dissipation of temperature variance obtained by *TV-R*, *TV-E* and *TV-M* for Pr= 10 at Re_τ= 395 with the explicit heat flux model

6.5.3.2.4 Streamwise Heat Flux

Fig. 6.39a presents the streamwise heat fluxes obtained by *TV-R* and *TV-E* using both turbulence models. In contrast to the implicit model (Fig. 6.33a), the explicit heat flux model demonstrates potential capability to capture the streamwise heat flux.

6.5.3.2.4.1 Effect of Mixed Time Scale

Results obtained for the streamwise heat fluxes after inclusion of the mixed time scale are presented in Fig. 6.39b. The profile obtained with the non-linear turbulence model is in a good agreement with the reference data. However, it should be noted that if the flow field is not predicted at an acceptable level of accuracy, the heat flux model could potentially deliver a remarkable discrepancy or even become numerical unstable, as demonstrated here when using the linear turbulence model (*LS*). Further, it may suggest that the explicit heat flux model combined with advanced flow field model is the most promising approach to address the longstanding shortcoming of heat flux models in predicting heat fluxes in homogeneous directions.

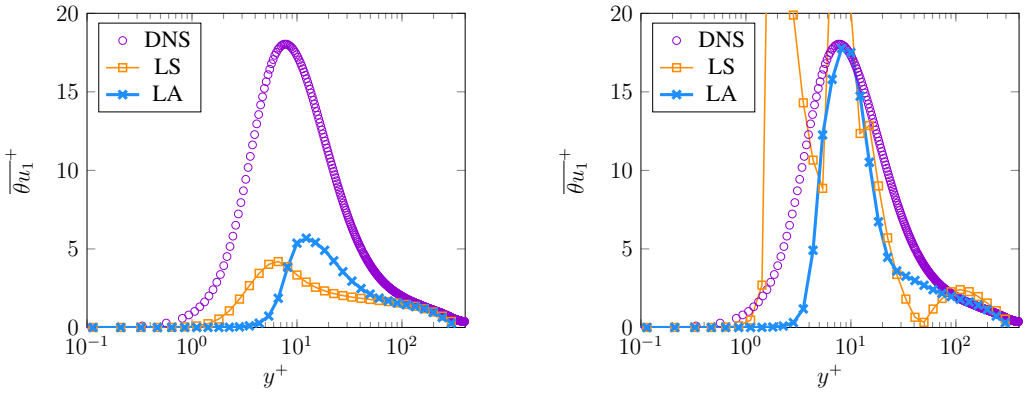

(a) *TV-R* and *TV-E* (b) *TV-M*

Figure 6.39: Streamwise heat flux variance obtained by *TV-R*, *TV-E* and *TV-M* for Pr= 10 at Re_τ= 395 with the explicit heat flux model

6.5.3.2.5 Wall-Normal Heat Flux

Fig. 6.40a depicts the wall-normal heat fluxes obtained by *TV-R* and *TV-E*. It can be observed that the explicit heat flux model is capable to predict the wall-normal heat flux fairly accurate except for regions very close to the wall ($y^+ < 10$), irrespective of turbulence model.

6.5.3.2.5.1 Effect of Mixed Time Scale

Inclusion of the mixed time scale improves prediction accuracy in the near-wall region, when the non-linear turbulence model is used, 6.40b, which is indicative of

relevance of the thermal time scale in near-wall region. In contrast, using the linear turbulence model for the flow field leads to a significant error. Therefore, it may be deduced that the thermal time scale plays an integral role to capture the thermal field of high Pr number fluids, however, the flow field needs to be accurately predicted.

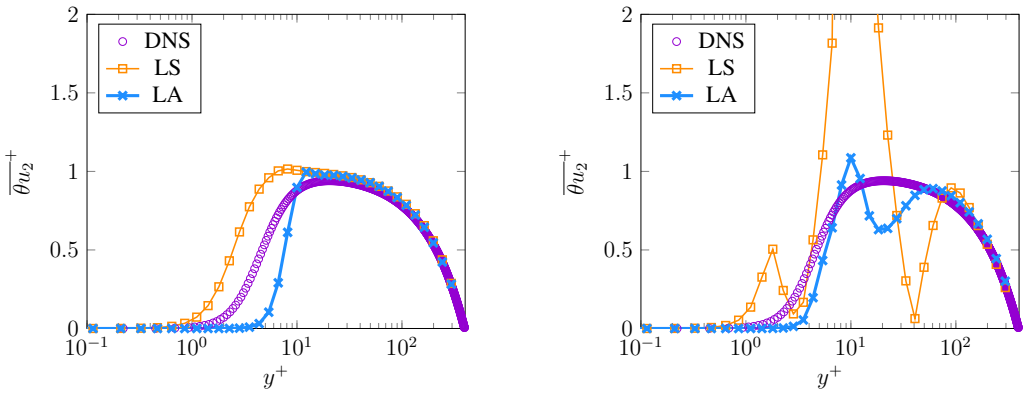

(a) *TV-R* and *TV-E* (b) *TV-M*

Figure 6.40: Wall-normal heat flux obtained by *TV-R*, *TV-E* and *TV-M* for Pr= 10 at Re_τ= 395 with the explicit heat flux model

6.5.3.2.6 Thermal to Mechanical Time Scale

Fig. 6.17 shows the ratios of thermal to mechanical time scale obtained from different approaches, *TV-E* and *TV-M*. It clearly can be seen that the explicit heat flux model has the capability to provide accurate results when the flow field is accurately captured and reliable information for thermal time scale is provided (via an additional transport equation for ε_θ). Moreover, including this time scale into the heat flux model leads to significant improvements when the non-linear turbulence model is used. Moreover, the results confirm again that the thermal time scale is essential for accurate prediction of turbulent thermal field of high Pr number fluids.

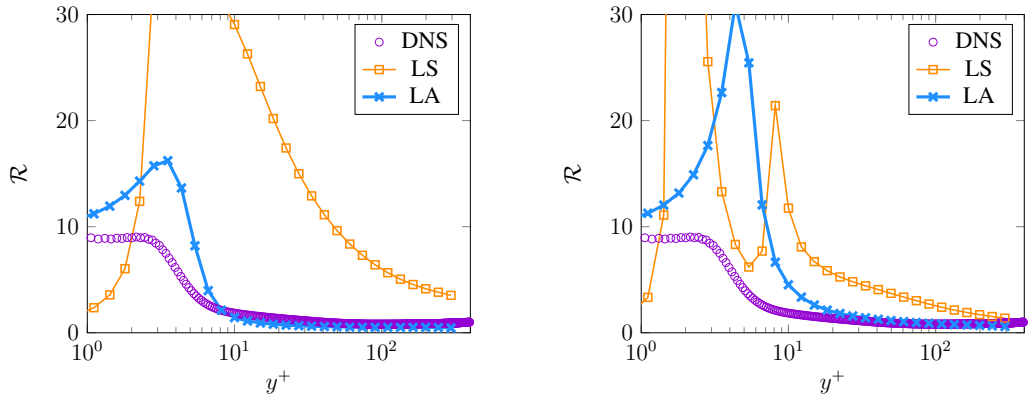

(a) *TV-E* (b) *TV-M*

Figure 6.41: Ratio of thermal to mechanical time scale obtained by *TV-E* and *TV-M* for Pr= 10 at Re_τ= 395 with the explicit heat flux model

6.6 Conclusion and Outlook

In this study, the implicit and explicit heat flux models have been thoroughly assessed. This includes the application of the models to turbulent wall-bounded shear flows of different Prandtl number fluids. Further, sensitivity of both models with respect to the prediction accuracy of the flow field has been studied.

It turns out the implicit framework (*AHFM-NRG* formulation) suffers from some fundamental shortcomings dealing with turbulent thermal fields. Most notably, it is incapable of providing accurate results even for first order statistics such as mean temperature irrespective of the Prandtl number. The shortcoming most likely traces back to the inability of the implicit model to establish a consistent coupling with the flow field, which leads to inconsistent response to the flow field prediction accuracy. This makes model calibration and tuning extremely difficult. Moreover, the implicit model does not show any meaningful sensitivity to heat fluxes in homogeneous directions irrespective of the Prandtl number, which renders this as incapable to address the longstanding issue of heat flux models to capture heat fluxes in homogeneous directions.

In contrast, the explicit framework appears to able to deal with complex turbulent thermal fields of different working fluids. In particular, the model is capable to provide results at an acceptable level of accuracy when the flow field is predicted accurately. Moreover, it turns out the explicit formulation is able to address the main

issues of heat transfer models and shows promising capability to capture the heat flux in homogeneous directions.

Based on the obtained results, it may be concluded that the explicit formulation offers a promising and reliable framework to predict turbulent thermal fields. However, there are still some issues that need to be addressed. In particular, current formulation of the explicit model includes only the mechanical time scale, which has shown to be not sufficient dealing with fluids with Prandtl numbers different than unity. Inclusion of the thermal time scale to the model has shown to be necessary, particularly to predict second order statistics (temperature variance and heat flux) of working fluids with low and high Prandtl numbers. However, this study only shows the necessity of the thermal time scale. Further investigation towards model validation and calibration when thermal time scale is included, particularly for low Prandtl number fluids, is required and will be addressed in the future.

Addendum

Funding This work was supported using start-up funds from the University of Missouri-Kansas City.

Acknowledgment The authors would like to thank Hagen Müller [64] for providing the OpenFOAM source code for the here investigated explicit heat flux model.

Conflict of interest The authors declare no conflict of interest.

6.6.1 Nomenclature

	Name
$b_{ij} = \overline{u_i u_j}/2k - 1/3\delta_{ij}$	Reynolds stress anisotropy tensor
c_p	specific heat capacity at constant pressure
k	kinetic energy
p	pressure fluctuations
u_i	velocity fluctuations
$\overline{u_i u_j}$	Reynolds stress tensor
Pr	Prandtl
$\mathcal{R} = \tau_\theta/\tau_m$	mechanical to thermal time scale ratio

Re	Reynolds number
$Re_\tau = U_\tau \delta / \nu$	turbulent Reynolds number
S_T	source terms in temperature equation
T	mean temperature
$T_\tau = \rho / c_p q_w U_\tau$	friction temperature
U_i	mean velocity
$U_\tau = Re_\tau \nu / \delta$	friction velocity
$\alpha = \lambda / \rho c_p$	thermal diffusivity
δ	channel half height
δ_{ij}	Kronecker delta
ε	dissipation of kinetic energy
ε_θ	dissipation of the temperature variance
$\overline{\theta^2}$	temperature variance
λ	thermal conductivity
ν	kinematic viscosity
ν_t	turbulent kinematic viscosity
θ	temperature fluctuations
$\overline{\theta u_i}$	turbulent heat flux
ρ	density
$\tau_m = k / \varepsilon$	mechanical time scale
$\tau_\theta = \overline{\theta^2} / 2\varepsilon_\theta$	thermal time scale
$\tau = \sqrt{\tau_m \tau_\theta}$	mixed time scale
$\overline{(\,)}$	mean value
$()^*$	dimensionless value

CHAPTER 7

CONCLUSION AND OUTLOOK

In this dissertation, several aspects concerning turbulent heat transfer have been investigated. This includes the Reynolds Analogy for steady and unsteady-state simulations, the second law of thermodynamics as a tool to evaluate heat flux models and the Reynolds Analogy extended with a GGDH term for LES simulations. Furthermore, implicit and explicit heat transfer models and sensitivity of these heat flux models towards the inclusion of thermal time scale were thoroughly assessed.

Concerning steady state calculations, the Reynolds Analogy can provide acceptable results for first order statistics in non-homogeneous directions, but fails for homogeneous directions. Regarding unsteady simulations, it fails to guarantee basic properties of an appropriate sub-grid scale model, especially in the near-wall region. The model shows an inappropriate response to mesh resolution and pushes the simulations towards direct numerical simulations regardless of any grid resolution, leading to the misprediction of sub-grid values. This could lead to enormous prediction errors when the near-wall behavior is of importance. Moreover, for unsteady simulations of low Pr number fluids, it is demonstrated that an isotropic mesh away from the solid surface is necessary to avoid mispredictions. In contrast for high Pr number fluids where an extremely high resolution mesh along with specific spacing close to the wall is inevitable. Further, for these Pr numbers, it is shown that a transport equation for ε_θ is necessary to predict the thermal time scale in good agreement with the reference data.

Furthermore, the predictive capabilities of the Reynolds Analogy to determine entropy production in accordance to the second law of thermodynamics have been thoroughly assessed. This includes the application of the analogy to turbulent wall-bounded shear flows at different Reynolds and Prandtl numbers within steady and unsteady state calculations. In case of steady-state calculations, the Reynolds Analogy is only capable of predicting acceptable results for mean and fluctuating entropy generation of working fluids with Pr numbers around unity. However, it fails for the fluctuating values

when departed from unity Pr number. Concerning unsteady calculations, the previous mentioned misprediction of sub-grid values leads to a misprediction of sub-grid entropy production, particularly for low and high Prandtl numbers. Moreover, the results suggest that optimization efforts for low Pr number fluids need to be focused on minimizing viscous dissipation while efficient heat transfer is the key to reducing irreversibility of a process when dealing with high Pr number fluids. Both mechanism are equally important for fluids with a Pr number around unity. The obtained results confirm that using a zero-equation approach (the Reynolds Analogy) cannot be used reliably, especially when relying on entropy generation/optimization strategies and for working fluids with non-unity Prandtl numbers. This strongly suggest moving forward to more advanced turbulence heat transfer models that are consistent with the second law of thermodynamics.

To overcome the shortcomings of the Reynolds Analogy, an anisotropic extension of the analogy has been proposed and evaluated. The prominent features of the proposed model are that firstly, it accounts for variable fluid properties and anisotropic effects in the unresolved temperature scales, secondly, no ad-hoc treatments or dynamic procedure are required to obtain correct near-wall behavior, and thirdly, the formulation is consistent with the second law of thermodynamics. It is shown that the model is able to predict sub-grid scale heat fluxes in a physically consistent way. This was confirmed by comparison with DNS for several test cases, e.g. turbulent heated channel flow and strongly heated air flow in a vertical pipe.

In this dissertation, the implicit and explicit heat flux models have been thoroughly assessed. This includes the application of the models to turbulent wall-bounded shear flows of different Prandtl number fluids. Further, sensitivity of both models with respect to the prediction accuracy of the flow field has been studied. It turns out the implicit framework (*AHFM-NRG* formulation) suffers from some fundamental shortcomings dealing with turbulent thermal fields. Most notably, it is incapable of providing accurate results even for first order statistics such as mean temperature irrespective of the Prandtl number. The shortcoming most likely traces back to the inability of

the implicit model to establish a consistent coupling with the flow field, which leads to inconsistent response to the flow field prediction accuracy. In contrast, the explicit framework appears to able to deal with complex turbulent thermal fields of different working fluids. In particular, the model is capable to provide results at an acceptable level of accuracy when the flow field is predicted accurately. Moreover, it turns out the explicit formulation is able to address the main issues of heat transfer models and shows promising capability to capture the heat flux in homogeneous directions. Based on the obtained results, it may be concluded that the explicit formulation offers a promising and reliable framework to predict turbulent thermal fields. However, there are still some issues that need to be addressed. In particular, current formulation of the explicit model includes only the mechanical time scale, which has shown to be not sufficient dealing with fluids with Prandtl numbers different than unity. Inclusion of the thermal time scale to the model has shown to be necessary, particularly to predict second order statistics (temperature variance and heat flux) of working fluids with low and high Prandtl numbers. However, this study only shows the necessity of the thermal time scale. Further investigation towards model validation and calibration when thermal time scale is included, particularly for low Prandtl number fluids, is required and will be addressed in the future.

REFERENCES

[1] Hiroyuki Abe, Hiroshi Kawamura, and Yuichi Matsuo. "Surface heat-flux fluctuations in a turbulent channel flow up to Ret=1020 with Pr=0.025 and 0.71". In: *Int. J. Heat Fluid Flow* 25.3 (2004), pp. 404–419. DOI: 10.1016/j.ijheatfluidflow.2004.02.010.

[2] Kenichi Abe, Yong-jun Jang, and Michael A. Leschziner. "An investigation of wall-anisotropy expressions and length-scale equations for non-linear eddy-viscosity models". In: *Int. J. Heat Fluid Fl.* 24.2 (2003), pp. 181–198. ISSN: 0142727X. DOI: 10.1016/S0142-727X(02)00237-0.

[3] Muhammad Idrees Afridi, Muhammad Qasim, and Abid Hussanan. "Second law analysis of dissipative flow over a riga plate with non-linear Rosseland thermal radiation and variable transport properties". In: *Entropy* 20.8 (2018). ISSN: 10994300. DOI: 10.3390/e20080615.

[4] Muhammad Idrees Afridi, Muhammad Qasim, and Oluwole D. Makinde. "Entropy Generation Due to Heat and Mass Transfer in a Flow of Dissipative Elastic Fluid Through a Porous Medium". In: *J. Heat Trans.* 141.2 (2019). ISSN: 15288943. DOI: 10.1115/1.4041951.

[5] Goodarz Ahmadi et al. "A thermodynamical formulation for chemically active multiphase turbulent flows". In: *Int. J. Eng. Sci.* 44 (2006), pp. 699–720. DOI: 10.1016/j.ijengsci.2006.06.001.

[6] Joong-hun Bae et al. "Effects of large density variation on strongly heated internal air flows". In: *Phys. Fluids* 18 (2006), p. 75102. DOI: 10.1063/1.2216988.

[7] Emilio Baglietto. "An algebraic heat flux model in STAR-CCM+ for application to innovative reactors". In: *The 14th International Topical Meeting on Nuclear Reactor Thermalhydraulics*. Toronto, 2011. URL: https://inis.iaea.org/search/search.aspx?orig{_}q=RN:47071158.

[8] Robert Bergant and Iztok Tiselj. “Near-wall passive scalar transport at high Prandtl numbers”. In: *Phys. Fluids* 19.6 (2007). ISSN: 10706631. DOI: 10.1063/1.2739402.

[9] Robert Bergant and Iztok Tiselj. “On the role of the smallest scales of a passive scalar field in a near-wall turbulent flow”. In: *Heat Mass Trans.* 42.5 (2005), pp. 411–426. ISSN: 09477411. DOI: 10.1007/s00231-005-0025-2.

[10] Robert Bergant, Iztok Tiselj, and Gad Hetsroni. “Resolution requirements for DNS of turbulent heat transfer near the heated wall at Prandtl number 5.4”. In: *American Society of Mechanical Eng.* Vol. 369. 1. New York, 2001, pp. 273–287.

[11] Bruno Chaouat. “The State of the Art of Hybrid RANS/LES Modeling for the Simulation of Turbulent Flows”. In: *Flow, Turb. and Combustion* 99.2 (2017), pp. 279–327. ISSN: 15731987. DOI: 10.1007/s10494-017-9828-8.

[12] Subhash Chander Chetal et al. “The design of the Prototype Fast Breeder Reactor”. In: *Nuclear Eng. Design* 236.7-8 (2006), pp. 852–860. ISSN: 00295493. DOI: 10.1016/j.nucengdes.2005.09.025.

[13] Stanley Corrsin. “On the Spectrum of Isotropic Temperature Fluctuations in an Isotropic Turbulence”. In: *J. Appl. Phys.* 22 (1951), pp. 469–473. DOI: 10.1063/1.1699986.

[14] Bart J. Daly and Francis H. Harlow. “Transport equations in turbulence”. In: *Phys. Fluids* 13.11 (1970), pp. 2634–2649. ISSN: 10706631. DOI: 10.1063/1.1692845.

[15] Matthieu Duponcheel et al. “Assessment of RANS and improved near-wall modeling for forced convection at low Prandtl numbers based on les up to Ret = 2000”. In: *Int. J. Heat Mass Trans.* 75 (2014), pp. 470–482. ISSN: 00179310. DOI: 10.1016/j.ijheatmasstransfer.2014.03.080. URL: http://dx.doi.org/10.1016/j.ijheatmasstransfer.2014.03.080.

[16] Paul A. Durbin. “On the k-3 stagnation point anomaly”. In: *Int. J. Heat Fluid Flow* 17.1 (1996), pp. 89–90. ISSN: 0142727X. DOI: 10.1016/0142-727X(95)00073-Y.

[17] Thomas M. Eidson. “Numerical simulation of the turbulent Rayleigh-Bérnard problem using subgrid modelling”. In: *J. Fluid Mech.* 158 (1985), pp. 245–268. DOI: 10.1017/S0022112085002634.

[18] Said Elghobashi and Brian E. Launder. “Turbulent time scales and the dissipation rate of temperature variance in the thermal mixing layer”. In: *Phys. Fluids* 26.9 (1983), pp. 2415–2419. ISSN: 10706631. DOI: 10.1063/1.864426.

[19] Richard Farran and Nilanjan Chakraborty. “A direct numerical simulation-based analysis of entropy generation in turbulent premixed flames”. In: *Entropy* 15.5 (2013), pp. 1540–1566. ISSN: 10994300. DOI: 10.3390/e15051540.

[20] Dmitry Goryntsev et al. “Analysis of cycle variations of liquid fuel-air mixing processes in a realistic DIS IC-engine using Large Eddy Simulation”. In: *Int. J. Heat Fluid Flow* 31 (2010), pp. 845–849. DOI: 10.1016/j.ijheatfluidflow.2010.04.012.

[21] Dmitry Goryntsev et al. “Application of LES for Analysis of Unsteady Effects on Combustion Processes and Misfires in DISI Engine”. In: *Oil Gas Sci. Technol. - Rev. IFP Energies nouvelles* 69.1 (2014), pp. 129–140. DOI: 10.2516/ogst/2013125.

[22] Christopher J. Greenshields. *OpenFOAM Programmer’s Guide Version 3.0.1*. URL: http://foam.sourceforge.net/docs/Guides-a4/ProgrammersGuide.pdf.

[23] Mikhail S. Gritskevich et al. “Development of DDES and IDDES formulations for the k-ω shear stress transport model”. In: *Flow, Turb. and Combustion* 88.3 (2012), pp. 431–449. ISSN: 13866184. DOI: 10.1007/s10494-011-9378-4.

[24] Günther Grötzbach. “Anisotropy and Buoyancy in Nuclear Turbulent Heat Transfer – Critical Assessment and Needs for Modelling”. In: *Forschungszentrum Karlsruhe in der Helmholtz-Gemeinschaft* (2007).

[25] Günther Grötzbach. “Challenges in low-Prandtl number heat transfer simulation and modelling”. In: *Nuclear Eng. Design* 264 (2013), pp. 41–55. ISSN: 00295493. DOI: 10.1016/j.nucengdes.2012.09.039. URL: http://dx.doi.org/10.1016/j.nucengdes.2012.09.039.

[26] Kemal Hanjalić. “Modelling of Buoyancy Driven Turbulent Flows”. In: *ER-COFTAC / IAHR Workshop on Refined Turb. Modelling* (2008), pp. 1–27.

[27] Kemal Hanjalić and Brian E. Launder. *Modelling Turbulence in Engineering and the Environment*. Cambridge University Press, 2011. ISBN: 9781139013314. DOI: https://doi.org/10.1017/CBO9781139013314.

[28] Kemal Hanjalić, Mirza Popovac, and Muhamed Hadžiabdić. “A robust near-wall elliptic-relaxation eddy-viscosity turbulence model for CFD”. In: *Int. J. Heat Fluid Flow* 25.6 (2004), pp. 1047–1051. ISSN: 0142727X. DOI: 10.1016/j.ijheatfluidflow.2004.07.005.

[29] Christian Hasse, V Sohm, and B Durst. “Numerical investigation of cyclic variations in gasoline engines using a hybrid URANS/LES modeling approach”. In: *Comput. Fluids* 39 (2010), pp. 922–929. DOI: 10.1016/j.compfluid.2009.07.001.

[30] Seyyed Mostafa Hosseinalipour et al. “On the effects of convecting entropy waves on the combustor hydrodynamics”. In: *Applied Thermal Eng.* 110 (2017), pp. 901–909. ISSN: 13594311. DOI: 10.1016/j.applthermaleng.2016.08.220. URL: http://dx.doi.org/10.1016/j.applthermaleng.2016.08.220.

[31] Ying Huai. “Large eddy simulation in the scalar field”. PhD thesis. Technische Universität Darmstadt, 2006.

[32] *Implementation Guide LienCubicKE*. URL: https://personalpages.manchester.ac.uk/staff/david.d.apsley/turbmod.pdf.

[33] Nuri Z. Ince and Brian E. Launder. “On the Computation of Buoyancy-Driven Turbulent Flows in Closed Cavities”. In: *Int. J. Heat Fluid Flow* 10.TFD/87/9 (1987), pp. 110–117.

[34] Raad Issa. “Solution of the implicitly discretised fluid flow equations by operator-splitting”. In: *J. Comput. Phys.* 62 (1985), pp. 40–65. DOI: 10.1016/0021-9991(86)90099-9.

[35] Farhard A. Jaberi and Paul J. Colucci. “Large eddy simulation of heat and mass transport in turbulent flows. Part 2: scalar field”. In: *Int. J. Heat Mass Trans.* 46 (2003), pp. 1827–1840. DOI: 10.1016/S0017-9310(02)00485-4.

[36] Yu Ji et al. “Entropy generation analysis and performance evaluation of turbulent forced convective heat transfer to nanofluids”. In: *Entropy* 19.3 (2017), pp. 1–18. ISSN: 10994300. DOI: 10.3390/e19030108.

[37] Yan Jin and Heinz Herwig. “Turbulent flow and heat transfer in channels with shark skin surfaces: Entropy generation and its physical significance”. In: *Int. J. Heat Mass Trans.* 70 (2014), pp. 10–22. ISSN: 00179310. DOI: 10.1016/j.ijheatmasstransfer.2013.10.063. URL: http://dx.doi.org/10.1016/j.ijheatmasstransfer.2013.10.063.

[38] Hiroshi Kawamura, Hiroyuki Abe, and Kenji Shingai. “DNS of turbulence and heat transport in a channel flow with different Reynolds and Prandtl numbers and boundary conditions”. In: *Turb. Heat Mass Trans.* July (2000), pp. 15–32.

[39] Hiroshi Kawamura, Abe Hiroyuki, and Yuichi Matsuo. “DNS of turbulent heat transfer in channel flow with respect to Reynolds and Prandtl number effects”. In: *Int. J. Heat Fluid Flow* 20 (1999), pp. 196–207.

[40] Hiroshi Kawamura et al. “DNS of turbulent heat transfer in channel flow with low to medium-high Prandtl number fluid”. In: *Int. J. Heat Fluid Flow* 19 (1998), pp. 482–491.

[41] Joseph H. Keenan. “Availability and irreversibility in thermodynamics”. In: *British J. Applied Phy.* 2.7 (1951), pp. 183–192. ISSN: 05083443. DOI: 10.1088/0508-3443/2/7/302.

[42] Sasa Kenjereš. *Numerical Modelling of Complex Buoyancy-Driven Flows*. University Delft, 1999, p. 278. ISBN: 9090124284.

[43] Sasa Kenjereš, S. B. Gunarjo, and Kemal Hanjalić. “Contribution to elliptic relaxation modelling of turbulent natural and mixed convection”. In: *Int. J. Heat Fluid Flow* 26.4 SPEC. ISS. (2005), pp. 569–586. ISSN: 0142727X. DOI: 10.1016/j.ijheatfluidflow.2005.03.007.

[44] Sasa Kenjereš and Kemal Hanjalić. “Convective rolls and heat transfer in finite-length Rayleigh-Bénard convection: A two-dimensional numerical study”. In: *Phy. Review* 62.6 (2000), pp. 7987–7998. ISSN: 1063651X. DOI: 10.1103/PhysRevE.62.7987.

[45] Sasa Kenjereš and Kemal Hanjalić. “Prediction of turbulent thermal convection in concentric and eccentric horizontal annuli”. In: *Int. J. Heat Fluid Flow* 16.5 (1995), pp. 429–439. ISSN: 0142727X. DOI: 10.1016/0142-727X(95)00051-Q.

[46] Arshad Khan et al. “Irreversibility analysis in unsteady flow over a vertical plate with arbitrary wall shear stress and ramped wall temperature”. In: *Results in Phy.* 8 (2018), pp. 1283–1290. ISSN: 22113797. DOI: 10.1016/j.rinp.2017.12.032. URL: https://doi.org/10.1016/j.rinp.2017.12.032.

[47] P. Kiš and Heinz Herwig. “Natural convection in a vertical plane channel: DNS results for high Grashof numbers”. In: *Heat Mass Trans.* 50.7 (2014), pp. 957–972. ISSN: 14321181. DOI: 10.1007/s00231-014-1305-5.

[48] Markus Klein. “Towards LES as an engineering tool”. Habilitation. Technische Universität Darmstadt, 2008.

[49] Markus Klein, Amsini Sadiki, and Johannes Janicka. “A digital filter based generation of inflow data for spatially developing direct numerical or large eddy simulations”. In: *J. Comput. Phys.* 186 (2003), pp. 652–665. DOI: 10.1016/S0021-9991(03)00090-1.

[50] Ulrich Kleinhans et al. “Ash formation and deposition in coal and biomass fired combustion systems: Progress and challenges in the field of ash particle sticking and rebound behavior”. In: *Progress in Energy and Combustion Sc.* 68

(2018), pp. 65–168. ISSN: 03601285. DOI: 10.1016/j.pecs.2018.02.001. URL: https://doi.org/10.1016/j.pecs.2018.02.001.

[51] Fabian Kock. *Bestimmung der lokalen Entropieproduktion in turbulenten Stroemungen und deren Nutzung zur Bewertung konvektiver Transportprozesse*. Shaker Verlag, 2003. ISBN: 3832220585.

[52] Fabian Kock and Heinz Herwig. "Local entropy production in turbulent shear flows: A high-Reynolds number model with wall functions". In: *Int. J. Heat Mass Trans.* 47.10-11 (2004), pp. 2205–2215. ISSN: 00179310. DOI: 10.1016/j.ijheatmasstransfer.2003.11.025.

[53] Chi-Ming Lam and Klaus Bremhorst. "A modified form of the k-ϵ model for predicting wall turbulence". In: *J. of Fluids Eng.* 103.3 (1981), pp. 456–460. ISSN: 1528901X. DOI: 10.1115/1.3240815.

[54] Brian E. Launder. "Heat and Mass Transport". In: *Topics in Applied Physics: Turb.* (1976), pp. 231–287.

[55] Brian E. Launder. "On the Computation of Convective Heat Transfer in Complex Turbulent Flows". In: *J. Heat Trans.* 110.4b (1988), p. 1112. ISSN: 00221481. DOI: 10.1115/1.3250614.

[56] Brian E. Launder and Brian I. Sharma. "Application of the energy-dissipation model of turbulence to the calculation of flow near a spinning disc". In: *Letters in Heat and Mass Trans.* 1.2 (1974), pp. 131–137. ISSN: 00944548. DOI: 10.1016/0094-4548(74)90150-7. arXiv: arXiv:1011.1669v3.

[57] Fue-Sang Lien, Wen-Lih Chen, and Michael A. Leschziner. "Low-Reynolds-Number Eddy-Viscosity Modelling Based on Non-Linear Stress-Strain/Vorticity Relations". In: *Eng. Turb. Modelling and Experiments* (1996), pp. 91–100. DOI: 10.1016/b978-0-444-82463-9.50015-0.

[58] Douglas K. Lilly. "A proposed modification of the Germano subgrid-scale closure method". In: *Phys. Fluids* 4.3 (1992), pp. 633–635. DOI: 10.1063/1.858280.

[59] Oluwole D. Makinde. “Entropy analysis for MHD boundary layer flow and heat transfer over a flat plate with a convective surface boundary condition”. In: *Int. J. Exergy* 10.2 (2012), p. 142. ISSN: 1742-8297. DOI: 10.1504/ijex.2012.045862.

[60] Sandro Manservisi and Filippo Menghini. “A CFD four parameter heat transfer turbulence model for engineering applications in heavy liquid metals”. In: *Int. J. Heat Mass Trans.* 69 (2013), pp. 312–326. ISSN: 00179310. DOI: 10.1016/j.ijheatmasstransfer.2013.10.017.

[61] Florian R. Menter and Thomas Esch. “Elements of Industrial Heat Transfer Predictions”. In: *XVI Congresso Mech. Eng.* 2001.

[62] Robert N. Meroney. “An algebraic stress model for stratified turbulent shear flows”. In: *Computers and Fluids* 4.2 (1976), pp. 93–107. ISSN: 00457930. DOI: 10.1016/0045-7930(76)90015-3.

[63] Parviz Moin et al. “A dynamic subgrid-scale model for compressible turbulence and scalar transport”. In: *Phys. Fluids* 3 (1991), pp. 2746–2757. DOI: 10.1063/1.858164.

[64] Hagen Müller, Bassam A. Younis, and Bernhard Weigand. “Development of a compact explicit algebraic model for the turbulent heat fluxes and its application in heated rotating flows”. In: *Int. J. Heat Mass Trans.* 86 (2015), pp. 880–889. ISSN: 00179310. DOI: 10.1016/j.ijheatmasstransfer.2015.03.059.

[65] Yang Na and Thomas J. Hanratty. “Limiting behavior of turbulent scalar transport close to a wall”. In: *Int. J. Heat Mass Trans.* 43.10 (2000), pp. 1749–1758. ISSN: 00179310. DOI: 10.1016/S0017-9310(99)00258-6.

[66] Yasutaka Nagano. *Modelling Heat Transfer in Near-Wall Flows*. Cambridge University Press, 2010, pp. 188–247. ISBN: 9780511755385. DOI: 10.1017/cbo9780511755385.008.

[67] Franck Nicoud et al. “Using singular values to build a subrid-scale model for large eddy simulations”. In: *Phys. Fluids* 23 (2011), p. 85106. DOI: 10.1063/1.3623274.

[68] Kaushal Nishad et al. “LES Based Modeling and Simulation of Spray Dynamics including Gasoline Direct Injection (GDI) Processes using KIVA-4 Code”. In: *SAE 2012 World Congress & Exhibition*. SAE International, 2012. DOI: 10.4271/2012-01-1257.

[69] Kaushal Nishad et al. “Numerical Investigation of Flow through a Valve during Charge Intake in a DISI-Engine using Large Eddy Simulation”. In: *Energies* 12.13 (2019), p. 2620. DOI: 10.3390/en12132620.

[70] OECD Nuclear Energy Agency. “Handbook on Lead-bismuth Eutectic Alloy and Lead Properties, Materials Compatibility, Thermal- hydraulics and Technologies”. In: *OECD-NEA handbook, Chapter 9* (2015), pp. 617–646. DOI: ISBN978-92-64-99002-9.

[71] OECD Nuclear Energy Agency. *Technology Roadmap Update for Generation IV Nuclear Energy Systems: Preparing Today for Tomorrow’s Energy Needs*. Tech. rep. 2014. URL: https://www.gen-4.org/gif/upload/docs/application/pdf/2014-03/gif-tru2014.pdf.

[72] Alexander M. Obukhov. *Structure of the temperature field in turbulent flow*. Tech. rep. DTIC Document, 1968.

[73] Nora A. Okong’o and Josette Bellan. “Direct numerical simulation of a transitional supercritical binary mixing layer: Heptane and nitrogen”. In: *J. Fluid Mech.* 464 (2002), pp. 1–34. ISSN: 00221120. DOI: 10 . 1017 / S0022112002008480.

[74] OpenFOAM. *Block Mesh*. 2020. URL: https://cfd.direct/openfoam/user-guide/v8-blockMesh/.

[75] Ivan Otić. “One equation subgrid model for liquid metal forced convection”. In: *The 8th International Topical Meeting on Nuclear Reactor Thermal-Hydraulics*. Shanghai, 2010.

[76] Ivan Otić and Günther Grötzbach. “Turbulent heat flux and temperature variance dissipation rate in natural convection in lead-bismuth”. In: *Nuclear Sc. Eng.* 155.3 (2007). ISSN: 00295639. DOI: 10.13182/NSE07-A2679.

[77] Ivan Otić, Günther Grötzbach, and Martin Woerner. “Analysis and modelling of the temperature variance equation in turbulent natural convection for low-Prandtl-number fluids”. In: *J. Fluid Mech.* 525 (2004), pp. 237–261. ISSN: 00221120. DOI: 10.1017/S0022112004002733.

[78] Dario Paes et al. “Study of asphaltene deposition in wellbores during turbulent flow”. In: *J. Petroleum Sc. Eng.* 129 (2015), pp. 77–87. ISSN: 09204105. DOI: 10.1016/j.petrol.2015.02.010. URL: http://dx.doi.org/10.1016/j.petrol.2015.02.010.

[79] Pradeep Pantangi, Ying Huai, and Amsini Sadiki. “Mixing Analysis and Optimization in Jet Mixer Systems by Means of Large Eddy Simulation”. In: *Micro and Macro Mixing* (2010), pp. 205–226.

[80] Suhas V. Patankar, Cheng H. Liu, and Ephraim Sparrow. “Fully Developed Flow and Heat Transfer in Ducts Having Streamwise-Periodic Variations of Cross-Sectional Area”. In: *J. Heat Trans.* 99.2 (1977), p. 180. ISSN: 00221481. DOI: 10.1115/1.3450666. URL: http://heattransfer.asmedigitalcollection.asme.org/article.aspx?articleid=1436662.

[81] Suhas V. Patankar and Dudley Spalding. “A calculation procedure for heat, mass and momentum transfer in three-dimensional parabolic flows”. In: *Int. J. Heat Mass Trans.* 15 (1972), pp. 1787–1806. DOI: 10.1016/0017-9310(72)90054-3.

[82] Shia-Hui Peng and Lars Davidson. “On a subgrid-scale heat flux model for large eddy simulation of turbulent thermal flow”. In: *Int. J. Heat Mass Trans.* 45 (2002), pp. 1393–1405. DOI: 10.1016/S0017-9310(01)00254-X.

[83] Marzio Piller. “Direct numerical simulation of turbulent forced convection in a pipe”. In: *Int. J. for Numerical Methods in Fluids* 49.6 (2005), pp. 583–602. ISSN: 0271-2091. DOI: 10.1002/fld.994.

[84] Thierry Poinsot and Denis Veynante. *Theoretical and Numerical Combustion*. 3rd ed. by the authors, 2017. DOI: 978-2-7466-3990-4.

[85] Stehphen B. Pope. *Turbulent Flows*. Cambridge University Press, 2009. ISBN: 978-0-521-59886-6.

[86] Fernando Porté-Agel et al. “Atmospheric stability effect on subgrid-scale physics for large-eddy simulation”. In: *Adv. Water Resour.* 24 (2001), pp. 1085–1102. DOI: 10.1016/S0309-1708(01)00039-2.

[87] Amin Rasam, Geert Brethouwer, and Arne V. Johansson. “An explicit algebraic model for the subgrid-scale passive scalar flux”. In: *J. Fluid Mech.* 66 (2017), pp. 541–577. DOI: 10.1016/j.ijheatfluidflow.2017.06.007.

[88] Janardhana G. Reddy et al. “Colloidal study of unsteady magnetohydrodynamic couple stress fluid flow over an isothermal vertical flat plate with entropy heat generation”. In: *J. Molecular Liquids* 252 (2018), pp. 169–179. ISSN: 01677322. DOI: 10.1016/j.molliq.2017.12.106. URL: https://doi.org/10.1016/j.molliq.2017.12.106.

[89] Florian Ries, Johannes Janicka, and Amsini Sadiki. “Thermal transport and entropy production mechanisms in a turbulent round jet at supercritical thermodynamic conditions”. In: *Entropy* 19.8 (2017). ISSN: 10994300. DOI: 10.3390/e19080404.

[90] Florian Ries et al. “Database of near-wall turbulent flow properties of a jet impinging on a solid surface under different inclination angles”. In: *Fluids* 3.1 (2018), p. 5. ISSN: 23115521. DOI: 10.3390/fluids3010005.

[91] Florian Ries et al. “Entropy Generation Analysis and Thermodynamic Optimization of Jet Impingement Cooling Using Large Eddy Simulation”. In: *Entropy* 21.2 (2019), p. 129. ISSN: 1099-4300. DOI: 10.3390/e21020129. URL: http://www.mdpi.com/1099-4300/21/2/129.

[92] Florian Ries et al. “Evaluating large eddy simulation result based on error analysis”. In: *Theor. Comp. Fluid Dyn.* (2018). DOI: 10.1007/s00162-018-0474-0.

[93] Florian Ries et al. “Near-wall thermal processes in an inclined impinging jet: analysis of heat transport and entropy generation mechanisms”. In: *Energies* 11.6 (2018). ISSN: 19961073. DOI: 10.3390/en11061354.

[94] Florian Ries et al. “Numerical analysis of turbulent flow dynamics and heat transport in a round jet at supercritical conditions”. In: *Int. J. Heat Fluid Fl.* 66 (2017), pp. 172–184. DOI: 10.1016/j.ijheatfluidflow.2017.06.007.

[95] Wolfgang Rodi. “The predictions of free turbulent boundary layers by use of a two-equation model of turbulence”. In: (1972).

[96] Ferry Roelofs et al. “Status and perspective of turbulence heat transfer modelling for the industrial application of liquid metal flows”. In: *Nuclear Eng. Design* 290.March 2011 (2015), pp. 99–106. ISSN: 00295493. DOI: 10.1016/j.nucengdes.2014.11.006.

[97] Christopher Rutland. “Large-eddy simulations for internal combustion engines - A review”. In: *Int. J. Engine Res.* 12 (2011). DOI: 0.1177/1468087411407248.

[98] Amsini Sadiki and Kolumban Mutter. “On thermodynamics of turbulence: development of first order closure models and critical evaluation of existing models”. In: *J. Non-Equilibrium Thermodynamics* 25.2 (2000), pp. 131–160. ISSN: 03400204. DOI: 10.1515/JNETDY.2000.009.

[99] Ideen Sadrehaghighi. “Mesh Generation in CFD”. In: *CFD Open Series* July 2018 (2017), p. 151. DOI: 10.13140/RG.2.2.26522.54721/2.

[100] Pierre Sagaut. *Large Eddy Simulation for incompressible Flows: An Introduction*. Springer-Verlag Berlin Heidelberg New York, 2006. ISBN: 978-3-540-26344-9.

[101] Rohit Saini et al. "Entropy Effects of Near Wall Modeling in the Improved-Delayed-Detached-Eddy-Simulation Methodology". In: *Entropy* (2018). DOI: 10.3390/e20100771.

[102] Maria Vittoria Salvetti and Sanjoy Banerjee. "A priori tests of a new dynamic subgrid-scale model for finite-difference large-eddy simulation". In: *Phys. Fluids* 7 (1995), pp. 2831–2847. DOI: 10.1063/1.868779.

[103] Khalid M. Saqr et al. "CFD modelling of entropy generation in turbulent pipe flow: Effects of temperature difference and swirl intensity". In: *Applied Thermal Eng.* 100 (2016), pp. 999–1006. ISSN: 13594311. DOI: 10.1016/j.applthermaleng.2016.02.014. URL: http://dx.doi.org/10.1016/j.applthermaleng.2016.02.014.

[104] Bastian Schmandt and Heinz Herwig. "Diffuser and nozzle design optimization by entropy generation minimization". In: *Entropy* 13.7 (2011), pp. 1380–1402. ISSN: 10994300. DOI: 10.3390/e13071380.

[105] Helmut Schmidt and Ulrich Schumann. "Coherent structure of the convective boundary layer derived from large-eddy simulations". In: *J. Fluid Mech.* 200 (1989), pp. 511–562. DOI: 10.1017/S0022112089000753.

[106] Thomas Schulenberg and Robert Stieglitz. "Flow measurement techniques in heavy liquid metals". In: *Nuclear Eng. Design* 240.9 (2010), pp. 2077–2087. ISSN: 00295493. DOI: 10.1016/j.nucengdes.2009.11.017. URL: http://dx.doi.org/10.1016/j.nucengdes.2009.11.017.

[107] Afaque Shams et al. "Assessment and calibration of an algebraic turbulent heat flux model for low-Prandtl fluids". In: *Int. J. Heat Mass Trans.* 79 (2014), pp. 589–601. ISSN: 00179310. DOI: 10.1016/j.ijheatmasstransfer.2014.08.018. URL: http://dx.doi.org/10.1016/j.ijheatmasstransfer.2014.08.018.

[108] Mohsen Shehata and Donald M. McEligot. “Mean strucure in viscous layer of strongly-heated internal gas flows. Measurements”. In: *Int. J. Heat Mass Trans.* 41 (1998), pp. 4297–4313. DOI: 10.1016/S0017-9310(98)00088-X.

[109] Ronald M. C. So and Charles G. Speziale. “A Review of Turbulent Heat Transfer Modeling”. In: *Ann. Rew. Heat Trans.* 10.10 (1999), pp. 177–220. ISSN: 1049-0787. DOI: 10.1615/annualrevheattransfer.v10.70.

[110] Thomas P. Sommer, Ronald M. C. So, and H. S. Zhang. “Heat Transfer Modeling and the Assumption of Zero Wall Temperature Fluctuations”. In: *J. Heat Trans.* 116.4 (1994), p. 855. ISSN: 00221481. DOI: 10.1115/1.2911459.

[111] Philippe R. Spalart and V. Venkatakrishnan. “On the role and challenges of CFD in the aerospace industry”. In: *Aeronautical J.* 120.1223 (2016), pp. 209–232. ISSN: 00019240. DOI: 10.1017/aer.2015.10.

[112] Joseph H. Spurk and Aksel Nuri. *Strömungslehre - Einführung in die Theorie der Strömungen*. 2010. ISBN: 9783642131424. DOI: 10.1007/978-3-642-13143-1.

[113] Iztok Tiselj et al. “Effect of wall boundary condition on scalar transfer in a fully developed turbulent flume”. In: *Phys. Fluids* 13.4 (2001), pp. 1028–1039. ISSN: 10706631. DOI: 10.1063/1.1350899.

[114] Mohsen Torabi et al. “Challenges and progress on the modelling of entropy generation in porous media: A review”. In: *Int. J. Heat Mass Trans.* 114 (2017), pp. 31–46. ISSN: 00179310. DOI: 10.1016/j.ijheatmasstransfer.2017.06.021. URL: http://dx.doi.org/10.1016/j.ijheatmasstransfer.2017.06.021.

[115] John C. Vogel and John Eaton. “Combined heat transfer and fluid dynamic measurements downstream of a backward-facing step”. In: *J. Heat Trans.* 107 (1985), pp. 922–929.

[116] Bingchen Wang et al. “A complete and irreducible dynamic sgs heat-flux modelling based on the strain rate tensor for large-eddy simulation of thermal con-

vection". In: *Int. J. Heat Fluid Flow* 28 (2007), pp. 1227–1243. DOI: 10.1016/j.ijheatfluidflow.2007.06.001.

[117] Bingchen Wang et al. "A general dynamic linear tensor-diffusivity subgrid-scale heat flux model for large-eddy simulation of turbulent thermal flows". In: *Numer. Heat Trans.* 51 (2006), pp. 205–227. DOI: 10.1080/10407790601102274.

[118] Bingchen Wang et al. "New dynamic subgrid-scale heat flux models for large-eddy simulation of thermal convection based on the general gradient diffusion hypothesis". In: *J. Fluid Mech.* 604 (2008), pp. 125–163. DOI: 10.1017/S0022112008001079.

[119] Linwei Wang, Nader Karimi, and Manosh C. Paul. "Gas-phase transport and entropy generation during transient combustion of single biomass particle in varying oxygen and nitrogen atmospheres". In: *Int. J. Hydrogen Energy* 43.17 (2018), pp. 8506–8523. ISSN: 03603199. DOI: 10.1016/j.ijhydene.2018.03.074. URL: https://doi.org/10.1016/j.ijhydene.2018.03.074.

[120] Linwei Wang et al. "Numerical modelling of unsteady transport and entropy generation in oxy-combustion of single coal particles with varying flow velocities and oxygen concentrations". In: *Applied Thermal Eng.* 144 (2018), pp. 147–164. ISSN: 13594311. DOI: 10.1016/j.applthermaleng.2018.08.040. URL: https://doi.org/10.1016/j.applthermaleng.2018.08.040.

[121] Wei Wang et al. "Entropy generation analysis of fully-developed turbulent heat transfer flow in inward helically corrugated tubes". In: *Num. Heat Trans.; Part A: Applications* 73.11 (2018), pp. 788–805. ISSN: 15210634. DOI: 10.1080/10407782.2018.1459137. URL: https://doi.org/10.1080/10407782.2018.1459137.

[122] Zellman Warhaft. "Passive Scalars in Turbulent Flows". In: *Annual Rev. Fluid Mech.* 32.2 (2000), pp. 203–240.

[123] Vince Wong and Douglas K. Lilly. “A comparison of two dynamic subgrid closure methods for turbulent thermal convection”. In: *Phys. Fluids* 6 (1995), pp. 1016–1023. DOI: 10.1063/1.868335.

[124] Bassam A. Younis, Charles G. Speziale, and Timothy T. Clark. “A rational model for the turbulent scalar fluxes”. In: *Proceedings of the Royal Society A: Math., Physical and Eng. Sc.* 461.2054 (2005), pp. 575–594. ISSN: 14712946. DOI: 10.1098/rspa.2004.1380.

[125] Matthias Ziefuss and Amirfarhang Mehdizadeh. “A comprehensive assessment of the Reynolds Analogy in predicting heat transfer in turbulent wall-bounded shear flows”. In: *Int. J. Heat Fluid Fl.* 81.January (2020), p. 108527. ISSN: 0142727X. DOI: 10.1016/j.ijheatfluidflow.2019.108527. URL: https://doi.org/10.1016/j.ijheatfluidflow.2019.108527.

[126] Matthias Ziefuss et al. “Entropy generation assessment for wall-bounded turbulent shear flows based on reynolds analogy assumptions”. In: *Entropy* 21.12 (2019), pp. 1–26. ISSN: 10994300. DOI: 10.3390/e21121157.

VITA

Matthias Ziefuss was born on December 22nd, 1989 in Iserlohn in Germany. He grew up in the same city and graduated from Stenner Gymnasium in 2009. Then, Mr. Ziefuss attended the Rheinisch-Westfälische Technische Hochschule Aachen, where he earned his Bachelor of Science in Computational Engineering Science 2015. While working as a science assistant at the Fraunhofer Institute for Production Technology, he earned 2017 his Master of Science in Computational Engineering Science with a focus on rocket science and thermal-fluid dynamics. In 2018, he started his Ph.D. at the UMKC.